On Natural Convection in a Large Civil Gas Turbine



Daniel Fahy
St. Catherine's College

A thesis submitted for the degree of

Doctor of Philosophy

Trinity 2020

Department of Engineering Science

University of Oxford

Abstract

As a large civil gas turbine is cooling following operation, natural convective flows develop, which can lead to numerous issues. The ability to predict and understand this transient shutdown cooling cycle is becoming increasingly more important. However, this has proven to be extremely difficult owing to the complex nature of the flow physics and its dependency on a large number of parameters.

Two sophisticated experimental facilities that simulate the natural convective flow field during shutdown cooling of a large civil gas turbine, have been designed and commissioned. This has allowed for the influence of numerous features to be investigated, which has helped to increase understanding of these flow fields. Furthermore, a robust thermocouple probe has been developed that allows for accurate measurements in a natural convective boundary layer, along with a novel method of determining heat flux fluctuations.

An extensive experimental study has shown that the overall heat transfer in a non-isothermal concentric annulus is adequately captured by isothermal correlations when the area-averaged temperature difference is used, as the local heat flux is dominated by the local radial temperature gradient. This finding was validated up to a diameter ratio of 1.5, which is applicable to the majority of the main gas path.

The interaction between the induced draft in the main gas path (due to natural convection) and obstructions in this area has been proven to be critical in defining the severity of thermal rotor bow – the thermal gradient that develops across the rotor drum during shutdown. Two viable solutions to help alleviate rotor bow have been developed: jet impingement cooling at the top of the annulus, and circumferentially non-uniform emissivity distributions.

Acknowledgements

Firstly, I would like to sincerely thank Prof. Peter Ireland for his supervision and guidance throughout this project. His support and belief has allowed me to thrive and grow as an engineer.

Without the amazing staff at the Oxford Thermofluids Institute, this project would not have been possible. The administration, workshop, instrumentation, IT and maintenance teams have helped me enormously with their consistent, high-quality work.

I would like to thank Rolls-Royce plc. and EPSRC for funding this work. Thanks also to the many engineers at Rolls-Royce that I have had the pleasure to deal with in the last four years. A special mention to Dr. Leo Lewis for his keen interest and advice.

I had the pleasure of working closely with Dr. Andrew Dann and Dr. Priyanka Dhopade during this work. I gained a wealth of knowledge from this and I am extremely thankful to have had that opportunity.

I would like to thank my friends in the lab for making this whole experience so enjoyable – with a special mention to Dr. Alex Murray and Dr. Andrew Pilkington for their help and guidance, and also to the CDT cohort.

I would also like to thank my parents and brother, and my dear grandmother for always supporting me.

Finally, and most importantly, I would like to wholeheartedly thank my beautiful wife-to-be, Samantha. She has been my biggest supporter and encourager. I dedicate this thesis to you.

Contents

List of Figures **v**

List of Tables **x**

Nomenclature **xi**

1 Introduction **1**
1.1 Background . . . 1
1.2 Scope of Project . . . 4
1.3 Contributions of Work . . . 5
1.4 Layout of Thesis . . . 7

2 Literature Review **9**
2.1 Natural Convection Basics . . . 9
2.2 Overview of Relevant Natural Convection Research . . . 12
2.2.1 Flow Structure in a Cylindrical Annulus . . . 12
2.2.2 Heat Transfer Correlations . . . 13
2.2.3 Transition to Turbulence . . . 17
2.2.4 Alternative Configurations . . . 18
2.3 Natural Convection in Gas Turbines . . . 21
2.4 Conclusions . . . 24

3 Experimental Facility Design **26**
3.1 Scaling . . . 26
3.2 Facility Overview . . . 29
3.2.1 ExCITE Shutdown Facility . . . 29
3.2.2 RoBo Facility . . . 30
3.3 Thermal Boundary Condition Control . . . 33
3.4 Infrared Thermography . . . 37
3.4.1 Calibration Methods . . . 39
3.4.2 Directional Emissivity Calculation . . . 42
3.5 Radiation Flux Calculation . . . 43
3.6 Conclusions . . . 46

4 Temperature Traverse Probe Design **47**

4.1 Introduction . . . 47
4.1.1 Thermocouple Operating Principle . . . 48
4.2 3D Conjugate Probe Simulation . . . 50
4.2.1 Model Definition . . . 51
4.2.2 Results . . . 53
4.3 1D Conduction Model Investigation . . . 56
4.3.1 Model Definition . . . 56
4.3.2 Initial Results . . . 60
4.3.3 Parameter Investigation . . . 63
4.4 Experimental Validation . . . 64
4.5 Conclusions . . . 66

5 Commissioning 68
5.1 Initial Testing . . . 68
5.1.1 RoBo Facility . . . 68
5.1.2 ExCITE Facility . . . 70
5.2 Heat Flux Measurements . . . 71
5.2.1 Temperature Traverses . . . 71
5.2.2 Radiation . . . 75
5.2.3 IR Camera Measurements . . . 76
5.3 Conclusions . . . 77

6 Thermal Boundary Condition Study 78
6.1 Introduction . . . 78
6.2 Concentric Cylinder Study . . . 81
6.2.1 Non-Isothermal Boundary Conditions . . . 81
6.2.2 Diameter Ratio Effects . . . 89
6.3 Conical Geometry . . . 91
6.4 Overall Heat Transfer . . . 93
6.5 Conclusions . . . 96

7 Natural Convection in a Large Cylindrical Annulus 97
7.1 Introduction . . . 97
7.2 Steady-State Results . . . 98
7.2.1 Temperature Profiles . . . 98
7.2.2 Heat Transfer . . . 101
7.3 Unsteady Measurements . . . 103
7.3.1 Theory . . . 103
7.3.2 Experimental Results . . . 104
7.3.3 Comparison to CFD . . . 105
7.4 Obstructions . . . 109
7.5 Conclusions . . . 110

8 Installation Effects on Rotor Bow 112
8.1 Introduction . . . 112
8.2 Open-Ended Annulus Effects . . . 112
8.2.1 Steady-State Measurements . . . 112

8.2.2 Transient Measurements . . . 116
8.3 Obstruction Effects . . . 121
8.4 Conclusions . . . 127

9 Shutdown Cooling Model Development 129
9.1 Introduction . . . 129
9.2 Model Definition . . . 129
9.3 Comparison to RoBo Tests . . . 135
9.4 Extension to Engine . . . 136
9.4.1 Uniform Starting Temperatures . . . 139
9.4.2 Non-Uniform Starting Temperature . . . 144
9.4.3 Outer Casing Heat Flux Alterations . . . 146
9.5 Conclusions . . . 149

10 Rotor Bow Mitigation Strategies 152
10.1 Introduction . . . 152
10.2 Forced Air Flow . . . 152
10.2.1 Experimental Results . . . 153
10.2.2 Numerical Model . . . 157
10.2.2.1 Jet Impingement Shutdown Model Modification . . . 157
10.2.2.2 Model Validation . . . 160
10.2.2.3 Engine Conditions . . . 161
10.3 Emissivity Distribution . . . 165
10.3.1 Experimental Results . . . 166
10.3.2 Numerical Model . . . 169
10.3.2.1 Model Validation . . . 170
10.3.2.2 Engine Conditions . . . 170
10.4 Periodic Rotations . . . 174
10.5 Conclusions . . . 177

11 Auxiliary Zone Cooling 179
11.1 Introduction . . . 179
11.2 Port Venting . . . 180
11.3 End Wall Venting . . . 182
11.4 Heat Flux Fluctuations . . . 185
11.5 Transient Cooling Effects . . . 187
11.6 Conclusions . . . 189

12 Conclusions and Future Work 191
12.1 Conclusions . . . 191
12.2 Future Work . . . 194
12.3 Final Remarks . . . 195

References 196

A Correlation for Natural Convection in a Horizontal Annulus 209

B Uncertainty Analysis 212

B.1 Convective heat flux 212
B.2 Radiative Heat Flux 214

List of Figures

1.1 Cross-sectional schematic of a typical large civil gas turbine highlighting the two areas where natural convective flows are of interest. . . . 3
1.2 Typical evolution of rotor thermal gradient during shutdown. 4

2.1 Typical velocity and temperature boundary layer profiles for natural convection from a heated vertical plate. 11
2.2 Schematic of the typical natural convective flow features present in a laminar, moderate diameter ratio concentric annulus with a hotter inner surface. 13
2.3 Schematic of the equivalent conductivity in a horizontal annulus . . . 15
2.4 Local Nusselt number variation for natural convection from a horizontal cylinder. 22
2.5 Schematic of the typical natural convective flow features present in industrial gas turbines during shutdown. Recreated from [85]. 23

3.1 All possible values of Ra_{D_i} experienced in an engine auxiliary zone during the shutdown period. 28
3.2 Rayleigh number vs. inner surface temperature. 29
3.3 Design overview of the ExCITE shutdown facility 31
3.4 Design overview of the RoBo facility. 34
3.5 The ExCITE shutdown facility. 35
3.6 The RoBo facility. 35
3.7 Heater control loop system schematic. 36
3.8 Heater Mat locations of both experimental facilities. 38
3.9 Thermocouple locations on the outer cylinder of the ExCITE shutdown facility. 39
3.10 Schematic of the components of thermal radiation that will be detected by the IR camera. 40
3.11 Flat-plate calibration piece in the ExCITE facility. 42
3.12 Measured directional emissivity of painted Rohacell and aluminium. . 43
3.13 Schematic of how the view factor is determined using Hottel's crossed-string method [44]. 44
3.14 Simplified schematic of a radiosity resistance network that is used to find the radiation heat flux in a concentric annulus. 44

4.1 Schematic of possible thermocouple wire arrangements. 49
4.2 Voltage generated and Seebeck coefficient for type K thermocouples. 50
4.3 Outline of the probe simulation domain. 52
4.4 Section view of the probe domain mesh. 52
4.5 Temperature contour results from the conjugate simulation. 53
4.6 Predicted thermal boundary layer profile for the unobstructed case and the simulated values that would be recorded by the thermocouple probe. 54
4.7 Nusselt number distributions for $d = 300$ μm. 56
4.8 Schematic of how the thermocouple has been discretised into finite volumes. 57
4.9 Schematic of fluid temperature and velocity field used as inputs for the 1D probe model. 58
4.10 Values of Ri that the probe may experience during operation. 59
4.11 Probe 1D model initial results. 61
4.12 1D model wire temperatures and constituent heat fluxes for $L_n = 0$ and 12 mm. 62
4.13 Surface contour giving the temperature error predicted by the 1D model for combinations of ∇T_f and V_f. 63
4.14 Temperature traverse probes that were used for experimental validation of 1D model. 65
4.15 Experimental radial temperature profile for the three different probes 66
4.16 Schematic of temperature probe assembly. 67

5.1 Mat-averaged Nusselt numbers for seven rotation tests of an isolated inner cylinder assembly of the RoBo facility. 69
5.2 Inner cylinder circumferential temperature profile of the RoBo inner surface. 70
5.3 ExCITE shutdown facility initial commissioning results 71
5.4 Example air temperature measurements from the RoBo facility. . . . 72
5.5 Example linear fitting to the conductive sub-layer. 74
5.6 Inner wall circumferential heat flux for three repeats of a test on the RoBo facility. 74
5.7 Effect of inner and outer surface emissivity on the radiative heat transfer between infinite concentric cylinders. 75
5.8 Centreline calibration map of $\tau\varepsilon$ for the five IR cameras (denoted by the markers), for the ExCITE facility. 77

6.1 Cross-sectional schematic of the RoBo experimental facility. 80
6.2 Annular cross-section of the upper area of the RoBo experimental rig. 80
6.3 Definition of the imposed temperature boundary conditions for a given ΔT_c 81
6.4 Measured wall convective heat flux for the Tc test cases. 83
6.5 Radial temperature profiles for Tc test cases. 85
6.6 Schematic of the natural convective flow features present in moderate and narrow diameter ratio concentric annuli, with a hotter inner surface. 86
6.7 RMS of the temperature fluctuations for two Tc cases. 87

6.8 Measured wall convective heat flux for the Bc test cases. 89
6.9 Equivalent conductivity both the Tc and Bc test campaigns. 90
6.10 Inner wall equivalent conductivity for different diameter ratios. . . . 91
6.11 Inner wall equivalent conductivity for various isothermal and non-isothermal test at the conical section with $Dr = 1.50$. 92
6.12 Radial temperature measurements at a conical traverse plane. 94
6.13 Mean equivalent conductivity for isothermal and non-isothermal cases. 95

7.1 Schematic of ExCITE shutdown facility. 98
7.2 Inner surface thermal boundary layers for $Ra_{D_i} = 2.1 \times 10^9$. 99
7.3 Radial temperature measurements at $Ra_{D_i} = 1.5 \times 10^9$ and $Dr = 2$. 100
7.4 Temperature profiles at $Ra_{D_i} = 1.5 \times 10^9$ and $Ra_{D_i} = 2.1 \times 10^9$ . . . 101
7.5 Temperature fluctuations at $Ra_{D_i} = 1.5 \times 10^9$ and $Ra_{D_i} = 2.1 \times 10^9$. 102
7.6 Measured inner surface heat flux distribution from the ExCITE facility. 102
7.7 Mean equivalent conductivity for both facilities. 103
7.8 Example inner surface heat flux fluctuations for $Ra_{D_i} = 2.1 \times 10^9$ and $Dr = 2$. 105
7.9 Comparison of radial temperature profiles between CFD and experiments. 106
7.10 CFD results of the ExCITE facility 107
7.11 CFD and experimental inner surface Nusselt number fluctuations. . . 108
7.12 Standard deviation of inner surface Nusselt number fluctuations. . . 108
7.13 Cross section of ExCITE facility with obstruction included. 109
7.14 Temperature measurements for obstructed cases. 110

8.1 Measured wall convective heat fluxes for open-ended cases A-C. . . . 114
8.2 Temperature profiles for case A open-ended and sealed. 115
8.3 Temperature fluctuations for case A open-ended and sealed. 116
8.4 Measured wall convective heat fluxes for open-ended cases D-F. . . . 117
8.5 Transient cooling temperature measurements starting from Ra_{D_i} 6.3×10^7 and $Dr = 1.25$. 118
8.6 Inner cylinder convective heat flux calculated using the lumped capacitance method. 121
8.7 Four rows of blades and vanes installed in a partially assembled RoBo facility. 122
8.8 Transient cooling temperatures at the top and bottom of the inner cylinder starting from Ra_{D_i} 6.3×10^7 and $Dr = 1.25$. 124
8.9 Top-to-bottom temperature difference for cases with different numbers of blade rows. 125
8.10 Inner wall Nusselt number distributions at the start of shutdown for the four test matrix given in table 8.2 126
8.11 IR camera measurements at of the inner cylinder in isolation, with four rows of blades. 128

9.1 Schematic of 2D conduction cooling model. 130
9.2 Modelled inner wall convective heat flux distributions compared to the experimental values 132

9.3 Bulk fluid temperature predicted by the correlation of Kuehn & Goldstein vs. value measured in the sealed concentric cases. 133
9.4 Flow chart outlining how the transient cooling process is modelled. . 135
9.5 Comparison of the temperatures predicted by the model to the experimental results. 136
9.6 Comparison of the top-to-bottom temperature difference predicted by the model to the experimental results. 137
9.7 Schematic of the engine geometry modelled in the shutdown model . 138
9.8 Modelled distribution of outer casing heat flux and experimental data taken from the ExCITE facility. 139
9.9 Predicted surface top-to-bottom temperature difference for different uniform starting temperatures 140
9.10 Predicted surface temperatures for different ventilation conditions . . 141
9.11 Simulated temperature contours during cooldown starting from 900 K. 142
9.12 Simulated inner surface heat flux during cooling starting from 900 K. 143
9.13 Predicted surface top-to-bottom temperature difference for different uniform starting temperatures 144
9.14 Predicted surface top-to-bottom temperature difference for different starting temperature distributions. 145
9.15 Predicted surface temperatures for different starting temperature distributions 146
9.16 Temperature contours during shutdown for different starting temperature distributions. 147
9.17 Predicted surface top-to-bottom temperature difference for different outer casing emissivity's. 148
9.18 Predicted surface top-to-bottom temperature difference for different outer casing distributions 149

10.1 Schematic of the RoBo facility with a DC fan feeding air into annulus at top-dead-centre. 153
10.2 Transient cooling temperature differences for forced air flow at $Re_j = 13,600$. 154
10.3 Transient cooling temperatures at top and bottom for forced air flow at $Re_j = 13,600$. 156
10.4 Transient cooling temperature differences for forced air flow at various mass flow rates. 157
10.5 Absolute value of peak ΔT^* vs. jet Reynolds numbers for the cooling cycle. 158
10.6 Comparison of the top-to-bottom temperature difference predicted by the model with impingement cooling compared to the experimental results. 161
10.7 Simulated top-to-bottom temperature difference and deflection profiles for different Reynolds number jets with a starting temperature of 900 K. 163
10.8 Simulated temperature contours during cooldown starting from 900 K uniform. 164

10.9 Simulated top-to-bottom temperature difference profiles for different Re_J with uniform starting temperatures of 900 and 500 K. 165
10.10 Axial cross-section schematic of the RoBo facility highlighting the altered emissivity distribution. 167
10.11 Experimental inner and outer cylinder top-to-bottom temperature differences for the baseline and altered emissivity cases. 167
10.12 Transient inner and outer cylinder temperatures for the baseline and altered emissivity cases. 168
10.13 Top-to-bottom temperature differences for different altered emissivity test conditions. 169
10.14 Comparison of experimental top-to-bottom temperature difference to the shutdown model. 171
10.15 Top-to-bottom temperature difference results for simulated engine geometry cases with altered emissivity profiles. 172
10.16 Simulated temperature distributions at various stages of the cooling cycle starting from 900 K uniform. 173
10.17 Top and bottom temperatures and heat fluxes on the rotor surface, with and without an altered circumferential casing emissivity 173
10.18 Simulated top-to-bottom temperature difference for 900 K uniform starting temperature cases with and without an altered circumferential casing emissivity, and ventilation. 175
10.19 Simulated top-to-bottom temperature difference and heat flux with periodic rotations, for 900 K uniform starting temperature case. . . . 176

11.1 Schematic of port venting arrangements of the ExCITE facility. . . . 180
11.2 Air temperature and k_{eq} measurements for port vent cases. 181
11.3 Infrared camera measurement of the inner cylinder surface at BDC for the TB port vented case 182
11.4 Schematic of the end wall venting arrangement of the ExCITE facility. 183
11.5 Air temperature and k_{eq} measurements for end-wall vent cases. . . . 184
11.6 Air temperature measurements for end wall vent cases with obstructions. The modified end wall case is also included. 185
11.7 Example inner surface Nusselt number fluctuations for the sealed, TB port vent and end wall vented cases. 186
11.8 Transient temperature measurements for the ExCITE facility with different ventilation arrangements 189

List of Tables

4.1 Properties of a type K thermocouple. 51
4.2 Comparison of the calculated Nusselt number for the different probe cases. 54

6.1 Geometric conditions for the six different test configurations studied. 79
6.2 Thermal boundary conditions for the nine Tc test cases. 82
6.3 Thermal boundary conditions for the nine Bc test cases. 88

8.1 Thermal boundary conditions for the open-ended test cases. 113
8.2 Test conditions for the obstruction study cases. 123

Nomenclature

Abbreviations

BDC	Bottom dead centre: $\theta = 180°$
CFD	Computational fluid dynamics
DES	Detached eddy simulation
DNS	Direst numerical simulation
FEA	Finite element analysis
KG	Kuehn & Goldstein correlation
LES	Large eddy simulation
PID	Proportional-integral-derivative
RH	Raithby & Hollands
RMS	Root-mean-square
TDC	Top dead centre: $\theta = 0°$

Greek Letters

Symbol	**Units**	**Description**
α	m^2/s	Thermal diffusivity
β	K^{-1}	Volumetric expansion coefficient
Δ	-	Top-to-bottom difference
ε	-	Emissivity
η'_T	m	Inner thermal length scale

θ	$^\circ$	Circumferential angle, positive clockwise from TDC
μ	Pa/s	Dynamic viscosity
ν	m^2/s	Kinematic viscosity
ρ	kg/m^3	Density
φ	$^\circ$	Angle relative to surface normal
φ_c	$^\circ$	Viewing angle relative to camera normal
Φ	-	Ratio of equivalent conductivity: $= k_{eq,BDC}/k_{eq,TDC}$
σ	W/m^2K^4	Stefan-Boltzmann constant $= 5.670 \times 10^{-8}$
τ	-	Transmissivity

Roman Letters

Symbol	**Units**	**Description**
A	K	Linear fitting coefficient
A_s	m^2	Surface area
A_w	m^2	Cross-sectional area of wire
B	K/m	Radial temperature gradient dT/dr
Bi	-	Biot number, $= hL/k$
C	-	Constant
c_p	J/kg K	specific heat capacity
C_{vb}	-	Model constant
D	m	Diameter
Dr	-	Diameter ratio
d	m	Probe to wall distance
E	W/m^2 K	Surface radiosity
F_c	-	Geometric factor modified from Raithby & Hollands
F_{io}	-	View factor
g	m/s^2	acceleration due to gravity
Gr	-	Grashof number, $= g\beta(T_1 - T_2)L_c^3/\nu^2$

H	m	Gap height $= (D_o - D_i)/2$
h	$\mathrm{W/m^2\,K}$	Heat transfer coefficient
J	$\mathrm{W/m^2\,K}$	Radiosity
k	$\mathrm{W/m\,K}$	Thermal conductivity
k_{eq}	-	Equivalent conductivity
L	m	Length
L_c	m	characteristic length
L_n	m	Probe wire length
$\dot{m}$	kg/s	Mass flow rate
N	-	Number of points used in curve fitting
Nu	-	Nusselt number
Pr	-	Prandtl number, $= \nu/\alpha$
Q	W	Heat flow
$\dot{q}$	$\mathrm{W/m^2}$	Heat flux
$\dot{q}'_s$	$\mathrm{W/m^2}$	Surface heat flux fluctuation
R	$\mathrm{m^{-2}}$	Radiosity resistance
r	m	radius
Ra	-	Rayleigh number, $= g\beta(T_1 - T_2)L_c^3/\nu\alpha$
Ra^*	-	Modified Rayleigh number, $= F_c Ra^*$
Re	-	Reynolds number $= \rho V L_c/\mu$
Ri	-	Richardson number $= Gr/Re_D^2$
S	V/K	Seebeck coefficient
T	K	Temperature
T'	K	Temperature fluctuation
T^*	K	Non-dimensional temperature $= (T - T_o)/(T_i - T_o)$
t	s	time
T_∞	K	Ambient temperature
T_{ad}	K	adiabatic wall temperature

T_B	K	Bulk fluid temperature
T_{bb}	K	Black-body temperature
T_c	K	Circumferential gradient in temperature
T_f	K	Fluid temperature
T_R	K	Reflected temperature
T_r	K	Radial temperature gradient
T_{ref}	K	Temperature to evaluate fluid properties
T_{sur}	K	Far-field temperature
V	m/s	Velocity
V_e	m^3	Volume
x	m	Distance

Subscripts

al	Aluminium
$cond$	Conduction
$conv$	Convection
cov	Cover
el	Electrical power
i	Inner surface
J	Jet
m	Mid-annulus
o	Outer surface
oo	Outer side of outer surface
rad	Radiation
roh	Rohacell
s	Surface
sp	Set-point
w	Wall

Chapter 1

Introduction

1.1 Background

As a large civil gas turbine is cooling following operation, natural convective flows develop. The thermal field that is established by these flows, in conjunction with conduction and radiation heat transfer within the engine, can lead to a number of issues that have the potential to damage engine components and affect operability. The ability to predict and understand this transient cooling cycle of a gas turbine has proven to be extremely difficult, owing to the complex nature of natural convective flow physics and its dependency on a large number of design parameters. Intensive computational fluid dynamics (CFD) techniques are required to adequately simulate natural convective heat transfer, even for relatively simple geometries. This, coupled with long engine cooling times (on the order of hours), restricts the practicality of current design tools.

However, the need to understand this transient cycle is becoming increasingly more important. The unceasing evolution of engine architecture, in the pursuit of increased efficiency, is expected to have an effect on the engine's cooling characteristics. Recent trends, such as the inclusion of a gearbox, larger fan and increasing number of

compressor stages, further complicates the engine architecture and cause it to differ ever more from the traditional arrangements, which drives the need for greater understanding of the natural convective heat transfer that occurs during shutdown.

A schematic of a typical large civil gas turbine is shown in figure 1.1 for reference. As an engine is cooling following operation, natural convection causes components to cool asymmetrically – the bottom sector cools faster than the top sector. Over a period of time, typically 30 minutes to 3 hours after shutdown, differential axial thermal expansion between the top and bottom of the rotor assembly causes the shaft to deflect. This phenomenon is known as rotor or thermal bow. There may already be some residual bow in a shaft for various reasons such as gravity sag and prior mechanical imbalance [77]. The casing will also distort in much the same way. Attempts to restart an engine whilst it is in this bowed state can lead to a number of issues related to vibrational rotor dynamics, damage to components and even blade tip rubs in severe cases [97]. The rotor dynamics problem is typically well understood [1], but the mechanisms that lead to the development of thermal bow are not.

All engines are affected by rotor bow to some degree, however the severity, duration and onset-time of this effect is usually unknown until full scale engine testing begins – potentially delaying engine development. A reasonable assumption might be that only engines with long unsupported shaft sections are hampered by rotor bow, such as those with many compressor stages. Yet, issues have been reported in all sizes of engines, from the relatively small helicopter arrangements [97], to large civil geared turbofans – recently, Pratt & Witney's large geared turbofan (PW1100G) garnered unwanted press attention due to long start-up times, which was a consequence of rotor bow [40].

The temperature difference between top-dead-centre (TDC) and bottom-dead-centre (BDC) of a component can be used as a direct indicator of the susceptibility of a component to rotor bow. The typical evolution of this temperature difference for a

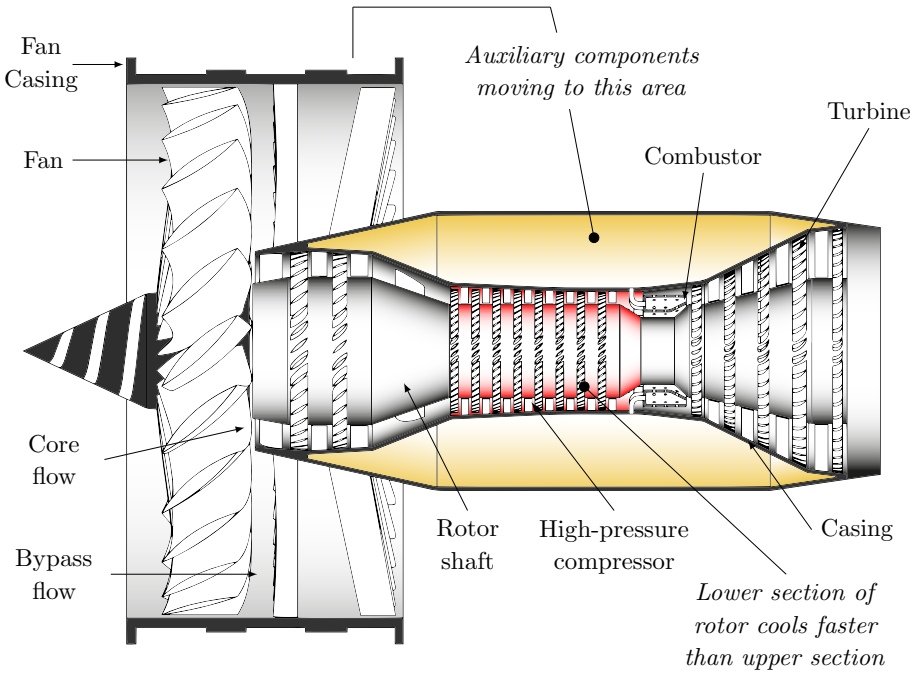

FIGURE 1.1: Cross-sectional schematic of a typical large civil gas turbine highlighting the two areas where natural convective flows are of interest: auxiliary zone (highlighted in yellow) and the high-pressure-compressor (highlighted in red).

gas turbine rotor drum during shutdown has been reproduced in figure 1.2, based on previous numerical and experimental studies [5, 97, 116]. The behaviour may also be present in other components. At the start of shutdown, there is no circumferential thermal gradient across the rotor. As the natural convective flow field develops, higher heat transfer from the lower section leads to a positive increase in bow. After a period of time, the magnitude of this difference reduces and a peak occurs. The thermal gradient then decays at a slower rate than the initial on-set period, until the engine reaches ambient conditions. The magnitude of the natural convection heat transfer coefficients reduces with temperature, which is why this elongated cooling trend persists. The large thermal mass of the engine, coupled with the relatively low heat transfer coefficients of the convecting fluid, leads to a long cooling time.

As the fan diameter is increased, the space available for auxiliary components on the fan casing is limited. This leads to a larger amount of temperature-sensitive parts being placed in the zone between the casing and bypass duct. Figure 1.1 highlights

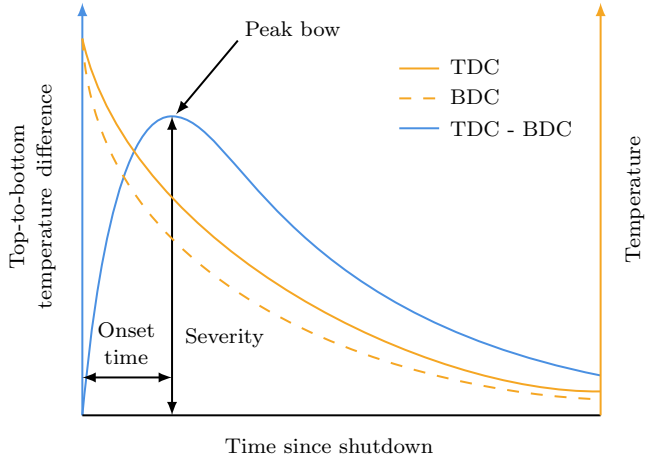

FIGURE 1.2: Typical evolution of rotor thermal gradient during shutdown. Based on data presented in [5, 97, 116].

this area. The natural convective flow field in this area is also not well understood. The initial temperature of the fluid in this area will be higher than that of the fan casing. Hence, the consequences of placing additional components in this zone are unknown – potential making these components prone to damage.

Therefore, for the reasons outlines above, it is imperative that the fundamental understanding of the natural convective heat transfer that occurs in an engine annulus during showdown is developed.

1.2 Scope of Project

The prediction of heat transfer during shutdown in large civil engines is an extremely complicated problem. In addition to the natural convective cooling, heat conduction in the rotor drum, especially along the shaft from the hot high-pressure turbine to the initially cooler high-pressure compressor, will be influential in determining the temperature distributions within components. Radiation heat transfer is also expected to be an important mechanism to consider. This, coupled with the intricate engine annulus geometry, interaction between the internal and ambient air, and limited previous work in the area, means that developing an efficient method to predict the shutdown cooling cycle is a daunting task. The cardinal aspect of this

is predicting the natural convective flow field, as this is where current methods are lacking. With this in mind, the scope of this particular project was to examine simplified representations of the engine annulus experimentally; thereby providing a greater fundamental understanding of the natural convective heat flow that is occurring during the transient shutdown cooling cycle.

1.3 Contributions of Work

The key contributions from this body of work are as follows:

1. Two sophisticated experimental facilities, that simulate the natural convective flow field during shutdown cooling of a large civil gas turbine, have been designed and commissioned. Dimensional similitude was achieved. The design of the rigs allowed for the influence of numerous features to be investigated, which has helped to increase understanding of these flow fields.

2. A low-cost, robust thermocouple probe has been developed that allows for accurate temperature measurements in a natural convective boundary layer, enabling the local heat flux to be measured. A novel technique for unsteady heat flux measurement has also been invented.

3. An extensive experimental study has shown that the overall heat transfer in a non-isothermal, low diameter ratio concentric annulus is adequately captured by isothermal correlations when the area-averaged temperature difference is used, as the local heat flux is dominated by the local radial temperature gradient. Furthermore, a shallow inner wall cone angle did not alter the heat transfer behaviour.

4. It has been proven that interaction between the incoming ambient air with obstructions in the main gas path is of critical importance in accurately predicting thermal bow.

5. A novel 2D conduction model has been developed and validated using experimental results. Application of the model to engine-representative conditions showed that reducing the total amount of energy contained in the rotor drum, by idling prior to shutdown, reduces the severity of thermal bow – irrespective of the initial metal radial temperature gradient.

6. Two viable thermal bow mitigation strategies have been presented: jet impingement cooling at the top of the annulus, and circumferentially non-uniform emissivity distributions. The strategies must be carefully matched to anticipated levels of top-to-bottom temperature difference so that large peaks in negative bow are not introduced.

7. End wall venting is a very effective method of reducing the overall air temperatures in the auxiliary zone during shutdown.

Portions of the work detailed here will be published in the following peer reviewed journal:

- D. Fahy and P. Ireland. The Effect of Wall Thermal Boundary Condition on Natural Convection Shutdown Cooling in a Gas Turbine. *Journal of Turbomachinery.* 2020. (accepted for ASME Turbo Expo 2020 and recommended for journal publication)

and has been published in the following peer-reviewed conference paper:

- D. Fahy, P. Ireland, L. Lewis and E. Raya. A Novel Experimental Technique for Investigating Natural Convective Heat Transfer in a Gas Turbine Annulus. In *Proceedings of the ASME Turbo Expo 2018: Turbomachinery Technical Conference and Exposition. Volume 5B: Heat Transfer.* ASME, 2018.

1.4 Layout of Thesis

Chapter 2 is a literature review. Previous works on natural convection in a concentric annulus and in gas turbines are explored.

Chapter 3 details the experimental design of two separate facilities. One that simulates the main gas path and another to investigate the auxiliary zone.

Chapter 4 presents a novel temperature probe design that has been developed through a combination of numerical simulations and a 1D conduction model.

Chapter 5 is a short commissioning study of both experimental facilities.

Chapter 6 gives the results of an extensive experimental campaign that quantified the effect of non-isothermal walls on natural convection in a concentric annulus. Diameter ratio effects are also considered.

Chapter 7 is an experimental investigation into turbulent natural convection in a large concentric annulus.

Chapter 8 looks at the impact of installation effects on the development of thermal bow. The configurations studied are an open-ended annulus and inclusion of obstructions.

Chapter 9 explains the development of a numerical conduction model that is based on the previous experimental results. The model allowed for the findings to be applied to engine-representative conditions.

Chapter 10 investigates the viability of three thermal bow mitigation strategies, both numerically and experimentally. The strategies are: impingement jet cooling in the upper section, controlled rotations of the shaft during shutdown, and non-circumferentially uniform emissivity distributions.

Chapter 11 presents cooling strategies for the auxiliary zone during shutdown cooling. The two strategies studied are: port venting end wall venting.

Chapter 12 summarises the main findings of the project before providing recommendations for future work.

Chapter 2

Literature Review

2.1 Natural Convection Basics

The main mechanism of heat transfer that is of interest for this shutdown cooling study is natural convection. The density of a fluid usually reduces as its temperature increases. Gravity causes the less dense fluid to rise, which creates the equivalent of a buoyancy force. When the hotter, less dense fluid rises, it is replaced by colder, denser fluid, thereby establishing a convection current [46]. The non-dimensional number that governs this type of flow is the Rayleigh number, given by equation 2.1. It is often described as the ratio between the buoyant and viscous forces.

$$Ra = \frac{g\beta(T_s - T_\infty)L_c^3}{\nu\alpha} \tag{2.1}$$

where g = acc. due to gravity, β = volumetric thermal expansion coefficient, T_s = surface temperature, T_∞ = ambient temperature, L_c = characteristic length of geometry, ν = kinematic viscosity and α = thermal diffusivity. β is well approximated by $1/T$ for ideal gases [46]. Ra is analogous to the Reynolds number for forced

convection flow, as in the flow will transition from laminar to turbulent at a particular value of Ra for a given geometry. Transition occurs at $Ra \approx 10^9$ for a flat plate [8].

Natural convection has been studied extensively in the past due to its applicability to a broad range of areas such as nuclear power and electronics cooling. Predicting natural convective flows is difficult due to the non-linear nature of the governing differential equations, and also the strong coupling between momentum and energy [88]. Hence, the majority of studies have been for simple geometries such as: plates, cylinders, square cavities and concentric annuli. Heat transfer is usually correlated in terms of a Nusselt number (Nu): the ratio of convective to conductive heat transfer. The bulk of heat transfer correlations for natural convective flows are semi-empirical [16]. The general form of these correlations is given in equation 2.2, which is derived from a scaling analysis of the boundary layer. C is a constant that varies based on the geometry in question. The exponent n is typically 1/4 for laminar flow and 1/3 for turbulent flow[8].

$$Nu = \frac{hL_c}{k} = CRa^n \tag{2.2}$$

where h = heat transfer coefficient and k = thermal conductivity of fluid. Figure 2.1 shows the typical velocity and temperature profiles of the boundary layer for natural convection from a vertical plate, when the plate is hotter than the ambient fluid [16]. It can be seen that the temperature variance is causing the hotter, less dense fluid near the wall to have an upward velocity. The velocity profile reaches a peak inside the boundary layer before reducing back down to zero. This is significantly different from a forced convection velocity profile where the peak is at the outer edge of the boundary layer. It has been shown that this peak also moves away from the wall as Ra is increased [109].

A theory for the turbulent thermal boundary layer profile has been developed by George & Capp [36], where the thermal profile is first divided into two regions, one

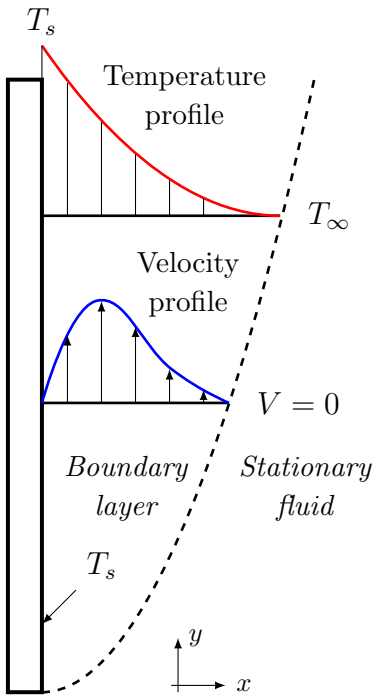

FIGURE 2.1: Typical velocity and temperature boundary layer profiles for natural convection from a heated vertical plate [16].

either side of the peak velocity location. The inner region is then further subdivided into a conductive sub-layer immediately next to the wall, followed by a buoyant sublayer. Calculations by Henkes & Hoogendoorn [41] confirmed the inner layer theory. The temperature profile is linear in the conductive sub-layer. This linear region has been measured experimentally by Cheesewright [17] for both laminar and turbulent natural convection from a vertical plate. The slope of this line, normal to the surface, can be used to calculate the wall heat flux, using Fourier's law:

$$\dot{q} = -k\frac{dT}{dx} \tag{2.3}$$

2.2 Overview of Relevant Natural Convection Research

While there are a limited amount of studies into natural convection in a gas turbine, both the main gas path and the auxiliary zone are well represented by a concentric annulus. Fortunately, natural convection in a cylindrical annulus has received a lot of attention, partly due to its practical applications, such as nuclear reactors, solar collectors and electricity cables [102]; but also because of interesting stability and flow transition phenomena.

2.2.1 Flow Structure in a Cylindrical Annulus

Figure 2.2 shows the typical flow features of a moderate diameter ratio cylindrical annulus when the inner cylinder is hotter than the outer and the flow is laminar [3, 8, 16]. A boundary layer grows on the inner cylinder, as fluid near the bottom of the inner cylinder heats up, becomes less dense and rises along this surface. An unsteady buoyant plume then emanates at the top of the inner cylinder and impinges on the outer cylinder – leading to high heat transfer on the outer surface. The fluid then cools down and descends along the outer surface, creating an outer boundary layer and establishing crescent shaped recirculating cells. A stagnant region of fluid is usually observed in the lower section of the annulus, which causes low heat transfer to the outer cylinder.

The diameter ratio ($Dr = D_o/D_i$) has a large effect on the flow structures in a concentric annulus. The landmark work of Powe *et al.* [11, 86] categorised the flow into three distinct regions, based on the diameter ratio. For wide gap annuli ($Dr > 1.71$), 2D oscillatory flow occurs. For $1.24 < Dr < 1.71$ (moderate gap width), this transitions to a 3D spiral flow pattern, and at $Dr < 1.24$ (narrow gap-width) multi-cellular flow occurs. All of these regimes occur above a critical Rayleigh number of approximately 1708; below this 2D stable flow occurs. Experimental

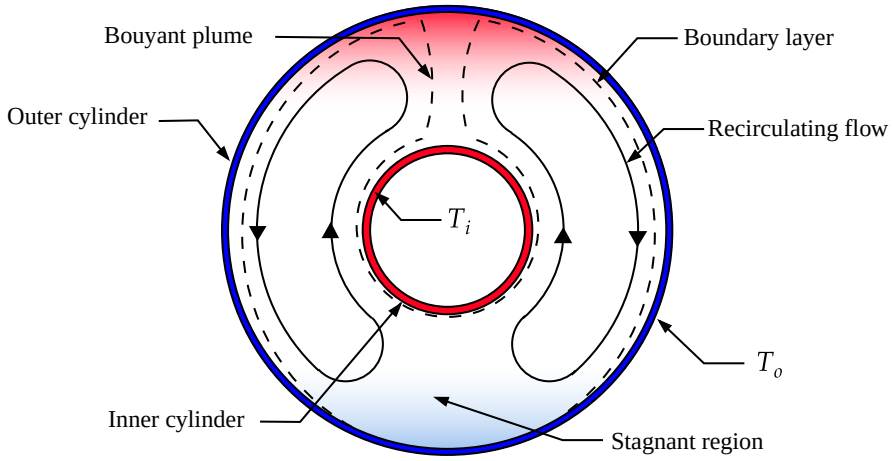

FIGURE 2.2: Schematic of the typical natural convective flow features present in a laminar, moderate diameter ratio concentric annulus with a hotter inner surface.Reproduced from [3, 8, 16].

observations of Rao *et al.* [89] confirmed the 3D spiral flow pattern and transition number. Multi-cellular flow was also confirmed by Rao *et al.*, but there was some discrepancy in the position of the boundary at $Dr = 1.24$. Nevertheless, the work of Powe *et al.* has proven to be an important reference for flow in a concentric annulus. Angeli [3] gives a detailed review of flow transitions for this geometry. The auxiliary zone of a gas turbine will fall in the wide-gap region ($Dr \approx 2$); the compressor gas path will typically be categorised by a moderate gap in the front stages, and narrow gap in the rear. Diameter ratios in the range $1.12 \leq Dr \leq 2$ have been studied in this thesis.

2.2.2 Heat Transfer Correlations

The concept of equivalent conductivity (k_{eq}), first introduced by Beckmann [7], provides an intuitive parameter for quantifying the natural convection heat transfer between concentric cylinders. Firstly, the analytical solution for heat conduction in a two-dimensional concentric annulus is [88]:

$$Q_{cond} = \frac{2\pi k(T_i - T_o)}{\ln(D_o/D_i)} \tag{2.4}$$

This is the total heat flow that would occur if the fluid was a solid. The equivalent conductivity is the ratio between the convective heat flux and this conductive heat flux that would occur if the fluid was stationary.

$$k_{eq} = \frac{\dot{q}_{i,conv}}{\dot{q}_{i,cond}} \tag{2.5}$$

Using the standard expression for convective heat flux ($\dot{q}_{i,conv} = hA\Delta T$), equation 2.5 can be written in terms of Nu_{D_i}, shown in equation 2.6. Thus, the equivalent conductivity is analogous to a Nusselt number that uses a conduction shape factor as the characteristic length. The advantage of using k_{eq} is that the magnitude of this number explicitly shows the enhancement in heat transfer that is occurring due to the motion of the fluid.

$$k_{eq} = Nu_{D_i} \frac{\ln(D_o/D_i)}{2} \tag{2.6}$$

The typical distribution of k_{eq} for a high diameter ratio, laminar flow case is shown in figure 2.3, recreated from [57]. The outer cylinder heat flux is largest at TDC, due to the impinging plume, and near zero at BDC because of the stagnant region of air. The inner cylinder heat flux is largest in the lower region, where the boundary layer is thinner. It then drops sharply at TDC near where the plume emerges. This type of circumferential asymmetry in heat flux causes rotor bow in a gas turbine during shutdown. A numerical parametric study of Prandtl number and diameter ratio by Kuehn & Goldstein [54] showed the top-to-bottom difference in heat flux increased on both surfaces with increasing Dr, but the lowest ratio tested was 3 and the Rayleigh number was 100. Numerical work of Powe *et al.* [87] at narrow gap-widths showed that the transition to a multi-cellular flow regime does not alter the overall heat transfer, but it does redistribute the local values. Dyko and Vafai [25] propose the existence of a further four convective states in this multicellular

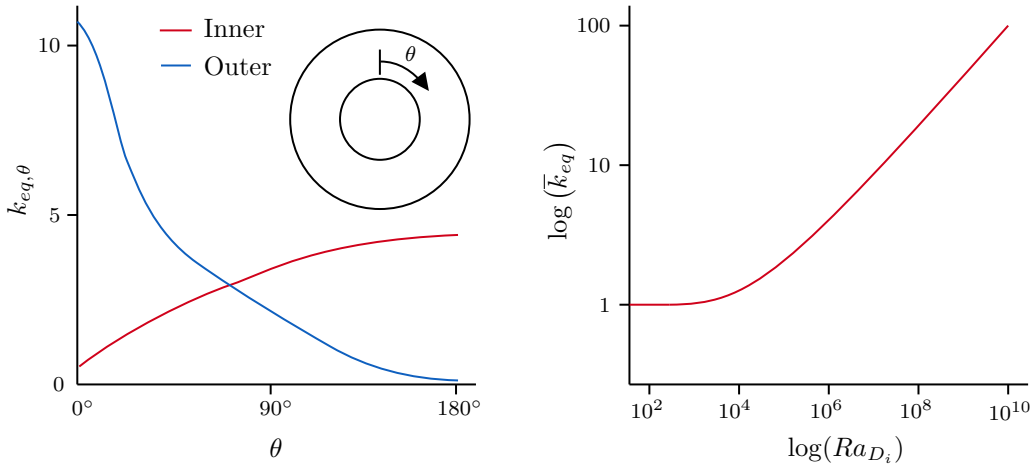

FIGURE 2.3: *Left:* Schematic of the equivalent conductivity distribution in a laminar, $Dr = 2.6$, concentric annulus [55]. *Right:* Schematic of the mean equivalent conductivity as Rayleigh number increases. [3].

region.

Figure 2.3 also shows the typical variation of the mean equivalent conductivity versus Rayleigh number for this geometry, reproduced from [3, 102]. A conductive limit is reached when the combined width of the inner and outer boundary layers is approximately equal to the gap width, hence the equivalent conductivity is equal to one. As the diameter ratio is increased, the heat transfer approaches that of a cylinder in isolation.

Many correlations have been proposed for the overall heat transfer in a concentric annulus. A comprehensive review has been compiled by Teertstra & Yovanovichz [102]. The seminal work of Kuehn & Goldstein [55–57] gives a prediction method that has been shown to be accurate over a wide range of conditions, both laminar and turbulent, and also captures the conductive limit region [16, 46, 102]. Their method is based on a conduction layer model, where the annular region is divided into a conductive film near the surface of each cylinder and a central region that has an average bulk temperature: T_B. The full details of this powerful method are included in Appendix A of this thesis for completeness.

Some discussion on the selection of the appropriate characteristic length for the

annular geometry is seen in the literature, as not only the diameters but also their ratio has been shown to affect the overall heat transfer. As described by Bejan [8], the inner diameter is the sensible choice for the vertical dimension as the overall heat transfer rate is set by the smallness of D_i rather than D_o. An expression has been developed by Raithby & Hollands [88] that allows for different diameter ratios to be compared, which is predicated on a conductive layer model similar to Kuehn & Goldstein's [57]. Itoh *et al.* [45] also defined a characteristic length that allowed for the comparison of different diameter ratio cases, but the Raithby & Hollands method has a stronger theoretical foundation. Although it should be mentioned that their derivation is based on the assumption that the heat transfer scales with Ra to the power of 1/4, which is typically true for laminar natural convection. Equation 2.7 defines this geometric factor (F_c), which has been altered to conform to Ra_{D_i} as opposed to Ra_H in the original publication, where H is the annular gap height.

$$Ra^* = F_c Ra_{D_i} = \frac{\ln(D_o/D_i)^4}{D_i^3 \left(D_i^{-3/5} + D_o^{-3/5}\right)^5} Ra_{D_i} \tag{2.7}$$

The magnitude of natural convective heat flux is intrinsically linked to the magnitude of the wall surface temperature. Steady state conjugate analysis of this geometry conducted by Bubnovich & Kolesnikov [15, 53] confirmed this. The long time-scales of solid component transient cooling coupled with the short time-step requirement of the fluid domain leads to extremely computationally expensive simulations – such as those conducted by Smith [97]. Born *et al.* [13] stated that a conjugate shutdown analysis of a steam turbine is not feasible due to the difference in time-scales between the fluid and solid. Recently, Maffulli *et al.* [67] have developed an adaptive time-stepping method that can significantly reduce simulation time. Topel *et al.* [107] used empirical correlations and manufacturer data to provide thermal boundary conditions for a finite-element model in order to predict the start-up of a solar gas turbine, with reasonable success.

2.2.3 Transition to Turbulence

Kuehn & Goldstein [56] used pressurised nitrogen to experimentally test configurations up to $Ra_{D_i} = 1.6 \times 10^8$ with $Dr = 2.6$. Interferometer measurements showed that the upper portion of the plume becomes turbulent at $Ra_{D_i} = 3.1 \times 10^7$ ($Ra^* = 2.8 \times 10^6$). The entire plume becomes turbulent at $Ra_{D_i} = 3.9 \times 10^7$ ($Ra^* = 3.5 \times 10^6$), but the inner cylinder boundary layer remains laminar. At $Ra_{D_i} = 1.6 \times 10^8$ ($Ra^* = 1.4 \times 10^7$), the upper portion of the inner cylinder boundary layer becomes turbulent. A similar transition method was confirmed by Fisher and Ball [32] using high-frequency temperature measurements. At $Dr = 8.4$, the plume was found to be weakly turbulent at $Ra_{D_i} = 10^7$ ($Ra^* = 5.9 \times 10^7$). As Ra increases, the radial location of turbulence moves towards the inner cylinder. McLeod & Bishop [70] used pressurised gas at cryogenic temperatures to test up to $Ra_{D_i} = 2.6 \times 10^8$, at $Dr \approx 5$. Postulated flow structures are provided, based on temperature fluctuation and spectral information. Transition occurs on the inner cylinder at $Ra_{D_i} = 1.3 \times 10^8$ ($Ra^* = 1.7 \times 10^8$). Increased mixing of the turbulent plume with the adjacent stagnant air lead to a more uniform temperature distribution in the upper region. Even at these high values of Ra, a stagnant region of air is still present in the lower region of the annulus. The configuration factor of Raithby & Hollands was found to adequately capture the overall heat transfer of these turbulent test cases [70].

A comprehensive description of transition to chaos is given by Labonia and Guj [63], who used hot-wire measurements in an annulus with $Dr = 2.4$ and up to $Ra_{D_i} = 10^6$ ($Ra^* = 5.6 \times 10^4$). The authors state that this route to chaos is not expected to occur in smaller gap width annuli, where multicellular Rayleigh-Bérnard type structures occur in the upper annulus.

Numerical studies into turbulent natural convection in a horizontal annulus have also been completed. While the flow structure in a turbulent horizontal annulus is fully three-dimensional, some 2D studies do exist [14, 23, 31], which agree with some

experimental results, but the general consensus is that 3D simulations are required in order to fully grasp the unsteady flow field. A DNS study was conducted by Fukuda *et al.* [33], but computational resources limited the upper Rayleigh number that could be studied. Fukuda *et al.* [34] conducted an LES study; the predictions generally agreed well with experimental results, apart from some discrepancies in the upper annulus when compared to the experimental results of McLeod & Bishop [70]. An LES study by Padilla & Silveira-Neto [81] showed an increase in the rate of change in the mean Nusselt number vs. Ra when the flow becomes turbulent, a feature that occurs in many natural convective flows [8]. Results at two diameter ratios ($Dr = 2$ & 2.6) highlighted that a smaller gap width inhibits the advection heat transfer. Kenjeres & Hanjalic [47] implemented an algebraic model for the turbulent heat flux model. This model proved to be crucial in the transitional regime where the turbulence was confined to the plume region with laminar or stagnant flow elsewhere in the annulus. As Ra was increased, more intensive mixing of the buoyant plume reduced the extent of the recirculating regions, leaving a larger stagnant section. Recent advancements in natural convective turbulent heat flux modelling have also been made by Pilkington [84].

2.2.4 Alternative Configurations

The vast majority of natural convective studies in a horizontal annulus employ isothermal boundary conditions with sealed end walls. Experimental facilities are typically of small inner cylinder diameters ($D_i \leq 100$ mm). However, there are some exceptions that are relevant to the gas turbine analogy.

Natural convection in an annulus open at one end has been studied by Desai and Vafai [22], both numerically and experimentally. Tests were conducted at $Dr = 2.9$ using a constant heat flux boundary condition. The results showed a strong interaction with the ambient fluid that enhanced the heat transfer from the annulus. The bulk flow field was characterised by cold air being drawn into the lower section and hot air

exiting the upper section. As the annulus was quite shallow ($0.5D_i$), findings on the axial variation of heat flux were limited. Vafai *et al.* [110] studied natural convection in a narrow annulus ($Dr = 1.1$) where both ends were open. The same general flow features were observed as the one end open case. Heat transfer was higher near the cylinder opening and reduced towards the axial mid-plane. Numerical results by Yeh [115] also showed this trend. A short parametric study by Vafai *et al.* [110] investigated the influence of the axial length and diameter ratio on the mean heat transfer in an annulus with both ends open. A larger gap width caused an increase in Nusselt number at all Ra. An increase in Ra also increased the penetration depth of the ambient air. These authors proposed that an optimum length exists for a given gap width that maximises the heat transfer.

High Rayleigh numbers are often attained experimentally by using a pressurised annulus and foreign gases. A horizontal concentric annulus experimental facility that is of similar scale to a gas turbine was not found in the literature. Kitamura *et al.* [50] conducted natural convective experiments for an isolated cylinder in water up to diameters of 800 mm. Misumi *et al.* [73] tested an isolated cylinder in air up to diameters of 1200 mm. A constant heat flux boundary condition was employed, giving Rayleigh numbers up to 6×10^{11}. The circumferential Nusselt number distribution showed an interesting trend in both studies at the largest diameter cylinders: a large peak in heat transfer appears around $\theta = 30°$ that is larger in magnitude than the heat transfer at BDC (TDC = 0° and BDC = 180°). This has been attributed to a 3D separation. Bardon & Garnier [6] tested a 2500 mm cylinder with axial fins, using a constant heat flux to give $Ra = 5 \times 10^{13}$. A similar heat flux distribution to Misumi *et al.* was measured.

Both the main gas path and auxiliary zones of a large civil gas turbine contain sections with either a rising or falling annulus line. There have been very few studies of natural convection from a horizontal conical geometry. Lewandowski & Leble [66] developed a theory for natural convection from a horizontal cone in isolation, with

experimental results up to $Ra = 2 \times 10^8$. The mean Nusselt number correlation follow the expected form: $CRa^{1/4}$. Oosthuizen [79] also conducted an experimental campaign on a horizontal cone in isolation. The author hypothesised that for shallow cone angles (up to 10°), the natural convective heat transfer from an isothermal horizontal cone is isolation, can be derived by integrating the equivalent cylindrical correlation evaluated at each 2D cross-section.

During the transient cooling cycle of an engine, the circumferential distribution of wall temperature will not be constant, as this is what causes rotor bow. Understanding the influence of non-isothermal walls on the heat flux distribution is critical. Koh & Price [52] developed analytical solutions for an isolated non-isothermal cylinder. Natural convection from a non-isothermal plate immersed in a temperature stratified medium has been studied numerically by Yang *et al.* [114]. The conclusion from this work was that solutions based on the local temperature difference alone were not adequate to predict the surface heat flux. The approximate method of Raithby & Hollands [88] can be formulated to give the local heat transfer from a non-isothermal cylinder in a variable temperature fluid. The mean value of this method is identical to the value obtained from a calculation based on the area-averaged temperature difference.

Work has been published previously that incorporated constant heat flux walls, which may provide useful insights. Experimental investigations into a horizontal annulus, where the outer wall is isothermal and the inner wall is a constant heat flux have been completed by Van de Sande & Hamer [111] and Kumar & Keyhani [61]. Numerical work by Mahfouz [68] with these boundary conditions showed qualitatively similar streamlines to the inner isothermal case, up to $Ra = 10^5$. Kumar [62] showed numerically a strong dependence on diameter ratio. Glakpe *et al.* [37] conducted a 2D laminar study with constant heat flux boundary conditions on both surfaces. They found that the outer cylinder temperature distribution was similar in profile to the heat flux profile from the isothermal case. Bejan [8] stated that heat transfer

correlations developed for isothermal wall systems are in reasonable agreement with the corresponding uniform flux conditions, when Ra is based on the average temperature difference. The example cited was a rectangular enclosure, which shows similar trends to a concentric annulus.

2.3 Natural Convection in Gas Turbines

There is an extensive body of work that examine an assortment of different natural convective flows, yet only a limited number have focused on a gas turbine. These studies tend to be numerical owing to the difficulties in measuring bow experimentally, and the large number of design parameters. A recent detailed numerical parametric study of rotor bow has been completed by Smith [97] and Smith *et al.* [95]. Using simplified geometries that were analogous to a gas turbine compressor, and a conjugate CFD and FEA modelling procedure, the work highlighted some complex, non-linear interactions of various compressor design features that influenced the severity, on-set time and duration of rotor bow. For example, increasing the rotor diameter increases the stiffness of the shaft, but also allowed for a larger thermal gradient to develop across the rotor. Smith & Neely [98] also showed that the inlet and outlet geometry of a helicopter gas turbine has a substantial impact on bow.

Baldassarre & Fontana [5] have developed a model that predicts the deflection of a gas turbine rotor shaft during shutdown cooling. The circumferential variation of convective heat flux (which drives the thermal gradient required to deflect the shaft) is modelled by using a distribution given by Oertal [78]. This variation in local heat flux has been reproduced in figure 2.4, where Nu_θ is the local value that is normalised by the value at BDC. This distribution applies to a horizontal cylinder in isolation. This simple correlation was successful in validating the model of Baldassarre & Fontana [5], but it is not applicable to a concentric annulus case as the diameter ratio has been shown to alter the local distribution of heat flux [87].

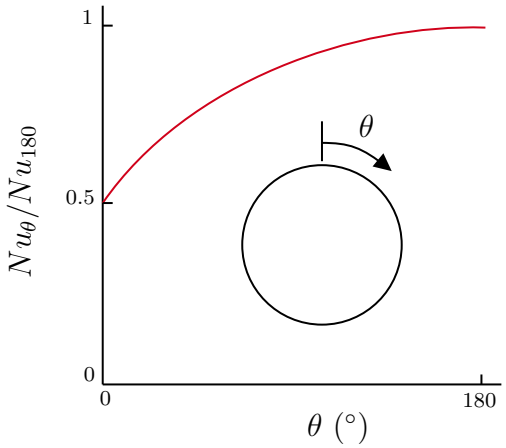

FIGURE 2.4: Local Nusselt number variation for natural convection from a horizontal cylinder. Reproduced from Oertel [78].

Tisarev *et al.* [105] have conducted an experimental and numerical investigation into the shutdown cooling of a micro gas turbine ($D_o = 110$ mm). The reduced number of components of a micro gas turbine (one stage compressor and turbine) has allowed for a full conjugate model of the engine to be simulated. The authors highlighted the importance of including radiation to adequately capture the shutdown temperatures. Velocity vectors showed ambient air entering the lower section of the annulus and exiting at the top, creating a fully 3D flow field. In general, the higher starting temperature components developed a larger thermal gradient.

Experimental work into rotor bow has also been completed recently by Smith [96, 97] who examined the deflection of a hollow cylinder in isolation as it cooled from $Ra_{D_i} \approx 7.7 \times 10^7$. Zhuo *et al.* [116] also conducted cooling tests and a compressor disc assembly. While these works both produced the expected rotor bow trend, neither included an outer casing.

Natural convection cooling flows in industrial gas and steam turbines have been a keen interest of researchers and manufacturers, due to their implications on operational flexibility and component life [13, 83]. Compared to a civil gas turbine, industrial turbine casings are relatively thick and cool down over a number or days [69]. This means that the outer casing becomes hotter than the inner shaft, which creates

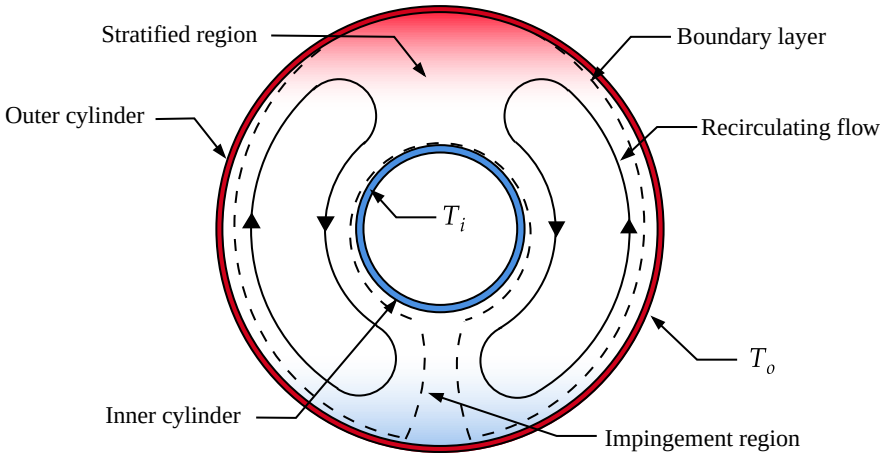

FIGURE 2.5: Schematic of the typical natural convective flow features present in industrial gas turbines during shutdown. Recreated from [85].

a fundamentally different type of flow field, as described by Pilkington [85]. A schematic of this is shown in figure 2.5. Hot air ascends the outer casing, leading to a stratified region of air in the upper section and thus low heat transfer from the casing. This flow in-turn leads to an impingement cooling effect at the bottom of the casing. This mismatch in heat flux causes the casing to distort – referred to as 'cat-back'. Reddy [90] developed an axisymmetric transient cooling model. The author noted the important role of natural convection in the cooling process and the difficulties in predicting this heat transfer with current tools.

Barring is a widely used technique in industrial gas and steam turbines to counteract the unwanted thermal distortions during cooling, and hence reducing the start-up times. Barring involves continuous slow rotations of the shaft so that a thermal gradient does not develop [106]. Pilkington [83] investigated the effect of introducing/extracting air from the upper region combustor section of an industrial gas turbine. Extracting air was found to be more effective than an impinging jet in reducing casing distortions.

2.4 Conclusions

While natural convection has been studied extensively, the complex nature of the flow due to the strong coupling of the energy and momentum equations means that the analysis has been largely limited to simplified configurations. Thus, there is quite a lot about this type of flow that is still unknown. In relation to a gas turbine, the following four relevant gaps in the literature have been identified:

1. Non-isothermal boundary conditions.
    - The vast majority of previous studies of a concentric annulus employ isothermal wall boundaries. It is unknown how non-isothermal temperature distributions, which undoubtedly occur during shutdown cooling, affect the convective heat flux.
2. Conical geometry.
    - Only two studies have been observed that examine natural convection from a cone. No sources were found that examined a conical inner section in a concentric enclosure – a geometry that is a very good approximation for large portions of the main gas path of an engine.
3. Interaction between ambient and main gas path air.
    - The idealised case of a sealed concentric annulus may not adequately capture the shutdown cooling of a gas turbine, due to the interaction between the ambient air with the main gas path. Studies by Desai and Vafai [22] and Vafai *et al.* [110] elude to a strong interaction between both bodies of fluid. Understanding how this interaction impacts the circumferential distribution of heat flux in a gas turbine may be crucial for developing accurate shutdown cooling prediction methods.
4. Obstructions.

- It is unknown how the rotor blades, stators and struts in the main gas path, and various ancillary components in the auxiliary zone influence the natural convective flow field during shutdown.

Despite recent advancements in numerical studies, the long transient cooling time of a gas turbine, the mismatch in time-step between the solid and fluid domain, and the level of CFD fidelity required, limits the current feasibility of large fluid simulations. Any added complexity, such as ambient air interaction and obstructions, will only exacerbate this assertion. Therefore, an investigation into how various basic design features – which are applicable to a gas turbine – alter the convective heat flux distribution in a concentric annulus can help illuminate a pathway to develop an efficient method of predicting engine temperature distribution during a transient shutdown cooling cycle. The four parameters outlined above have been investigated in this thesis through a series of experimental campaigns, which are detailed in the forthcoming chapters.

Chapter 3

Experimental Facility Design

Two experimental facilities that are capable of investigating natural convective flows in a large civil gas turbine have been developed: The RoBo[1] rig and the ExCITE[2] shutdown facility. This chapter will outline the design methodology and instrumentation of both facilities. The RoBo facility investigates the natural convective flows that occur in the main gas path, while the ExCITE shutdown rig models the zone between the main gas path outer casing and bypass duct inner wall.

3.1 Scaling

As mentioned in Chapter 2, the Rayleigh number (equation 2.1) can be used to characterise natural convective flows. Ideally, the facility would operate at ambient pressure, which would allow for greater flexibility and operation. Thus, the two design variables in the Rayleigh number definition that can be used to define operating point of the experimental facility are the characteristic length (L_c) and a temperature difference (ΔT). A concentric circular annulus is the most appropriate geometry to model both regions of interest. The inner cylinder diameter (D_i) is used as the characteristic length. It is set at an engine representative value of 760 mm for this

[1] RoBo is an acronym for rotor bow.

[2] The ExCITE name is the title of the program that funded the experimental facility manufacture.

analysis. The diameter ratio Dr was set as 2 – a value indicative of the auxiliary zone of a large civil gas turbine.

At the start of shutdown, the temperature of the engine components will be relatively high ($\approx$ 700 K) and the inner and outer annulus walls will be similar temperatures. As the components cool down at various rates, distinct heat transfer driving temperature differences (ΔT) will be present, until eventually the engine reaches equilibrium with its surroundings. Large changes in temperature during the shutdown period will inevitably lead to large changes in fluid properties. It is important to consider this when evaluating the fluid properties used in the definition of the Rayleigh number: β, ν, and α, as these values can alter the value of Ra substantially. While the film temperature ($(T_i + T_o)/2$) is often used, Bishop [10] proposed a volume weighted reference temperature given by equation 3.1. D_m is the average of the diameters: $(D_i + D_o)/2$. This formulation is used to compute the values for figure 3.1. This formulation has been validated experimentally by McLeod & Bishop [70], and numerically by Braga & de Lemos [14]. At very large diameter ratios, the temperature weighting approaches the recommended values of Siebers [94] for a vertical flat plate.

$$T_{ref} = \left(\frac{D_m^2 - D_i^2}{D_o^2 - D_i^2}\right) T_i + \left(\frac{D_o^2 - D_m^2}{D_o^2 - D_i^2}\right) T_o \tag{3.1}$$

Figure 3.1 gives Ra_{D_i} at all possible combinations of inner wall temperature (T_i) and outer wall temperature (T_o) that may be experienced during a shutdown cooling cycle, with D_i at an engine representative value of the main gas path outer casing. It is clear that the largest values of Rayleigh number occur when T_i is hot and T_o is ambient air. Interestingly, the peak value along this line does not occur at the highest value of T_i – this is due to the changes in fluid properties. A similar surface plot is obtained when diameters representative of high-pressure compressor are used in the definition of Ra. This Ra would be applicable wherever ambient air interacts

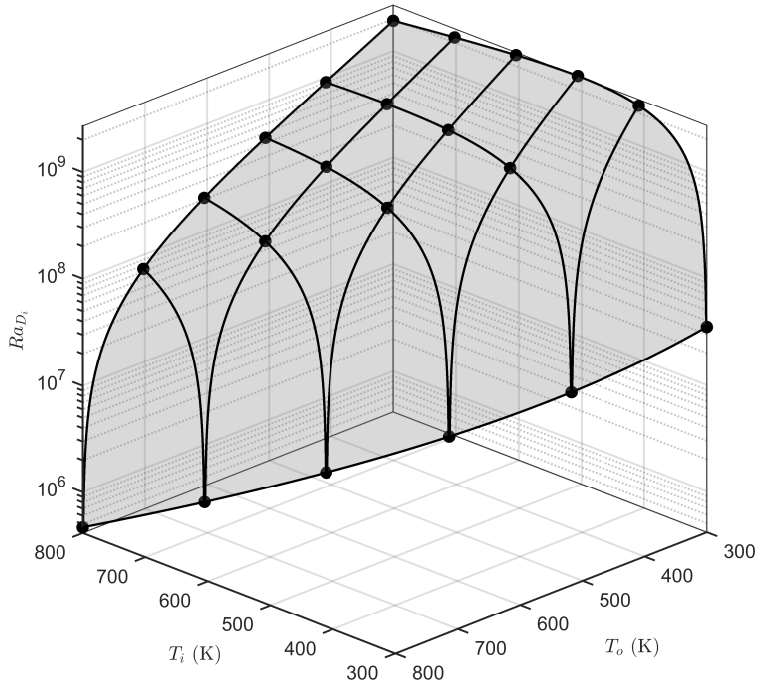

FIGURE 3.1: All possible values of Ra_{D_i} experienced in an engine auxiliary zone during the shutdown period. $D_i = 760$ mm, $Dr = 2$.

with gas turbine components post-operation.

The line extracted for which T_o is equal to ambient air ($\approx$ 295 K) – where the peak Rayleigh numbers are experienced – is plotted in figure 3.2, denoted as 'Base'. High temperatures are hard to replicate experimentally, as they require specialised materials and large amounts of electrical power. Since Ra scales with the cube of the characteristic length, a modest increase in L_c allows for a large drop in the surface temperature required to match the peak engine Rayleigh number. Lower temperatures have numerous advantages, such as: less radiation heat transfer (which is advantageous when measuring convective heat transfer), wider range of available materials, and lower power requirements. A $1.08D_i$ scaled line is included in figure 3.2. The dashed lines indicate that this scale allows for experimental testing at a surface temperature of 373 K that will match the peak engine Ra experienced during shutdown.

The above rationale was used to determine the scale of the ExCITE shutdown facility.

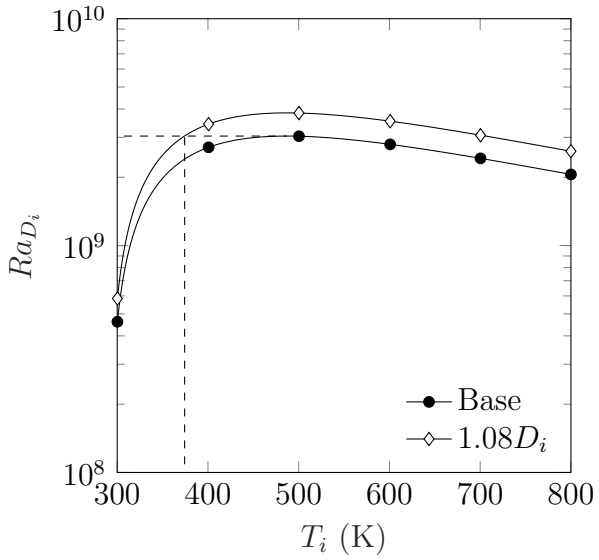

FIGURE 3.2: Rayleigh number vs. inner surface temperature with $T_i - T_\infty$ used as the temperature difference. $D_i = 760$ mm.

The RoBo facility however is approximately 0.6 scale of a modern civil gas turbine engine high-pressure compressor drum diameter. This compromise allowed for a far greater number of test configurations and engine design features to be investigated. Although Ra_{D_i} is lower than engine values, the all-important diameter ratio Dr is matched to engine geometry. Consequently, the experimental Ra^* values (see equation 2.7 for definition) are matched to a full-scale civil gas turbine compressor.

3.2 Facility Overview

3.2.1 ExCITE Shutdown Facility

Figure 3.3 shows a schematic of the ExCITE shutdown facility, giving the main dimensions and key design features. The purpose of this rig is to simulate the natural convective flow field in the auxiliary zone of a modern large civil gas turbine, which is well-represented by concentric cylinders. The inner structure is manufactured from 5 mm aluminium. The interior on the inner cylinder is fully encompassed by heater pads adhered to its surface – details of this are given in section 3.3. The cylinder is connected to a central shaft through six point contacts; three at each end. This

point contact arrangement significantly reduces any end conduction effects. The inner shaft assembly can rotate to allow testing at different orientations.

A layer of 1 mm Rohacell[3] is bonded to the exterior of the inner cylinder. This is used for infrared thermography measurements, as detailed in section 3.4. The outer surface of the Rohacell is painted with a high-emissivity matt black paint.

The outer cylinder is also manufactured from 5 mm aluminium. Unlike the inner assembly, it is unheated. Type K thermocouples are adhered to the outer surface, so that the temperature profile can be obtained. The details of this are shown in figure 3.7. The outer assembly is mounted on linear rails that allow for exact positioning and easy assembly/disassembly. The end plates are made from 15 mm clear acrylic attached to a linear bearing that again allows exact positioning; while in-turn allowing for sealed and ventilated tests. The relatively thick acrylic allowed for the ends surfaces to be modelled as adiabatic – the thermal resistance ($L/(kA_s)$) of the aluminium outer cylinder is 0.02% of the acrylic plate value. A rubber strip is used to create a tight seal between the cylindrical assemblies and the plates. Threaded rods are used to secure the end plates and outer assembly in place.

IR cameras and temperature traverse probes are located at 45° increments on one half of the annulus, again shown in figure 3.3. The cameras view the exact centre of the inner cylinder, thus the temperature probes are 100 mm away from the axial centre. Each traverse mechanism consists of a high-accuracy lead screw driven rail controlled by a NEMA stepper motor. The linear system has a repeatability of 0.005 mm [104]. Figure 3.5 shows the installed facility.

3.2.2 RoBo Facility

A similar design philosophy has been employed for the RoBo facility. Figure 3.4 gives an outline of the main design features. The inner assembly construction of

[3]Rohacell is an extruded closed-cell structural foam that has a low thermal conductivity ($k_{roh} \approx$ 0.03 W/m K). Type 51 IG-F has been used here [29].

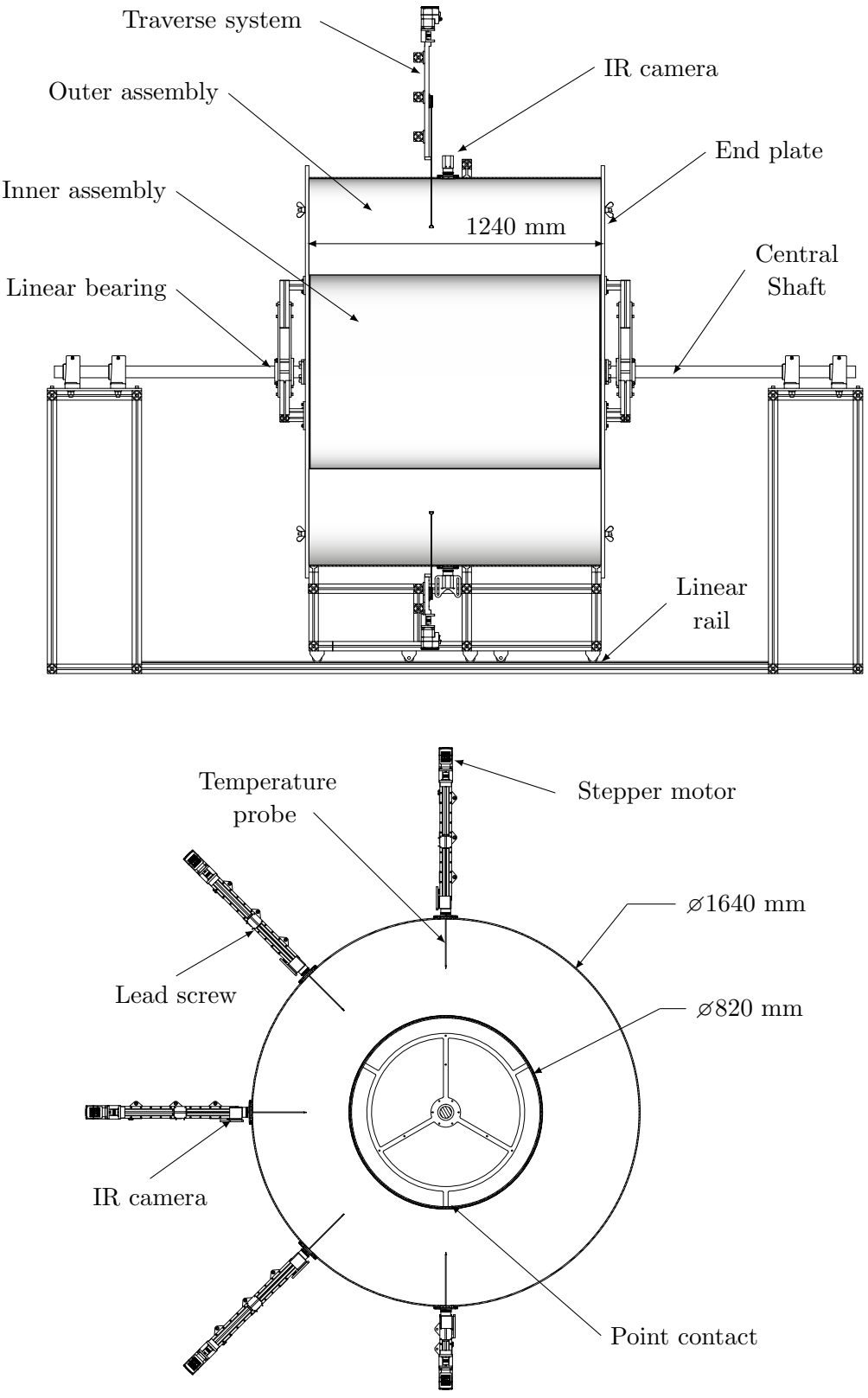

FIGURE 3.3: Design overview of the ExCITE shutdown facility. Further details of the inner assembly are given in figure 3.8.

heater mats, an aluminium substrate and a layer of Rohacell is identical to the larger ExCITE facility, except the Rohacell used in this case is 0.5 mm thick. Other common design features are: a shaft mounted inner assembly, a linear rail mounted outer assembly, point contact supports, and acrylic end plates attached to linear bearings. A 38 mm layer of insulation (Superwool 607, $k = 0.08$ W/m K [74]) is attached to the rear of the heater mats. Details about the mats are given later in section 3.3.

The inner assembly does differ from the ExCITE facility as the inner annulus line is no longer constant. The RoBo facility contains a 5° hade angle conical section, in addition to the cylindrical section. This geometry is an excellent approximation of the typical main gas path rising annulus line of a large civil gas turbine high-pressure compressor - where flow is going from right-to-left when looking at figure 3.4. Moreover, as outlined in Chapter 2, no experimental work on natural convection from a conical annulus has been published, to the best of the author's knowledge.

The smaller size of the RoBo facility makes it feasible to use heater mats to also control the outer cylinder temperature profile. Three separate outer cylinders of identical construction have been manufactured at diameters of: 366, 406, 446 mm. This allowed testing at gap widths of 20, 40, and 60 mm respectively. This means that the diameter ratios are matched to a typical civil gas turbine ($Dr = 1.12$, 1.25, 1.37), although the peak Rayleigh number is lower.

A five-axis radial traverse system is used to measure the air temperature profiles at 45° intervals. Figure 3.4 shows a schematic of this. The system can be moved to different axial locations, which will be defined in figure 6.2. While the same probes as the ExCITE facility are used, the traverse mechanism is different. The probes are attached to a lead screw that is driven through a bevel gear. The five rails are combined in a timing belt system that allows one stepper motor to traverse all five probes simultaneously, if desired. Due to the low backlash of the system, the probe

head location repeatability has been tested and found to be < 0.1 mm over a 60 mm traverse. Although this value is higher than the ExCITE facility arrangement, it is still acceptable. Since only one stepper motor was required, this system was much less expensive to implement than the ExCITE arrangement. Figure 3.6 shows the installed RoBo facility.

3.3 Thermal Boundary Condition Control

Knowledge of the wall thermal boundary conditions is critical for these experimental facilities. Accurate control of the wall temperature is achieved using discrete heater mats, an embedded thermocouple and a feedback control loop system. A diagram of this system is shown in figure 3.7. A heater mat is composed of a serpentine copper path (wire or etched foil) encased in silicone rubber. One side is attached to the metal substrate using high-temperature double sided adhesive. The construction allows the flexibility to mould to the metal surface. Each mat draws approximately 200 W and have been custom manufactured for both facilities.

A type K thermocouple is embedded in the metal substrate such that the bead is located as close to the outer edge as possible. A high-conductivity silver epoxy is used to cement the position of a thermocouple. A hole in the silicon mat allows for the wires to pass neatly. The temperature reading is recorded using a National Instruments cDAQ data acquisition unit. A LabVIEW script uses this reading as the input to a PID control loop system. The software in turn outputs a DC control voltage between 0-10 V that is proportional to the difference between the thermocouple reading and the temperature set-point. Each heater mat has a dedicated thermocouple and control voltage. The loop can operate at a frequency of $1 - 4$ Hz [76].

Purpose-built heater power control units have been commissioned for these facilities. Mains power is supplied to the unit and is then delivered to sixteen solid-state relays. The burst-fire relays (Crydom PMP2425W [21]) modulate the output power

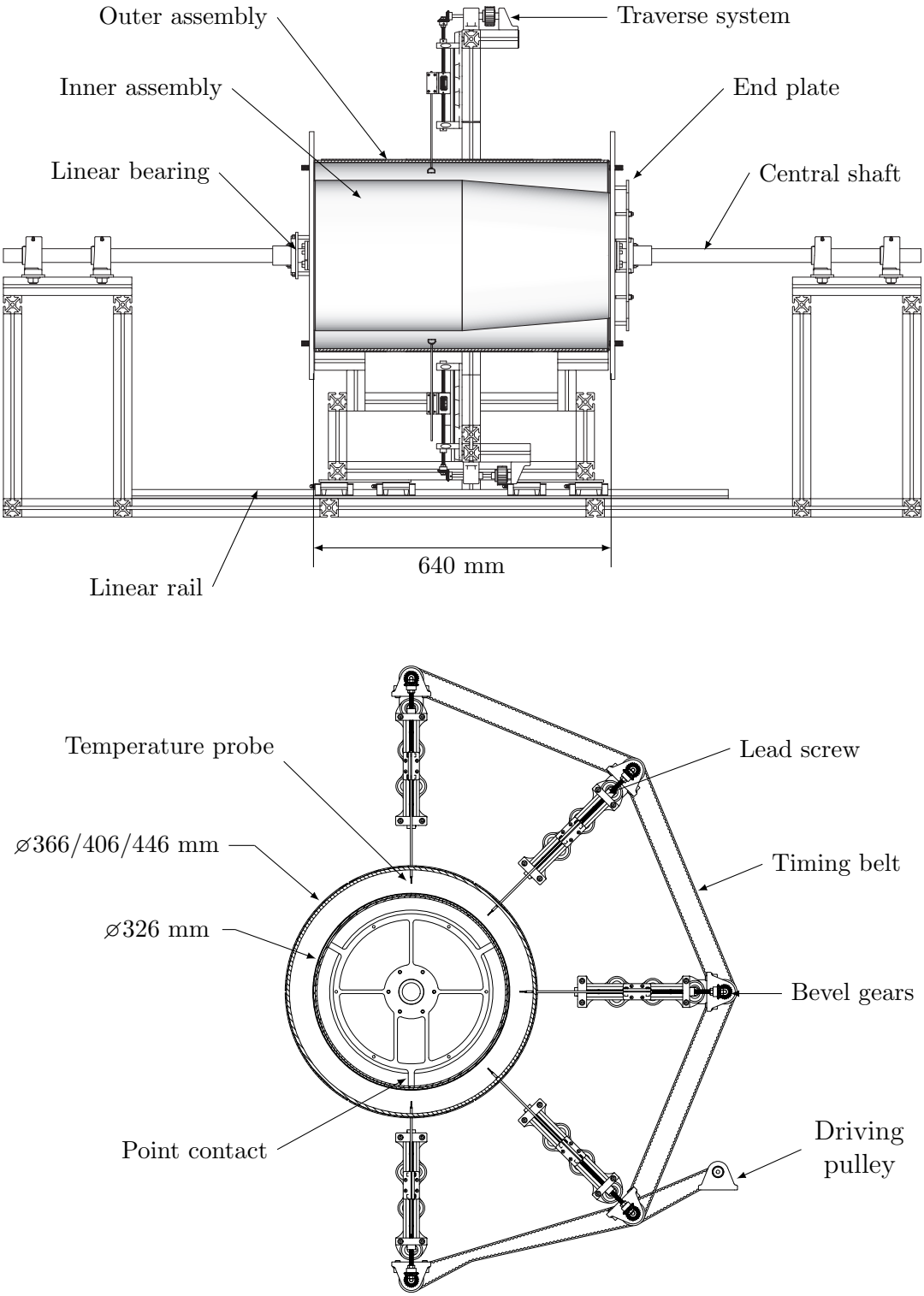

FIGURE 3.4: Design overview of the RoBo facility. Further details of the inner assembly are given in figure 3.8.



FIGURE 3.5: The ExCITE shutdown facility.

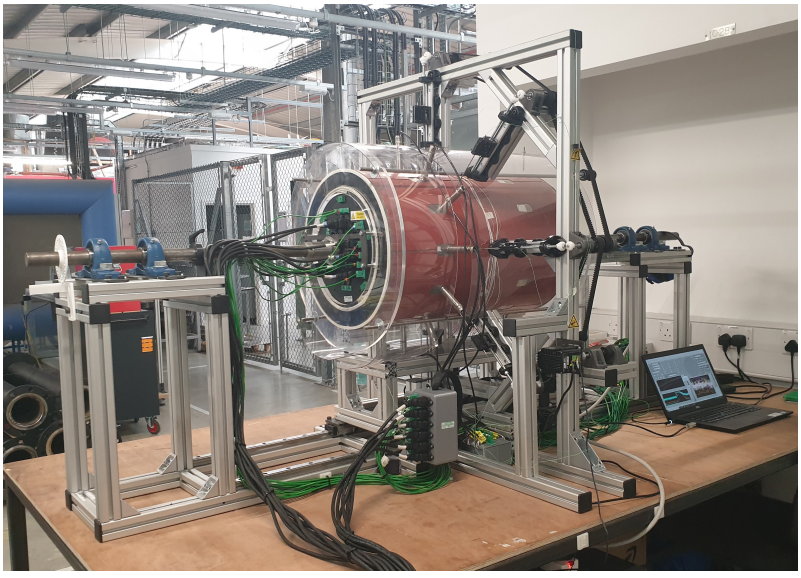

FIGURE 3.6: The RoBo facility.

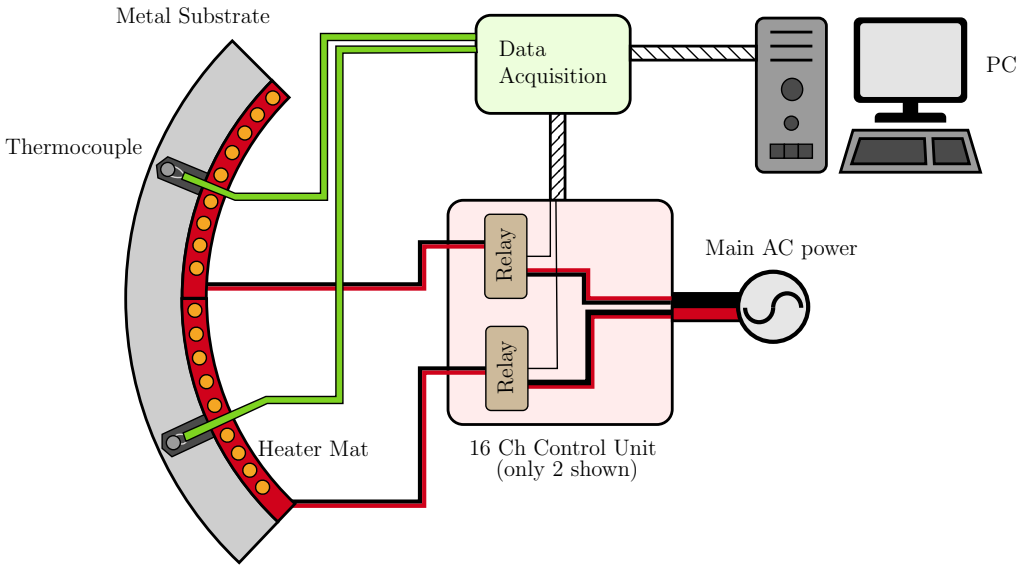

FIGURE 3.7: Heater control loop system schematic.

to each mat based on the applied control voltage. Each relay is rated for 25 A at 230 V making this a power-dense unit. Over-temperature projection is attained by thermal fuses attached to each heater mat; if one of these fuses trips then power to all channels is shut off.

This system has numerous advantages but perhaps most importantly it allows precise and accurate control of the wall thermal boundary condition. In addition to isothermal conditions, circumferentially and axially varying distributions are also attainable, owing to the high number of channels. Furthermore, the temperature and control voltage signals can be recorded easily as they are passed through a PC. The control voltage can be used to calculate the amount of electrical power that is dissipated in each mat, which can be correlated to the measured heat fluxes on the outer surface. It is also possible to set the control signal at a steady voltage level – thus giving a constant heat flux boundary condition.

The RoBo facility uses sixteen heater control channels: five on the inner cylinder and cone respectively, and six on the outer cylinder. The ExCITE facility uses forty: eight circumferentially and five axially on the inner cylinder. Figure 3.8 shows the mat and thermocouple locations for both facilities. The temperature of the outer cylinder

on the ExCITE rig is not controlled; thus, it has twelve thermocouples adhered to the outer surface to obtain the temperature boundary condition. Figure 3.9 shows the location of these twelve thermocouples. Both sides have been instrumented to inspect the symmetry of the results – every 22.5° on the traverse side and every 45° on the opposite side.

As the RoBo rig has only one axial mat per inner assembly section, guard heating was also implemented by embedding a cartridge heater and thermocouple in each of the support structure point contacts (see figure 3.4). However, during commissioning it was found that guard heating had a negligible impact. Thus, the guard heaters were not used during testing due to the extra resources that would have been required. Guard heaters are not required on the ExCITE facility as the outer-most mats essentially serve this purpose.

3.4 Infrared Thermography

The popularity of infrared thermal cameras measurements for heat transfer experiments has grown rapidly in recent years. This type of device detects the thermal radiation being emitted by a body and a calibration procedure allows this signal to be converted into a surface temperature measurement [4]. It provides a full view of the thermal field, as opposed to a point measurement obtained from a thermocouple or heat flux gauge. Transient measurements can also provide detailed information of the flow field. Five Optris PI640 cameras have been installed on the ExCITE shutdown facility. These powerful devices provide a 480 x 640 pixel resolution view, a sensitivity of 75 mK, spectral range of 8 to 14 µm, a frame rate of 32 Hz and have a quoted accuracy of ±2°C [80].

One of the limitations of using IR cameras in an experimental setting is obtaining optical access to view the internal surfaces. Widely used transparent materials (such as glass and acrylic) do not allow the transmission of infrared radiation. Instead,

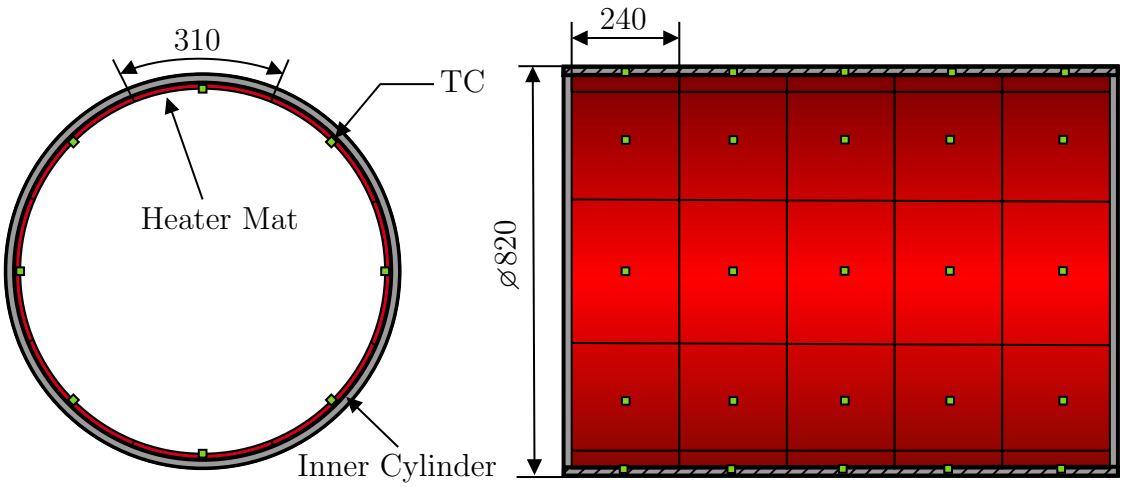

(a) ExCITE

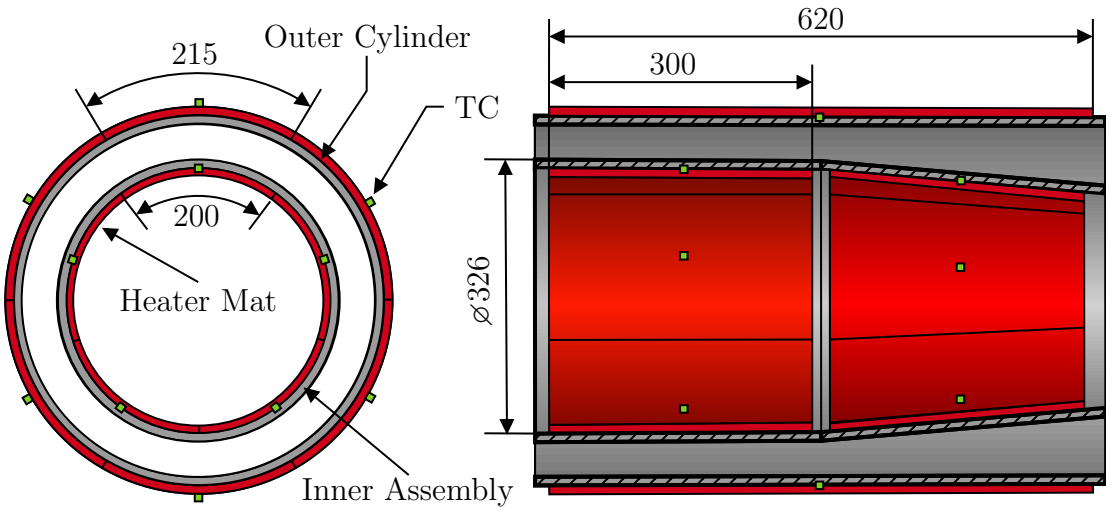

(b) RoBo

FIGURE 3.8: Heater Mat locations of both experimental facilities. Green squares represent the location of an embedded thermocouple.

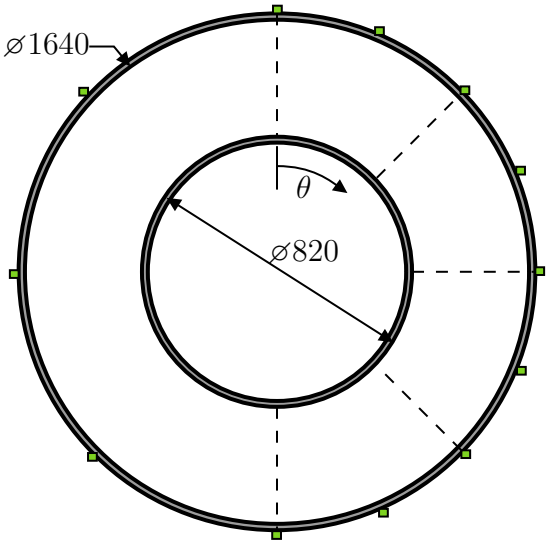

FIGURE 3.9: Thermocouple locations (green squares) on the outer cylinder of the ExCITE shutdown facility.

specialised IR windows are required. The size of available IR windows is limited. ⌀65 germanium windows are installed in the ExCITE facility as they have an adequate transmission in the spectral range of interest [27]. Five windows are required to capture the full top-to-bottom circumferential profile of the ExCITE inner surface.

The infrared cameras measure the outer surface temperature of the Rohacell, which has been painted matt black in order to increase its emissivity. The rear of the Rohacell will be at the control point temperature of the metal. Since the thickness and thermal conductivity of the Rohacell are known, the local heat flux through the Rohacell can be calculated. This measurement technique then gives a full surface distribution of heat flux as it operates like a large heat flux gauge. A similar rationale has been used by Laveau *et al.* [65] for forced convection heat transfer measurements of turbine end-walls in a high-speed wind tunnel. This study used Kapton film as the insulating layer.

3.4.1 Calibration Methods

All bodies above absolute zero emit thermal radiation [44]. Careful calibration of an infrared camera installation is required in order to obtain meaningful measurements.

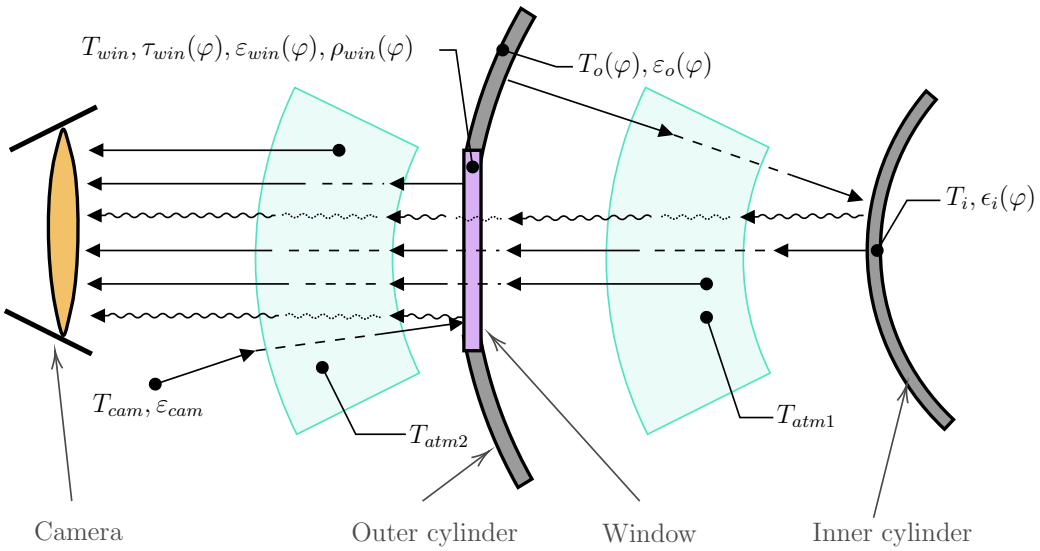

FIGURE 3.10: Schematic of the components of thermal radiation that will be detected by the IR camera. Blue squares represent volumes of air.

Minkina & Dudzik [72] provide an in-depth discussion of the sources of error. Figure 3.10 shows a simplified representation of the components of thermal radiation that will be detected by the IR camera. The signal is composed of the radiation emitted from the surface of interest, reflections from the surroundings, and reflections from the window surface due to the close proximity of the camera. Radiative properties have a dependence on the angle between the surface normal and the emitted radiation – φ.

Due to the short distance between the inner surface and the camera, the transmission of the atmosphere can be assumed to be equal to one [35]. This assumption allows the signal to be formulated by the following equation:

$$\sigma T_{bb}^4 = \sigma\tau\varepsilon(\varphi)T_w^4 + \sigma(1 - \tau\varepsilon(\varphi))T_R^4 \tag{3.2}$$

where σ = Stefan-Boltzmann constant, T_{bb} = black-body temperature measured by the camera, τ = transmission of the IR window, ε = emissivity, T_w = wall temperature and T_R = reflected temperature. A similar procedure has been used successfully in various wind tunnel heat transfer experiments [43, 75]. The factory

calibration is used to measure T_{bb}. T_R should account for all surrounding reflections and may vary from pixel-to-pixel.

The emissivity of a surface is known to vary with viewing angle, and different materials follow different trends [44]. An in-situ calibration has been completed that measures this variation, while also accounting for any installation effects such as camera-window reflections. A flat-plate test piece with an identical construction to the inner cylinder assembly (heater mat, aluminium, Rohacell) has been manufactured with four type K thermocouple adhered to the Rohacell outer surface. The plate measures 50 x 50 mm, which means its surface area is small when compared to the total enclosed surface area of the ExCITE facility. Figure 3.11a shows the flat-plate installed. When the plate was heated, all of the reflections were at ambient temperature [48], T_{bb} is measured by the camera and T_w is averaged from the four thermocouples. This means the only unknown in equation 3.2 is $\tau\varepsilon$. The shaft mounted inner structure can then be rotated so that the plate is in a different location of the camera's field of view, producing a calibration map of $\tau\varepsilon$ vs. viewing angle. Figure 3.11b shows an example image captured by the camera, the red square is the calibration plate. In this condition, equation 3.2 can be rearranged to solve for $\tau\varepsilon(\varphi_c)$, as shown in equation 3.3. θ_c is the angle relative to the camera normal. The value of $\tau\varepsilon$ at $\varphi_c = 0°$ (normal to the camera plane) was found to be 0.86.

$$\tau\varepsilon(\varphi_c) = \frac{T_{bb}^4 - T_\infty^4}{T_s^4 - T_\infty^4} \tag{3.3}$$

Reflective markers are used in order to align the camera viewing angle between different tests, as the relative position of objects may have moved since the calibration procedure. Kirollos & Povey [49] employed a similar methodology using circular markers. Aluminium tape ($\varepsilon \approx 0.1$) is used to mark the global angular positions of the inner cylinder. As the emissivity of the tape is different to the inner cylinder surface, the location of the markers can be seen to a high degree of accuracy. This

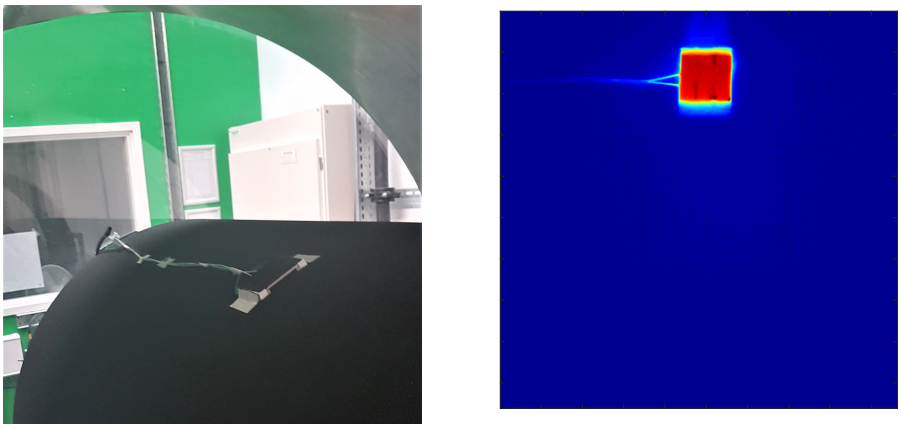

(a) (b)

FIGURE 3.11: **a:** Flat-plate calibration piece installed in the ExCITE facility. **b:** Example IR camera measurement of this test piece heated.

feature also allows the data from five cameras to be blended together into one image. The markers can be seen in figure 11.3 in section 11.2.

3.4.2 Directional Emissivity Calculation

The directional emissivity properties of the painted Rohacell and aluminium can be determined ex-situ using a flat plate test piece and a similar experimental method to the previous section. The results of this are shown in figure 3.12. The Rohacell has been fitted to the curve given by equation 3.4, which was proposed by Elfner *et al.*[28]. A least-squares fitting method gave the following coefficient values: $C_0 = 0.016$, $C_1 = 0.97$, and $C_3 = 0.004$; which gives an R^2 value of 0.983. The aluminium profile follows the expected behaviour of a dielectric material. The experimental values have been fitted to equation 3.5, based on the work of Howell [44]. The best-fit coefficient values for this cure are: $n = 4.02$ and $k = 11.64$, giving an $R^2 = 0.98$.

$$\varepsilon(\varphi) = 1 - \left(C_0 \frac{\pi}{\cos\left(C_1 \varphi\right)} + C_2 \right) \tag{3.4}$$

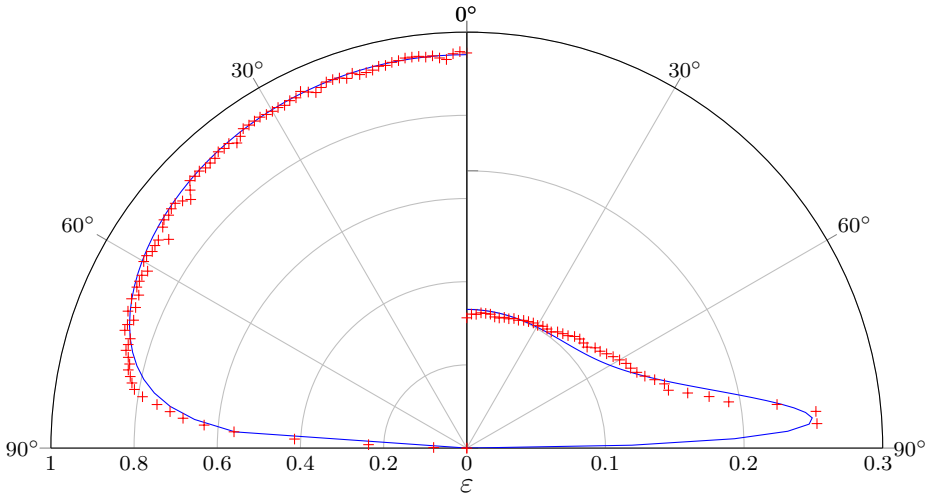

FIGURE 3.12: Measured directional emissivity of painted Rohacell (left) and aluminium (right).

$$\varepsilon(\varphi) = \frac{1}{2}\left[\frac{4n\cos\varphi}{(n^2+k^2)\cos^2\varphi + 2n\cos\varphi + 1} + \frac{4n\cos\varphi}{\cos^2\varphi + 2n\cos\varphi + n^2 + k^2}\right] \tag{3.5}$$

3.5 Radiation Flux Calculation

Although the experimental facility operates at modest temperatures (< 100°C), it is still important to account for radiative heat transfer. A mathematical model has been developed to calculate the local radiative heat flux in the concentric cylinder section, to both the inner and outer surface, assuming that the surfaces are grey and diffuse, and the air is non-participating. Firstly, the inner and outer surface cross-section is discretised into small linear portions – each portion can then be considered isothermal [44]. Hottel's crossed-string method [16] can then be used to calculate the view factor for each individual section. Equation 3.6 gives the formula for an inner surface section to an outer section; figure 3.13 shows the variables used in the equation. This method is only applicable to two-dimensional geometry.

$$F_{io} = \frac{(l_1 + l_3) - (l_2 + l_4)}{2l_i} \tag{3.6}$$

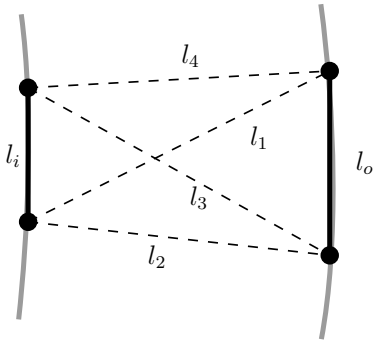

FIGURE 3.13: Schematic of how the view factor is determined using Hottel's crossed-string method [44].

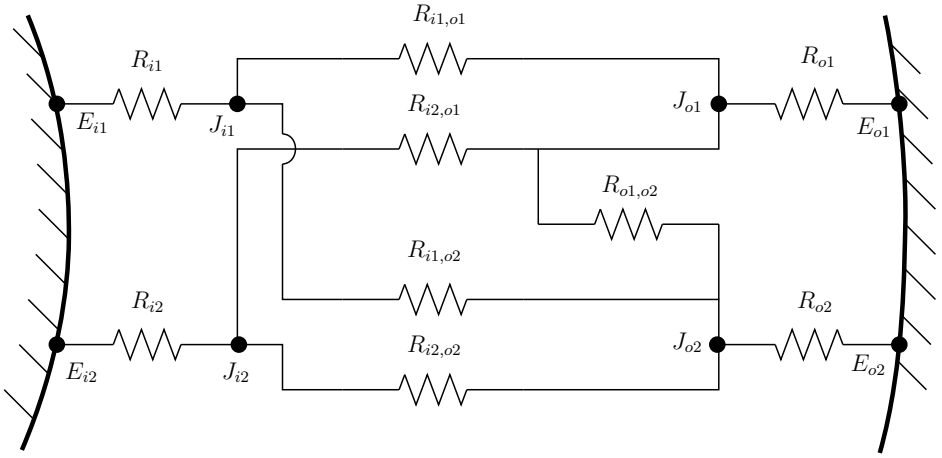

FIGURE 3.14: Simplified schematic of a radiosity resistance network that is used to find the radiation heat flux in a concentric annulus.

A radiosity resistance network is then defined. Figure 3.14 shows a simplified schematic with two nodes on each of the surfaces. This is extended to encompass the entire inner and outer surfaces. Equations 3.7 to 3.9 give the definitions of the symbols used in the schematic [16]. E is the black-body emission.

$$E_i = \sigma T_i^4 \tag{3.7}$$

$$R_i = \frac{1 - \varepsilon_i}{l_i e_i} \tag{3.8}$$

$$R_{io} = \frac{1}{l_i F_{io}} \tag{3.9}$$

Equating the heat flows at an inner surface node gives:

$$Q_i = \frac{E_i - J_i}{R_i} = \sum_{o=1}^{N_o} \frac{J_i - J_o}{R_{io}} \tag{3.10}$$

where N is the number of nodes. Similarly, equating the flows at an outer node gives equation 3.11. Note the inclusion of an extra summation term as the outer surface is concave and can therefore view portions of itself.

$$Q_o = \frac{E_o - J_o}{R_o} = \sum_{i=1}^{N_i} \frac{J_o - J_i}{R_{oi}} + \sum_{o=1}^{N_{o-1}} \frac{J_o - J_{o,o+1}}{R_{o,o+1}} \tag{3.11}$$

The temperature distributions of both surfaces are known, hence E can be defined. An initial guess of Q_o is made; from this J_o can be calculated. Equation 3.10 is then rearranged to solve for J_i. These values are substituted into equation 3.11 and it solved for J_o. This is completed for all of the nodes. This process is then iterated until the values of J converge, and hence the net radiative heat flux from each node is calculated. This method has been validated by comparing the results to the exact analytical solution of radiation heat transfer between infinite isothermal cylinders [44], given in equation 3.12.

$$\dot{q}_{io,rad} = \frac{\sigma \left(T_i^4 - T_o^4\right)}{\frac{1}{\varepsilon_i} + \frac{1 - \varepsilon_o}{\varepsilon_o} \left(\frac{D_i}{D_o}\right)} \tag{3.12}$$

Based on typical RoBo rig operating conditions (D_i = 326 mm, D_o = 406 mm, T_i = 100°C, T_o = 60°C, ε_i = 0.95, ε_o = 0.1), equation 3.12 gives 48.353 W/m^2; discretizing each surface into 128 nodes and applying the above method gives 48.349 W/m^2.

An uncertainty analysis of the radiative heat flux is given in Appendix B, which gives a typical uncertainty of 12%. This analysis also showed that the uncertainty of the IR camera measurement can be reduced by having high emissivity on the

inner cylinder and low emissivity on the outer cylinder surface – which has been implemented into the design of both facilities.

3.6 Conclusions

The key outcomes of the work presented in this chapter are as follows:

- The ExCITE facility has been designed and built. It is capable of simulating engine-representative Rayleigh numbers in the auxiliary zone during shutdown.
- An additional facility (RoBo rig) has been constructed that simulates the natural convective flow in a high-pressure compressor during shutdown cooling. The novel design of the rig allows for the influence of numerous features to be investigated.
- A sophisticated temperature control system has been developed for both rigs that allows for accurate control of the wall thermal boundary condition. Both isothermal and non-isothermal profiles can be defined.
- Methodologies for calibrating IR camera measurements and calculating the radiative heat flux from the measurement surface have also been developed.

Chapter 4

Temperature Traverse Probe Design

This chapter describes the design process and validation of a temperature probe that has been developed to allow for measurements in a natural convective experiment. The attractiveness of a high-quality temperature traverse probe is that both the wall heat flux and free-stream gas temperature can be determined accurately from a single measuring device.

4.1 Introduction

The local wall heat flux can be directly inferred from the thermal boundary layer profile [36]. A thermocouple traverse is used in both experimental facilities to measure this thermal boundary layer. A thermocouple consists of two dissimilar metal wires welded or soldered together at one end (the hot junction) forming a bead. In the conductive sub-layer of the boundary layer, the strong thermal fluid gradient can cause heat to be conducted away from the bead; thus, if this is the case, the temperature measurement will be lower than the actual fluid temperature. The conduction error may be reduced by designing the probe mount to have a length

of wire (L_n) parallel to the wall. Figure 4.1 shows a schematic of this arrangement; typical velocity and temperature profiles seen in a natural convective boundary layer are also included. However, this longer length of wire exposed to a higher temperature may also impact the response of the thermocouple and the surrounding flow field. Thus, the author conducted detailed design studies of the effect of thermocouple probe parameters on its accuracy.

A small diameter wire is desirable as it will be less intrusive while also giving a smaller cross-sectional area for heat to conduct away from the bead. Hence, a 76 μm wire gauge type K thermocouple is used. Type K has been selected due to it's low-cost, fast response and robustness.

Kulkarni et al. [12, 59, 60] have designed a similar type of probe for a forced convection thermal boundary layer. Their numerical work concluded that it is indeed the conduction away from the hot junction that is the dominant source of error, while also commenting that the flow field distortion caused by flow accelerating in the gap between the probe and the wall is insignificant. The design work presented here differs to that of Kulkarni at is focuses on natural convective flows. Moreover, the 1D model developed considers both wires, a bead, radiation and wire insulation.

4.1.1 Thermocouple Operating Principle

A temperature gradient along a metal wire generates a voltage – known as the thermoelectric effect [9]. The magnitude of this electro-motive force (emf) depends on a material property known as the Seebeck coefficient (S). The two wires of a thermocouple have a different Seebeck coefficient, thus the voltage difference generated can be determined by evaluating the integral given in equation 4.2, which is derived from equation 4.1.

$$\frac{dV_T}{dx} = S\frac{dT}{dx} \tag{4.1}$$

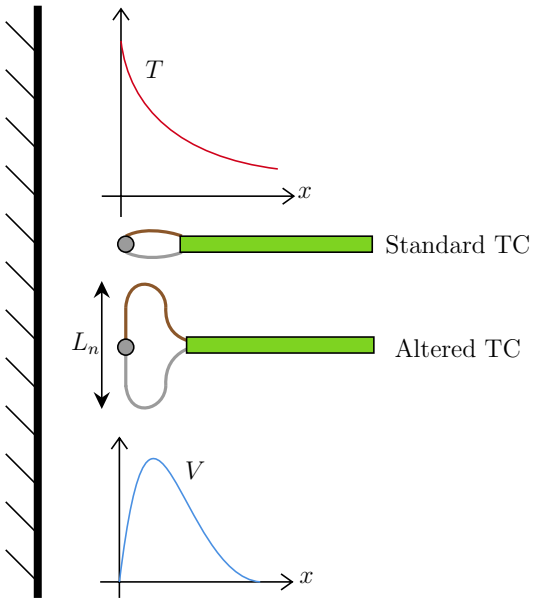

FIGURE 4.1: Schematic of possible thermocouple wire arrangements. Typical natural convection temperature and velocity profiles are also shown.

$$V_T = emf = \int_{T_1}^{T_2} S_1 dT - \int_{T_1}^{T_2} S_2 dT = \int_{T_1}^{T_2} \Delta S dT \tag{4.2}$$

It is clear form this equation why dissimilar metals are required, as no voltage would be produced if both wires had the same Seebeck coefficient. The hot junction temperature can only be evaluated when referenced to a cold junction temperature – typically 0°C. NIST provides a set of standard tables and functions for the output voltage for common thermocouple constructions [103]. The response of a type K thermocouple – composed of an alumel and a chromel wire – is shown in figure 4.2a with 0°C used as the reference temperature. The generated voltage is fitted to equation 4.3, valid from 0 to 1300°C:

$$emf = \sum_{i=0}^{N} c_i T^i + a_0 e^{a_1 (T - a_2)^2} \tag{4.3}$$

The coefficients of this equation are again from NIST [103]. Differentiating equation 4.3 gives the difference in Seebeck coefficient (ΔS) as a function of temperature. The

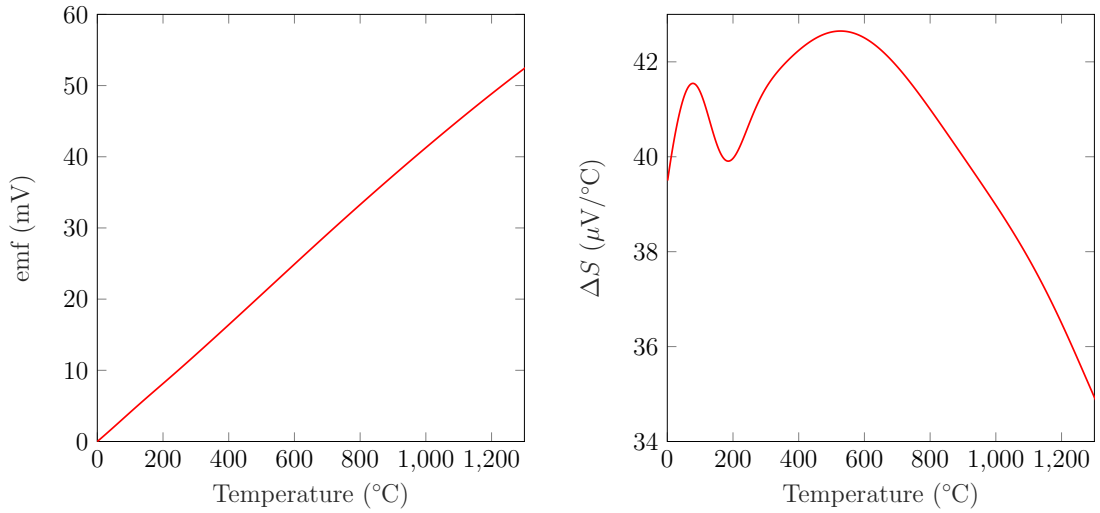

(a) (b)

FIGURE 4.2: **a:** Voltage generated in a type K thermocouple. Referenced to 0°C. **b:** Seebeck coefficient for type K thermocouple [103].

result is shown in figure 4.2b. The standard voltage responses that are provided assume that both wires experience the same temperature gradient. However, as this probe separates the wires in the vicinity of the hot junction, this may no longer be the case. To account for this in the probe design, S_1 is set constant as 18 μV/°C [9] and S_2 is then given as: $S_2 = \Delta S - S_1$. This allows for separate integral for each wire to be calculated using equation 4.2.

The material properties for alumel and chromel are given in table 4.1 [2, 30]. The bead material properties are assumed to be the average of both wires. The emissivity values are nominal and may vary by up to 30% [30] – this parameter is investigated in section 4.3.2. The geometric values have been determined using a micrometer. These properties are used in both the 3D numerical simulations and the 1D model.

4.2 3D Conjugate Probe Simulation

A conjugate CFD study has been conducted to investigate the altered TC arrangement. A vertical heated flat plate geometry is used for this study. Probe-to-wall distances (d)

TABLE 4.1: Properties of a type K thermocouple. [2, 30].

	Alumel	Chromel	Bead	Insulation
Diameter	76 μm	76 μm	285 μm	1 mm
Thermal Conductivity (W/mK)	29.77	19.2	24.5	0.3
Thermal diffusivity ($m^2/s \times 10^{-6}$)	6.61	4.91	5.76	
Emissivity	0.75	0.75	0.75	0.8

of 300μm, 1 mm and 10 mm have been simulated for $L_n = 0$ and 12 mm respectively. These values were chosen to be consistent with the experimental campaign described later in section 4.4. A baseline case with no probe was also conducted. ANSYS Fluent is used to perform the calculations, while the meshing is completed with ICEM.

4.2.1 Model Definition

Figure 4.3 shows a schematic of the solution domain, along with the applied boundary conditions for a $L_n = 12$ mm case. The heated wall is set as a uniform temperature of 373 K. The ambient wall is set as 300 K, which gives $Ra_{L_c} = 8.5 \times 10^5$ at the measurement location. The fluid was modelled as an ideal gas. An unstructured mesh was used; the size was circa 3 million elements for all six cases. The first cell height chosen so that $y^+ < 1$. Figure 4.4 shows a slice of the mesh for the $L_n = 12$ mm, $d = 300$ μm case. The $k - \omega$ SST turbulence model was chosen as this model has previously been used successfully for natural convective flows [85].

The area-averaged Nusselt number from the heated wall for the simulation without the probe was 32.1, all probe cases were within 1% of this number. The widely used Churchill & Chu correlation [20] for natural convection from a vertical flat plate gives a Nusselt number of 30.4 for these conditions, which indicates that the simulation technique has adequately captured the heat transfer physics.

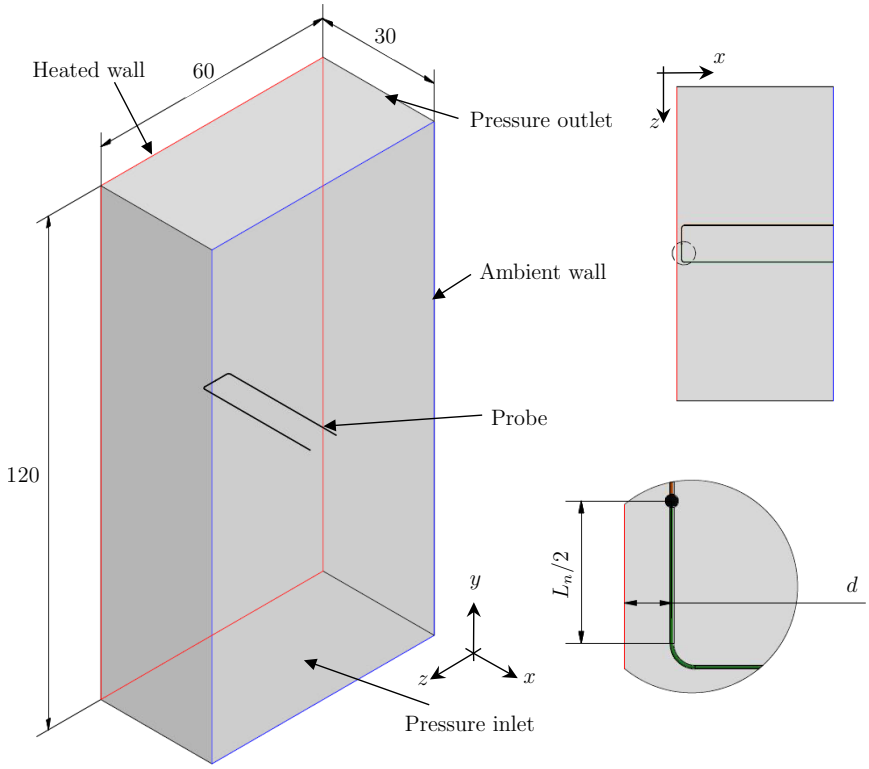

FIGURE 4.3: Outline of the probe simulation domain. All dimensions are in mm.

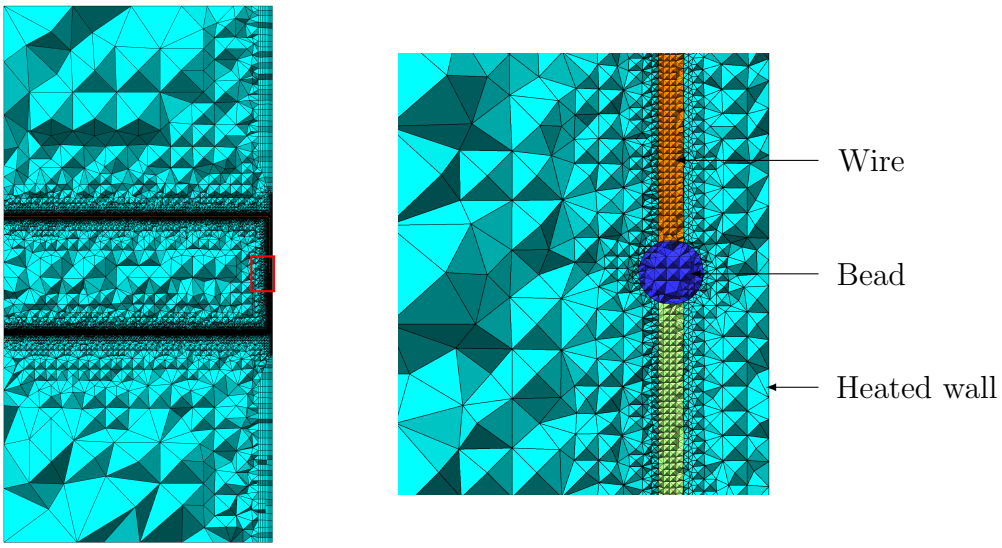

FIGURE 4.4: Section-view of the mesh at the middle y plane for the $L_n = 12$ mm, $d = 300$ μm case. A detailed view of the bead region is also shown.

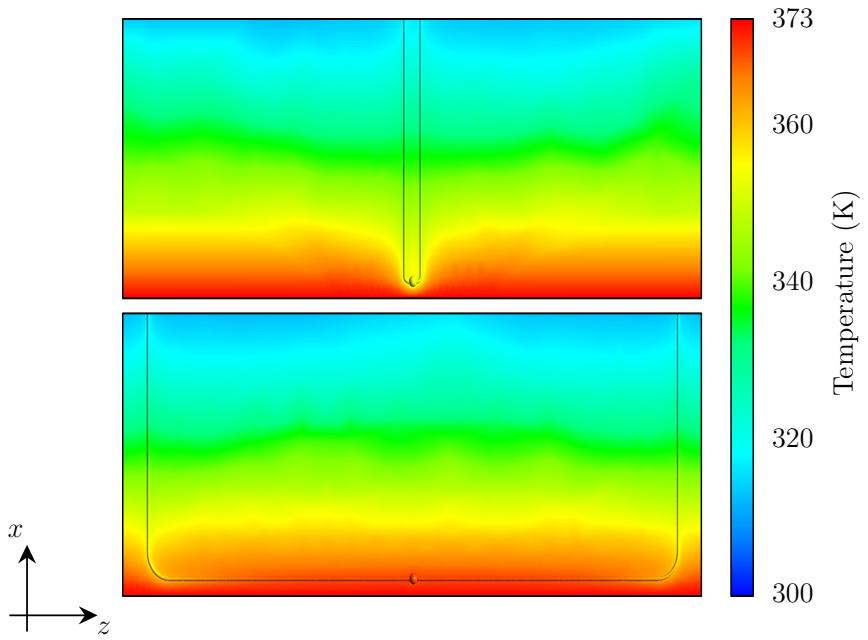

FIGURE 4.5: Temperature contours from the conjugate simulation on the middle y plane for $L_n = 0$ mm (top) and $L_n = 12$ mm (bottom), at $d = 300$ μm.

4.2.2 Results

Figure 4.5 shows the temperature contours on the central plane normal to the y-axis as defined in figure 4.3, for the $d = 300$ μm cases. It is evident from the $L_n = 0$ mm case that the bead temperature is significantly lower than the surrounding fluid (6 K); whereas the temperatures are very similar (< 1 K) in the $L_n = 12$ mm case.

The voltage output that would be produced by the simulated probe is determined by using equation 4.2 and the method outlined in section 4.1.1, for the line through the centroid of both wires and the bead. Figure 4.6 shows the thermal boundary profile normal to the heated wall for the simulation without a probe, compared to the values that would be measured by the thermocouple for the six simulated cases. It is clear from this figure that the conduction away from the bead in the region of a strong thermal fluid gradient has a large impact on the measurement acquired. Orientating a section of the wire normal to the heated wall has eradicated this source of error. In this new arrangement, the two wire temperature profiles vary slightly from each other (max 1.5 K), but this effect is also captured in the calculation method; therefore, the

TABLE 4.2: Comparison of the calculated Nusselt number for the different probe cases.

Case	Nu	Calculation Method
No probe	12.7	from wall heat flux.
No probe	12.6	from thermal boundary layer slope.
$L_n = 0$ mm	11.7	slope between $d = 300$ μm and 1 mm points.
$L_n = 12$ mm	12.4	slope between $d = 300$ μm and 1 mm points.

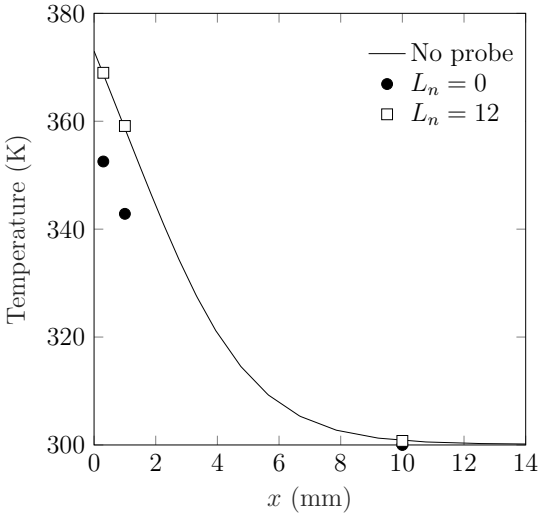

FIGURE 4.6: Predicted thermal boundary layer profile for the unobstructed case and the simulated values that would be recorded by the thermocouple probe.

effect can be deemed negligible.

Table 4.2 gives a comparison of the calculated Nusselt number for the different cases. Examining the case without a probe, the slope of the conductive sub-layer method agrees very well with the value based on the computed wall heat flux: $< 1\%$ difference. The Nusselt number, calculated using the slope of the two measurement points in the linear sub-layer, for the $L_n = 0$ mm probe is 7.9% lower than the actual value. Applying the same method to the $L_n = 12$ mm reduces this error in Nu to 2.4%. This result demonstrates that a more accurate measurement of heat flux can be obtained from this altered thermocouple arrangement.

The results of these simulations can also be used to examine any obtrusive effects of placing the probe in the thermal boundary layer. The unobstructed flow case

shown in figure 4.6 indicates that the linear sublayer extended for 3 mm at this measurement location, which is 10 times larger than the diameter of the bead. This situation was representative of the majority of the heated cylinder boundary layer experiments discussed in Chapter 6.

Figure 4.7a gives the local Nusselt number along the heated wall central plane for the $d = 300$ μm and the unobstructed case. The large localised peak underneath the probe in the $L_n = 0$ mm case immediately stands out. This peak is not present in the 12 mm case. This indicates that this large increase in heat flux is not solely attributed to the flow being accelerated in the gap between the probe and the wall. However, the Nu profile downstream of the probe matches that of the no probe case, confirming that the probe has not obstructed the overall flow.

Figure 4.7b shows Nu along the wall in the z direction, i.e. parallel to the L_n principal axis, at $x = 60$ mm. Interestingly, peaks in Nusselt number at ± 6 mm are seen in the $L_n = 12$ mm case. This is the location where the wires are rotated 90° so that they are perpendicular to the heated wall. Examining again the temperature contour in figure 4.5, this is where a strong temperature gradient begins to appear in the wire. The gradient in the wire is causing the air between the wall and probe to be cooler than the section where there is no thermal gradient ($z = 0$). It is this cooler air near the heated wall that is causing the sharp increase in local heat flux. The finding also applies to the $L_n = 0$ mm case.

The velocity contour along the z central plane does show some fluid being diverted towards the wall underneath the bead. This is causing a slight difference in the local Nusselt number when compared to the unobstructed case – as can be seen at $z = 0$ for the $L_n = 12$ mm case in figure 4.7b. However, this effect is much less significant than the thermal gradient in the wire impact. The flow acceleration will also reduce as the probe is placed further away from the wall. Hence, this effect can be safely neglected, which agrees with the conclusions of Kulkarni [59].

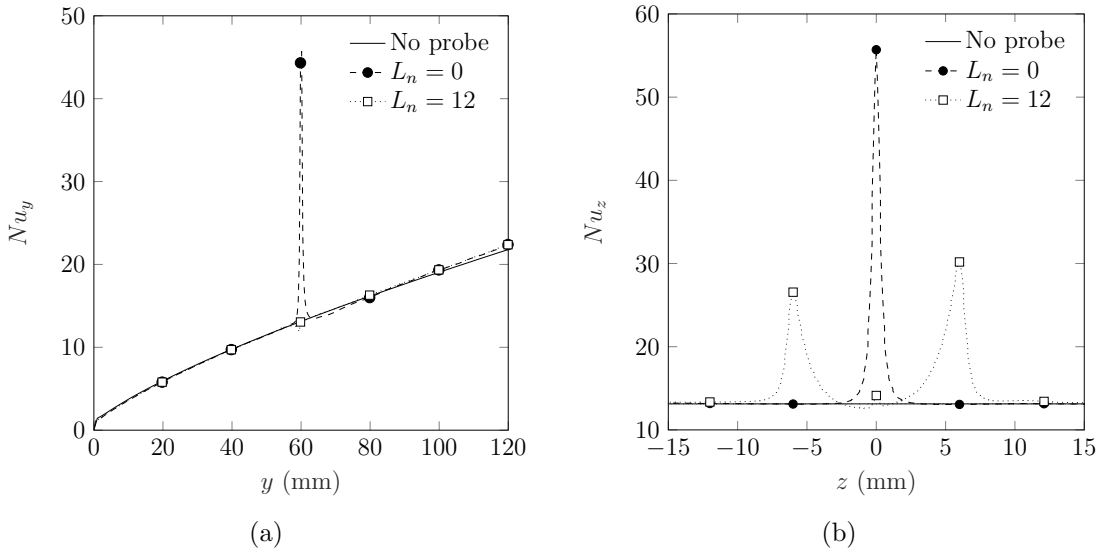

(a) (b)

FIGURE 4.7: **a:** Nu_y along the domain centreline for the unobstructed, $L_n = 0$ and 12 mm cases at $d = 300$ μm. **b:** Nu_z at $x = 60$ mm for the same test cases.

4.3 1D Conduction Model Investigation

Now that the concept of placing a section of wire parallel to the heated surface has been shown to improve the temperature and heat flux reading in a natural convective boundary layer, a 1D conduction model has been developed in order to determine the optimum design of the probe, while also investigating the effect of various parameters.

4.3.1 Model Definition

Firstly, the probe wire is discretised into cell-centered finite volumes to represent both the thermocouple wires and the bead – see figure 4.8. The bead is represented as one cell with the volume of a sphere. The remainder of the elements are modelled as cylinders, similar to the technique used by Prabhu [42] and Kulkarni [59]. A finite difference method is used solve the 1D transient heat equation. Applying an energy balance to an element yields equation 4.4. V_e is the volume of the element, i is the iteration, Δt is the time step. The limit of the size of the time step is set by: $\Delta T < \Delta x^2/2\alpha$ [16]. The heat flux summation term consists of conduction to

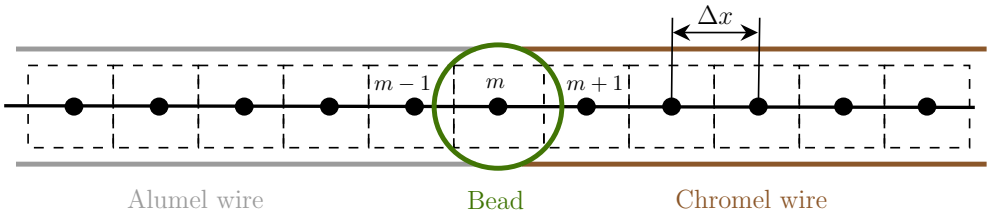

FIGURE 4.8: Schematic of how the thermocouple has been discretised into finite volumes, represented by the dashed lines, for the 1D model.

each neighbouring node, convection to the ambient fluid, and radiation – as shown in equation 4.5. It is assumed that the wire and beads only radiate to the hot inner surface: T_{sur}. Neumann boundary conditions are applied at the ends of the wire: $dT/dx = 0$. Equation 4.5 is equated to equation 4.4 and rearranged to solve for T_m^{i+1}. The solution is time-marched explicitly until it has converged to a steady state.

$$\sum \dot{Q}^i = \rho V_e c_p \frac{T_m^{i+1} - T_m^i}{\Delta t} \tag{4.4}$$

$$\sum \dot{Q}^i = \frac{k_1 A_w}{\Delta x}\left(T_{m-1}^i - T_m^i\right) + \frac{k_2 A_w}{\Delta x}\left(T_{m+1}^i - T_m^i\right) + h_s A_s (T_{f,m} - T_m^i) + \varepsilon_w \sigma A_s \left(T_{sur}^4 - (T_m^i)^4\right) \tag{4.5}$$

Subscripts 1 & 2 refer to each wire, s refers to the bead and f is a fluid property. Fluid temperature and velocity fields are required as inputs for this model – in order to evaluate h_s and T_f. These are provided from a CFD simulation of a cylindrical section of the RoBo facility at $Dr = 1.25$ and a gap height (H) of 40 mm, for the initial study. The influence of these input parameters however will be explored later in section 4.3.3. Figure 4.9 indicates how the fluid temperature and velocity fields are defined in order to simulate L_n. The fields are mirrored about the bead to allow both wires to be modelled in one-dimension. The length of wire parallel to the wall (L_n) will experience a constant temperature and velocity field, as indicated by the

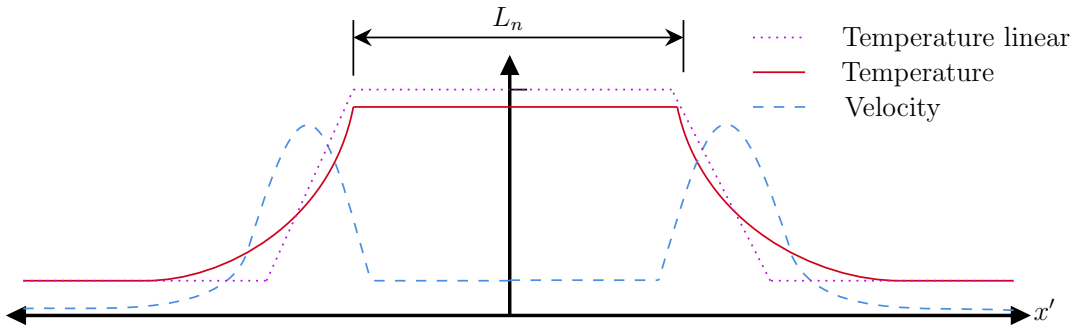

FIGURE 4.9: Schematic of fluid temperature and velocity field used as inputs for the 1D probe model.

horizontal line sections. Different values of the distance between the heated wall and the probe can be simulated by placing the horizontal line section at different heights. x' is used to denote the distance along the wire.

The wire length is set to double the annulus height to ensure the insulated boundary condition that is applied to the cold junction end of the wire is appropriate. Inclusion of this adiabatic length was found to be important in previous studies [51]. The fluid temperature is set to ambient outside of the annulus. The heated wall temperature is used as T_{sur} for nodes contained in the annulus; whereas the wire nodes outside radiate to ambient: T_∞. For test cases in section 4.3.3, the fluid temperature profile is approximated as linear with a given gradient, this is represented as the dotted line in figure 4.9.

Correlations are required in order to evaluate the convective heat transfer coefficients: h_s. It is not known a priori whether the appropriate correlation for Nusselt number at the probe tip should be derived from natural of forced convection correlations. The Richardson number can be used to inform this decision. According to Sparrow *et al.* [99] the following limits were identified for the classes of convection for assisting flow:

$$Ri = \frac{Gr}{Re_D^2} \tag{4.6}$$

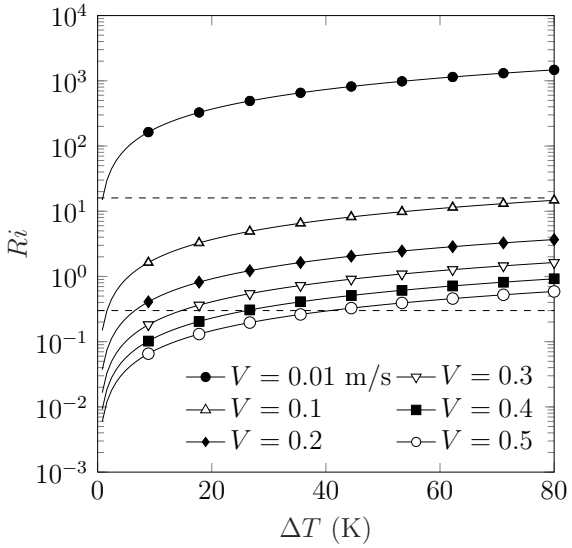

FIGURE 4.10: Values of Ri that the probe may experience during operation. The dashed lines are the boundaries defined by Sparrow *et al.* [99].

$0 < Ri < 0.3$	Forced convection
$0.3 < Ri < 16$	Mixed convection
$16 < Ri$	Natural convection

Assisting flow is defined as the buoyancy force having a positive component in the direction of the free-stream velocity. Velocities associated with natural convection are typically lower than 0.5 m/s. The range of expected temperatures in the experimental facility is 20-100°C. Figure 4.10 shows the possible Richardson numbers of the wire for the expected rig conditions. The dashed lines are the boundaries defined by Sparrow *et al.*

It is evident from this figure that all three regions are likely to be experienced during the probe traverse. For the cylindrical elements, Churchill & Bernstein's correlation for forced convection (Nu_F) over a cylinder in crossflow is used at $Pe = RePr > 2$ [18]. Below the latter range, low Re correction of Lange et al. [64] is applied, this tends to occur in the near-wall region. Churchill & Chu's correlation [19] is used to calculate the Nusselt number by natural convection (Nu_N). In the case of the

spherical bead, the correlation of Whitaker is used for forced [113], and Churchill [16] for natural convection. The ΔT required for the Rayleigh number is taken as the wire temperature minus the mid-annulus temperature. In the mixed convection regime, equation 4.7 is used to combine the forced and natural Nusselt number correlation, following the method of Rohsenow [91].

$$Nu = \left[Nu_F^3 + Nu_N^3\right]^{1/3} \tag{4.7}$$

Insulation has been modelled by calculating a thermal resistance across the insulation thickness. This value can then be used to determine the surface temperature of the insulation which is in-turn used in the convection heat transfer correlations. All values of h are updated at each time step.

4.3.2 Initial Results

Six values of L_n have been analysed. Figure 4.11a gives the difference between the temperature that would be measured by a type K thermocouple (T_{TC}) and the actual fluid temperature as the probe is moved away from the heated wall. T_{TC} has been calculated using equations 4.2 and 4.3. The CFD generated fluid temperature (solid) and velocity (dashed) fields used as inputs are defined in figure 4.11b. These are the radial profiles at the BDC of the annulus. The form of the error in temperature agrees extremely well with the 3D conjugate model presented in section 4.2: the largest error occurs where the air temperature gradient is greatest, and increasing L_n has the desired effect of reducing this error significantly. The error converges at $L_n = 12$ mm, which is approximately 150 times the diameter of the wire. The ≈ 1 K error outside of the thermal boundary layer that is common to all values of L_n is mainly caused by radiation from the hot inner wall to the probe.

Figure 4.12a gives the wire temperature predicted by the 1D model for the $L_n = 0$ and 12 mm cases, when the bead is in contact with the heated wall: $x = 0$. The

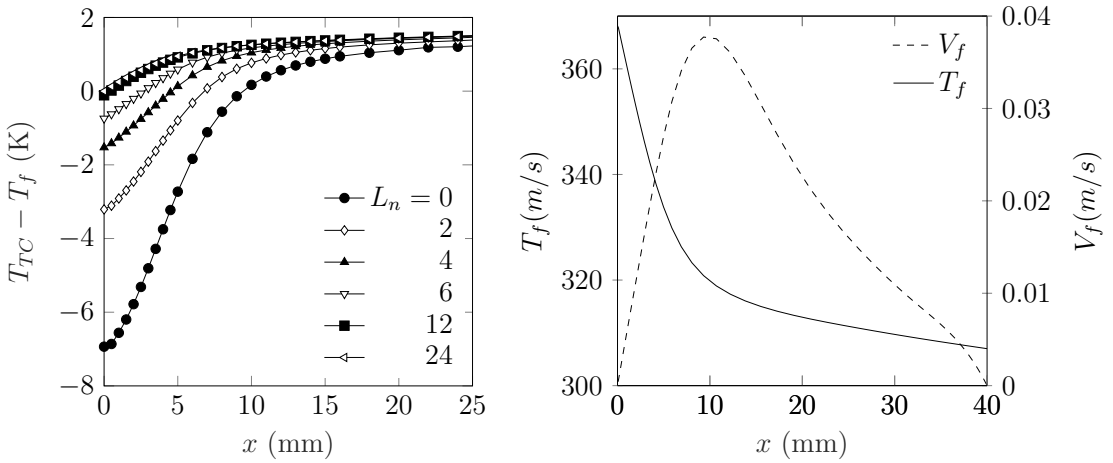

FIGURE 4.11: **a:** 1D model predicted difference between the fluid and measured temperature at for different values of L_n as the probe is moved in the x direction. The values of L_n are in mm. **b:** CFD generated fluid temperature (solid) and velocity (dashed) fields that are used as inputs for the 1D model.

dashed lines represent the fluid temperature. The heat fluxes from the bead element for these cases have been broken down into its constituent components (see equation 4.5); the results are shown in figure 4.12b. Positive values indicate heat flow out of an element. The large conductive heat flux in the near wall region for the $L_n = 0$ case is evident. This is balanced by a large negative convective heat flux – driven by the natural convection component of the heat transfer coefficient. A section of wire parallel to the wall nearly eradicates the conductive flux completely, which in turn has drastically reduced the convective heat transfer – as the ΔT driving this flux has also been reduced. The end result of this is a flat wire temperature profile at the bead, extremely close to the actual fluid temperature, as shown by the blue lines in figure 4.12a. The radiation fluxes for both cases are extremely similar, which is to be somewhat expected owing to the relatively low temperatures involved.

The CFD profiles for this study (figure 4.11b) were selected as the steepest air temperature gradient occurred along this line. The velocities at this location however are very low. The profiles at other annular positions, where the velocity peak was higher (0.1 m/s) but the temperature gradient was lower, were also used as model

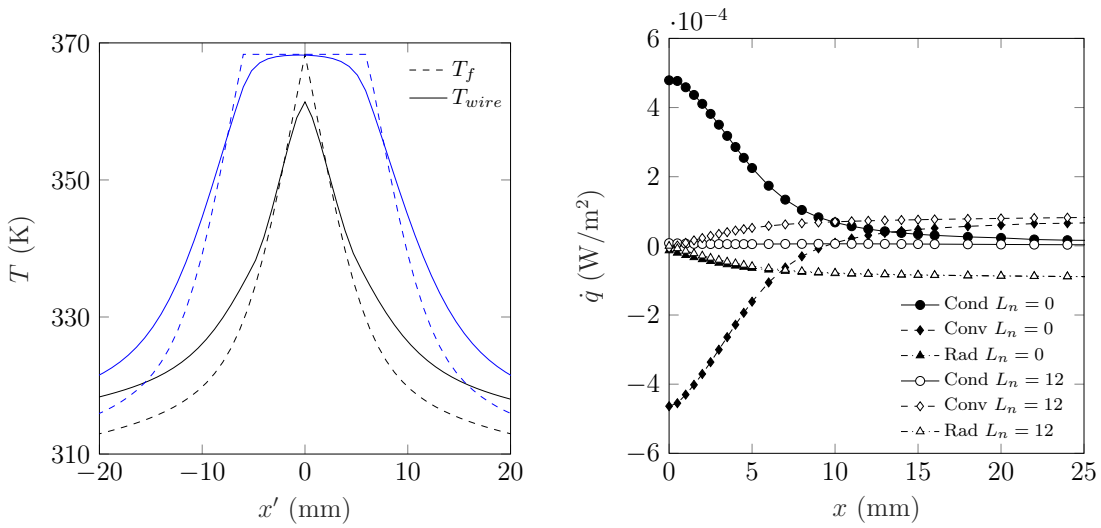

FIGURE 4.12: **a:** 1D model predicted wire temperatures for the $L_n = 0$ (black) and 12 (blue) cases. $x = 0$ in both cases. **a:** Constituent node heat fluxes for the bead element for the corresponding cases.

inputs, however the error was lower than those presented in figure 4.11a.

The sensitivity of the findings to the modelling input parameters was investigated for the $L_n = 0$ case, namely: inclusion of insulation, wire emissivity and heat transfer coefficient definition. Increasing the wire insulation up to the largest possible practical value did not have any significant impact. Doubling the convective heat transfer coefficient (h) tended to reduce the wire temperature error, whereas halving its value increased the error by 2 K at $x = 0$. The model was recomputed with h halved, for increasing values of L_n. Although the initial error was larger, the temperature difference between the fluid and thermocouple again converged for $L_n = 12$ mm.

Setting the emissivity to 0 does get rid of the ≈ 1 K offset observed in the mid-annulus for all values of L_n. Since this offset is lower than the measurement uncertainty, and the main objective is to measure temperature in the conductive sub-layer, this error was deemed negligible. Should this probe design be used for higher temperature measurements, application of a radiation correction method should be investigated.

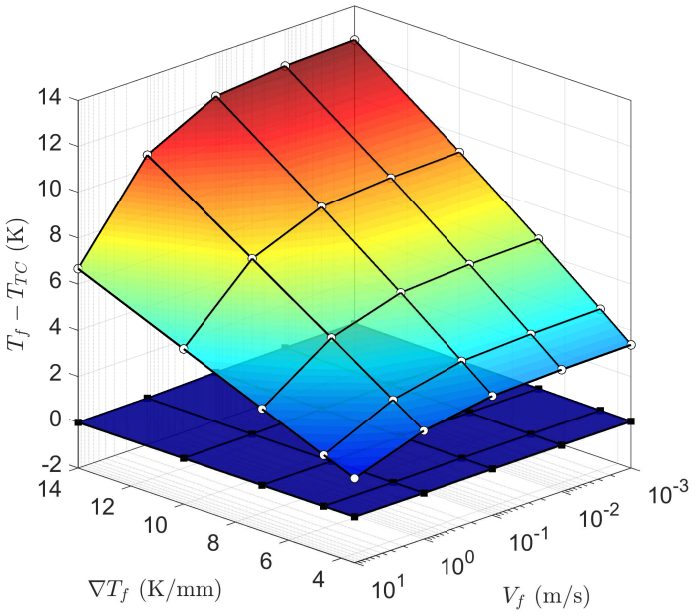

FIGURE 4.13: Surface contour giving the temperature error predicted by the 1D model for combinations of ∇T_f and V_f. Results are shown for the $L_n = 0$ (white dots) and $L_n = 12$ (black squares) cases. $T_f = 370$ K and $x = 0$ mm at the bead location in all cases.

4.3.3 Parameter Investigation

The model investigation has been extended in an attempt to produce a solution that is independent of the required CFD fluid profiles that were used in the previous section. The air temperature profile is now modelled as a piece-wise linear polynomial, as shown by the dotted line in figure 4.9 on page 58. The fluid temperature at the bead is set as 370 K in all cases, and 300 K for the horizontal section of the dotted curve. Five thermal gradients (∇T_f's) between 3.5 and 14 K/mm have been studied. ∇T_f for the CFD profile used in section 4.3.2 was approximately 7 K/mm. The fluid velocity is set to a constant value, again five values have been investigated between 0 and 10 m/s. Figure 4.13 gives the response surface for the various flow conditions specified. $L_n = 0$ mm is indicated by the white dots; whereas $L_n = 12$ mm results are displayed by the black squares. Note that the velocity axis is logarithmic. $T_f = 370$ K and $x = 0$ mm in all cases.

The results of the $L_n = 0$ case indicate that the error increases with ∇T_f, and reduces as V_f is increased. It is evident that the reduction in error that is possible by having $L_n \geq 12$ mm is not influenced by either the fluid temperature or velocity gradient presented here – even for a very severe case of 14 K/mm. The 1D model results are now independent of the CFD input parameters.

4.4 Experimental Validation

An experimental study was conducted in order to validate the findings from the previous sections. Three probe designs were used: $L_n = 0$, 12, 24 mm. A type K, 76 μm wire thermocouple was used in all cases. A component has been designed that holds the wire at the correct L_n and allows both wire to return neatly to a central tube, thereby reducing the intrusiveness of the technique. The outer diameter of the tube was only 3 mm. The component was 3D printed on a liquid resin printer which has a resolution of 100 μm. The material has a low thermal conductivity (approximately 0.23 W/m K) [100]. Figure 4.14 shows the probes that have been manufactured.

It is apparent from this image that the L_n section of probe wire is not perfectly straight; this may lead to a larger temperature difference between the two thermocouple wire materials and thus introduce a new error into the measurement. This was investigated by artificially increasing the temperature of one wire in the L_n region for the computation of the emf (see equation 4.2). However, the effect was negligible for any reasonable temperature difference that may be caused by this effect.

Radial temperature traverses were conducted at the bottom of the cylindrical annulus of the RoBo facility at a diameter ratio of 1.25 and a 60 K radial temperature difference, which gives $Ra_{D_i} = 8.4 \times 10^7$. These boundary conditions matched those of the CFD study used in section 4.3.2, to allow a direct comparison to the 1D model.

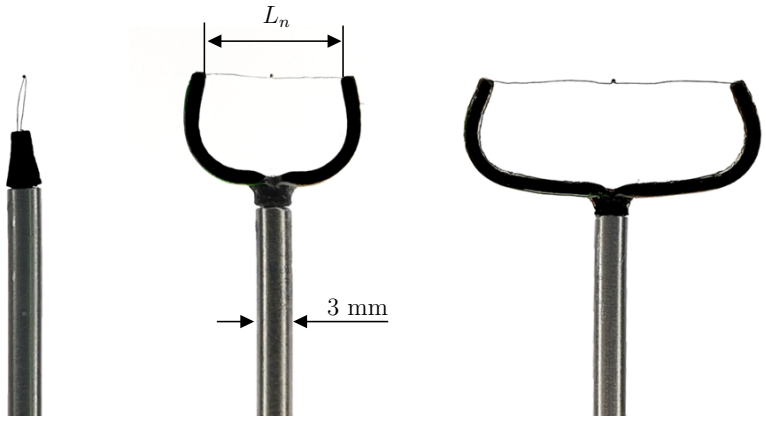

FIGURE 4.14: Temperature traverse probes that were used for experimental validation of 1D model. $L_n = 0$, 12, 24 mm.

Figure 4.15b shows the measured profiles for the three different probes. The trend agrees extremely well with that of the 1D model. The maximum difference between the $L_n = 0$ and $L_n = 12$ case was 7 K, which occurs in the vicinity of the heated wall, where the fluid temperature gradient is largest. This difference reduces as the probe moves further away from the wall. There is very little difference in measurements in the free-stream. Critically, the reading remained consistent as L_n was increased further to 24 mm, which is again consistent with the 1D model. Using the slope of the conductive sub-layer to calculate the wall heat flux, there is a 7% difference between the $L_n = 0$ and $L_n = 12$ case.

Figure 4.15 shows the percentage difference in measured temperature between the baseline ($L_n = 0$) case and the $L_n \neq 0$ cases, for both the experimental and modelled probes. This data shows that the probe temperature reading has increased by up to 10% by using this alternative arrangement. The 1D model does under-predict the error. However, if the convective heat transfer coefficient (h) is reduced in the model, then the results compare extremely well. The prediction for $0.5h$ is included in this chart. The discrepancy may be attributed to the selection of the driving temperature difference in the modelling procedure, or indeed the idealisation of the thermocouple bead as a sphere.

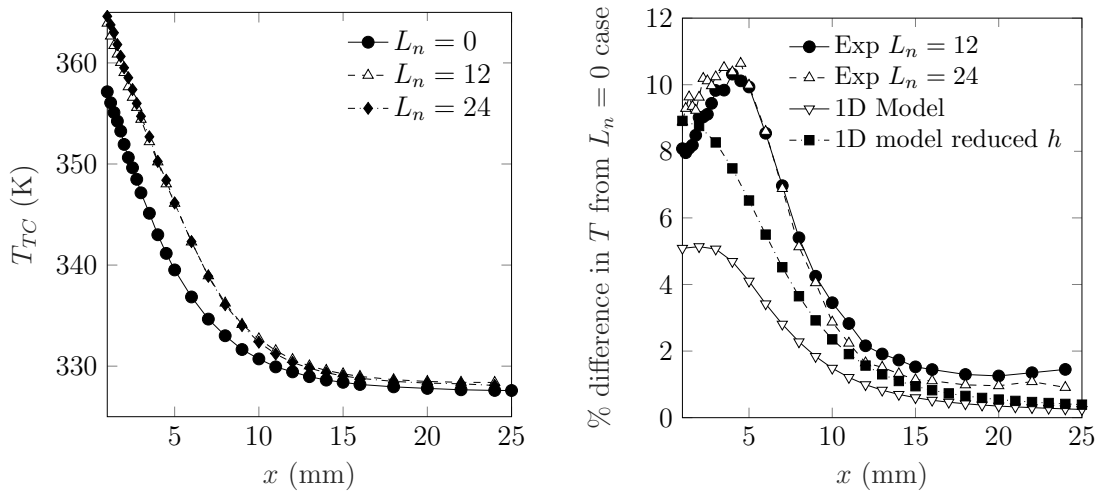

(a) (b)

FIGURE 4.15: **a:** Experimental radial temperature profile for the three different probes. **b:** Percentage difference between a traverse with $L_n \neq 0$ and the baseline $L_n = 0$ case. Predicted results from the 1D model are also shown.

4.5 Conclusions

A low-cost, minute, robust thermocouple probe has been developed which allows for accurate temperature measurements in a natural convective boundary layer. This in turn reduces the error in measuring the wall heat flux. All of the scenarios explored in this chapter confirm the finding that the conduction error of the probe has been reduced significantly by holding a portion of the wire parallel to the heated surface, without any adverse effects. A 1D model has been produced and validated that indicates that the optimum length of this section of wire, for this experimental configuration, is 12 mm ($157D_{wire}$). Although the initial model required CFD profiles as inputs, the parameter investigation section proved that the reduction in conduction error was independent of these inputs.

The thermocouple probe is incorporated in the traverse mechanisms in both the RoBo and ExCITE facilities. An advantage of this technique is that it measures the convective heat flux to the air directly; thus, the findings are decoupled from the radiative heat transfer characteristics of the experiment. This measurement

technique is used extensively throughout the remainder of this thesis. A detailed uncertainty analysis is given in Appendix B.

An additional component has been designed that allows the probe to measure the outer wall thermal boundary layer. Figure 4.16a shows a schematic of this arrangement, along with the inner wall probe configuration. Another advantage of this design is that the same thermocouple is used for both the inner and outer boundary layers, and it is easily altered in-situ. Figure 4.16b shows the probe installed in the RoBo facility.

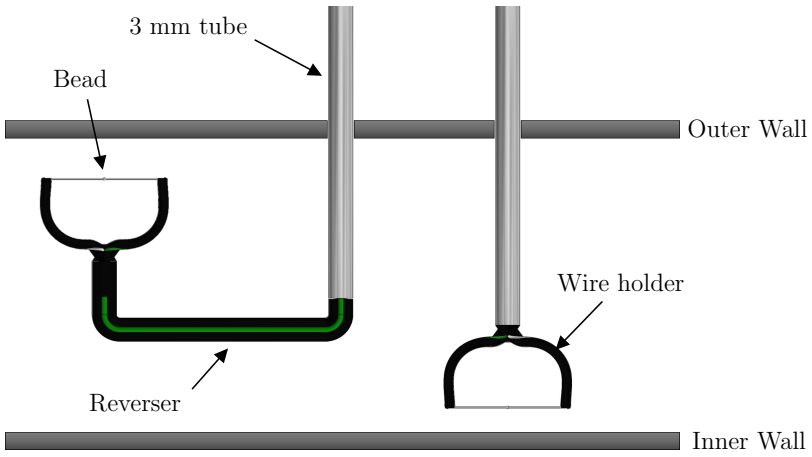

(a)



(b)

FIGURE 4.16: **a:** Schematic of the probe assembly for outer wall measurements (left) and inner wall measurements (right). **b:** The inner wall measurement probe installed in the RoBo facility.

Chapter 5

Commissioning

5.1 Initial Testing

5.1.1 RoBo Facility

The inner assembly of the RoBo facility was first tested in isolation in order to investigate the uniformity of the rig construction. For each test, the inner metal temperature was set to 60°C. The thermal boundary control system was capable of maintaining this temperature to ±0.1°C in steady-state. Steady-state was reached approximately 45 minutes after start-up. The shaft-mounted assembly of the inner cylinder allowed for this test to be repeated at multiple rotations, where a different mat can be placed at TDC. The measured electrical power into each mat (Q_{el}) can be used to calculate the mat-averaged Nusselt number using equation 5.1.

$$Nu_{D_i} = \frac{[Q_{el} - \sigma\varepsilon A_s(T_s^4 - T_\infty^4)]\, D_i}{kA_s(T_s - T_\infty)} \tag{5.1}$$

Figure 5.1 shows Nu_{D_i} for a total of seven separate rotation tests. $\theta = 0°$ is top-dead-centre and $\theta = 180°$ is bottom-dead-centre. The overall trend is encouraging and the general shape is similar to the profile from figure 2.4. Some asymmetry is

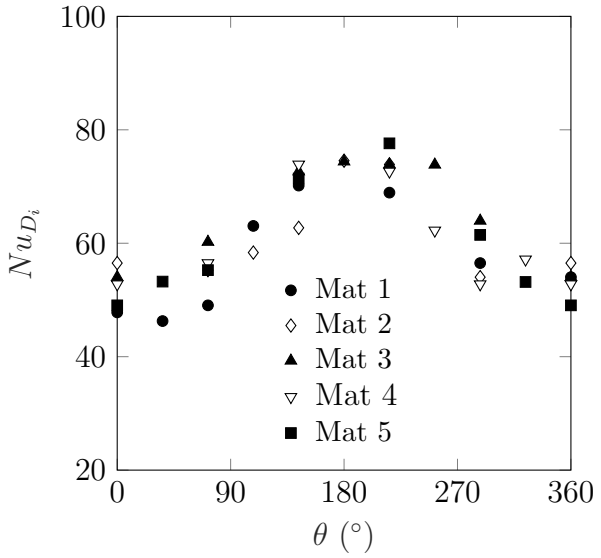

FIGURE 5.1: Mat-averaged Nusselt numbers for seven rotation tests of an isolated inner cylinder assembly of the RoBo facility. TDC is 0° and BDC is 180°.

observed in lower section; this is likely due to the installation of the facility in a large open room – this will not be a concern when the outer cylinder is in place. The area-averaged Nu across all tests is 58.7. The widely used Churchill-Chu correlation [19] for natural convection from a horizontal cylinder is isolation gives a value of 57.2. This result gives confidence that any subsequent results from the RoBo rig will be independent of the inner cylinder rotation and construction.

The discrete mat construction of the rigs allows non-isothermal profiles to be defined. A 10°C maximum circumferential difference (ΔT_c) has been imposed on the cylindrical inner of the RoBo facility by setting the desired values at each temperature control point. This is shown as the dotted line in figure 5.2. Further details of how the wall temperature profile is defined is given later in section 6.1. Since the outer cylinder has been removed, optical access to the inner surface is far less restrictive than the annular cylinder configuration so IR cameras from the ExCITE facility can be used to measure the surface temperature. This is shown for two different rotations (solid and dashed lines) in figure 5.2. Four cameras are required to capture the circumferential profile, hence the different coloured lines for each test. Values are averaged over an

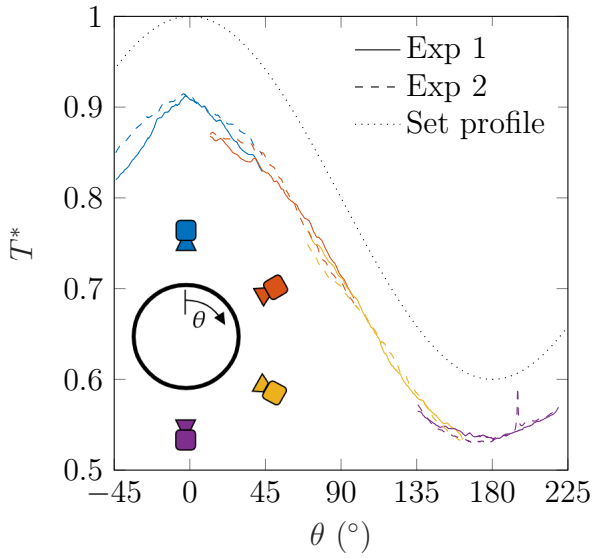

FIGURE 5.2: Inner cylinder circumferential temperature profile of the RoBo inner surface, measured with IR cameras for a non-isothermal wall boundary. Different colours correspond to each separate camera.

axial distance of 20 pixels ($\approx$ 15 mm), centred at the mid-axial location of the inner cylinder. Temperature is non-dimensionalised as:

$$T^* = \frac{T - T_\infty}{T_i - T_\infty} \tag{5.2}$$

where T_i is the inner cylinder temperature. The control points for the solid lines in this figure were located at 0°, 72° and 144°; whereas they are at 36°, 108° and 180° for the dashed line curves. The measured values are lower than the set profile because of the heat conduction across the layer of Rohacell. The close agreement between these two cases indicates that the three control points are sufficient in defining the desired non-isothermal wall temperature profile.

5.1.2 ExCITE Facility

The thermal control system was also successfully able to maintain the inner cylinder metal temperature to ±0.1°C on the ExCITE facility. Figure 5.3a shows the steady-state outer cylinder temperature measurements, for a case where the inner cylinder

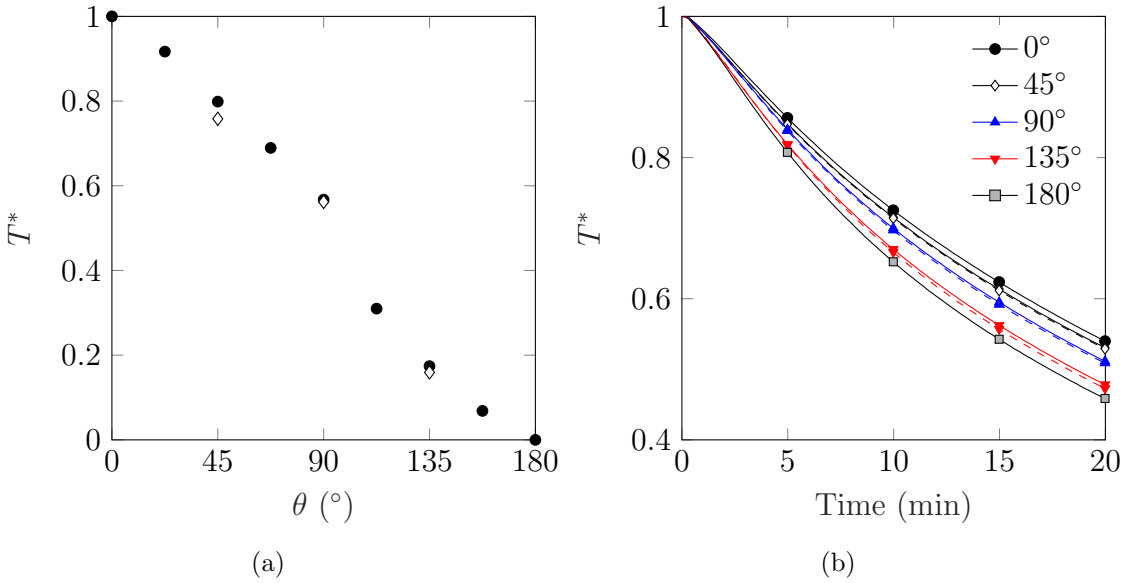

FIGURE 5.3: **a:** Outer cylinder temperature measurements from the ExCITE facility. **b:** Inner cylinder transient cooling temperatures from the initial testing of the ExCITE facility.

temperature was set to 90°C uniform. Black markers are located on the IR camera side of the rig, whereas white markers are on the opposite side (see figure 3.9). The results show good symmetry. The overall trend in temperature is as expected.

The symmetry of the inner cylinder can be examined by looking at the temperature curves in figure 5.3b. These are the central mat metal thermocouples as the rig is cooling following a steady-state test at $Ra_{D_i} = 2.1 \times 10^9$. Solid lines are on the IR camera instrumented side; dashed lines are from the other side. The close match between the corresponding solid and dashed lines indicates a symmetrical thermal field. It is also interesting to see a faster cooling rate as θ increases, which is the expected trend in heat transfer coefficient magnitude.

5.2 Heat Flux Measurements

5.2.1 Temperature Traverses

Before undertaking a detailed experimental campaign, the appropriate amount of time needed at a traverse point, in order to obtain an average temperature, must be

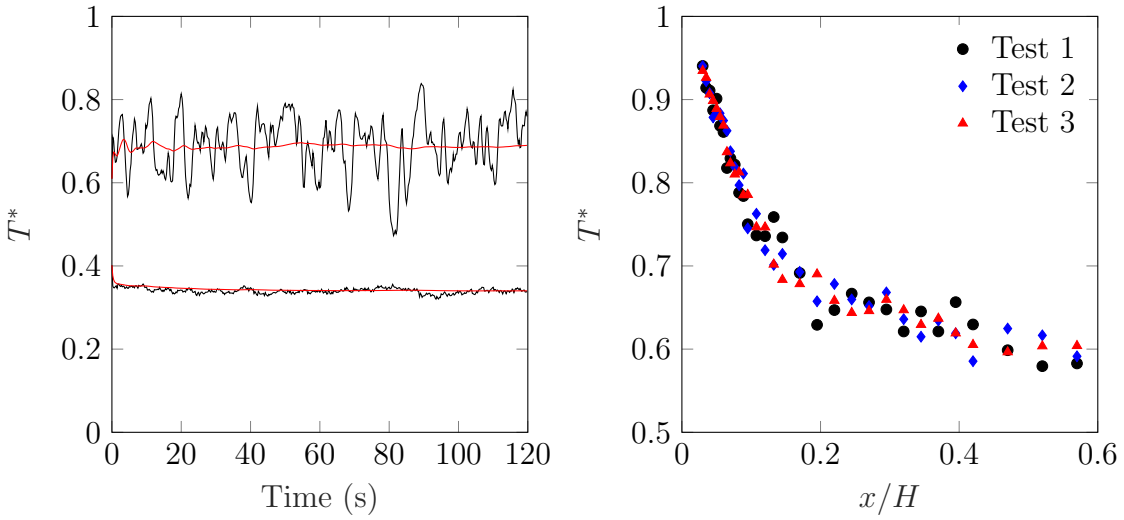

FIGURE 5.4: **a:** Temperature signals at 45° (upper line) and 135° (lower line) at a traverse point in the RoBo rig, $Ra_{D_i} = 6.3 \times 10^7$ and $Dr = 1.25$. Red lines represent the cumulative average. **b:** Three repeats of inner wall temperature traverses at 45° for these test conditions.

determined. The black lines in figure 5.4a are temperature signals, recorded at 4 Hz, on the RoBo facility. The test conditions were: $Ra_{D_i} = 6.3 \times 10^7$ and $Dr = 1.25$. The upper line is at $\theta = 45°$ and the lower black line is at 135°. It is evident that the flow field is unsteady in the upper section of the annulus. Red lines represent the cumulative average at each measurement point. From these results it was decided that 60 seconds was adequate to obtain an accurate steady-state temperature reading – the standard deviation of the measurement converged by this point and the average temperature value changed by < 0.3 K beyond this point.

Figure 5.4b shows three repeats of a temperature probe traverse at $\theta = 45°$ (largest unsteadiness) with the aforementioned test conditions. Each run was conducted on a different day. x is the radial distance from the inner cylinder. T^* is not equal to 1 at the wall due to the layer of Rohacell. The repeatability of the measurements is very good, especially in the conductive sub-layer. All five traverse probes were completed simultaneously in tests 1 & 2; only the 45° probe was traversed in test 3. The data does appear somewhat smoother in test 3 but as the conductive

sub-layer measurements were not affected, it was decided to complete all traverses simultaneously. This allows for a much larger test matrix to be considered than if separate traverses were required. This finding was applied to all RoBo facility tests. Subsequent traverse points were more concentrated in the conductive sub-layer, with a measurement every 0.2 mm. Some influence of the wake from the 90° probe on the 45° probe was observed in the ExCITE facility, potentially due to the higher Rayleigh number, so these traverses were conducted individually.

As mentioned in Chapter 4, the local heat flux is determined from the slope of a line fitted to the conductive sub-layer of the thermal boundary layer. In order to do this, the start and end traverse points must be decided. The first point is 0.4 mm from the surface. A least-squares line fitting method is then applied for an increasing number of radial traverse points. Upon examining the R^2 value, it becomes clear where the linear fitting should end. Figure 5.5a shows an example of this for a 45° and 90° traverse on the RoBo facility. The higher unsteadiness at 45° manifests itself as a lower R^2 value – this is accounted for in the uncertainty analysis presented in Appendix B. On average, 10-12 points are used in the fitting procedure. Figure 5.5b shows the fitted lines along with the temperature measurements. Ebadi *et al.* [26] presented an exact integral method that evaluates the heat flux from a turbulent boundary layer; however, Pilkington [85] showed that the linear best fit procedure gives very similar results.

The calculated convective heat flux values for the three tests previously shown in figure 5.4b are given in figure 5.6, along with the uncertainty bands (see appendix B). Good agreement between the tests is observed. This, coupled with the adequate levels of uncertainty, gives confidence in the experimental traverse method and probe design.

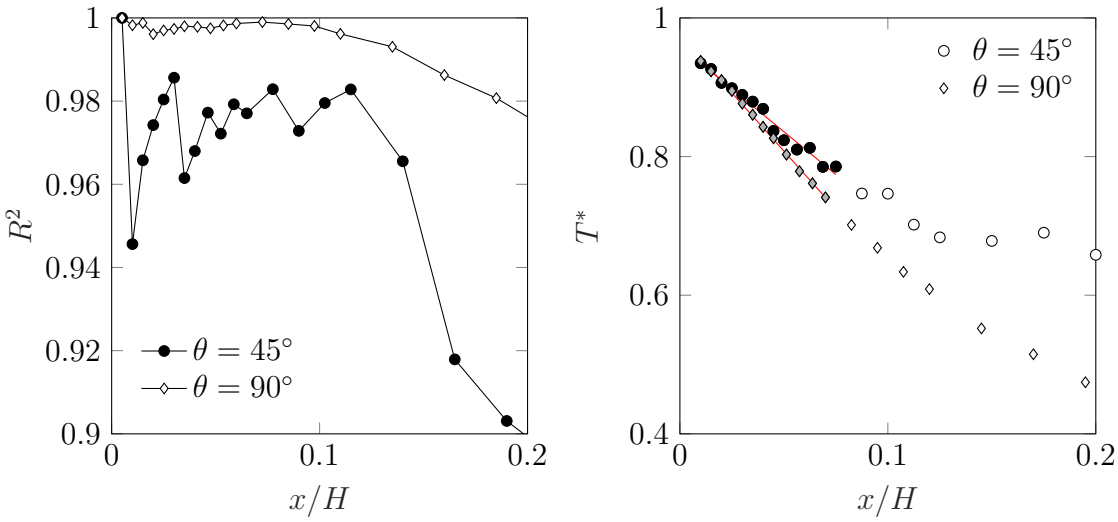

FIGURE 5.5: **a:** R^2 values of a linear fitted to the conductive sub-layer for increasing numbers of traverse points **b:** Radial temperature profiles with a line fitted to the conductive sub-layer. Filled markers represent the points used in the fitting.

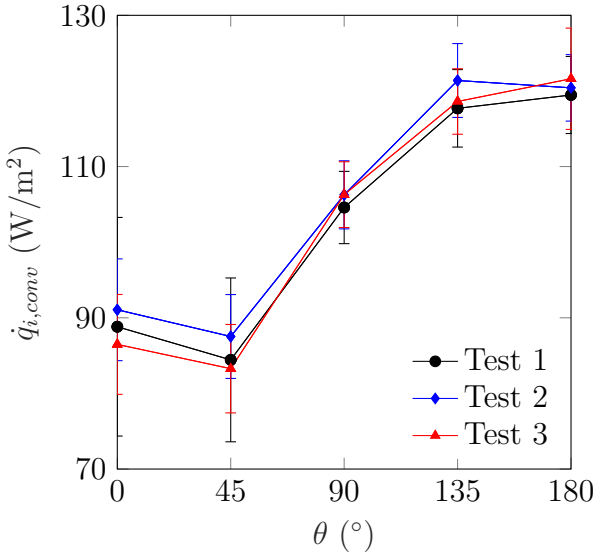

FIGURE 5.6: Inner wall circumferential heat flux for three repeats of a test on the RoBo facility, with $Ra_{D_i} = 6.3 \times 10^7$ and $Dr = 1.25$. Uncertainty is calculated using the method given in appendix B.

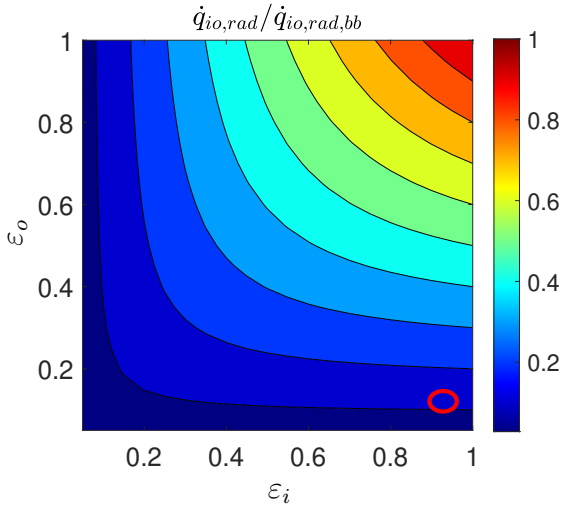

FIGURE 5.7: Effect of inner and outer surface emissivity on the radiative heat transfer between infinite concentric cylinders at $Dr = 1.25$. The red marker indicates the approximate values of the RoBo experimental rig.

5.2.2 Radiation

It is worth comparing the magnitude of radiation heat transfer to the convective heat fluxes from figure 5.6 ($Ra_{D_i} = 6.3 \times 10^7$ and $Dr = 1.25$). The mean value of $\dot{q}_{i,conv} = 100.6$ W/m^2, whereas the radiation heat transfer (calculated using the method outlined in section 3.5) is $\dot{q}_{i,rad} = 48.5$ (W/m^2) – nearly 50% of the convective value. Radiation has been deliberately suppressed in these experiments to reduce uncertainty in the infrared measurements, by tuning the values of emissivity. The temperatures of the inner and outer surface for this test case are 100°C and 60°C respectively. Using these temperatures, figure 5.7 shows the magnitude of $\dot{q}_{io,rad}$ for all possible combinations of ε_i and ε_o, calculated using equation 3.12 (analytical solution for net radiation between infinite isothermal cylinders). The values are normalised by the black-body condition (maximum possible value of radiative heat transfer): $\varepsilon_i = \varepsilon_o = 1$. The red circle indicates the experimental condition.

It is evident that the radiative heat flux in this experiment ($\approx$ 33% of total) is towards the lower end of what is possible. Since radiation scales with the fourth power of temperature, accounting for radiative heat transfer in predicting shutdown

cooling of a large gas turbine will be very important.

5.2.3 IR Camera Measurements

The measured heat flux from the IR camera method (described in section 3.4) was also investigated during the commissioning period. Despite an extensive and careful calibration procedure and optimised inner and outer surface emissivities, the alignment of the measured surface temperature between separate cameras away from their respective centres was not at an acceptable level. Away from the camera centre, the surrounding reflections have a larger influence on the measurement but the main reason for this was that the overall top-to-bottom difference in surface temperature was approximately 3°C. The heat flux calculation close to the camera centre did give an accurate result, but an uncertainty analysis of this measurement gave a value much higher than the temperature traverse equivalent. Therefore, traverses are used to measure steady-state heat fluxes for the remainder of the work presented, as more information is obtained on account of the higher accuracy.

The steady-state IR camera and Rohacell technique would be more appropriate in cases where larger thermal gradients are present, such as the data shown in figure 5.2 or if a constant heat flux boundary condition was applied. The data in figure 5.2 also has a lower uncertainty than measurements on the ExCITE facility as IR windows were not required. Valuable insights into the enclosed flow field can still be gained from analysing the transient IR temperature measurements. The technique is explained in detail in Chapter 7.

The calibration map is required for these unsteady measurements. The values of $\tau\varepsilon(\varphi_c)$ calculated from equation 3.3 are shown in figure 5.8 for the five separate cameras, at the axial centreline of the image. This in-situ calibration accounts for both reflections and the angular dependence of emissivity. A curve in the form of equation 5.3 is fitted to the data with $C_0 = 0.676$ and $C_1 = 0.323$.

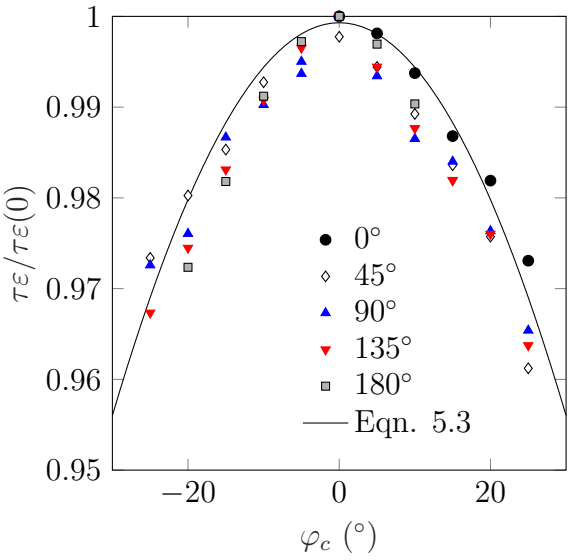

FIGURE 5.8: Centreline calibration map of $\tau\varepsilon$ for the five IR cameras (denoted by the markers), for the ExCITE facility.

$$\frac{\tau\varepsilon}{\tau\varepsilon(0)} = C_0 + C_1 \cos(\varphi) \tag{5.3}$$

5.3 Conclusions

Both the RoBo and ExCITE facilities were commissioned following the procedures described in this chapter. The results presented here indicate that any findings are independent of the rig rotation or construction. Temperature probe traverses have been shown to be very repeatable and are within an acceptable uncertainty level. The importance of accounting for radiation heat transfer when investigating shutdown cooling of a gas turbine has also been justified.

Chapter 6

Thermal Boundary Condition Study

6.1 Introduction

During the shutdown cooling period of a gas turbine, a circumferential temperature gradient will develop on both the inner and outer annulus walls. The construction of the RoBo facility presents the opportunity to investigate the ramifications of non-isothermal boundary conditions on the natural convective flow field in a concentric annulus. Furthermore, the influence of the diameter ratio and inner cylinder cone angle can also be explored.

An extensive experimental campaign of temperature traverses has been conducted that includes six separate geometric conditions. The properties of each condition that have been analysed is given in table 6.1, where 'Shape' indicates the inner assembly profile. All numbers are in millimetres, apart from the diameter ratio (Dr) and the configuration factor (F_c). The gap width is denoted by H. It has been previously mentioned that the inner cylinder diameter is the appropriate scaling variable for natural convection in a concentric annulus [8]. However, to compare annuli at

TABLE 6.1: Geometric conditions for the six different test configurations studied.

Shape	D_i	D_o	Dr	H	F_c ($\times 10^{-4}$)
Cylinder	326	446	1.37	60	4.72
Cylinder	326	406	1.25	40	0.996
Cylinder	326	366	1.12	20	0.066
Cone	298	446	1.50	74	15.0
Cone	298	406	1.36	54	4.45
Cone	312	406	1.30	47	2.20

different diameter ratios, a further geometric factor is required. The configuration factor of Raithby & Hollands [88] is again defined in equation 6.1.

$$Ra^* = F_c Ra_{D_i} = \frac{\ln(D_o/D_i)^4}{D_i^3 \left(D_i^{-3/5} + D_o^{-3/5} \right)^5} Ra_{D_i} \tag{6.1}$$

This definition has been successfully used in previous studies to correlate differing diameter ratio concentric cylindrical annuli [70]. The value for each experimental geometric configuration is included in table 6.1. Itoh *et al.* [45] correlate different diameter ratio results using: $\sqrt{r_i r_o}/\ln(r_o/r_i)$ as the characteristic length. While this does give similar results, the Raithby and Hollands factor is preferred due to its stronger theoretical foundation.

Figures 6.1 and 6.2 show schematics of the experimental facility that highlight the positions of the control point thermocouples and traverse plane locations. Three separate outer cylinders of identical construction can be installed in order to produce the desired diameter ratios. The cylindrical traverse plane is 240 mm away from the left-hand side end plate; thus is should not be experience any end wall effects.

The top-to-bottom circumferential temperature distribution is modelled as a cosine profile by specifying values at each of the thermocouple locations seen in the previous figures. The inner assembly has a control point at 0°, 72° and 144°; whereas the outer cylinder has points at 0°, 60°, 120° and 180°. Using ΔT_c to denote the magnitude of

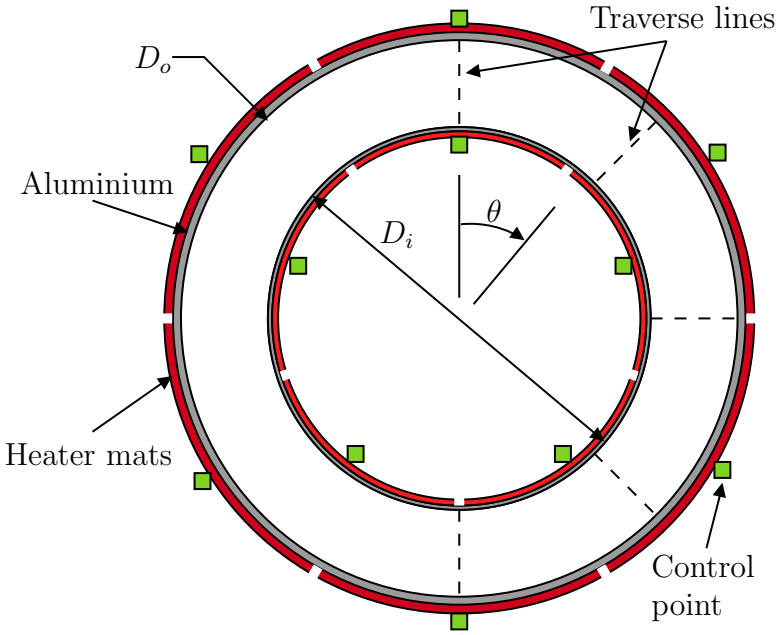

FIGURE 6.1: Cross-sectional schematic of the RoBo experimental facility. Green squares are embedded thermocouple.

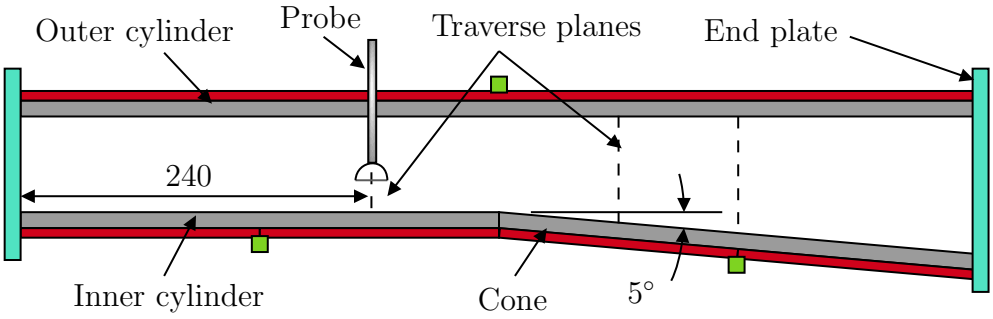

FIGURE 6.2: Annular cross-section of the upper area of the RoBo experimental rig. The dashed lines represent the traverse planes.

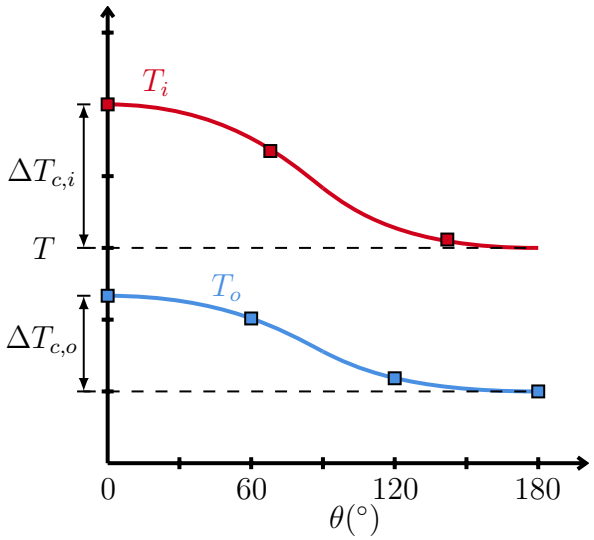

FIGURE 6.3: Definition of the imposed temperature boundary conditions for a given ΔT_c. The square markers represent locations of the control set-points.

the overall top-to-bottom temperature difference, the value at each control point is given by equation 6.2. The temperature always decreased with θ (negative gradient) since this is representative of a shutdown cooling cycle. A pictorial representation of this is shown in figure 6.3. The facility is capable of maintaining a ΔT_c of up to 20°C on both the inner and outer assemblies.

$$T_{sp} = \left(T_{\theta=0} - \frac{\Delta T_c}{2}\right) + \frac{\Delta T_c}{2}(\cos\theta) \tag{6.2}$$

6.2 Concentric Cylinder Study

6.2.1 Non-Isothermal Boundary Conditions

The initial series of experiments completed (which will be referred to collectively as *Tc* – top constant) was a full factorial test matrix for $\Delta T_{c,i}$ and $\Delta T_{c,o} = 0$, 10 and 20°C respectively. This gives a total of nine different thermal boundary condition combinations. The details of each test are shown in table 6.2, where all temperatures are in Celsius. ΔT_r denotes the radial difference in wall temperature

TABLE 6.2: Thermal boundary conditions for the nine Tc test cases. All temperatures are in Celsius. Ra_{D_i} at $\theta = 0°$ is held constant at 6.3×10^7 in all cases.

	Key	$\Delta T_{c,i}$	$\Delta T_{c,o}$	$T_{i,t}$	$T_{o,t}$	$T_{i,b}$	$T_{o,b}$	$\Delta T_{r,t}$	$\Delta T_{r,b}$	ΔRa_{D_i}
A	–●–	0	0	100	60	100	60	40	40	0
B	–■–	10	0	100	60	90	60	40	30	1.3×10^7
C	–▼–	20	0	100	60	80	60	40	20	2.7×10^7
D	-○-	0	10	100	60	100	50	40	50	-2.1×10^7
E	-□-	10	10	100	60	90	50	40	40	-8.7×10^6
F	-▽-	20	10	100	60	80	50	40	30	5.5×10^6
G	···●···	0	20	100	60	100	40	40	60	-4.5×10^7
H	···■···	10	20	100	60	90	40	40	50	-3.3×10^7
I	···▽···	20	20	100	60	80	40	40	40	-1.9×10^7

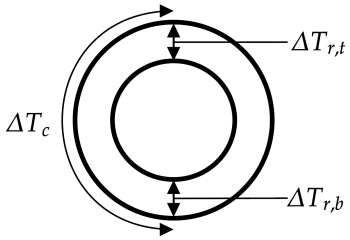

at a given angular location. The Rayleigh number (Ra_{D_i}) at the top of the annulus remained constant for all nine test cases: 6.3×10^7. The local radial temperature difference ($T_i - T_o$) is used in the Rayleigh number definition. Fluid properties are evaluated using Bishop's [10] weighted average formula (equation 3.1) with these two temperatures. The last column of table 6.2 gives the difference in Rayleigh number between TDC and BDC ($\Delta Ra = Ra_{\theta=0} - Ra_{\theta=180}$) for a given test. The nine tests cover the following range: $-4.5 \times 10^7 < \Delta Ra < 2.7 \times 10^7$ – approximately 70% above and 40% below the constant value at TDC. Traverses were completed using both the inner and outer probe arrangements, at the inner cylinder traverse plane where $Dr = 1.25$.

The convective heat flux has been calculated from the slope of the linear temperature profile found in the conductive sub-layer, as was described in section 5.2.1. Figure 6.4a shows the measured values of inner wall heat flux for all nine cases; the corresponding outer wall fluxes are shown in figure 6.4b. The most striking finding from this

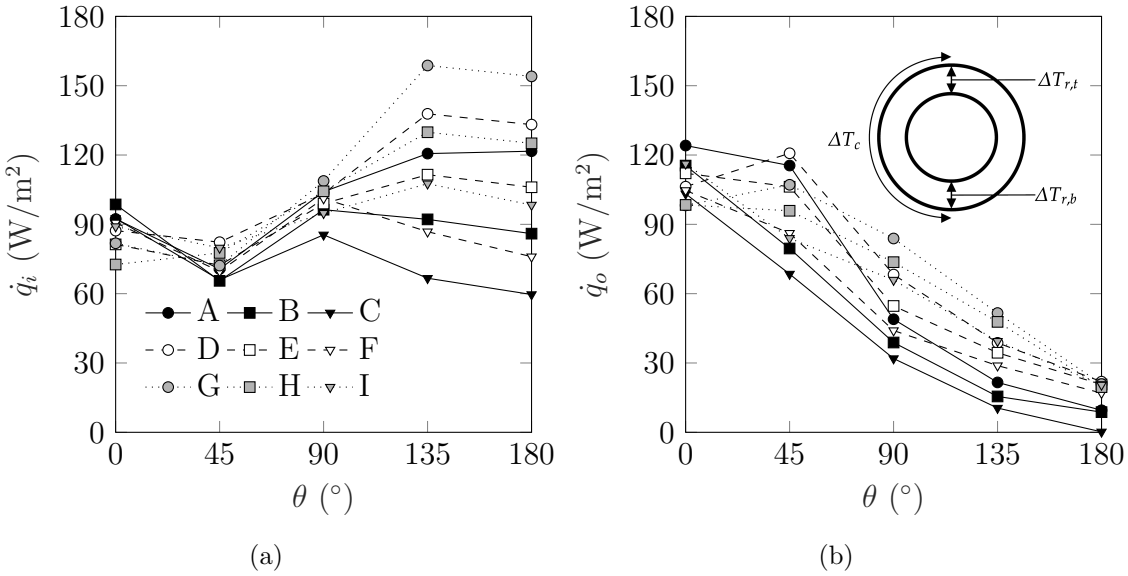

FIGURE 6.4: **a:** Measured inner wall convective heat flux for the Tc test cases. Ra_{D_i} at $\theta = 0°$ is held constant at 6.3×10^7 in all nine cases. $Dr = 1.25$. See table 6.2 for the legend key. **b:** Corresponding outer wall convective heat flux for these nine cases.

campaign is that $\dot{q}_i$ at TDC, where Ra_{D_i} is constant, remained relatively unchanged for all nine cases – even though the inner wall heat flux in the lower section of the annulus varied significantly. The standard deviation of $\dot{q}_{\theta=0}$ was < 8 W/m^2. In case G, the heat flux at 180° was 85% higher than the value at 0°; in contrast, $\dot{q}$ at 180° was 35% lower than TDC in case C. It appears that the heat flux at 0° is somewhat independent of the thermal history of the inner boundary layer as it develops from BDC up to this point, for the ranges of $\Delta T_{c,i}$ and $\Delta T_{c,o}$ that were tested.

The inner surface heat flux at 45° was also close and shows similar values to those at TDC, in some cases it is even lower. This may be linked to separation effects of the flow from the inner cylinder as thermal instabilities cause plumes and recirculating cells to form. This will be examined in more detail later. The low deviation in heat flux at 45° across the nine cases is not replicated in the outer cylinder heat flux measurements. However, the general trend in the local heat flux profile is as expected. The buoyant plume from the inner cylinder impinging on the outer cylinder at TDC leads to high heat transfer at this point, which then reduces gradually as θ increases.

The radial temperature profiles for three cases are shown in figure 6.5. These are: the isothermal case (A), the case that has the lowest magnitude of Ra_{D_i} at BDC (C) and the case that has the highest magnitude of Ra_{D_i} at BDC (G). The mid-annulus temperatures at 45° are extremely close to the values at TDC, in fact it is slightly higher for the isothermal wall case. This helps explain the lower value of inner surface heat flux seen here. The typical description of a crescent-shaped recirculating cell, which is often used for natural convection in a cylindrical annulus, would give an increasing bulk temperature profile towards TDC. The near-constant bulk temperature from 0° to 45° indicates that the flow field may have become multicellular in this upper region. The reference chart of Powe *et al.* [86] indicates that the current Dr is very close to the boundary of multicellular flow inception.

Outside of the inner cylinder boundary layer at BDC, there is little difference between the air and outer surface temperature. This leads to very low heat transfer into the outer casing at this region, for all test cases. When this effect is coupled with the large impingement heat transfer at TDC on the casing, a substantial circumferential difference in heat flux is observed.

Analysis of the temperature fluctuations ($T^{'}$) will be used in order to provide a qualitative description of the flow field. This assumes that the thermal fluctuations are analogous to the velocity fluctuations; an assumption that has been previously used by McLeod and Bishop [70], and the results of Fukuda *et al.* [33] show a strong coupling of these two parameters. While the acquisition rate used in these experiments is too low to obtain useable power spectral density information, the root-mean-square of the temperature signal gives a strong indication of the unsteadiness. Figure 6.5d shows this parameter for the isothermal test case (A).

A stagnant region in the lower section of the annulus is evident by the very low values of $T^{*'}$ at 135° and 180°. The 90° line shows a peak near each wall, the locations correspond to where the largest magnitudes of velocity are expected. Therefore, this

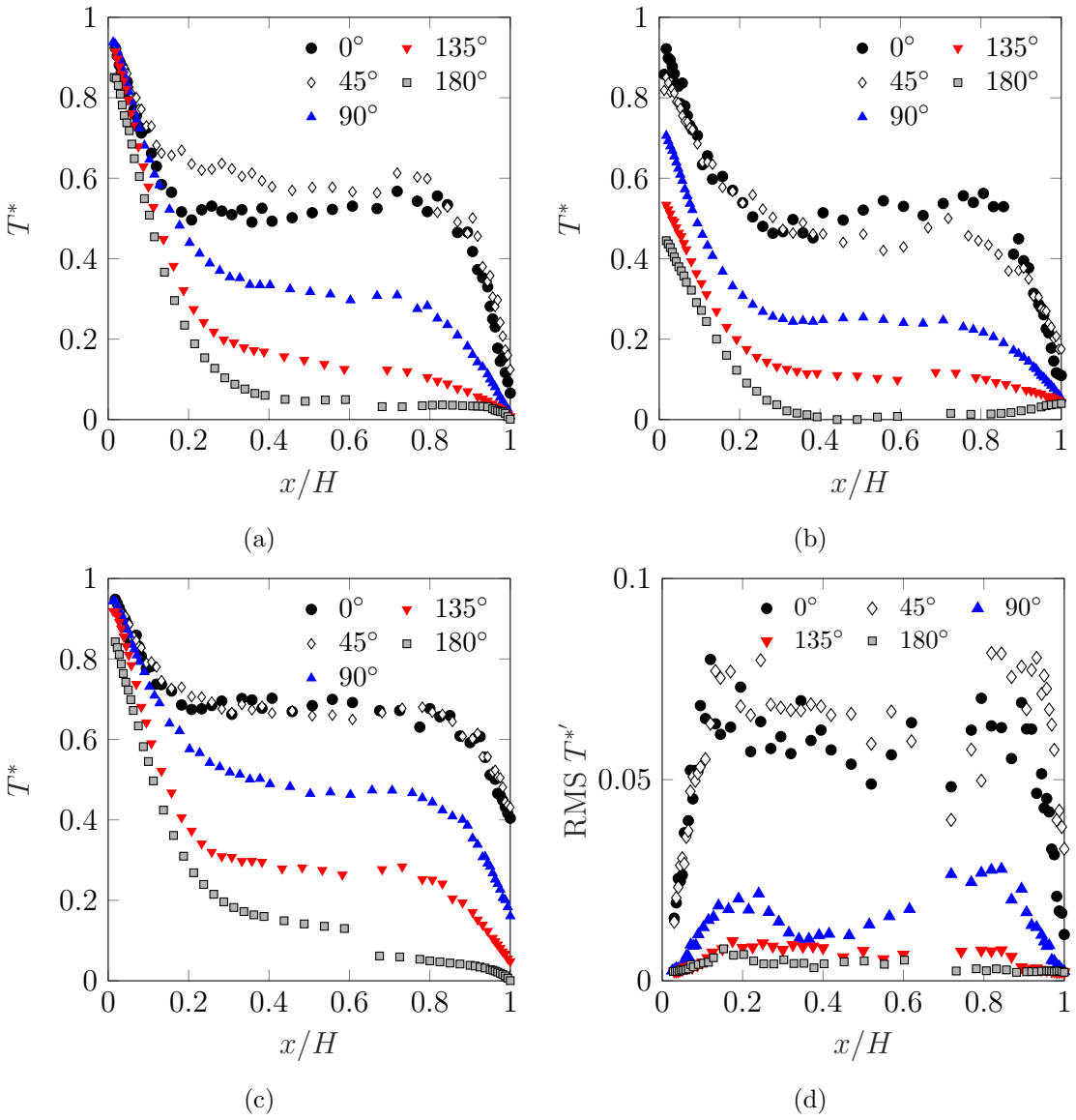

FIGURE 6.5: **a:** Radial temperature profiles for case A. $\Delta Ra_{D_i} = 0$. **b:** Radial temperature profiles for case C. $\Delta Ra_{D_i} = 2.7 \times 10^7$. **c:** Radial temperature profiles for case G. $\Delta Ra_{D_i} = -4.5 \times 10^7$. **d:** RMS of the temperature fluctuations for case A. $\Delta Ra_{D_i} = 0$.

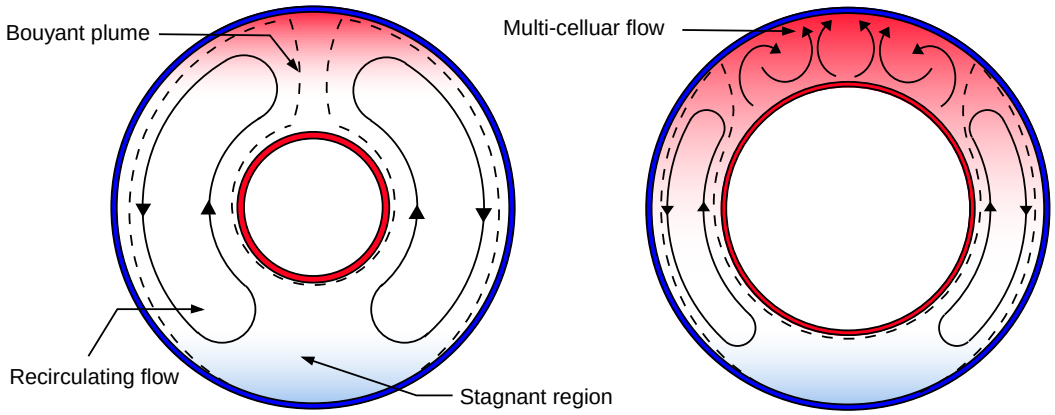

FIGURE 6.6: Schematic of the typical natural convective flow features present in a concentric annulus with a hotter inner surface. Reproduced from [3, 8, 16, 86, 87]. *Left:* Moderate diameter ratio. *Right:* Narrow diameter ratio (RoBo Rig).

radial distribution indicates a recirculating cell with a stationary central core – a structure synonymous with natural convection in a concentric annulus. In contrast to this, the upper section shows large fluctuations throughout the whole radial gap, apart from the conductive sub-layer next to the walls. This explains why the bulk fluid temperature is near isothermal from 0° to 45°, as highlighted in figure 6.5a. This furthermore crystallises the finding that the flow is multicellular in the upper region. Powe *et al.* [87] proposed that this type of flow structure in a narrow annulus does not vary the overall heat flux for a given Ra, but it does redistribute the local variations. Figure 6.6 shows the schematic of natural convective flow features in a moderate diameter ratio cylinder [3, 8, 16], which was discussed previously in section 2.2. This figure also shows the assumed multi-cellular flow structure present in the RoBo experiments that was orignally described by Powe [86, 87].

Similar results for cases C and G are given in figure 6.7. Both cases again show a stagnant region at BDC. The inner surface fluctuations for case C are lower than the other two cases; this surface does have a lower average Ra. However, $T^{*'}$ does remain high as the radial distance increases in the upper sections. Evidence of a larger recirculating cell structure below the multicellular region are also present in

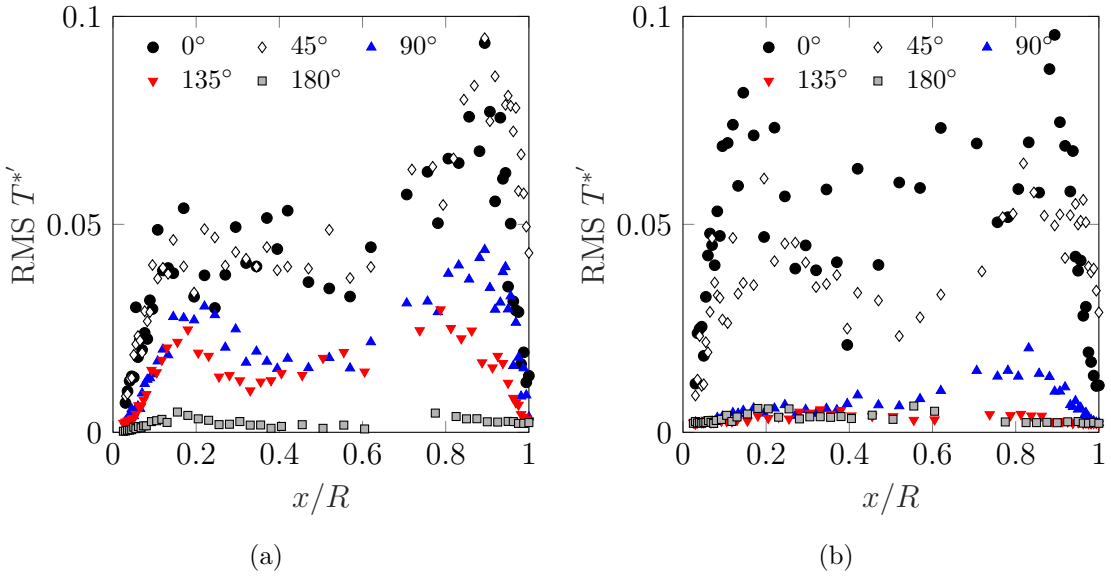

FIGURE 6.7: **a:** RMS of the temperature fluctuations for case C. $\Delta Ra_{D_i} = 2.7 \times 10^7$. **b:** RMS of the temperature fluctuations for case G. $\Delta Ra_{D_i} = -4.5 \times 10^7$.

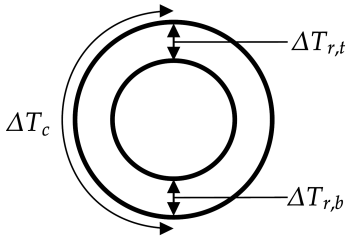

these non-isothermal cases.

The main conclusion of the preceding analysis was that the inner wall heat transfer at TDC was strongly dependent on the local Rayleigh number and thus weakly coupled to the circumferential thermal history. A further test campaign (referred to as *Bc* – bottom constant) has been completed but now Ra_{D_i} at 180° is held constant. Again, this consisted of a full factorial test matrix for $\Delta T_{c,i}$ and $\Delta T_{c,o} = 0$, 10 and 20°C respectively. The geometric conditions of the facility were identical to the *Tc* campaign. Table 6.3 contains all of the relevant information for each of these nine cases. Limitations of the facility mean that inner and outer wall temperatures are 80°C and 40°C at $\theta = 180°$, so that circumferential differences of up to 20°C can be imposed and ΔT_r is matched to the *Tc* campaign at $\theta = 0°$. Ra_{D_i} at BDC for the *Bc* campaign is therefore 8.2×10^7. Test I is common to both series.

TABLE 6.3: Thermal boundary conditions for the nine *Bc* test cases. All temperatures are in Celsius. Ra_{D_i} at $\theta = 180°$ is held constant at 8.2×10^7 in all cases.

	Key	$\Delta T_{c,i}$	$\Delta T_{c,o}$	$T_{i,t}$	$T_{o,t}$	$T_{i,b}$	$T_{o,b}$	$\Delta T_{r,t}$	$\Delta T_{r,b}$	ΔRa
A		0	0	80	40	80	40	40	40	0
B		10	0	90	40	80	40	50	40	1.4×10^7
C		20	0	100	40	80	40	60	40	2.6×10^7
D		0	10	80	50	80	40	30	40	-2.4×10^7
E		10	10	90	50	80	40	40	40	-1×10^7
F		20	10	100	50	80	40	50	40	2.1×10^6
G		0	20	80	60	80	40	20	40	-4.6×10^7
H		10	20	90	60	80	40	30	40	-3.2×10^7
I		20	20	100	60	80	40	40	40	-1.9×10^7

The inner and outer surface heat fluxes for these cases are shown in figure 6.8. Conversely to figure 6.4a, the heat flux at BDC is now relatively unchanged – the standard deviation of $\dot{q}$ was again < 8 W/m^2. These results corroborate the previous campaign findings that the local radial temperature difference dominates the inner wall heat transfer. This conclusion has now been confirmed for the inner cylinder at both TDC and BDC. The outer casing heat flux at $\theta = 180°$ is also consistent for all nine *Bc* cases.

All seventeen cases are now non-dimensionalised to give the local equivalent conductivity, using equation 6.3. The local radial temperature difference is used for each point. dT/dr is the slope of the radial temperature profile that is directly measured by thermocouple probe. r is the wall radius on whichever surface is being evaluated.

$$k_{eq,\theta} = \frac{\dot{q}_{conv}}{\dot{q}_{cond}} = \frac{r(dT/dr)\ln(r_o/r_i)}{T_{i,\theta} - T_{o,\theta}} \tag{6.3}$$

Figure 6.9 shows the local k_{eq} on both surfaces. Encouragingly, all of the various thermal profile cases collapse down to a single trend. It was for this reason that the previous results were shown as $\dot{q}$, as from k_{eq} alone it is not immediately obvious that the heat flux at TDC may be higher than BDC (see case C in figure 6.4a). All

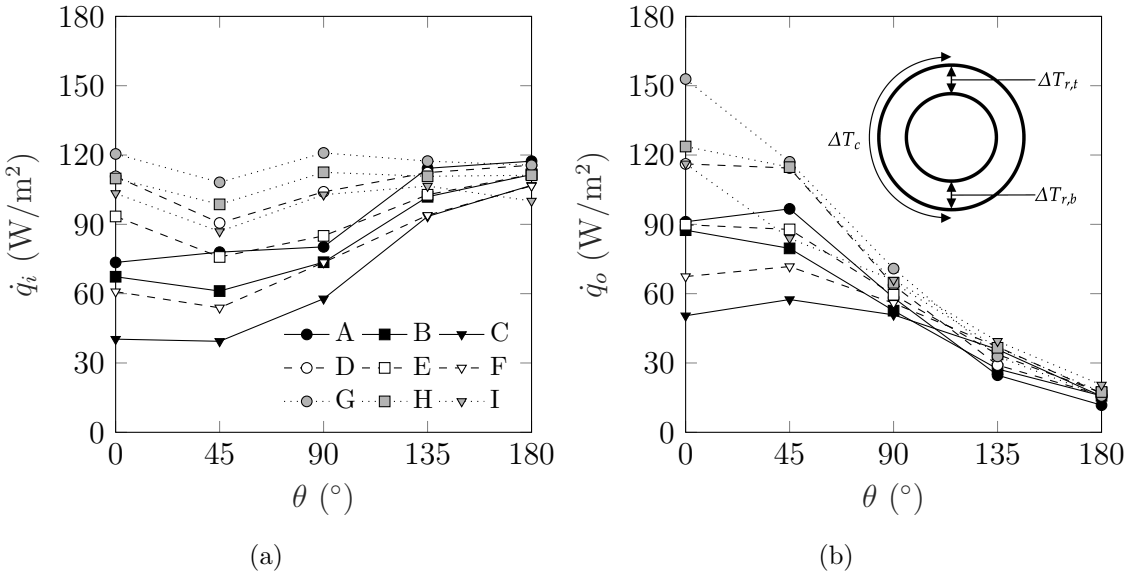

(a) (b)

FIGURE 6.8: **a:** Measured inner wall convective heat flux for the *Bc* test cases. Ra_{D_i} at $\theta = 180°$ is held constant at 8.2×10^7 in all nine cases. $Dr = 1.25$. See table 6.3 for the legend key. **b:** Corresponding outer wall convective heat flux for these cases.

cases show a near constant value from 0° to 45°, owing to the assumed multicellular flow structure that was highlighted previously. $k_{eq,i}$ is also approximately constant between 135° and 180°. The average ratio across all tests between the two constant levels is 1.41:1, in favour of the lower section – this highlights one of the root causes of thermal bow. Overall, these results indicate that calculating the local heat flux on either surface using the local radial temperature gradient is sufficiently accurate, even when large circumferential variations in either wall temperature distribution are present.

6.2.2 Diameter Ratio Effects

Two further diameter ratios have been tested on the concentric cylindrical section: 1.12 and 1.37. Recall that all previous cases had $Dr = 1.25$. The inner cylinder diameter remained constant for all configurations. Further details can be found in table 6.1. A subset of isothermal and non-isothermal tests from the *Tc* and *Bc* campaigns were completed at these alternative diameter ratios, measuring the inner wall heat flux only. The equivalent conductivity for these cases are shown in figure

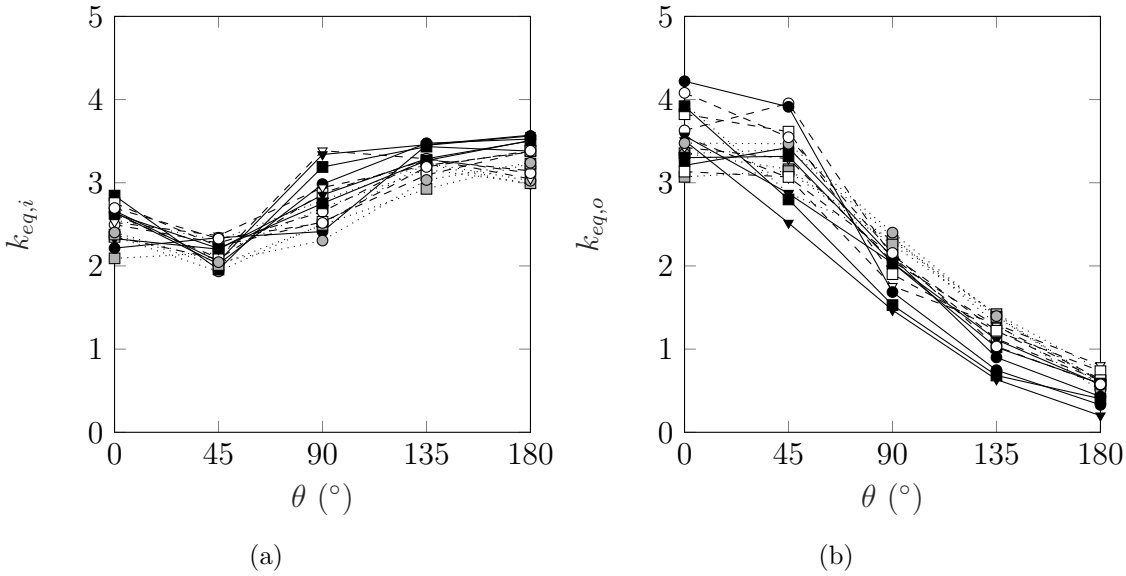

FIGURE 6.9: **a:** Inner wall equivalent conductivity both the *Tc* and *Bc* test campaigns. $Dr = 1.25$. **b:** Corresponding outer wall equivalent conductivity for these test cases.

6.10. The red curves correspond to $Dr = 1.37$, the blue to $Dr = 1.12$, while the black lines are from the previous section.

The heat flux curves again collapse down to a singular trend for a given diameter ratio. The overall heat flux increases with diameter ratio. This behaviour is expected as the inner wall to mid-radius air temperature difference increases. The $Dr = 1.12$ case is close to the conduction limit ($k_{eq} = 1$); this occurs when the radial gap is narrow enough that the thermal boundary layers on the inner and outer surface merge.

The general shape of the $k_{eq,i}$ curves in figure 6.10 are very similar at all three ratios: a constant section from 0° to 45° and a higher constant section from 135° to 180°. Interestingly, when the values of $k_{eq,i}$ are averaged across all tests, for a given Dr, the ratios between the higher and lower levels are 1.37, 1.41 and 1.39 for $Dr = 1.37$, 1.25 and 1.12 respectively. Thus, the asymmetry in heat flux between the upper and lower sections of the annulus appears to be independent of the diameter ratios tested here. Previously published results at larger Dr's tend to show a sharp decline in the heat flux from 45° to 0°, for both laminar and turbulent cases [23, 55, 58]. Hence,

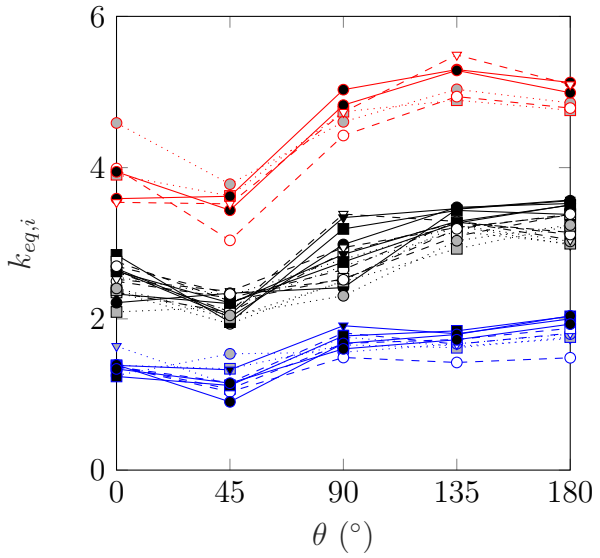

FIGURE 6.10: Inner wall equivalent conductivity for various isothermal and non-isothermal tests. Blue: $Dr = 1.12$; black: $Dr = 1.25$; red: $Dr = 1.37$.

this independence a manifestation of the suspected multicellular flow structure in the upper annulus, and will not hold at higher Dr.

6.3 Conical Geometry

The focus of this study will now shift to the conical section of the RoBo facility. As mentioned in Chapter 2, studies of natural convection from a horizontal conical geometry are scarce. This is the first time that an annulus composed of an inner conic and outer cylinder has been studied experimentally, to the authors knowledge.

As highlighted in the rig schematic in figure 6.2, there are two traverse planes along the 5° cone angle portion, which in conjunction with the various outer cylinder sizes, give the sectional dimensions outlined in table 6.1. One leg of the probe wire holder (see figure 4.16a on page 67) is extended such that the exposed wire is parallel to the cone surface for these tests.

A subset of the *Tc* and *Bc* campaigns were completed at all three diameter ratios. The $Dr = 1.30$ and 1.36 configurations displayed trends very similar to the concentric

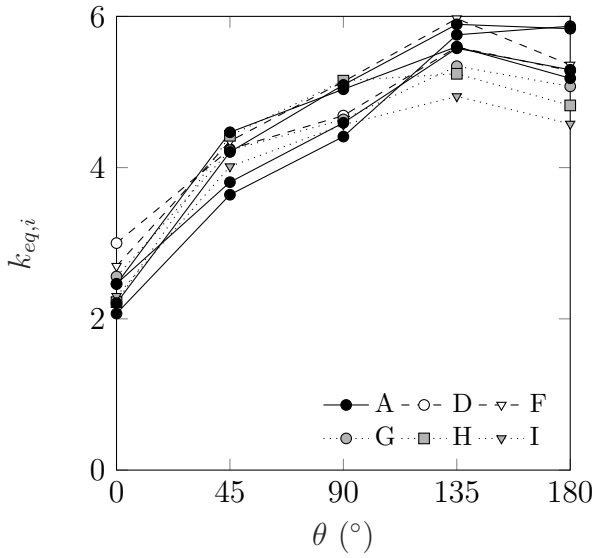

FIGURE 6.11: Inner wall equivalent conductivity for various isothermal and non-isothermal test at the conical section with $Dr = 1.50$. Refer to table 6.3 for values of $\Delta T_{c,i}$ and $\Delta T_{c,o}$ only.

cylinder results; giving an average ratio between the lower and upper constant level of 1.29 and 1.3 respectively. While this is 7% lower than the concentric cylinder cases, the comparable shape of the $k_{eq,i}$ profile indicates that the shallow cone angle has not altered the overall flow dynamics for these configurations.

The inner wall equivalent conductivities for the largest diameter ratio case (1.50) are shown in figure 6.11. The larger gap width has allowed for the upper limit of Ra_{Di} to be extended to 8.1×10^7. The overall trend is inherently different in the upper section of the annulus, as there is now a sharp decline in $k_{eq,i}$ from 45° to 0°. The $Dr = 1.36$ conical tests have the same inner cylinder diameter as the cases in figure 6.11, which indicate that it is indeed the change in Dr that has caused this disparity in the local $k_{eq,i}$ distribution.

Radial temperature profiles for the isothermal wall case where $Ra_{Di} = 6.3 \times 10^7$ and $Dr = 1.50$ are shown in figure 6.12a. The mid-annulus values on the 0° curve are similar to those observed the upper section of the isothermal cylinder $Dr = 1.25$ case from figure 6.5a. However, there is now a drastic fall in temperature by 45°, which explains the heat flux trend in the previous figure.

The temperature fluctuations for this test case are displayed in figure 6.12b in an attempt to elucidate the reason for this alternative heat flux distribution. The lower section of the annulus is again quite steady – indicating a stagnant region. There are two differences between the flow pattern here and those previously presented in section 6.2.1. Firstly, the overall magnitude of the fluctuations in the upper section are lower than the $Dr = 1.36$ case; secondly, while the $T^{*'}$ values at 0° remain relatively constant as x is increased, the 45° profile decays outside of the near wall region. All of this evidence illustrate a transition in the flow region to a singular plume at TDC. Powe *et al.* [86] placed the transition line from multicellular to 3D spiral flow at $Dr = 1.24$. It is worth noting that their classification was based on a range of studies close to the critical Rayleigh number: 1708. In this experimental campaign transition was found at a Dr between 1.37 and 1.50. It is unknown whether the cone angle has influenced the transition location. This transition is important as the difference in $k_{eq,i}$ between TDC and BDC is much greater than the multicellular regime, and it is this difference in heat flux that causes thermal bow. Encouragingly, even though the flow regime has transitioned, it is evident again that the circumferential profiles of heat flux are independent of the wall thermal boundary condition non-uniformities.

6.4 Overall Heat Transfer

As mentioned in section 6.1, the configuration factor, F_c (defined in equation 6.1), can be used to compare the overall heat transfer of differing diameter ratio configurations. Figure 6.13 shows the area-averaged equivalent conductivity for 90 separate experimental cases, consisting of: $1.12 \leq Dr \leq 1.50$, $3.3 \times 10^7 \leq Ra_{D_i} \leq 8.1 \times 10^7$ and $-4.6 \times 10^7 < \Delta Ra < 2.7 \times 10^7$. The black filled markers indicate an inner cylindrical geometry, whereas the white markers indicate an inner conical geometry. $\overline{Ra}_{Di}$ is based on the wall-averaged inner to outer temperature difference.

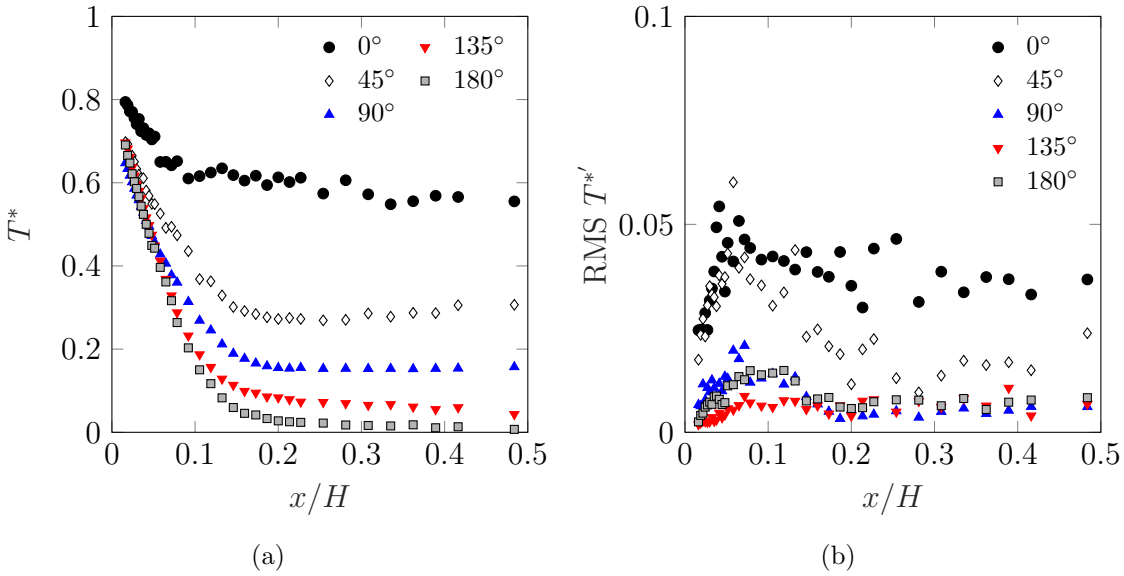

FIGURE 6.12: **a:** Radial temperature profiles for an isothermal test case with $\Delta Ra_{D_i} = 6.3 \times 10^7$ and $Dr = 1.50$, at a conical traverse plane. **b:** Corresponding temperature fluctuations for this case.

The correlation shown by the dot-dashed line in this figure is that of Raithby & Hollands [88]. An implicit assumption in their derivation of Ra^* is that $Nu \propto Ra_D^{1/4}$, which is a characteristic of laminar natural convection. The correlation of Kuehn & Goldstein [57] (stated in Appendix A) accounts for both laminar and turbulent regions in its definition, and uses both Ra_{D_i} and Ra_{D_o}. The values predicted by this correlation are shown as the grey markers (KG) in figure 6.13. The region bounded by dashed lines represents the range of approximately $\pm 10\%$ of the KG values.

Overall, there is excellent agreement between the current experimental results and previously published data. A number of important conclusions can be made based of this figure. Firstly, using F_c has successfully allowed for a comparison of different diameter ratios on a single curve. The heat transfer in a concentric annulus with non-isothermal wall distributions, where the thermal gradient is negative in the θ direction and $T_i > T_o$, can be correlated to the isothermal definitions if the Rayleigh number is based on the wall-averaged temperature difference. Bejan [8] has previously shown that this method of defining Ra works reasonably well when comparing uniform heat flux to isothermal cases in a rectangular enclosure. Therefore, it is encouraging to

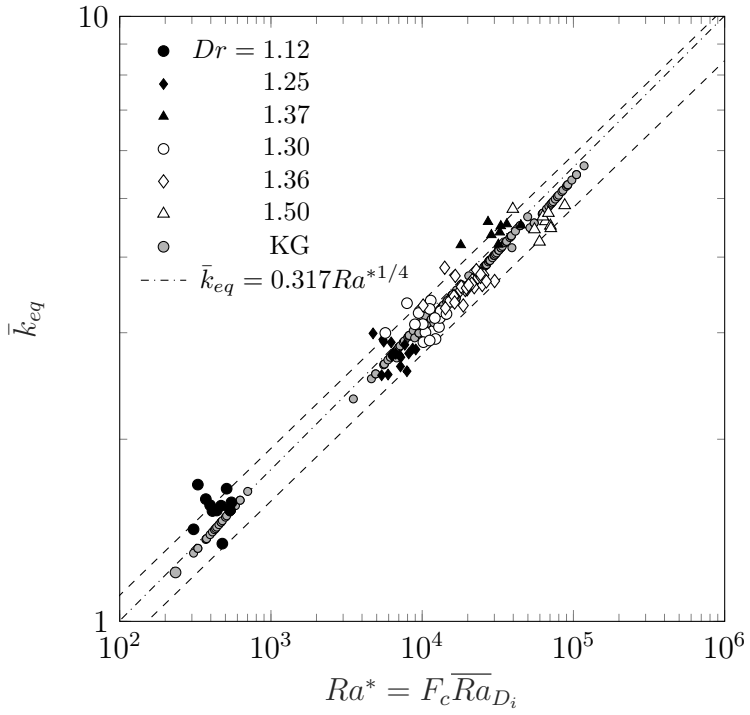

FIGURE 6.13: Mean equivalent conductivity for isothermal and non-isothermal cases at all six geometric conditions.

also observe this trend in a concentric enclosure.

Moreover, the conical inner section, at a 5° hade angle, has not affected the overall heat transfer. Oosthuizen [79] hypothesised that for shallow cone angles (up to 10°), the natural convective heat transfer from an isothermal horizontal cone is isolation, can be derived by integrating the equivalent cylindrical correlation evaluated at each 2D cross-section. This hypothesis has been extended to encompass a cone enclosed by a cylinder, with both isothermal and non-isothermal wall distributions.

Finally, two distinct flow regimes have been observed, which can be categorised neatly when compared to previous works [3, 82, 86]. While the distribution in the local heat flux trends is clearly dissimilar, the good agreement in figure 6.13 indicates that the differing regimes simply redistribute the local values without impacting the overall magnitude – coinciding with the numerical findings of Powe *et al.* [87].

6.5 Conclusions

The results of an extensive experimental campaign looking at the effect of non-isothermal walls on natural convection in a concentric annulus has been presented. The key finding is that the mean surface heat transfer for non-isothermal inner and outer profiles within the range $-0.4 < \Delta Ra/Ra^* < 0.4$, where the thermal gradient is negative in the θ direction, can be predicted using isothermal correlations for $3 \times 10^3 < Ra^* < 1 \times 10^5$ and $Dr < 1.50$.

Chapter 7

Natural Convection in a Large Cylindrical Annulus

7.1 Introduction

An experimental campaign has been conducted on the ExCITE facility, which simulates the flow field in the auxiliary zone of a large gas turbine during shutdown. The experimental procedure is identical to the thermal boundary condition study from the previous chapter. A schematic of the rig is shown in figure 3.3, indicating the positions of the IR cameras and traverse locations. Due to the larger scale of this facility, it was unfeasible to control the outer cylinder temperature, thus the boundary condition was not actively controlled but it was accurately quantified by thermocouples installed every 22.5°.

The ExCITE facility can achieve Rayleigh numbers in the range: $6.4 \times 10^8 < Ra_{D_i} < 2.1 \times 10^9$, inner surface temperatures up to 100°C and $Dr = 2$. The postulated flow structures of McLeod & Bishop [70] indicate that at this condition, the entire plume along with the upper half of the inner cylinder is turbulent. Equation 7.1 gives the inner thermal boundary layer length scale for natural convection from a vertical flat

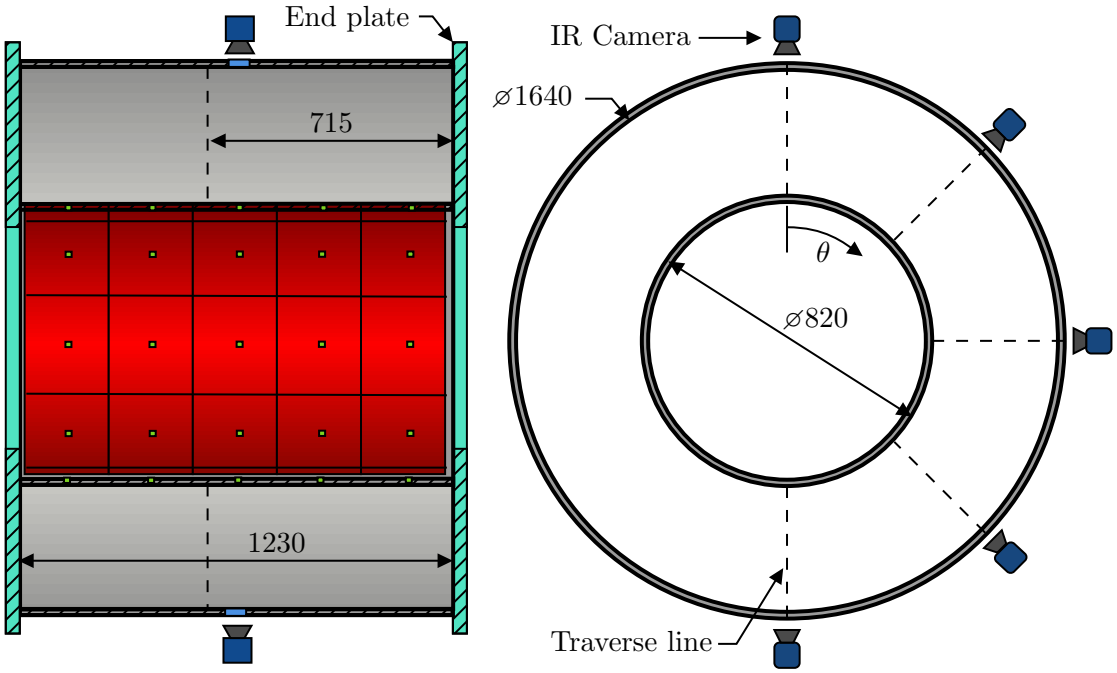

FIGURE 7.1: Schematic of ExCITE shutdown facility.

plate, which was derived by George & Capp [36] and modified by Siebers [94].

$$\eta'_T = \left(\frac{\alpha^2}{g\beta(T_s - T_\infty)}\right)^{1/3} \left(\frac{k_w}{k_\infty}\right) \left(\frac{T_w}{T_\infty}\right)^{0.14} \tag{7.1}$$

7.2 Steady-State Results

7.2.1 Temperature Profiles

Temperature traverses similar to those presented in the previous chapter were conducted, again at 45° intervals. Figure 7.2 shows the inner surface thermal boundary layer, normalised by the length scale given in equation 7.1. $Ra_{D_i} = 2.1 \times 10^9$ and T_∞ is the local radial temperature at $0.25H$ – T_m. The curves are given by equation 7.2 [36].

$$T^* = \begin{cases} 1 - 0.1(x/\eta'_T) & \text{for} \quad 0 \leq x/\eta'_T \leq 1.7 \\ 1.45(x/\eta'_T)^{-1/3} - 0.35 & \text{for} \quad 1.7 < x/\eta'_T \end{cases} \tag{7.2}$$

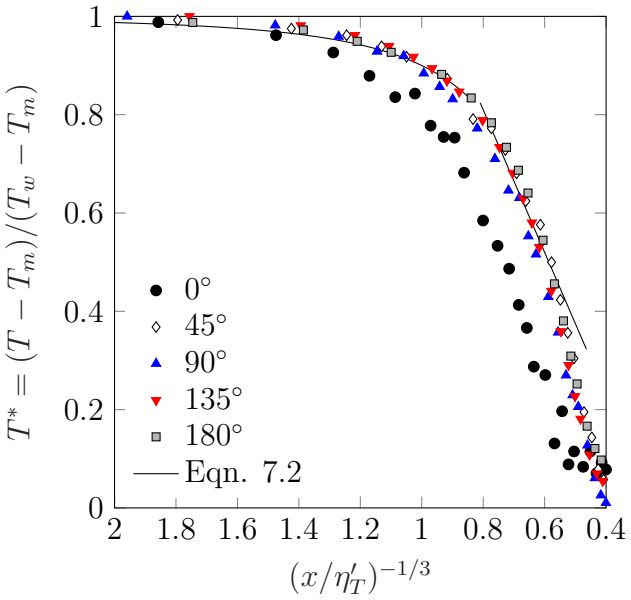

FIGURE 7.2: Inner surface thermal boundary layers for $Ra_{D_i} = 2.1 \times 10^9$ and $Dr = 2$.

There is excellent agreement in the conductive sub-layer, apart from the 0° traverse. The profiles in the buoyant sub-layer are somewhat similar, but the slope of the line from equation 7.2 is slightly flatter than the experimental results. The constants in equation 7.2 were chosen by George & Capp to match data from a vertical flat plate configuration so exact agreement was not expected. However, these results once again add certainty to the experimental technique and the heat flux calculation. Again, the 0° curve is very different. This is likely due to the flow field approximating a horizontal plate, where unsteady Rayleigh-Bérnard type cell are emanating from a heated surface.

The radial temperature profiles for $Ra_{D_i} = 1.5 \times 10^9$ are shown in figure 7.3a. The large size of the facility limited the extent of the traverse in the lower region. As the inner thermocouple probe head arrangement was used, the traverses in the upper section extend to 0.975; meaning the majority of the outer boundary layer is not captured. The 0° line is similar in magnitude to the RoBo cases, but there is a larger gap to the 45° mid-annulus value. The slight rise in temperature in the outer half of the 45° line hints at a recirculating flow structure.

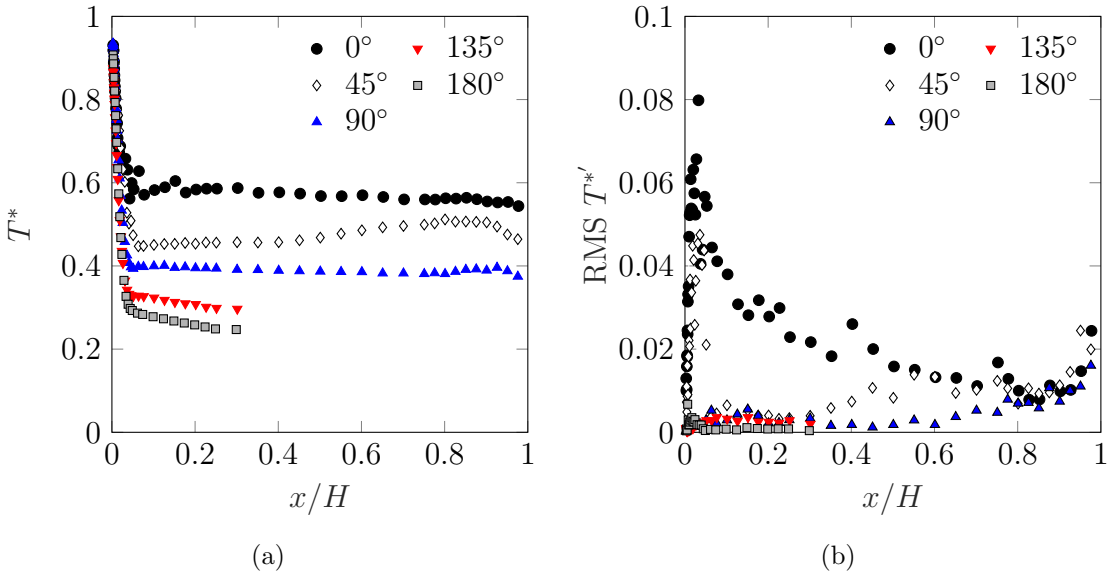

FIGURE 7.3: **a:** Radial temperature profiles for $Ra_{D_i} = 1.5 \times 10^9$ and $Dr = 2$, on the ExCITE facility. **b:** Corresponding temperature fluctuations for this case.

When compared to a similar type on thermal boundary condition test from the RoBo facility (inner isothermal and outer non-isothermal, see figure 6.5c), the lower section temperature profiles are different. The 180° curve in the present figure is much closer to 135° than the lower diameter ratio cases, which may indicate a larger stagnant region.

The corresponding temperature fluctuations for this case are shown in figure 7.3b. Peak values are observed at TDC, close to the inner surface. The magnitudes are very similar to the RoBo cases. $T^{*'}$ then decays as x increases, before rising again near the outer wall. This result is a near identical to the trends observed by McLeod & Bishop [70]. There is also a narrow peak near the inner surface at 45°. The rise in $T^{*'}$ near the outer wall at 90° indicates that the recirculating flow has at least reached this location.

Two further inner wall temperature profiles are shown in figure 7.4: $Ra_{D_i} = 6.5 \times 10^8$ and 2.1×10^9, which show very similar trends to the previous case. $T^{*'}$ for these cases is given in figure 7.5. While the lower Ra case is akin to the previous results but as Ra is increased, a different trend emerges. The profile at 45° is no longer

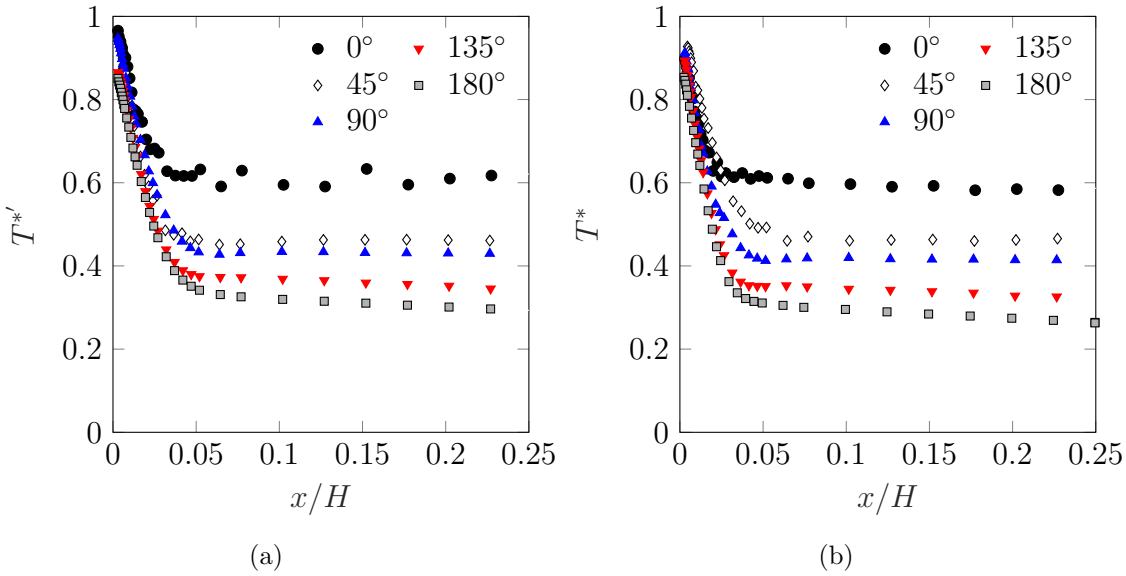

FIGURE 7.4: **a:** Radial temperature profiles for $Ra_{D_i} = 6.5 \times 10^8$ and $Dr = 2$. **b:** Radial temperature profiles for $Ra_{D_i} = 2.1 \times 10^9$

concentrated, and a clear peak in the near wall region at 90° emerges. This clearly shows the flow unsteadiness moving upstream as Ra is increased.

7.2.2 Heat Transfer

The inner wall heat flux distribution for these three cases is given in figure 7.6. The trend in the larger Ra cases in very similar to the RoBo cases at lower Ra and Dr. The mean equivalent conductivity for these cases (blue squares) is shown in figure 7.7; the data from all of the previous sealed annulus cases are also included. Values obtained from the Kuehn & Goldstein correlation [57], which is valid for turbulent natural convection, is shown for the ExCITE case inputs. The experimental values are approximately 30% below the correlation values – a much larger disparity than the previous cases. This may be due to the non-isothermal outer surface at this larger diameter ratio. Since the outer cylinder is now further away from the inner cylinder, the radial wall temperature difference has less influence on the local value of heat flux. Therefore, the main finding from the previous chapter cannot be applied to larger diameter ratios.

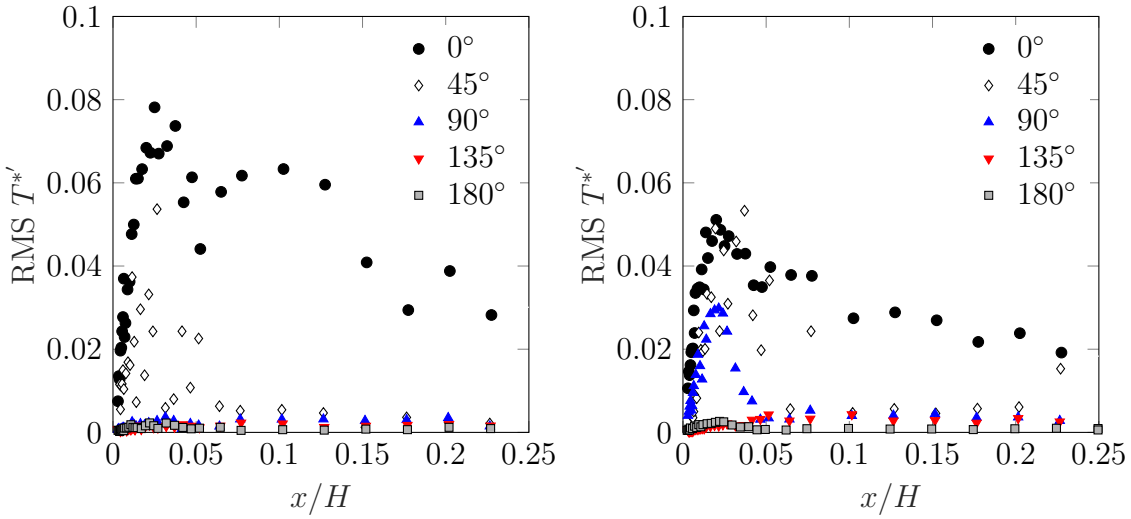

FIGURE 7.5: **a:** Radial temperature fluctuation profiles for $Ra_{D_i} = 6.5 \times 10^8$ and $Dr = 2$. **b:** Radial temperature fluctuation profiles for $Ra_{D_i} = 2.1 \times 10^9$

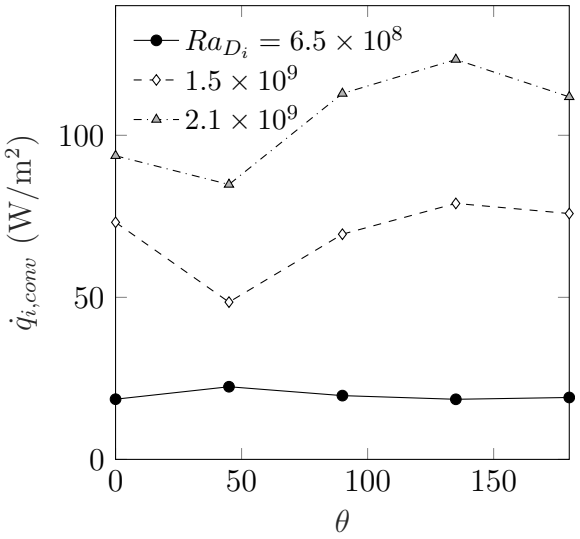

FIGURE 7.6: Measured inner surface heat flux distribution from the ExCITE facility.

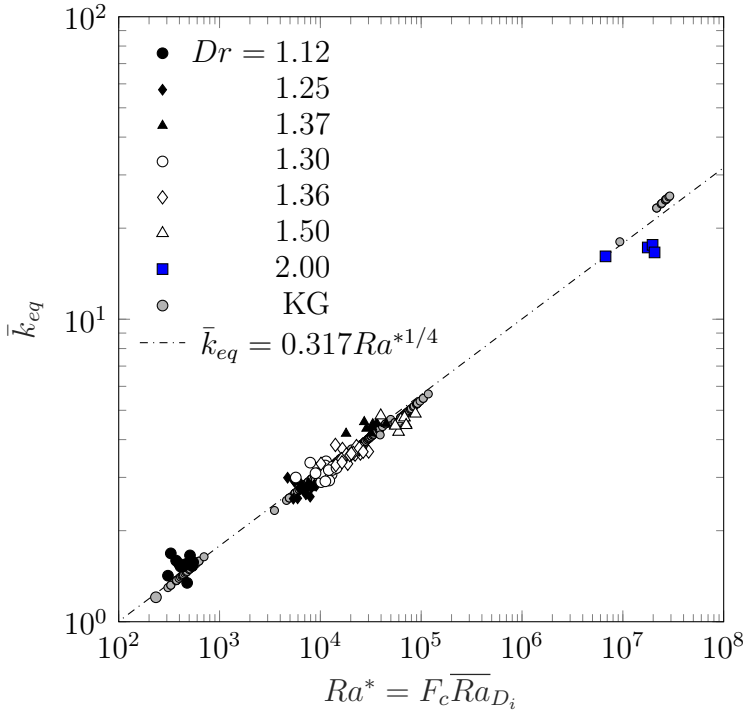

FIGURE 7.7: Mean equivalent conductivity for both facilities. Blue marks are from the ExCITE cases.

7.3 Unsteady Measurements

7.3.1 Theory

As mentioned in Chapter 5, while the IR camera results are unsuited for steady-state local heat flux calculations in this facility, valuable information can be gained from an unsteady measurement of the temperature signal. This method works as it is based on a temperature difference as opposed to an absolute magnitude of temperature, and the surface conductivity is approximately the same as the local fluid conductivity. Firstly, equation 3.2 can be rearranged to solve for the Rohacell surface temperature:

$$T_s = \left[\frac{T_{bb}^4 - (1 - \tau\epsilon(\theta))T_R^4}{\tau\epsilon(\theta)}\right]^{1/4} \tag{7.3}$$

The values of $\tau\epsilon(\theta)$ can be quantified from equation 5.3. T_R is fitted as the outer cylinder circumferential temperature distribution. A video sequence is recorded

at 32 Hz for 60 seconds, to obtain a time-averaged surface temperature ($\bar{T}_s$). The fluctuation in temperature at each frame is then given by equation 7.4.

$$T'_s = T_s - \bar{T}_s \tag{7.4}$$

This formulation provides the necessary boundary conditions for the computation of surface heat flux of 1D conduction into a semi-infinite solid, which is given by equation 7.5 [93]. As T'_s is used in the calculations, it is the heat flux fluctuation that is being computed.

$$\dot{q}'_s = \frac{\sqrt{\rho c_p k}}{\sqrt{\pi}} \left[\frac{T'_s(t)}{\sqrt{t}} + \int_0^t \frac{T'_s(t) - T'_s(\tau)}{(t-\tau)^{3/2}} d\tau \right] \tag{7.5}$$

If T'_s is assumed to be linearised locally, then the unsteady heat flux can be computed using equation (7.6) [93]. The thermal properties of Rohacell are: $\rho = 110$ kg/m^3, $c_p = 2300$ J/kgK and $k = 0.03$ W/m^{2}K [43]. A filter is required on the T'_s signal in order to evaluate this summation. A moving average of width 0.5 seconds is used.

$$\dot{q}'_s(t) = \frac{\sqrt{\rho c_p k}}{\sqrt{\pi}} \left[\frac{T'_s(t)}{\sqrt{t_n}} + \sum_{i=1}^{n-1} \left(\frac{T'_s(t_n) - T'_s(t_i)}{(t_n - t_i)^{1/2}} - \frac{T'_s(t_n) - T'_s(t_{i-1})}{(t_n - t_{i-1})^{1/2}} + 2\frac{T'_s(t_i) - T'_s(t_{i-1})}{(t_n - t_i)^{1/2} + (t_n - t_{i-1})^{1/2}} \right) + \frac{T'_s(t_n) - T'_s(t_{n-1})}{\sqrt{\Delta t}} \right] \tag{7.6}$$

7.3.2 Experimental Results

The results are most informative when viewed as a video sequence as the development of various features is observed, and a perception of the flow velocity is obtained. Figure 7.8 shows a single frame of $\dot{q}'_s(t)$ for $Ra_{D_i} = 2.1 \times 10^9$ and $Dr = 2$. The steady-state heat flux values (calculated from temperature traverses) for this case are shown previously in figure 7.6: 111 W/m^{2}K at BDC and 93 W/m^{2}K at TDC. The

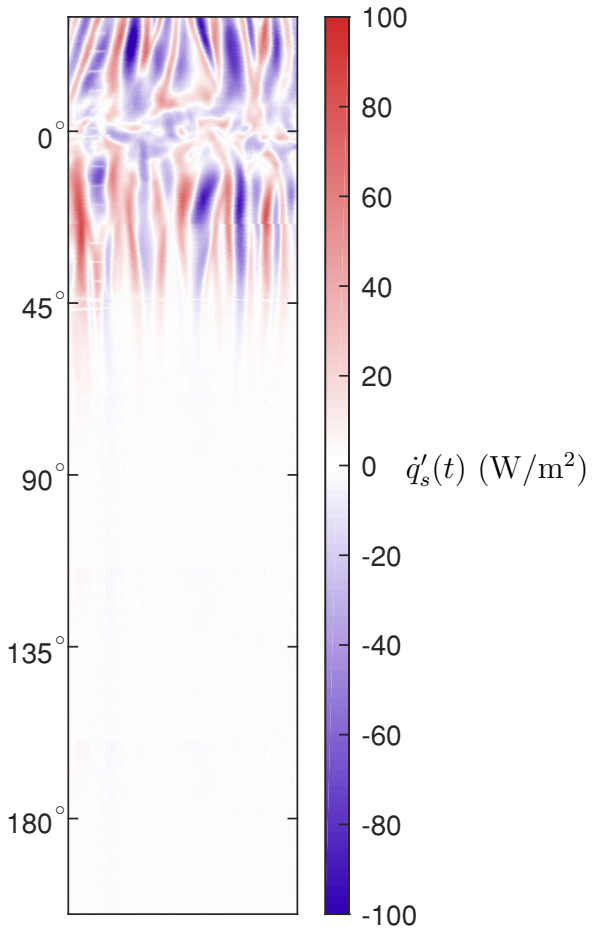

FIGURE 7.8: Example inner surface heat flux fluctuations for $Ra_{D_i} = 2.1 \times 10^9$ and $Dr = 2$.

surface heat flux is very steady from 90° onwards; this coincides with the low values of $T^{*'}$ from the traverse measurements. Upwards from 90°, alternating hot and cold streaks develop that increase in magnitude as TDC is approached. This pattern indicates the presence of Görtler vortices. The pattern is very different at TDC where the streaks from either side are colliding. This leads to a very unsteady $\dot{q}_s'$ pattern. It is interesting that $\dot{q}_s'$ TDC is very close in magnitude to the steady-state value.

7.3.3 Comparison to CFD

Dhopade [24] has developed a CFD methodology that uses DES to simulate the experimental configuration of the ExCITE facility. This method has been reproduced

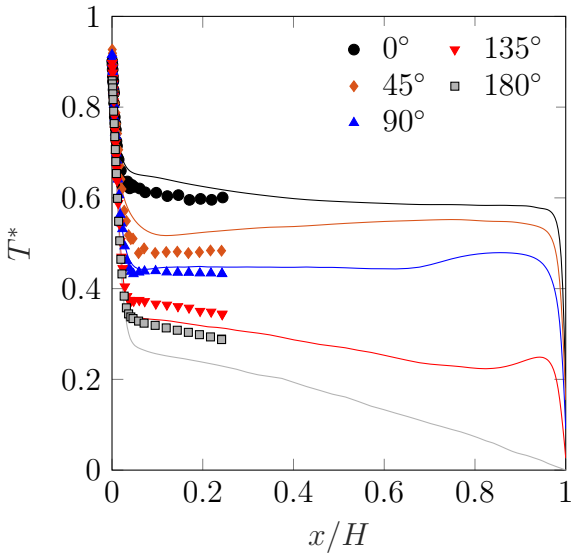

FIGURE 7.9: Radial temperature profiles for $Ra_{D_i} = 2.1 \times 10^9$ and $Dr = 2$, comparing CFD to experimental measurements.

in order to compare the unsteady heat flux experimental measurements. Firstly, figure 7.9 shows a comparison of the radial temperature profiles between the CFD and experimental results. The general shapes of the profile are captured but there is disagreement in the temperature magnitudes. This may be due to the outer temperature boundary profile definition or the radiation modelling. The mean inner surface equivalent conductivity from the CFD was 16.7, which is extremely close to the experimental value (16.6).

Figure 7.10a gives the time-averaged temperature contour at the axial mid-plane. The temperature is quite uniform in the upper section of the annulus and the plume is barely viable near TDC; this is a consequence of the large amount of mixing in this region at this turbulent Rayleigh number, as described by McLeod & Bishop [70]. Figure 7.10b gives the time-averaged velocity magnitude contour with vectors overlaid, at the axial mid-plane. The main flow features of natural convection in a moderate diameter ratio concentric annulus (see figure 6.6 on page 86) are evident: bouyant plume at TDC, stagnant lower region, and recirculating cells.

A comparison of the inner surface Nusselt number fluctuations between CFD (left)

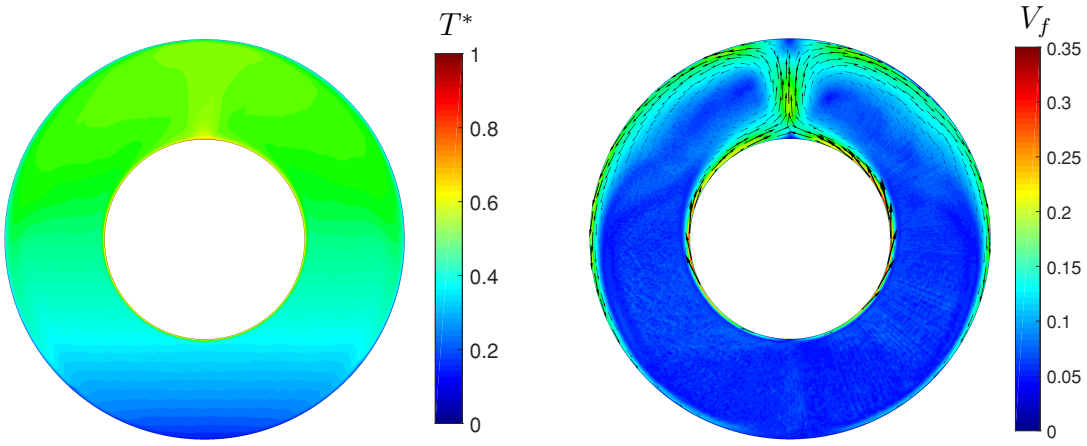

(a) (b)

FIGURE 7.10: **a:** CFD contour of average temperature for a sealed concentric annulus with $Ra_{D_i} = 2.1 \times 10^9$ and $Dr = 2$. Reproduced from the method developed by Dhopade [24]. **b:** Velocity magnitude and vectors for this case.

and experiments (right) is shown in figure 7.11. Encouragingly, the magnitudes and overall structures are very similar between both cases. A streak profile is also seen in the CFD results, however the inception point is observed further upstream in the experimental results and the streaks are slightly wider.

The CFD solution required a time step of 0.04 seconds, and was run for 20 seconds. Figure 7.12 shows the inner wall standard deviation of heat flux over this time period. Again, there is good agreement to the experimental results. The highest intensity fluctuations are observed from 10-30° in the experiment, and 10-45° in the CFD. This corresponds to the location of the alternative hot and cold streaks.

Overall, the agreement between the CFD and the experimental measurements adds confidence to the unsteady heat flux measurement technique. It has been shown that this method can be used to give a unique and useful insight into the heat transfer flow field development.

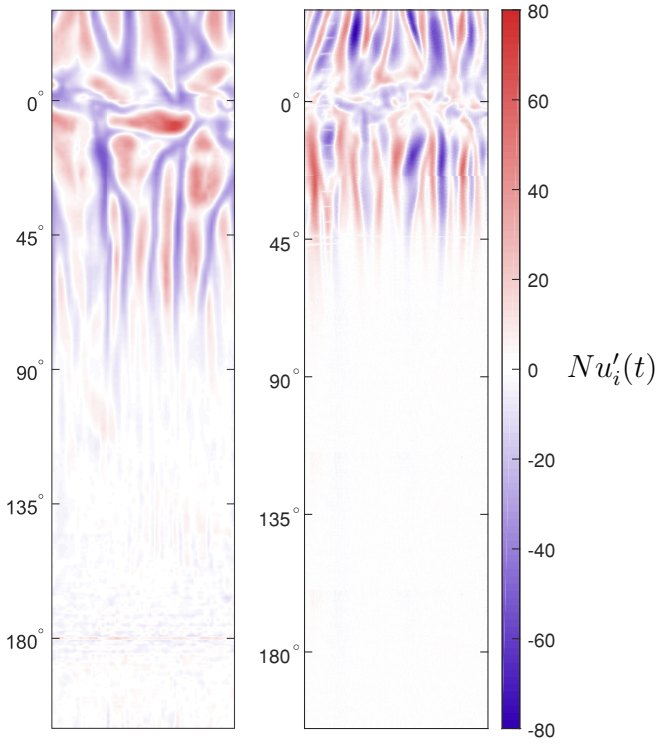

FIGURE 7.11: Inner surface Nusselt number fluctuations for $Ra_{D_i} = 2.1 \times 10^9$ and $Dr = 2$. *Left:* CFD. *Right:* Experimental measurements.

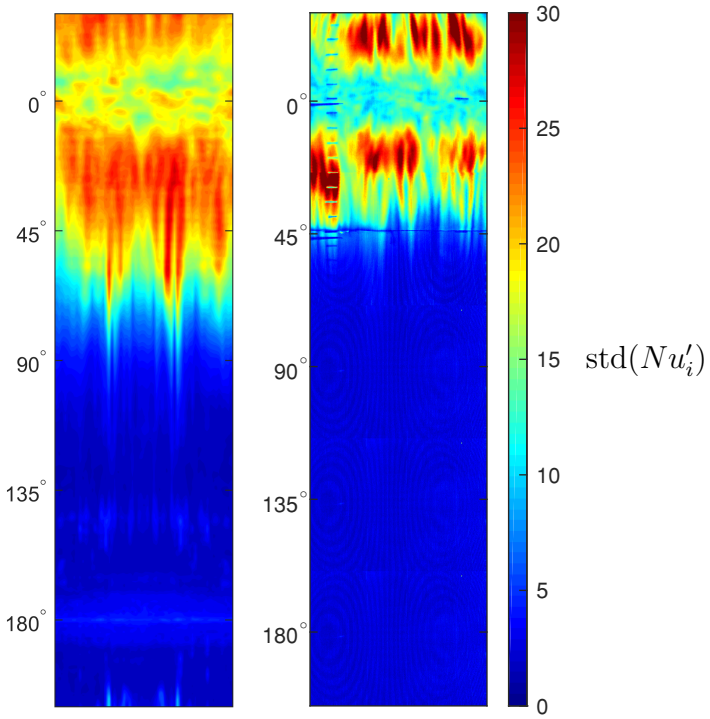

FIGURE 7.12: Standard deviation of inner surface Nusselt number fluctuations for $Ra_{D_i} = 2.1 \times 10^9$ and $Dr = 2$. *Left:* CFD. *Right:* Experimental measurements.

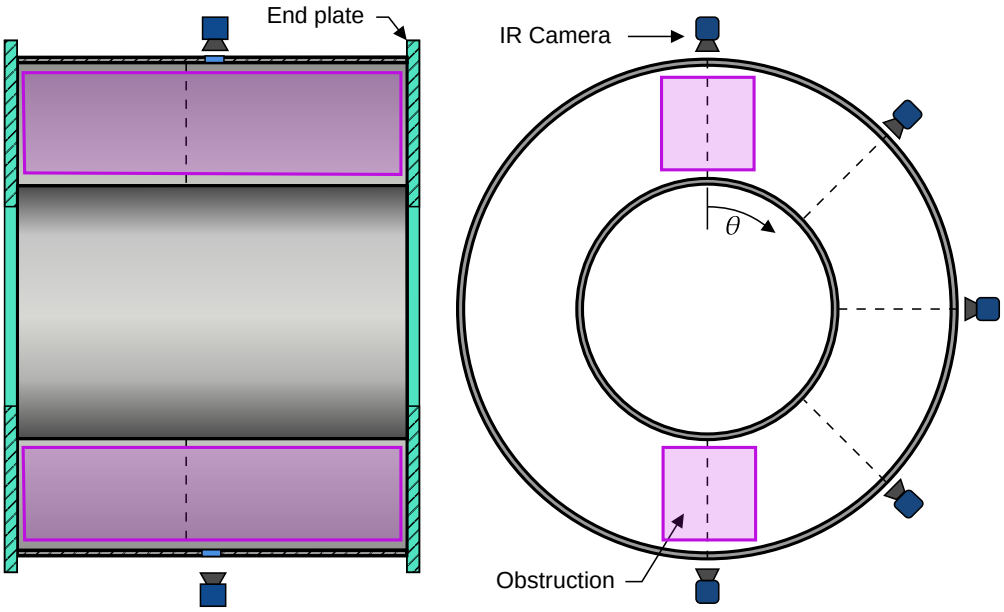

FIGURE 7.13: Cross section of ExCITE facility with obstruction (purple box) included. The box was placed at only of these locations for a given test.

7.4 Obstructions

The idealised case has allowed for insights into the fundamental natural convective flow structure of a large cylindrical annulus, but the auxiliary zone of a gas turbine is clustered as it contains many components, giving a very complex overall geometry that would be very difficult to simulate. An initial exploration into potential effects of obstructions has been completed. A cuboid-shaped obstruction has been manufactured from thin aluminium struts and polycarbonate facing, with dimensions of: 220 x 360 x 1200 mm. It can be placed at either TDC or BDC, as shown in figure 7.13. It occupies the entire axial length of the annulus.

The overall impact of the obstruction can be quantified by examining the outer cylinder temperature profile and the mainstream fluid temperatures. These results are shown in figure 7.14 for three separate cases: obstruction at top, bottom, and a clean annulus. $Ra_{D_i} = 2.1 \times 10^9$ in all cases. The obstruction is sitting in the stagnant region when it is placed at BDC and as it is outside of the thermal boundary

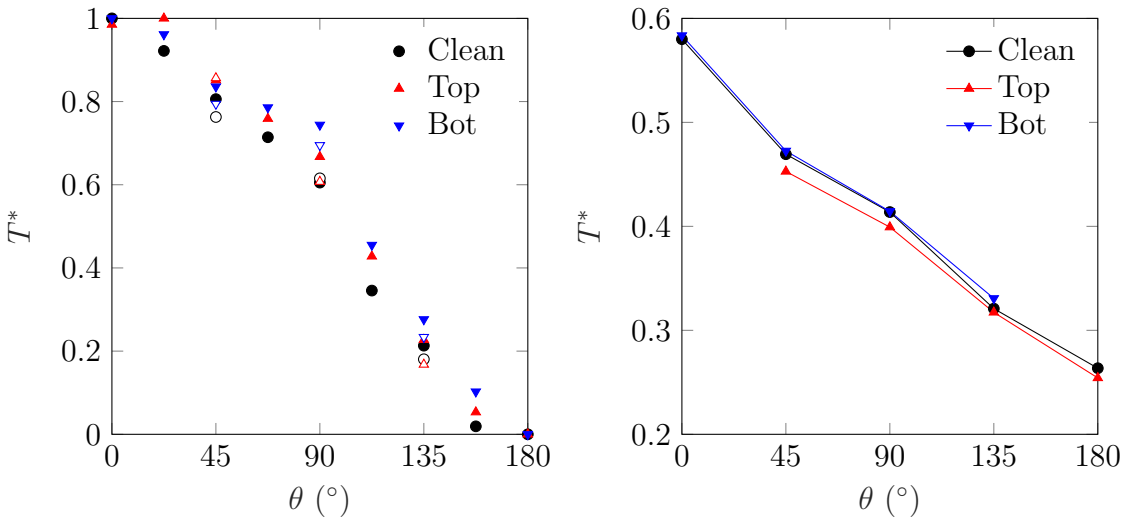

(a) (b)

FIGURE 7.14: **a:** Outer cylinder circumferential temperature distributions for clean and obstructed cases. $Ra_{D_i} = 2.1 \times 10^9$ **b:** Fluid temperature at $0.25H$ for these three cases.

layers, the mainstream air temperatures are nearly indistinguishable from the clean case. It has caused a slight increase in the outer cylinder temperatures in the lower section.

When placed at TDC, the obstruction will cause some disruption to the plume. It will likely lead to a plume emerging at either side of the box – this causes the slight reduction in air mainstream temperatures and a larger hot spot at the top of the outer cylinder. Referring back to the flow schematics in figure XX and the CFD results of clean case given in figure XX, this particular obstruction would not disturb the recirculating flow cells. Overall, there are subtle differences between the clean and obstructed cases, but the trends are similar.

7.5 Conclusions

An experimental campaign on the ExCITE shutdown facility has led to some interesting findings regarding natural convection in a large cylindrical annulus:

- The cases studied here with a non-isothermal outer wall gave an equivalent

conductivity approximately 30% below the correlation values (based on the average wall temperature difference). Therefore, the main finding from the previous chapter – that the heat transfer for non-isothermal tests cases can be accurately predicted by the area-averaged temperature values – cannot yet be extended to larger diameter ratios than those presented in Chapter 6.

- The work on this and the preceding chapter has shown that, on the whole, the use of an equivalent conductivity is a very useful way of correlating the heat data from many different boundary conditions and geometries with Rayleigh number.

- An unsteady heat flux visualisation method has been developed and validated using CFD. The technique provides a unique, full-surface insight into the heat transfer flow field.

- The obstruction cases presented here did not have any significant effect on the overall flow field.

Chapter 8

Installation Effects on Rotor Bow

8.1 Introduction

While the main gas path of a large civil gas turbine is well represented by a concentric annulus, during shutdown cooling the region of interest will neither be isolated from the ambient environment nor free of obstructions. In order to gain further insight into the process by which rotor bow develops, an initial exploration of these installation effects has been conducted experimentally, using the RoBo facility.

8.2 Open-Ended Annulus Effects

8.2.1 Steady-State Measurements

A simple modification to the RoBo facility allows for open-ended annulus experiments to be conducted. This configuration is more representative of a large civil gas turbine high-pressure compressor under shutdown conditions, when compared to the sealed annulus. The end plate on the inner cylinder side (see figure 6.2 on page 80) has been removed; the cone end plate remained in place. This arrangement was chosen as to concentrate testing on the concentric cylinder section – a geometry which has

TABLE 8.1: Thermal boundary conditions for the six test cases that were completed. All temperatures are in Celsius. Ra_{D_i} at $\theta = 0°$ is held constant at 6.3×10^7 for cases A-C, and Ra_{D_i} at $\theta = 180°$ is held constant at 8.2×10^7 for cases D-F.

	Key	$\Delta T_{c,i}$	$\Delta T_{c,o}$	$T_{i,t}$	$T_{o,t}$	$T_{i,b}$	$T_{o,b}$	$\Delta T_{r,t}$	$\Delta T_{r,b}$	ΔRa_{D_i}
A	-●-	0	0	100	60	100	60	40	40	0
B	-■-	20	0	100	60	80	60	40	20	2.7×10^7
C	···▾···	0	20	100	60	100	40	40	60	-4.5×10^7
D	-●-	0	0	80	40	80	40	40	40	0
E	-■-	20	0	100	40	80	40	60	40	2.6×10^7
F	···▾···	0	20	80	60	80	40	20	40	-4.6×10^7

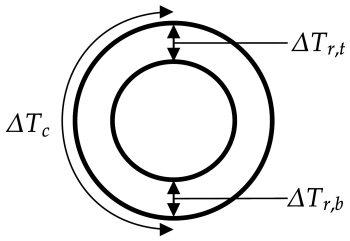

historically been studied in much more detail than the conical section. A subset of the *Tc* and *Bc* thermal boundary traverses have been conducted with this open-ended arrangement. Table 8.1 gives the details of each case. All traverses presented in this section were completed on the inner cylinder plane, which has the following geometric properties: $D_i = 326$mm $Dr = 1.25$, $H = 40$mm. The traverse plane is located 240 mm away from the opening axially.

The inner wall convective heat fluxes for cases A-C (*Tc* subset) are given in figure 8.1a. Black markers are the previously presented sealed cases; white markers are open-ended. Opening the cylinder end of the annulus has caused a dramatic increase in inner wall heat flux between 45° and 180°, when compared to the corresponding sealed cases; $\dot{q}_i$ at 0° actually shows a slight reduction. The top-to-bottom difference in heat flux – which is the condition that leads to thermal bow – is significantly larger in the open-ended cases. It does appear that $\dot{q}_i$ at 0°, where the local value of Ra_{D_i} is constant, is still relatively unaffected by either $\Delta T_{c,i}$ or $\Delta T_{c,o}$.

The outer wall heat fluxes for these cases, shown in figure 8.1b, are negative from 45°

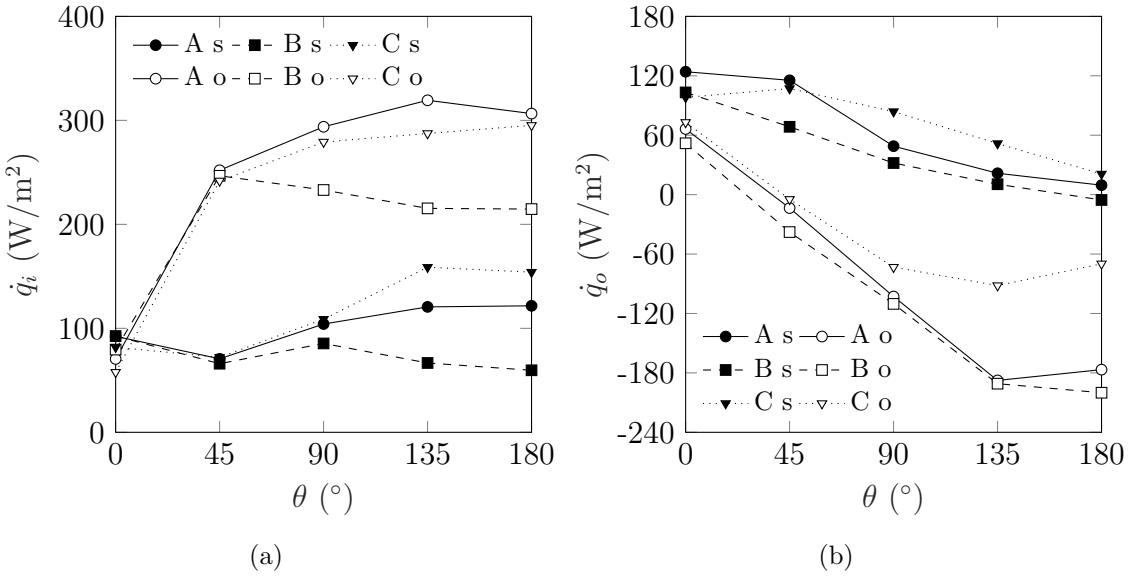

(a) (b)

FIGURE 8.1: **a:** Inner wall convective heat flux for cases A-C in table 8.1. Ra_{D_i} at $\theta = 0°$ is held constant at 6.3×10^7 Black markers are sealed cases (s) and white markers are open ended (o). **b:** The corresponding outer wall convective heat flux for these cases.

onwards. This means that the air temperature is now lower than the outer wall at these measurement locations; hence, the direction of heat flow is now from the outer wall into the annular air region. In fact, there is a complete reversal of top-to-bottom difference in $\dot{q}_o$ when compared to the sealed case.

The radial temperature profiles for the open-ended case A (isothermal walls) are shown in figure 8.2a; the sealed profiles are given in figure 8.2b. The open-ended case is non-dimensionalised by the maximum and minimum temperatures from the sealed case, to allow an easier comparison. Therefore, the ambient air temperature (T_∞) corresponds to $T^* = -0.92$. The mid-annulus T^* at both 135° and 180° is only slightly above ambient – signifying that a natural draft has been created that induces cold air into the lower section of the annulus. This leads to the high values of $\dot{q}_i$ and large negative values of $\dot{q}_o$. The induced cold air is heated as it ascends towards the upper section of the cylinder. As air is entering in the lower section, it must be exiting in the upper section; however, the mid annulus T^* is only slightly lower at 0° when compared to the sealed configuration. This reduction coupled with a mass flow

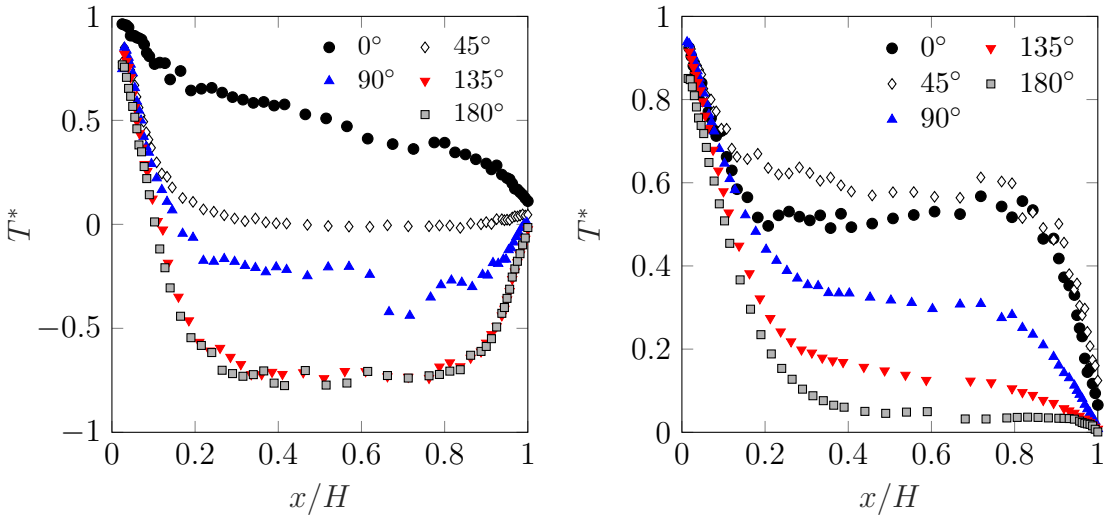

FIGURE 8.2: **a:** Radial temperature profiles for the open-ended case A. Ambient air temperature corresponds to $T^* = -0.92$. $Ra_{D_i} = 6.3{\times}10^7$
b: Radial temperature profiles for case A sealed.

of air exiting the annulus will lessen the impingement effect on the outer cylinder at TDC, thus lowering $\dot{q}_o$ at 0° when compared to the sealed case. Examining the 90° curve, a dip is observed just beyond 0.6. This is the radial location where the probe reverser arrangement has been installed (see figure 4.16a on page 67); thus the probe in now closer to the opening, which is why a reduction in T^* occurs. This highlights that the heat flux in now longer uniform in the axial direction, with higher values near the opening, which agrees with the numerical work of Vafai [110].

The temperature fluctuations for the open-ended case A are given in figure 8.3a. While the values of $T^{*'}$ immediately next to the wall remain low (as they are damped out by the viscous forces), the five traverse locations all show similar levels of unsteadiness. When compared to the sealed case (figure 8.3b), $T^{*'}$ at 45° is no longer consistent as x is increased, which suggests that the multicellular flow structure has been altered. Overall, the flow field is now dominated by the natural draft that has been created.

The remainder of the test conditions from table 8.1 (D-F) have been investigated to determine if the local heat flux at BDC is insensitive to $\Delta T_{c,i}$ or $\Delta T_{c,o}$. Ra_{D_i} at

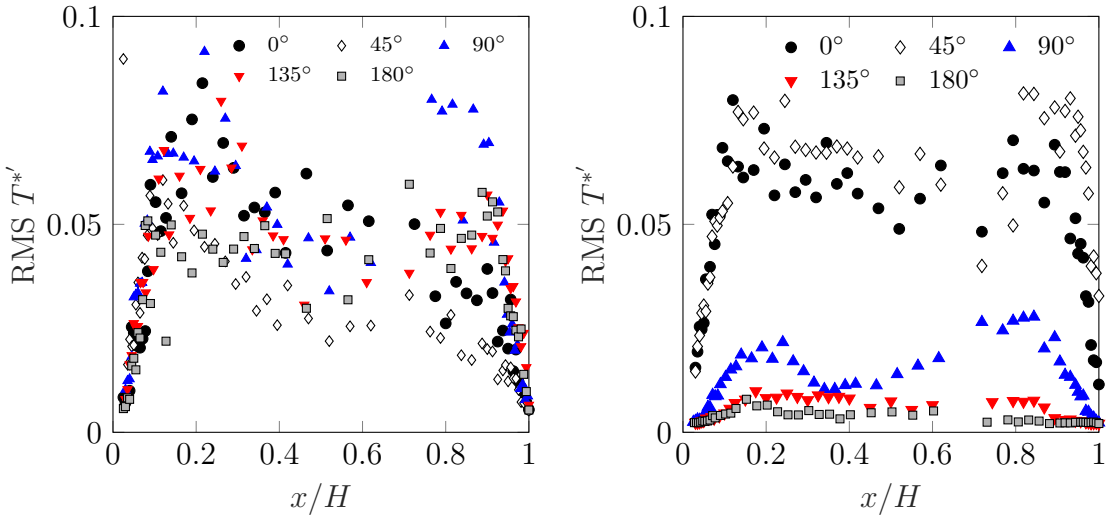

FIGURE 8.3: **a:** Temperature fluctuation profiles for the open-ended case A. $Ra_{D_i} = 6.3 \times 10^7$ **b:** Radial temperature fluctuation profiles for case A sealed.

$\theta = 180°$ is held constant at 8.2×10^7 for these cases – where Ra is calculated using $T_i - T_o$. The inner and outer wall heat fluxes are shown in figure 8.4. Encouragingly, the measured values at 180° are extremely well matched across all cases. This is an important result as it indicates that even though the overall flow dynamics are different for the open ended cases, the local radial temperature difference still has a strong influence on the local heat flux.

8.2.2 Transient Measurements

Rotor bow is a transient issue that develops during the cooling cycle of a gas turbine. An alternative experimental technique – transient cooling test – can be used to attain further understanding of the natural convective flow field; especially into the complex interactions of various design parameters. The procedure is initially identical to the steady-state process. Once a steady state is reached, the input power to all of the mats is cut simultaneously. All thermocouples signals are then recorded at 1 Hz as the facility cools down. Referring back to the cross-sectional schematic of the rig, shown in figure 6.1 on page 80, the inner assembly has a wall thermocouple at 0°,

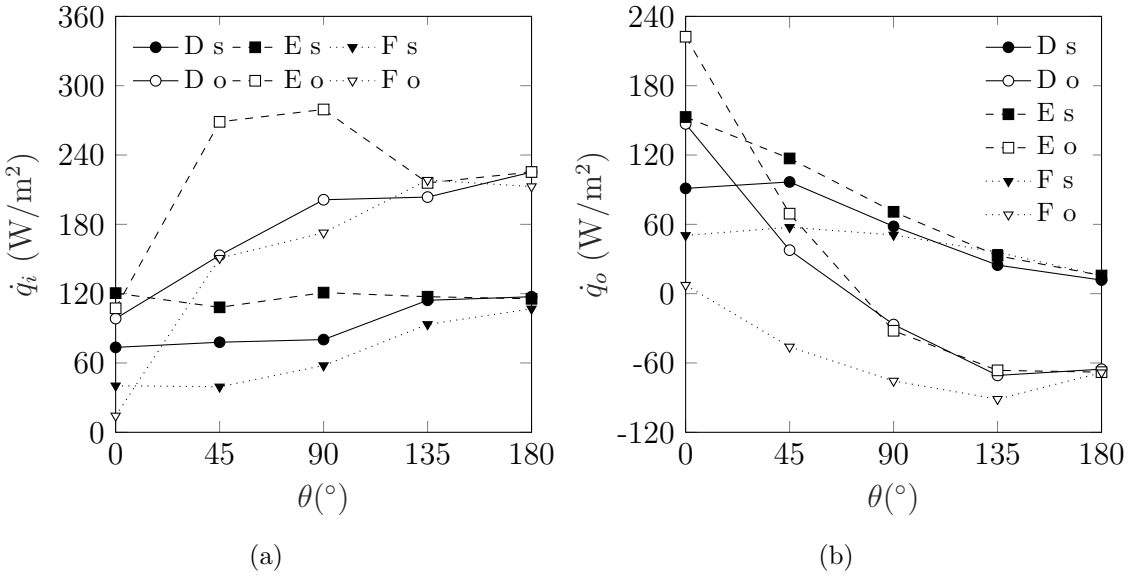

(a) (b)

FIGURE 8.4: **a:** Inner wall convective heat flux for cases D-F in table 8.1. Ra_{D_i} at $\theta = 180^\circ$ is held constant at 8.2×10^7 Black markers are sealed cases (s) and white markers are open ended (o). **b:** The corresponding outer wall convective heat flux for these cases.

72° and 144°; whereas the outer cylinder is instrumented at 0°, 60°, 120° and 180°. Figures 8.5a to 8.5c show the metal temperatures during the cooling cycle for the sealed (s) and open-ended (o) case. T^* is non-dimensionalised using T_∞. The initial thermal boundary conditions are case A (isothermal walls), given in table 8.1. The 'top' curves are all at 0°; 'bot' is the thermocouple at 144° on the inner assembly and 180° on the outer cylinder.

It is not surprising to see that the bottom cools faster than the top. Moreover, opening an end caused the entire apparatus to cool quicker – the natural draft causes more heat to be dissipated from the inner cylinder than the sealed case. The difference between top and bottom curves ($\Delta T^* = T^*_{top} - T^*_{bot}$) for a given component is shown in figure 8.5d, as this is a direct indicator of the level of thermal bow that can be reached. The typical bow profile is observed, which is caused by the initial larger heat flux in the lower section. After a period of time the difference in heat flux diminishes and peak temperature difference bow occurs. In the sealed case, the outer cylinder temperature difference is nearly double that of the inner cylinder. The

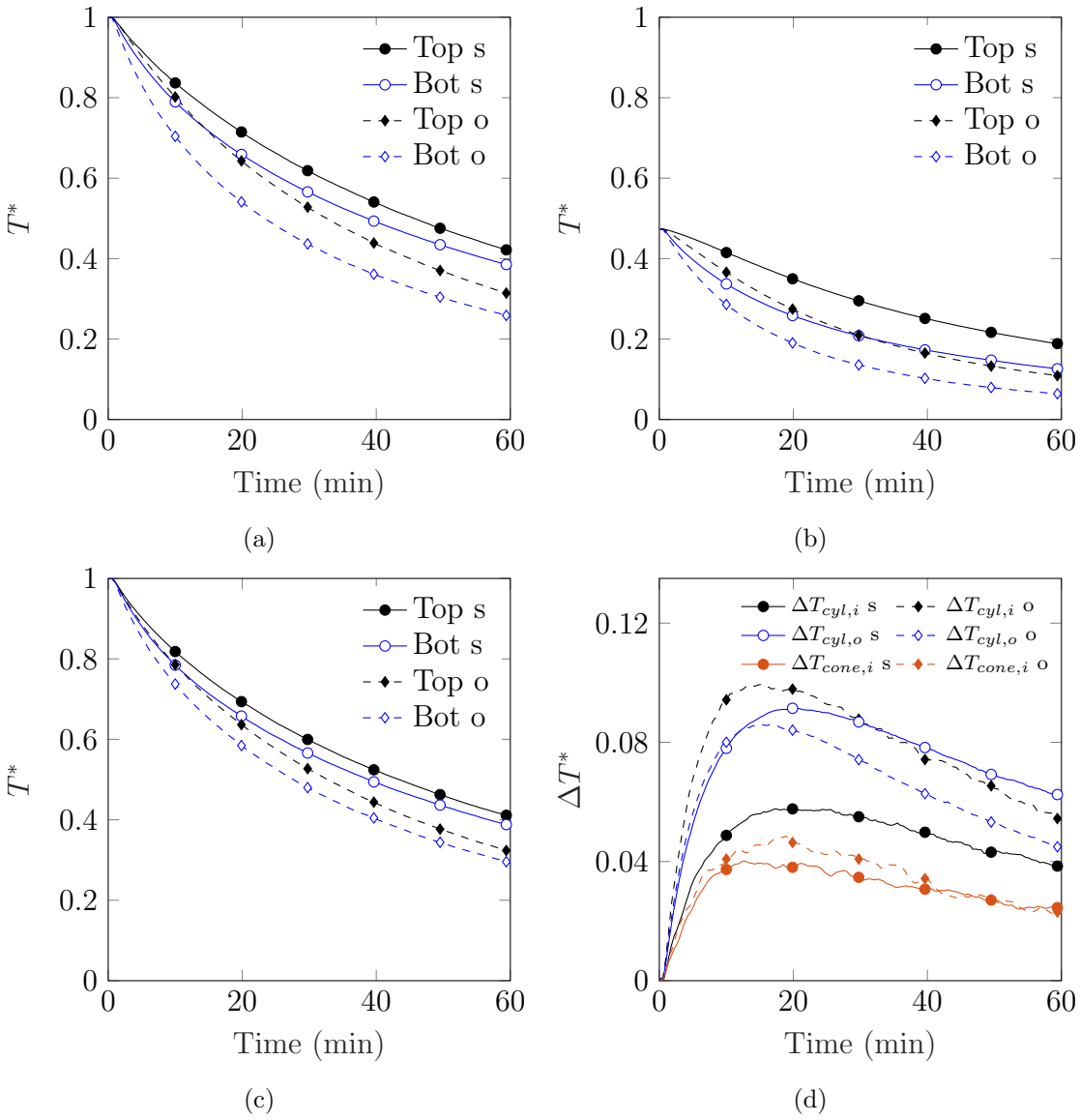

FIGURE 8.5: **a:** Transient cooling temperatures at the top and bottom of the inner cylinder starting from Ra_{D_i} 6.3×10^7 and $Dr = 1.25$. Both sealed and open-ended cases are shown. **b:** Outer cylinder temperatures. **c:** Cone section temperatures. **d:** Top-to-bottom temperature differences for each test case.

cone section does not reach as large a temperature difference as much as the inner cylinder – which may be due to the smaller inner diameter of this component.

Opening the cylinder end of the annulus has a caused a notable increase in the peak inner cylinder top-to-bottom temperature difference – a consequence that is consistent with the altered heat flux profiles measured in steady-state. The natural draft has also slightly reduced the on-set time of the peak inner cylinder temperature difference. The cone cooling curves (orange lines in figure 8.5d) show only a minimal difference between the sealed and open case; this may be because the end plate on the cone side of the rig remained in place. Steady-state measurements of the outer cylinder were vastly different for the sealed and open-ended case, yet the top-to-bottom temperature difference curves shows a similar peak. Hence, the inner cylinder top-to-bottom temperature difference is now larger than the outer cylinder in the open case – a reversal of the order from the sealed case.

A lumped capacitance analysis can be applied to these transient tests in order to estimate the heat fluxes throughout the cooling cycle. The inner assembly is divided into five sections, the outer into six – with the associated thermocouple for each lumped mass. The mass of the heater mats and insulation is ignored. The appropriateness of the lumped capacitance method can be examined by calculating the Biot number for each section, which is defined in equation 8.1. The characteristic length (L_c) used is the volume of metal divided by the convecting surface area. k_{al} is the conductivity of the aluminium. Using the maximum heat flux observed in the steady-state experiments to define a heat transfer coefficient (h), the Biot number for both the inner and outer sections is approximately 2.5×10^{-5}, which is $\ll 0.1$ – highlighting the suitability of this approach [91].

$$Bi = \frac{hL_c}{k_{al}} \tag{8.1}$$

The rate of change of the temperature can be used to calculate the total heat flow

using equation 8.2 [16]. V_e is the volume of the lumped mass; the material properties of the aluminium are: $k = 180$ W/mK, $\rho = 2700$ kg/m^3 and $c_p = 910$ J/kgK [16]. Radiation heat transfer in the annulus is calculated using the method outlined in section 3.5. For a sealed geometry, an end conduction heat loss correction can be tabulated by comparing the total amount of heat leaving the inner assembly to the heat loss from the outer cylinder. The difference between these two values can then be attributed to end conduction from the inner assembly. This value of heat is then converted to a h value so that it can be applied to the open-ended case also. Thus, the convective heat flux can be derived from subtracting both the radiation and end loss from the total heat flow.

$$Q = \rho c_p V \frac{dT}{dt} \tag{8.2}$$

The transient inner wall convective heat flux calculated with the lumped capacitance method is shown in figure 8.6a for the sealed case. The initial values at 0° and 72° are comparable to the steady-state results but the 144° value is larger. The reason for this unknown – it may be an end conduction effect of the facility. Nevertheless, all of the curves decay with time, as a reduction in metal temperature concurrently reduces the heat-transfer-coefficients and temperature difference between the metal and ambient. After approximately 20 minutes of cooling, the curves collapse down to very similar paths ($< 5\%$ difference in $\dot{q}_{i,conv}$); it is around this point that the peak top-to-bottom temperature difference occurs – as this is the point in time where the rate of change of $q_{i,conv}$ at the top and bottom of the cylinder are equal. The elongated fall in thermal bow seen post-peak is a consequence of the similarity of the heat flux cooling curves following the initial divergence.

The transient values of $\dot{q}_{i,conv}$ for the open-ended case are shown in figure 8.6b. A moving-average filter has been applied to the data to reduce the noise. Despite the much greater initial difference between top and bottom, the curves converge near

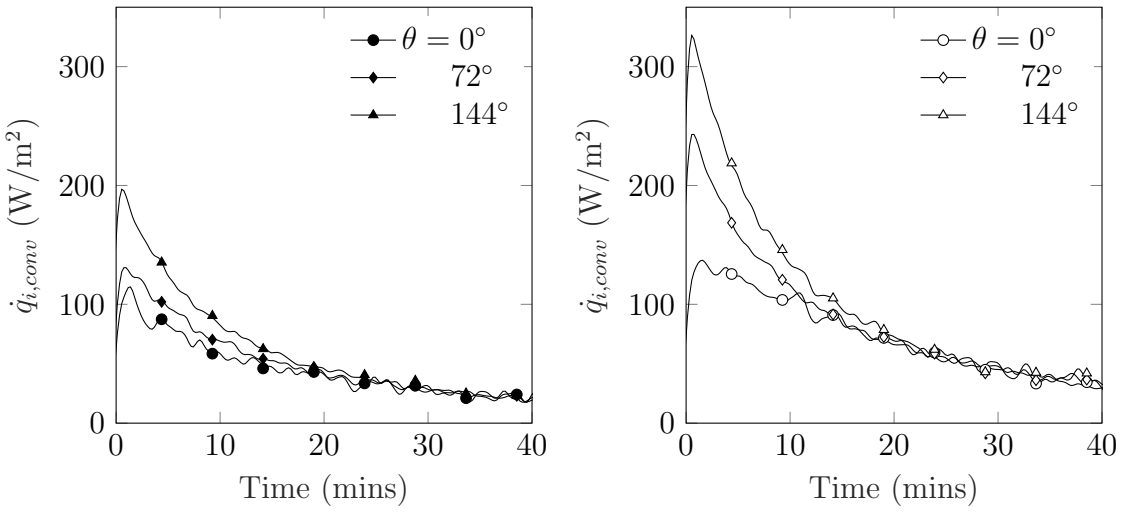

(a) (b)

FIGURE 8.6: **a:** Inner cylinder convective heat flux calculated using the lumped capacitance method, for the sealed case starting at Ra_{D_i} 6.3×10^7. $Dr = 1.25$. **b:** Corresponding values for the open-ended case.

the same time step as the sealed case. Here the peak values at 72° and 144° are well matched to the stead-state results and the value at 0° is larger, which indicates an axial gradient in convective heat transfer at the location.

8.3 Obstruction Effects

Investigating an unobstructed annulus has led to some valuable insights into natural convective flow physics. The next logical step to help demystify the process of shutdown cooling in a gas turbine is to introduce geometry representative of blade and vane rows. The influence of this on the development of rotor and casing bow has not been studied experimentally, to the author's knowledge. Smith [97] incorporated blades into his numerical studies by using a porous domain. Figure 8.7 shows a partly dismantled RoBo facility with four rows of obstructions installed. For assembly purposes, all obstructions needed to be mounted on the inner assembly, hence, stator vanes are also represented by blades. The blades have been 3D printed in an ABS plastic, which has a low conductivity (≈ 0.16 W/mK [16].) Each blade is identical,

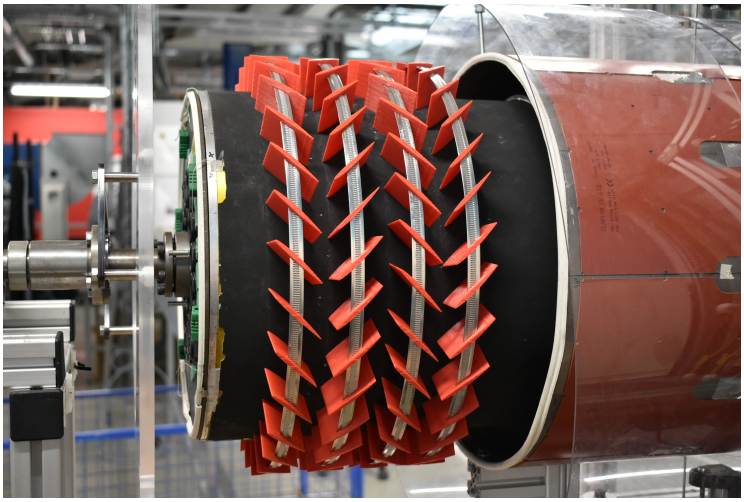

FIGURE 8.7: Four rows of blades and vanes installed in a partially assembled RoBo facility.

consisting of an extruded NACA 0006 profile [39]. All blades are at a 45° angle to the principal axis and each row has 30 blades – influence of the angle of attack, profile and number of blades are beyond the scope of this experimental campaign. An 8% tip gap was required for assembly purposes.

A temperature probe traverse may no longer provide a reliable value of wall heat flux for this arrangement, as the relative position of the probe in relation to the blade row exit could alter the findings. Hence, the transient experimental technique described in the preceding section was used for the obstruction tests. $Dr = 1.25$ and an initial Rayleigh number of 6.3×10^7 was defined to allow a comparison to these previous test cases. This leads to a test matrix of four configurations: a clean and obstructed annulus, both sealed and with the cylinder end open. The top and bottom metal temperatures during cooling for the inner cylinder, outer cylinder and cone are shown in figures 8.8a, 8.8b and 8.8c respectively, for all four configurations. These curves are then used to calculate the top-to-bottom temperature differences (ΔT^*) shown in figure 8.8d. A summary of the four tests is given in table 8.2 for reference. The 'Key' column indicates the line style and marker associated with a particular configuration, the colour may change.

Firstly, the influence of the blade rows without any axial ventilation can be compared

TABLE 8.2: Information about each of the four test cases that are presented in figure 8.8. $Dr = 1.25$ and all start at $Ra_{D_i} = 6.3 \times 10^7$ with isothermal walls.

Label	Key	Sealed	Blades
0s s	—○—	Yes	No
0s o	- ◇ -	No	No
4s o	- △ -	No	Yes
4s s	··□··	Yes	Yes

by looking at cases '0s s' and '4s s'. Both the inner and outer cylinder top-to-bottom temperature difference curves are matched in terms of severity. However, examination of the constituent temperature signals uncovers that the introduction of these blades and vanes has indeed affected the flow characteristics. It has curtailed the cooling rate at both the top and bottom of the inner cylinder in equal measure. The obstructions have likely disrupted any recirculating flow features that enhance heat transfer. The discrepancy in the outer cylinder curves is marginal. The outer wall heat flux distribution from the unobstructed, sealed case was defined by a large peak at 0°, as a result of the impinging plume from the inner cylinder, and little-to-no heat transfer at 180° as there is a stagnant region of air very close to temperature of the wall – these phenomena would not be as strongly affected by a disruption to the recirculating cells.

Introducing the blades to the sealed annulus did not change the magnitude of the peak top-to-bottom temperature difference in any components – the open-ended case however gives an entirely different trend. Case '4s o' gives a 35% higher peak in inner cylinder temperature difference when compared to the unobstructed open-ended case (0s o). The outer cylinder and the cone display only slight deviations. The bottom temperature curves in figure 8.8a highlight that the blades have not impeded the ambient air drawn into the lower section of the annulus. The top section lines though show a slower cooling rate when blades are present. The plausible causes of this are: a blockage effect of the blades that interferes with the hot air exiting in the upper section; the blades disrupt the natural draft as it ascends the annulus thus reducing

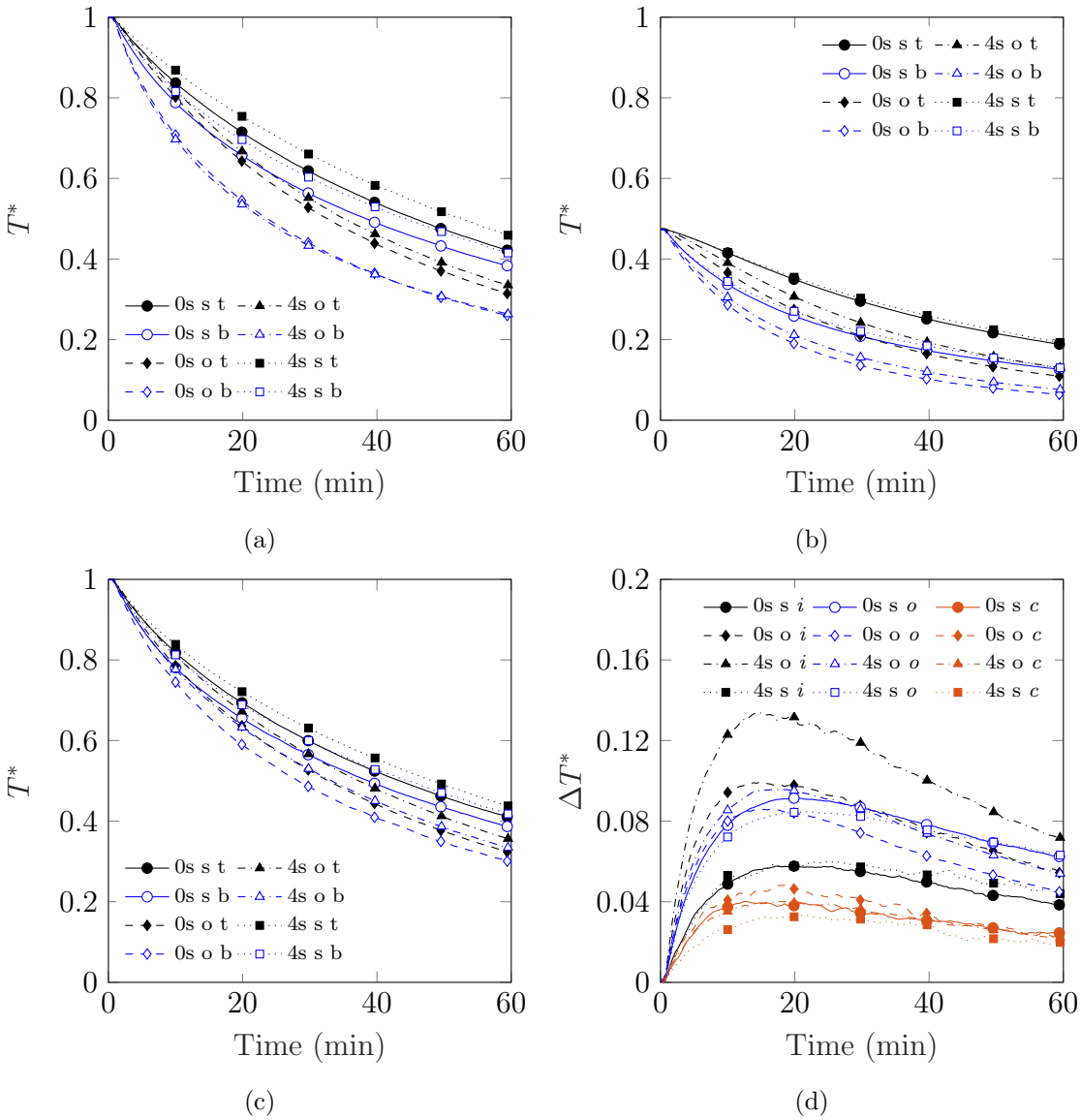

FIGURE 8.8: **a:** Transient cooling temperatures at the top (t) and bottom (b) of the inner cylinder starting from Ra_{D_i} 6.3×10^7 and $Dr = 1.25$. Information about the four cases is given in table 8.2. **b:** Outer cylinder temperatures. **c:** Cone section temperatures. **d:** Top-to-bottom temperature difference for each component from each of the four tests: i: inner cylinder; o: outer cylinder; c: inner cone.

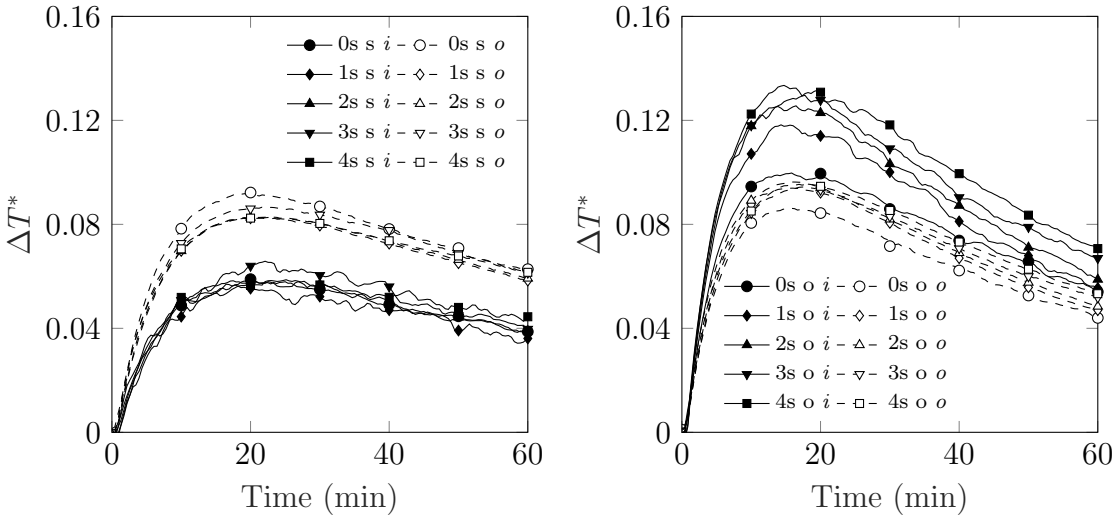

FIGURE 8.9: **a:** Top-to-bottom temperature differences for sealed cases with different numbers of blade rows. **b:** Top-to-bottom temperature differences for open-ended cases with different numbers of blade rows.

its ability to transfer heat away from the inner wall upper section. The combined effect of the axial ventilation and blades rows has caused a 140% increase in inner cylinder top-to-bottom temperature difference when compared to the baseline (0s s) case.

The inner and outer cylinder top-to-bottom temperature difference for differing numbers of blade rows is shown in figure 8.9a for the sealed annulus, and in figure 8.9b for the open-ended cases. Rows are added from right-to-left when looking at the facility in figure 8.7. There is minimal difference in the sealed cases, as expected. The open-ended cases show an initial large increase when one row is inserted, and then the peak begins to asymptomatically approach a final value that would not be far above the four row level. Increasing the number of blade rows did not reduce the on-set time of peak temperature difference.

Since the temperature probes cannot be used to determine the circumferential variation in heat flux for the obstructed cases, the transient lumped capacitance theory can be applied. Following the analysis method outlined in section 8.2.2, initial values

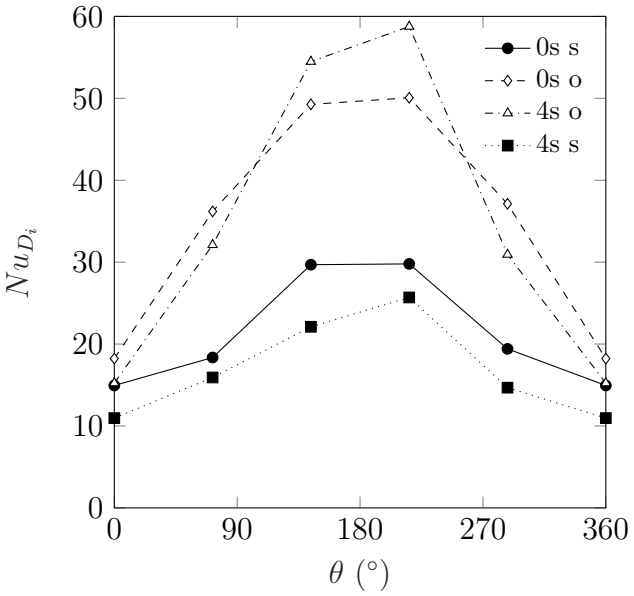

FIGURE 8.10: Inner wall Nusselt number distributions at the start of shutdown for the four test matrix given in table 8.2. Values are calculated using the transient lumped capacitance method.

of $\dot{q}_{i,conv}$ for each of the four tests configurations given in table 8.2 can be calculated. A Nusselt number is then defined using $(T_i - T_\infty)$ as the reference temperature difference. The peak values of heat flux, which occurs at the commencement of cooling (see figure 8.6), are given at each inner metal thermocouple location in figure 8.10. This represents an axially-averaged value for the inner cylinder, at a given θ location. The impact of the blades on the radiation heat flux has been omitted. The additional complexity required to calculate this is not warranted, since the overall temperatures are relatively low and the local value is dominated by the local radial gradient – which is not obstructed by the introduction of the blade rows. Thus, the standard method of calculating the radiation heat transfer given in section 3.5 has been employed.

The distributions are largely consistent with the aforementioned descriptions of the flow field. The bottom T^* curves for the open-ended cases from figure 8.8a show only a very slight increase in the overall heat flux near BDC, but the Nu_{D_i} profiles indicate that the convective heat flux has in fact increased in this region – potentially owing to additional mixing and accelerations of the flow as it navigates through the

blade passages. As the draft air ascends inside the annulus, the direction of the blade passage will either aid or disrupt this motion. Moreover, the left and right sides of the annulus will differ. Referring back to the image shown in figure 8.7, the shape of the side captured is '\/\/', whereas the other side will have a profile of '/\/\'. It is this difference in geometry that leads to the asymmetry in the lower section Nu_{D_i} curves for the 4s cases; unlike the 0s cases that are symmetrical.

Further qualitative understanding of this can be gained from IR camera images of the inner cylinder surface. The outer cylinder needs to be removed in order to capture this data, so a set-up that looks similar to that shown in figure 8.7 is used. Obviously this creates a different flow field to the concentric case but nonetheless, the results show interesting features that are likely to be present in both configurations. Figure 8.11 gives a snapshot of the inner cylinder Rohacell surface from camera angles of $\pm 90°$, when the inner surface is held constant at 100°C. A calculation process similar to the method in Chapter 3 is used to correct for surrounding radiance, but angle effects have not been included. The surroundings and blades have been omitted from the images. Alternating hot and cold streaks between the blade rows are observed – confirming the description of the flow previously stated. The difference in T^* between the streaks is approximately 0.1. A hot streak is formed wherever a '/\' profile is present. The asymmetry of the different sides is also evident.

8.4 Conclusions

An experimental investigation into the impact of installation effects on the natural convective flow field in a gas turbine has led to some key discoveries. The steady state open-ended traverses have highlighted that the induced natural draft amplifies the top-to-bottom difference in inner wall heat flux, which in-turn increases the severity of tΔT^*. The outer wall circumferential distribution of heat flux is also significantly different in the open-ended case. Despite the clear differences in the

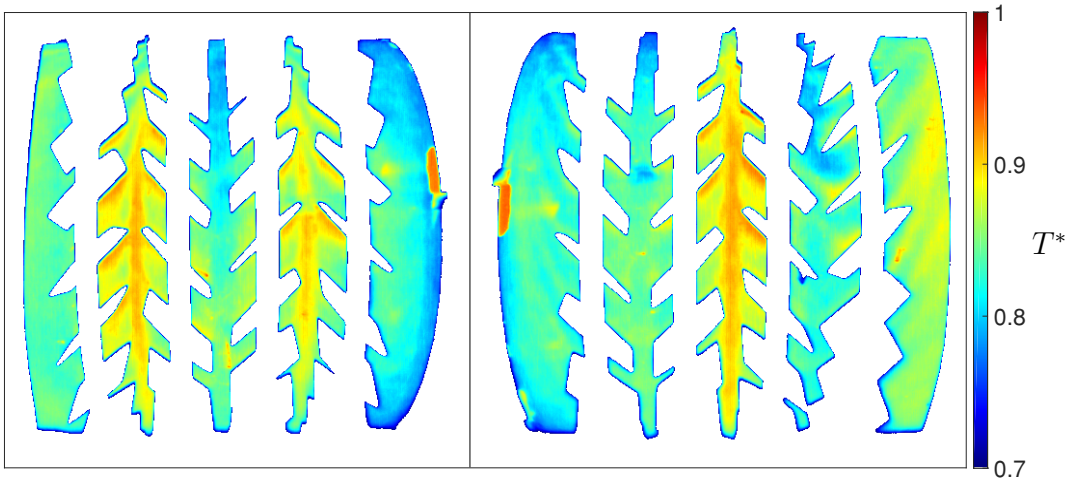

FIGURE 8.11: IR camera measurements at $-90°$ (left) and $90°$ (right) of the inner cylinder in isolation, with four rows of blades. Only the inner cylinder surface is shown. the edge closest to the centre are the front of the inner assembly.

overall flow field, the non-isothermal test conditions studied indicate that again that the local radial temperature difference strongly influences the local heat flux value.

The interaction between axial ventilation and blade rows has been found to be critical in defining the severity of thermal rotor bow. Therefore, it is imperative that this effect is included and captured correctly in order for a prediction method to be accurate. The experimental results here only represent a nominal compressor design; as such, future work should attempt to quantify the influence of axial ventilation on the following parameters: diameter ratio, blade spacing and angle, rising or falling annulus line, and axial depth.

Chapter 9

Shutdown Cooling Model Development

9.1 Introduction

A computational 2D conduction model has been developed by the author in order to simulate the natural convective cooling process of a gas turbine annulus. A finite-difference method is used to solve the governing differential equations. It will first be described, before being validated by the RoBo experimental results. Thereafter, the methodology will be extended to an engine-representative internal geometry.

9.2 Model Definition

A schematic of the model in shown in figure 9.1. The geometry is discretised into quadrilateral elements. By performing a control volume analysis on each element, a summation of the conduction fluxes from each neighbouring node can be balanced against the rate of change of internal energy for a given time step [16]. This methodology was used earlier in Chapter 4 – see equation 4.4 on page 57. In order to numerically compute a solution, boundary conditions are required on four surfaces,

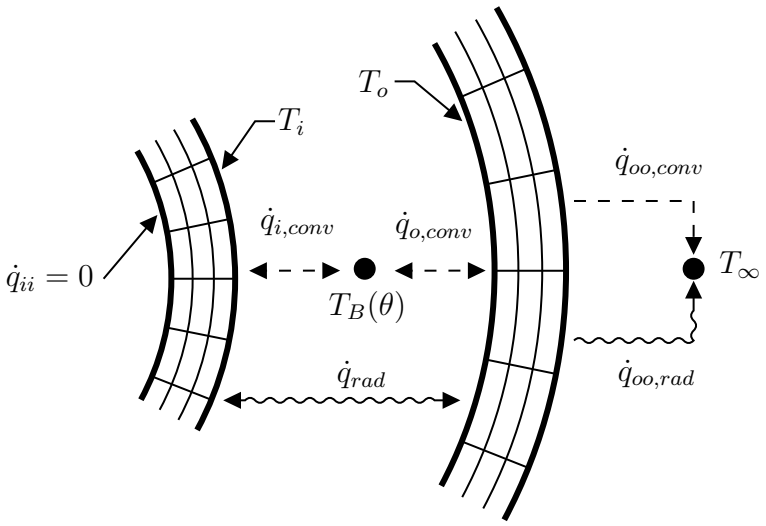

FIGURE 9.1: Schematic of 2D conduction cooling model.

along with an initial temperature distribution. This section describes how the boundary conditions are formulated.

One of the key aspects in the modelling procedure is defining the circumferential annulus air distribution and in-turn the local heat flux distributions on both the inner and outer annulus walls. The results of Chapters 6 and 8 have verified that the local radial temperature difference strongly influences the local convective heat flux, and in addition, previously published semi-empirical correlations for isothermal test cases can be applied to non-isothermal conditions for low diameter ratios. The modelling procedure begins by taking the temperature values of the inner and outer wall at a particular θ location and applies the widely used correlation of Kuehn & Goldstein [57] for natural convection between concentric cylinders (details in Appendix A). Not only is this correlation regarded as highly accurate over a large range of Rayleigh numbers [102], the calculation procedure outputs a bulk fluid temperature (T_B), which is very beneficial for the calculate procedure of this model – this point will be expanded upon later.

This correlation provides the average heat transfer coefficient for the inner and outer surfaces, however a method needed to be devised that relates these values to the local value for a given angular position. The local equivalent conductivity plots

from Chapter 6 (see figure 6.10 on page 91 for an example) indicate that the general shape on the heat flux collapses to a single curve, independent of the circumferential variation in temperature. This model assumed that k_{eq} is constant between TDC and 45°, varies linearly between 45° and 135°, and is again constant between 135° and BDC – a shape that represents the multi-cellular flow regime particularly well. This is applied to both the inner and outer surfaces. The ratio between the lower and upper constant sections is defined as follows:

$$\Phi = \frac{k_{eq,BDC}}{k_{eq,TDC}} \tag{9.1}$$

Knowing the required value of the average equivalent conductivity from Kuehn & Goldstein's correlation, the local distribution can now be determined by choosing a value of Φ. Thus, the circumferential distribution of k_{eq} on a surface can be determined by choosing only one variable. The optimum values of Φ for this model, for both the inner and outer surfaces, were tuned to best capture the behaviour of the unobstructed, sealed transient cooling experimental test, starting at $Ra_{D_i} = 6.3 \times 10^7$. A value of $\Phi_i = 2.1$ was found to best capture the severity and onset time of peak top-to-bottom temperature difference. This value is higher than the ratio observed in the steady-state k_{eq} curves: ~ 1.4; recall that the lumped capacitance calculation for this test also showed a ratio higher than the corresponding steady-state measurements. The reason for this discrepancy may be the simplified representation of the inner geometry in this model: end conduction, insulation and Rohacell are not included. The optimum ratio for the outer equivalent conductivity (defined in the same way) was found to be $\Phi = 0.05$.

The correlation is computed at each θ position, using the local radial values of wall temperature. The modelled local distribution of k_{eq} and bulk fluid temperature T_B can then be used to calculate the circumferential convective heat flux. Figure 9.2a shows the steady state heat flux distributions for the $Ra_{D_i} = 6.3 \times 10^7$ case with

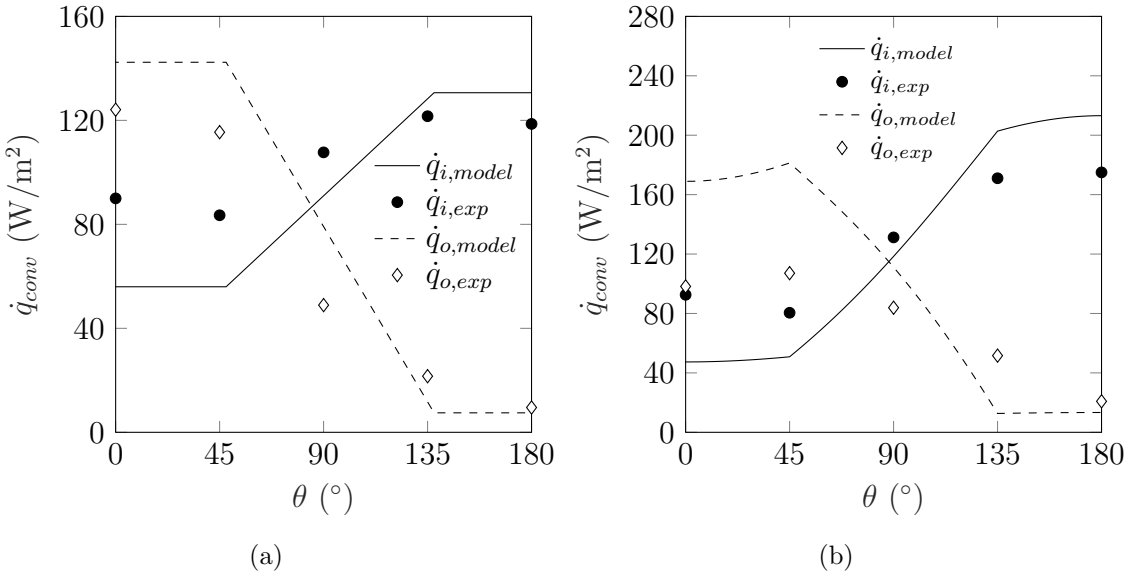

(a) (b)

FIGURE 9.2: **a:** Modelled convective heat flux distributions and the experimental values for $Ra_{D_i} = 6.3 \times 10^7$ with isothermal walls. **b:** Modelled inner wall convective heat flux distributions and the experimental values for $Ra_{D_i} = 6.3 \times 10^7$ at 0° and $\Delta T_{c,o} = 20$ °C

isothermal walls and $Dr = 1.25$. Figure 9.2b shows the local heat flux when the inner wall is isothermal, but there is a ΔT_c on the outer wall of 20°C (see case G in table 6.2 on page 82). The modelling method does capture the correct trend for non-isothermal test conditions. While the modelled values of Φ are higher than the steady-state measurements, they remain constant across all modelling conditions, which does mimic the experimental k_{eq} curves. This will allow for a fair comparison between all modelled cases.

Along with convective heat fluxes for both walls, the Kuehn & Goldstein correlation method also outputs a circumferential distribution of the bulk fluid temperature: $T_B(\theta)$. The difference between this and the local wall temperature is used to calculate local heat transfer coefficients. Figure 9.3 shows the averaged correlation value ($\overline{T}_{B,KG}$) versus the average bulk temperature measured in each of the thermal boundary condition study tests ($\overline{T}_{EXP,KG}$). All experimental points lie within ±1% of the KG predicted values.

The effect of ventilation and obstructions may be included by altering this bulk fluid

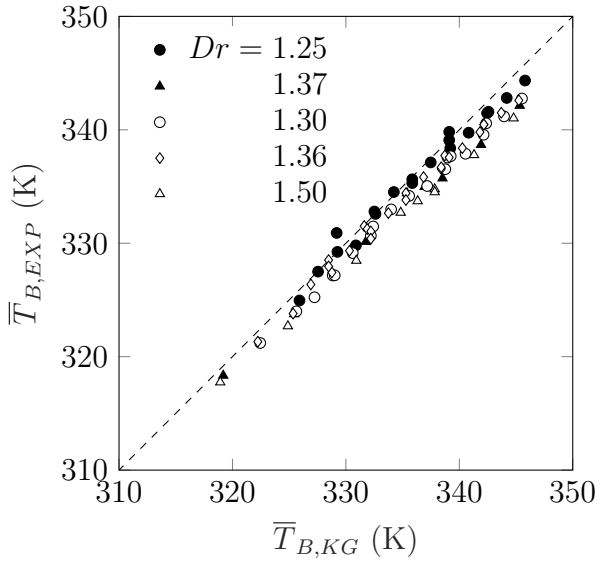

FIGURE 9.3: Bulk fluid temperature predicted by the correlation of Kuehn & Goldstein vs. value measured in the sealed concentric cases. All points lie within ±1%.

temperature circumferential distribution. It is assumed that the value of T_B at TDC remains unchanged from the correlation prediction, and that it reduces linearly to 135° where upon it remains uniform to BDC, the level at BDC is set by equation 9.2. This profile approximates well the mid-annulus air temperature measurements from the ventilation test cases. The effect of this altered T_B distribution will increase the difference between the inner wall heat flux at TDC and BDC respectively – mimicking the response observed in the experimental campaign. The only model input parameter which needs to be chosen is C_{vb}, which relates the T_B value at BDC to the ambient air (T_∞) The bulk fluid temperature at BDC is calculated by:

$$T_{B,\theta=180} = T_{i,\theta=180} - C_{vb}(T_{i,\theta=180} - T_\infty) \tag{9.2}$$

This definition allows $T_{B,\theta=180}$ to vary proportionally with the difference between the inner wall and ambient air during the transient cooling. A value of $C_{vb} = 0.93$ has been chosen as this best captured the cooling behaviour of the ventilated transient experimental test with four rows of blades, starting at $Ra_{D_i} = 6.3 \times 10^7$.

Radiative heat transfer is also modelled in the annulus using the method outlined in section 3.5. The values of emissivity are: $\varepsilon_i = 0.95$, $\varepsilon_o = 0.1$. As the RoBo facility has a layer of Rohacell on the inner surface, a 1D conduction calculation is performed in order to obtain the correct inner surface temperature for the radiation calculation.

Referring back to figure 9.1, a convective boundary condition also needs to be imposed on the outer mesh outer surface: $\dot{q}_{oo,conv}$. As can be seen in the images of the RoBo facility (figure 3.6 on page 35 and figure 8.7 on page 122), there is a thin clear polycarbonate protective cover around the outer cylinder – essentially creating another cylindrical annulus. Thus, the method described above for $\dot{q}_{i,conv}$ is replicated for this annulus. This does mean that the temperature profile of the polycarbonate cover is needed as a model input. It is assumed the cover is at ambient temperature at BDC ($T_{cov,\theta=180} = T_\infty$), increasing with a cosine profile to a maximum at TDC. The value at TDC was again tuned to best match the transient cooling of the sealed experimental cooldown case. An equation very similar to 9.2 is used to calculate the transient value of temperature the polycarbonate cover at TDC:

$$T_{cov,\theta=0} = T_\infty + C_{vb}(T_{o,\theta=0} - T_\infty) \tag{9.3}$$

A C_{vb} value of 0.4 was found to be the best fit. It is worth noting that this boundary condition definition will not be needed for the engine representative model. Radiation is also modelled in this outer annulus with $\varepsilon_{oo} = 0.9$.

The only remaining boundary condition that needs to be applied is a Neumann type condition at the inner surface of the inner mesh: $\dot{q}_{ii} = 0$. The model is run transiently for the required period of cooling time. The heat transfer coefficients are updated at each time step. Figure 9.4 gives a flowchart outlining the modelling process. MATLAB is used for the computations.

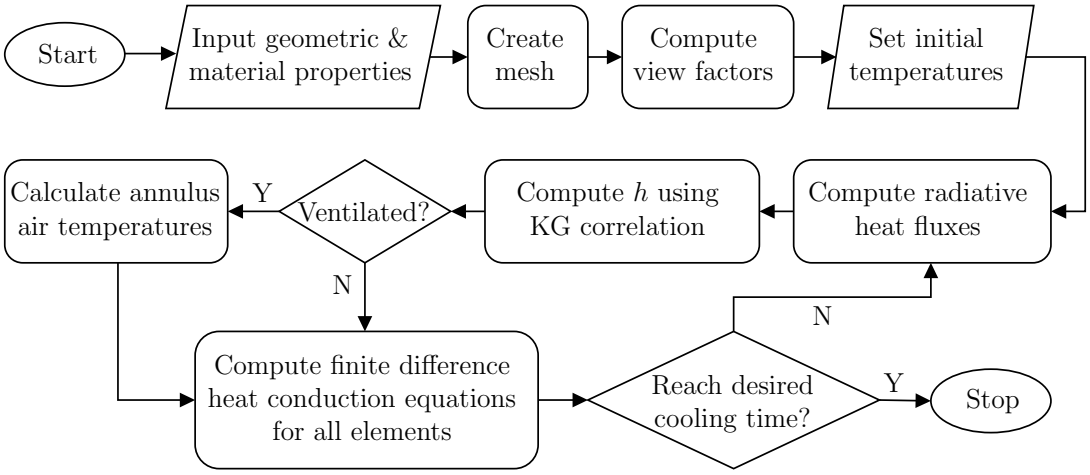

FIGURE 9.4: Flow chart outlining how the transient cooling process is modelled.

9.3 Comparison to RoBo Tests

Firstly, the model is compared to two variants of the RoBo cooldown tests: sealed and open with blade rows installed. Figure 9.5a shows the temperatures at top and bottom for both the inner and outer components during the cooling cycle. The conical section was not modelled. Recall that the thermocouple in the rig is actually at 144°, therefore it is at this value of θ that the comparison is made. The dashed lines in the figure are produced by the model, whereas solid lines are experimental results. There is strong agreement in both the rotor and casing during the initial cooling stage. The model does over-predict the cooling rate in the later stages of the cycle. There are a number of potential causes for this such as: simplified geometry, 2D approximation of the model, end conduction losses, warm air contained in the internal cavity of the RoBo rig. Despite this, the corresponding ΔT^* plot for this case, shown in figure 9.6a, is encouraging as it shows that the model can accurately capture the correct level of top-to-bottom temperature difference and onset time during this transient cooling process.

Figure 9.5b shows the transient temperatures for a ventilated case with four rows of blades. The only parameter which has been altered from the previous case is the annulus bulk fluid temperature: $T_B(\theta)$. Figure 9.6b gives the corresponding

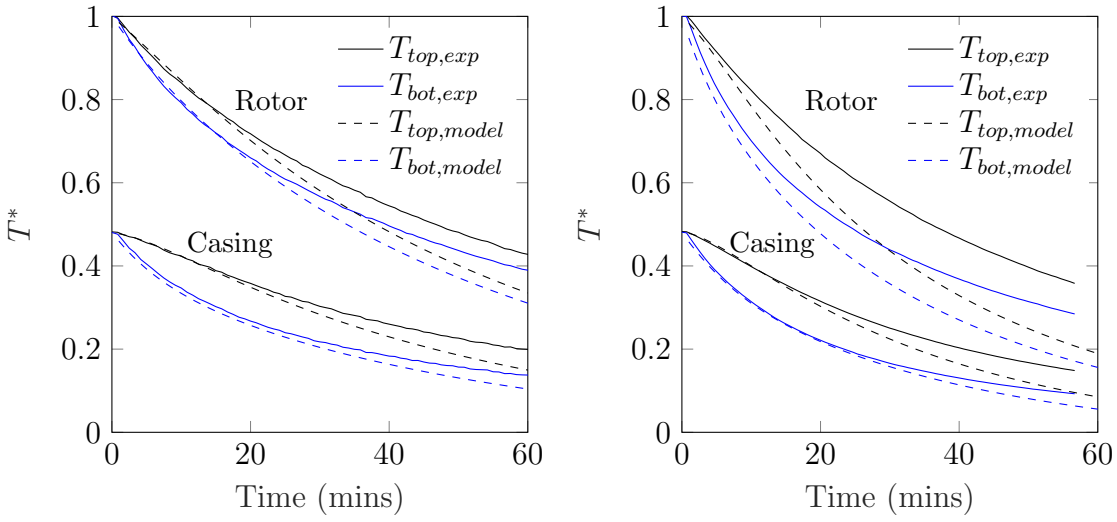

FIGURE 9.5: **a:** Comparison of the temperatures predicted by the model to the experimental result for a sealed annulus with $Ra_{D_i} = 6.3 \times 10^7$ and $Dr = 1.25$. **b:** Comparison to the open-ended experimental case with four rows of blades.

ΔT^* plot. The value of C_{vb} was iterated to provide the best match in peak ΔT^* – accordingly this produced a very good agreement in the casing ΔT^* curves as well. Similarly to the sealed test case, the model does over-predict the overall cooling rate of both components. However, these results, in conjunction with the sealed case, crystallise the finding that the model is capable of accurately predicting the correct levels of asymmetric convective cooling during the shutdown cycle. Furthermore, the vital aspect of modelling the interaction of the ventilation and blade row has been applied successfully and efficiently.

9.4 Extension to Engine

Once the empirical model had been developed to represent the experimental data, the procedure was used to model the shutdown process in a jet engine. Figure 9.7 shows the mesh and cross-sectional area of the geometry used in this more advanced cooling model. This geometry represents a typical of a full scale high-pressure compressor rotor disk. The mesh in composed of $\sim$ 3600 elements. The main

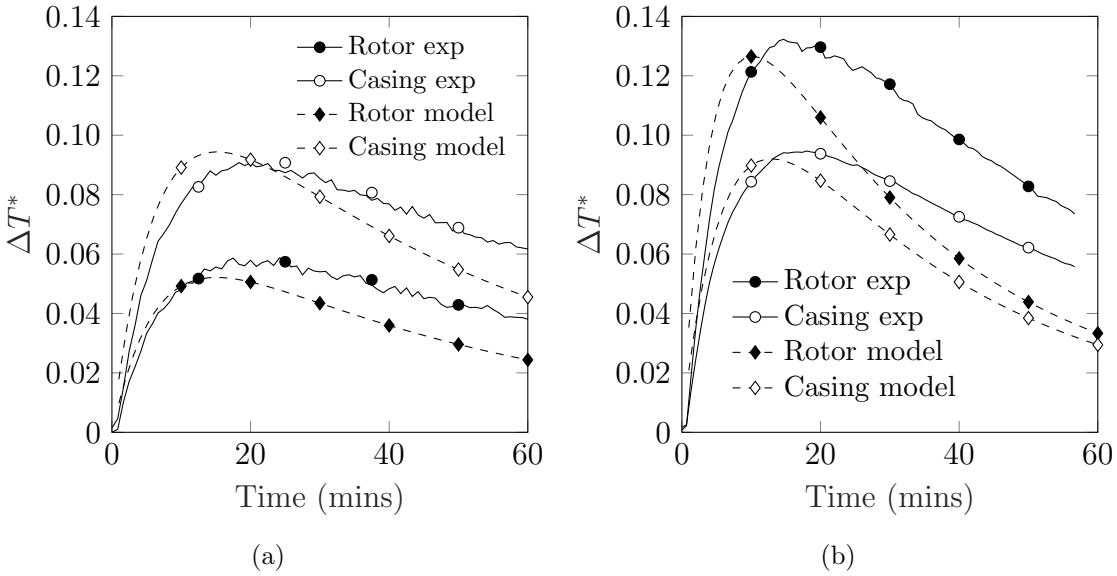

FIGURE 9.6: **a:** Comparison of top-to-bottom temperature difference predicted by the model to the experimental result for a sealed annulus with $Ra_{D_i} = 6.3 \times 10^7$ and $Dr = 1.25$. **b:** Comparison to the open-ended experimental case with four rows of blades.

geometric properties are: $D_i = 532$ mm, $Dr = 1.12$. The explicit finite-difference conduction model requires the volume of each element as an input, therefore the geometry can be made quasi-3D by setting the axial length of each specific element, as shown in the right-hand side sketch in figure 9.7. Material properties used are Inconel 718 [71], which is a common nickel-alloy used in a large civil compressor. The values are assumed to be constant with temperature and are defined as: $\rho = 8200$ kg/m^3, $k = 12$ W/m K and $c_p = 600$ J/kg K. Temperature variations of material properties can be included if desired but they did not affect any of the findings from this work. It is assumed that the deflection of the components can be directly inferred from the top-to-bottom temperature difference.

The main gas path heat flux evaluation procedure remains identical to section 9.2, as does the insulated boundary condition applied to the rotor inner surface nodes. The emissivity of both walls is set constant at a nominal value of 0.5.

The outer casing convection procedure needs to be updated as a clear polycarbonate protective cover is not present in a typical engine. The ExCITE facility experimental

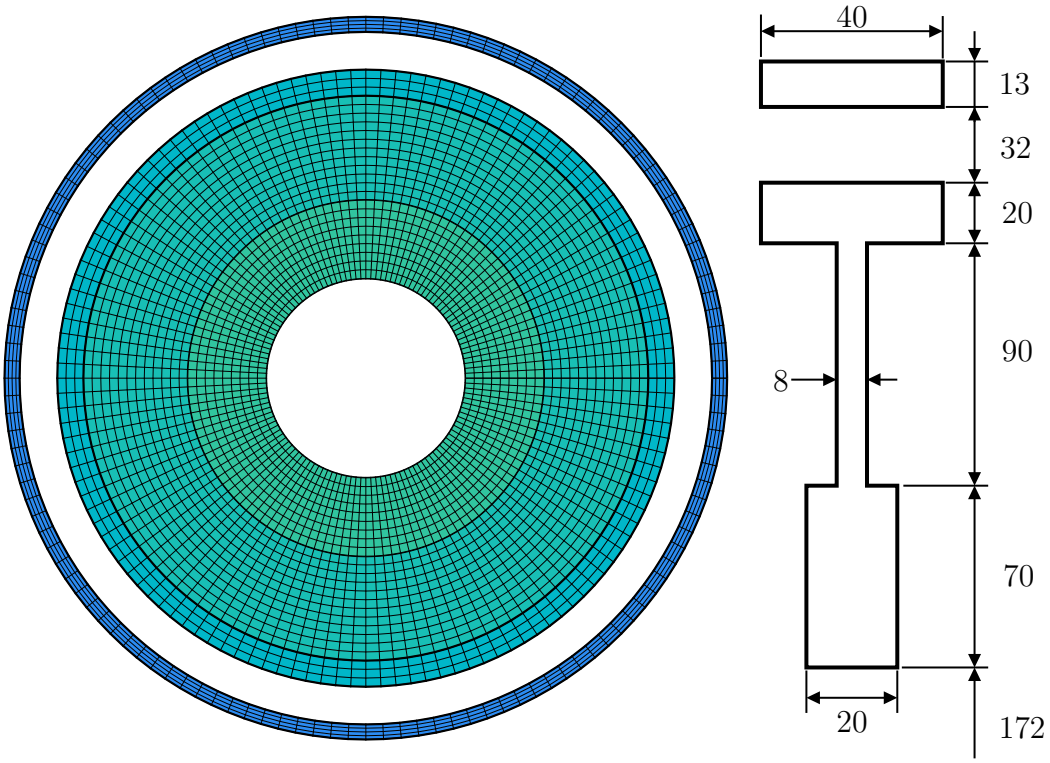

FIGURE 9.7: Schematic of the engine geometry modelled in the shutdown model, representing a typical high-pressure compressor disk. All dimensions are in mm.

results can be leveraged here as the main gas path casing essentially represents the inner surface of the auxiliary zone, which this facility simulates. As this zone is well approximated by concentric cylinders, the Kuehn & Goldstein correlation is again used. A diameter ratio of 2 is applied and the outer cylinder temperature is held constant at ambient. The distribution of the inner surface circumferential heat flux can be updated for this region based on the ExCITE facility results. Two transient cooling tests were completed, starting from $Ra_{Di} = 2.1 \times 10^9$; the lumped capacitance method was then used to find the initial peak values of convective heat flux from each section. The inner assembly was rotated by 22.5° for the second test to provide a more detailed distribution. The results of both tests are shown in figure 9.8, normalised by the area-averaged heat flux and the following fitted equation:

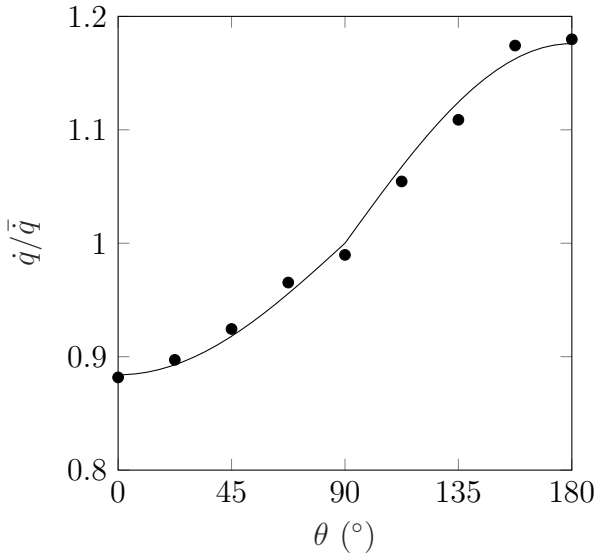

FIGURE 9.8: Modelled distribution of outer casing heat flux and experimental data taken from the ExCITE facility.

$$\dot{q}/\bar{\dot{q}} = \begin{cases} 1 - 0.116\cos\theta & \text{for} \quad 0° \leq \theta \leq 90° \\ 1 - 0.176\cos\theta & \text{for} \quad 90° \leq \theta \leq 180° \end{cases} \tag{9.4}$$

Radiation is also modelled in this auxiliary zone. A separate study was completed with a high number of elements to ensure the results are mesh independent. The procedure outlined in figure 9.4 is now applied to this more complicated geometry for various initial temperature distributions. Since this model does not include any heat transfer from the front and rear disk faces, or conduction from other components in the engine, the magnitudes of the cooling time will likely be longer than a real large civil gas turbine.

9.4.1 Uniform Starting Temperatures

The influence of the initial temperature and its interaction with ventilation is first investigated. This has practical implications as an engine may be run in an idling state (reduced shaft power) for a short period of time prior to shutdown, which will reduce the overall initial temperature. It is assumed that both the casing and rotor have

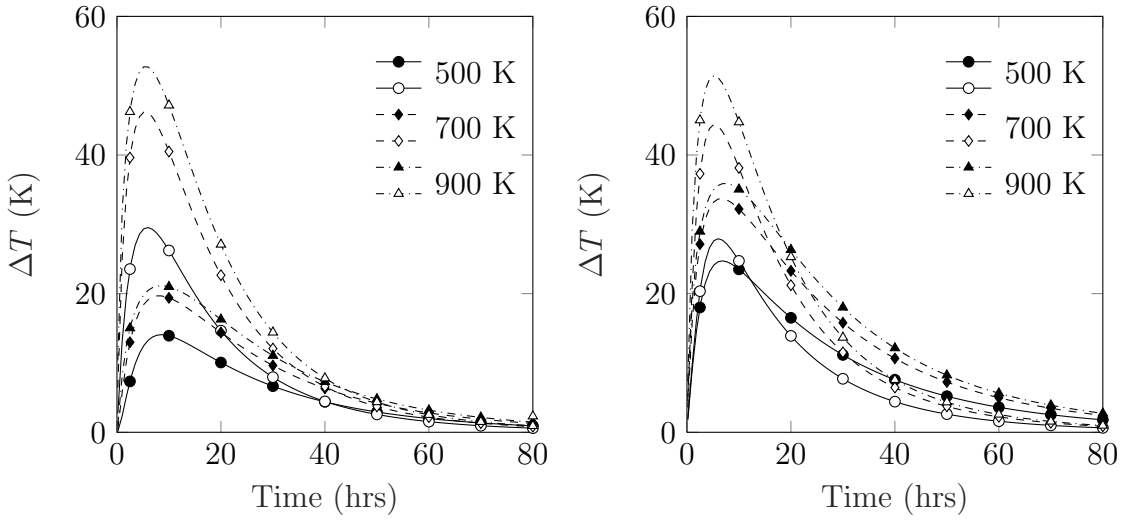

FIGURE 9.9: **a:** Predicted inner surface top-to-bottom temperature difference for different uniform starting temperatures. Black markers do not model ventilation, whereas the cases with white markers includes this effect. **b:** Outer surface top-to-bottom temperature difference for these cases.

the same initial, uniform temperature. Three values will be studied: 900, 700 and 500 K. Figure 9.9a shows the top-to-bottom temperature difference during cooling for the three cases; black markers do not model ventilation, whereas the cases with white markers includes this effect. Figure 9.9b shows the corresponding casing ΔT^* results. The absolute values of temperature are used as non-dimensionalising here obscures one of the key findings. The overall cooling time has increased dramatically from the RoBo cases – owing to the much larger mass of material.

It is evident that ventilation has a strong detrimental effect on the rotor ΔT. Unlike the RoBo experimental cases, the ventilation has also increased the amount of casing ΔT^*; however, the extent of this is not as severe as the rotor bow. Ventilation does tend to marginally expedite the on-set of peak ΔT in both rotor and casing. Similarly to the experimental cases in section 9.3, the peaks in ΔT develop synchronously for a given geometry; ventilation does not alter this finding.

Figure 9.10 shows the transient temperature profiles at top and bottom for the 900 K case, while figure 9.11 shows snapshots of the temperature contours produced by

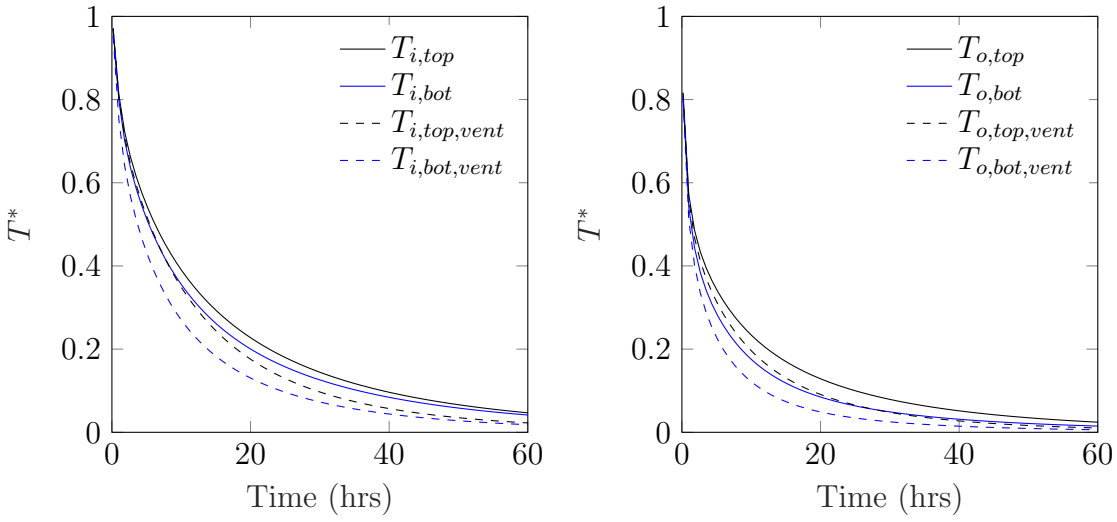

FIGURE 9.10: **a:** Predicted inner surface temperatures for different ventilation conditions, starting from 900 K uniform. **b:** Outer surface temperatures for these cases.

this model for both vented and non-ventilated cases. Initially, the top and bottom curves cool at the same rate; this is due to the radiation heat flux dominating the overall heat transfer at high temperatures. The curves then begin to deviate as the bottom section cools faster, which leads to the peak in ΔT. The casing reaches equilibrium with the air sooner than the rotor due to its lower thermal mass. While the ventilation modelling procedure does not alter the local air temperature at TDC, it causes both the top and bottom sections to cool quicker on both the casing and rotor. While this means that the engine will reach ambient temperature sooner, it does lead to a large increase in the amount of asymmetric cooling.

Further insight into the cooling process can be inferred from examining the convective and radiative heat fluxes separately. The fluxes at TDC and BDC of the rotor are given in figure 9.12a for the sealed case and in figure 9.12b for the ventilated case – both with a 900 K uniform starting temperature. As the casing and rotor temperatures are initially equal, no radiation heat transfer occurs. As the casing begins to cool, a large peak in radiative heat flux quickly develops, due to the high temperatures. The magnitude of the radiation heat transfer in this initial period

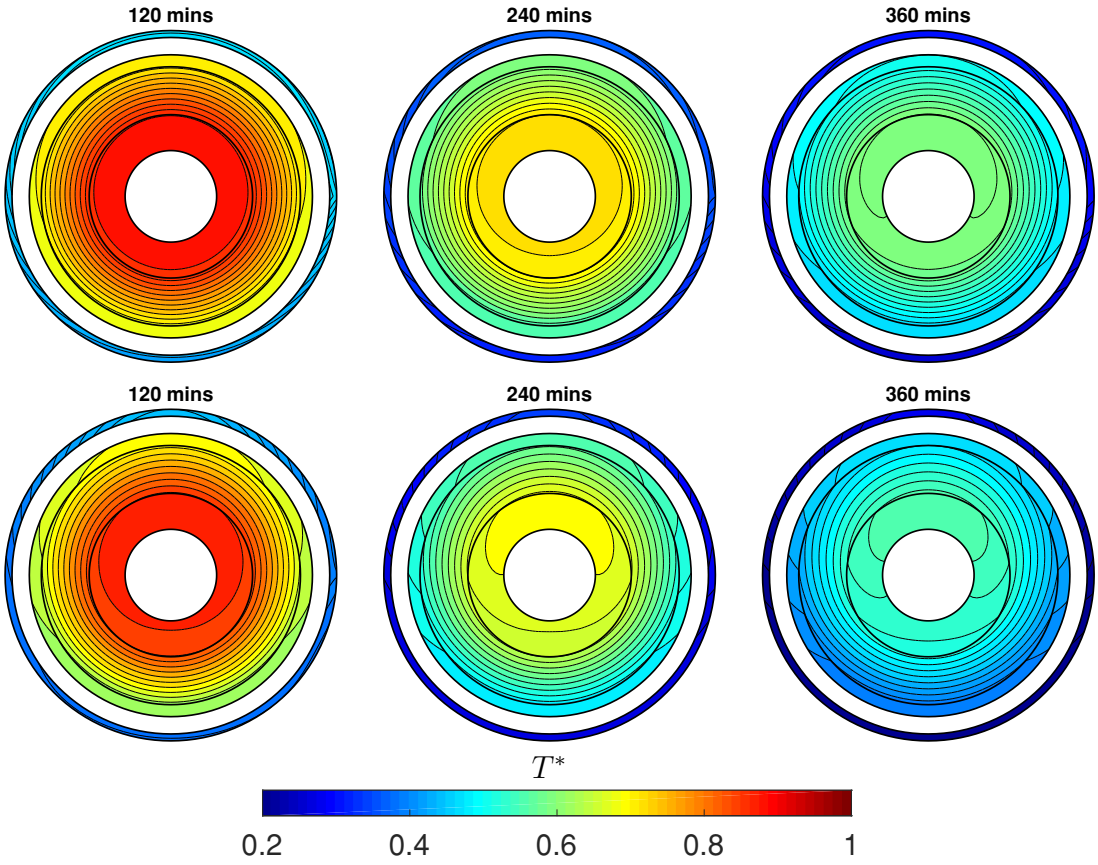

FIGURE 9.11: Simulated temperature contours during cooldown starting from 900 K. *Top:* No ventilation. *Bottom:* with ventilation.

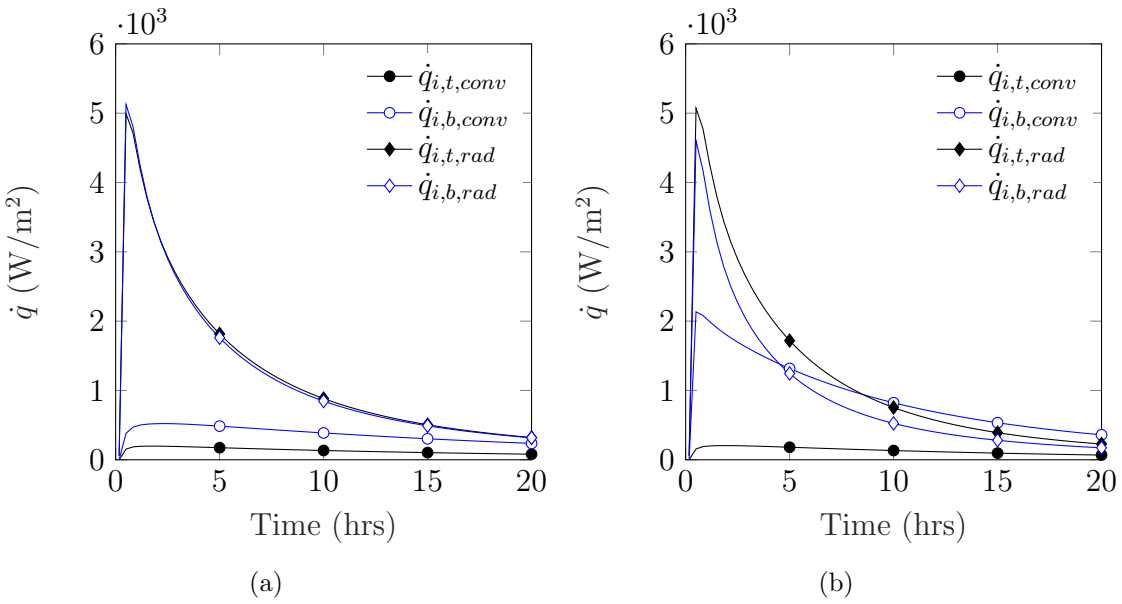

FIGURE 9.12: **a:** Simulated inner surface heat flux during cooling for a non-ventilated case starting at 900 K **b:** Inner surface heat flux for the corresponding ventilated case.

far exceeds the convective cooling for the sealed case. Ventilation at BDC has substantially increased the convective cooling in this area such that it begins to exceed the radiative heat flux as its (radiation) initial peak decays.

Referring back to figure 9.9, a higher initial temperature increases the severity of rotor and casing ΔT but does not change the on-set period. Furthermore, ventilation exacerbates this effect; it caused a 114% increase for the 500 K case and a 150% increase in the 900 K case. The non-dimensional version of this data is shown in figure 9.13. The order of the peaks has now reversed as the lowest starting temperature (500 K) has the largest ΔT^* on both the rotor and casing. This can be explained by examining the Rayleigh number calculated at the start of shutdown. Fluid properties are evaluated at the bulk fluid temperature, which comes from the method of Kuehn & Goldstein; T_∞ is used in the temperature difference. The values of Ra_{D_i} for the 500, 700, and 900 K cases are: 8.8×10^7, 6.5×10^7 and 4.2×10^7 respectively. Thus, they are in reverse order to the starting temperatures. Recall that a similar trend in Ra was observed in the scaling calculations in section 3.1. This scaling analysis showed a peak in Ra occured when the inner surface was at approximately 500 K.

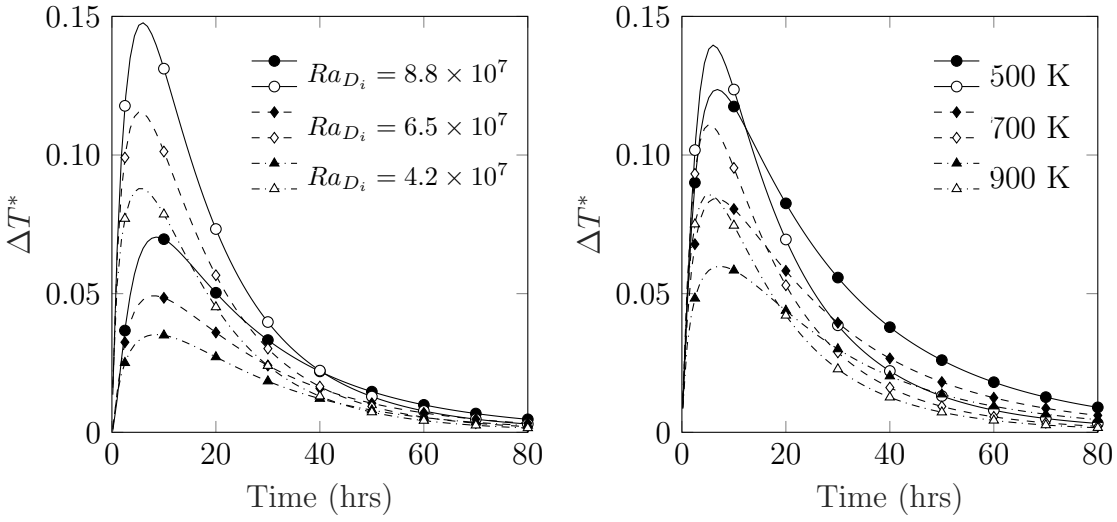

FIGURE 9.13: **a:** Predicted inner surface top-to-bottom temperature difference for different uniform starting temperatures. **b:** Outer surface top-to-bottom temperature difference for these cases.

Ra is now proportional to the magnitude of ΔT^*. It was for this reason that the results were first presented in their dimensional form; from figure 9.13 alone it is hard to decipher that a higher starting temperature directly leads to a larger amount of thermal rotor bow and thus larger deflections.

9.4.2 Non-Uniform Starting Temperature

The simulations in the previous section all had a uniform starting temperature. However, this is not necessarily the case in a real engine as a radial gradient in temperature may be present. The magnitude and direction of any such gradient will no doubt be influenced by the disk geometry, the idling time prior to shutdown and also a disk's relative position in the rotor assembly, amongst many other factors. In order to asses any potential impacts of a radial temperature gradient, some nominal cases are presented here. The geometry and modelling procedure remains unchanged. Ventilation effects are included in all cases. Two main variants are considered: A linear radial inward gradient from 900 K at the surface to 700 K at the central bore; and the reverse of this where the outer surface is at 700 K initially. The initial casing

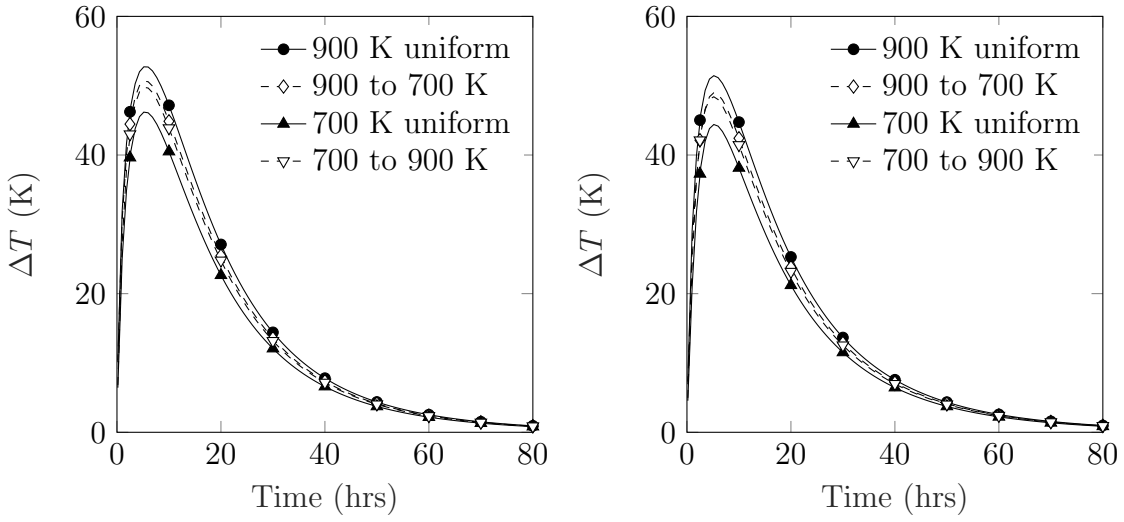

FIGURE 9.14: **a:** Predicted inner surface top-to-bottom temperature difference for different starting temperature distributions. **b:** Outer surface top-to-bottom temperature difference for these cases.

distribution is set to match the disk outer temperature. Figure 9.14 shows the rotor and casing top-to-bottom temperature differences for these cases, along with the uniform 700 and 900 K results from the previous section.

While the initial rotor surface temperature of the non-uniform cases varies by 200 K, both the rotor and casing ΔT curves are near identical. This result was unexpected as the large change in temperature distribution has neither altered the peak, onset time or duration of the bow. This seems to indicate that the magnitude of the peak temperature difference has a stronger correlation to the total amount of heat energy contained in the metal prior to shutdown rather than the initial radial temperature distribution. The uniform case lines also shown in figure 9.14 align with this hypothesis.

In order to gain a further insight into these non-uniform cases, figure 9.15 gives the transient temperatures at TDC and BDC for both the rotor and casing. Black lines are TDC points while blue lines represent BDC points. Temperature contour plots at specific times are also shown in figure 9.16 to give a clearer overall picture of the cooling process. The largest difference between the cases occurs in the first two

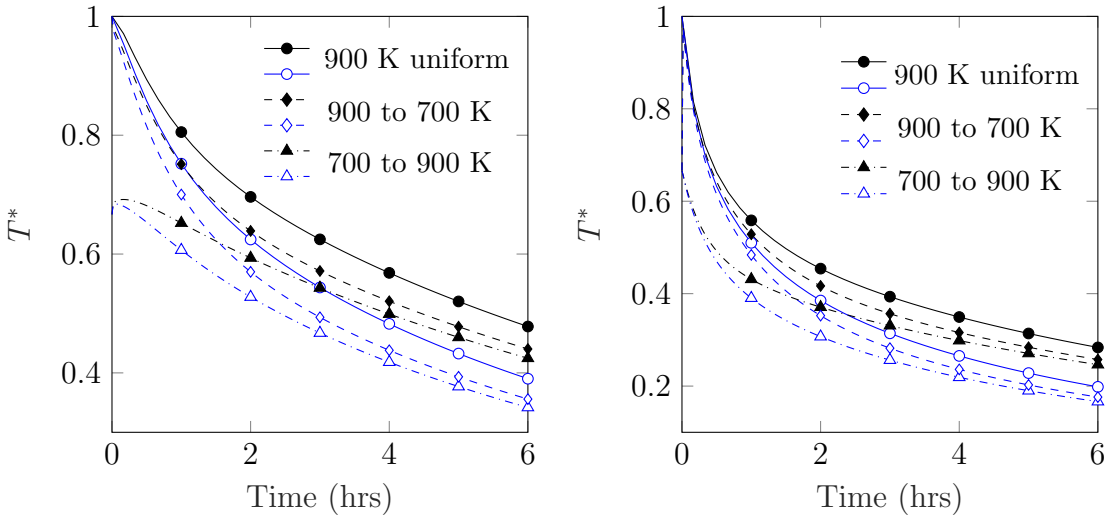

FIGURE 9.15: **a:** Predicted inner surface temperature at TDC (black lines) and BDC (blue lines) for different starting temperature distributions **b:** Outer surface temperatures for these cases.

hours of cooling. When compared to the 900 K uniform cases, the 900 to 700 K case has a steeper slope caused by increased conduction heat transfer to the central bore. A small degree of soak-back is seen at rotor TDC of the 700 to 900 K case, caused by heat conduction from the hotter central bore. Yet despite this disparity in the early stages, the cooling rate of all three cases are matched from roughly four hours onwards. The temperature contours show near identical distributions after ten hours.

9.4.3 Outer Casing Heat Flux Alterations

The casing outer surface in this model is treated as the inner surface of the auxiliary zone. As mentioned in the original problem definition, enhanced heat transfer may be required in this zone to reduce the air temperature during cooldown, in order to protect key engine components in this area. Therefore, the influence of the cooling rate of the outer casing on the rotor bow is now investigated. Recall that the model includes both radiation and natural convection heat transfer from this surface. The effect of the casing radiative heat flux is first examined by altering the emissivity of the outer casing surface: ε_{oo}. The ventilated 900 K uniform starting temperature

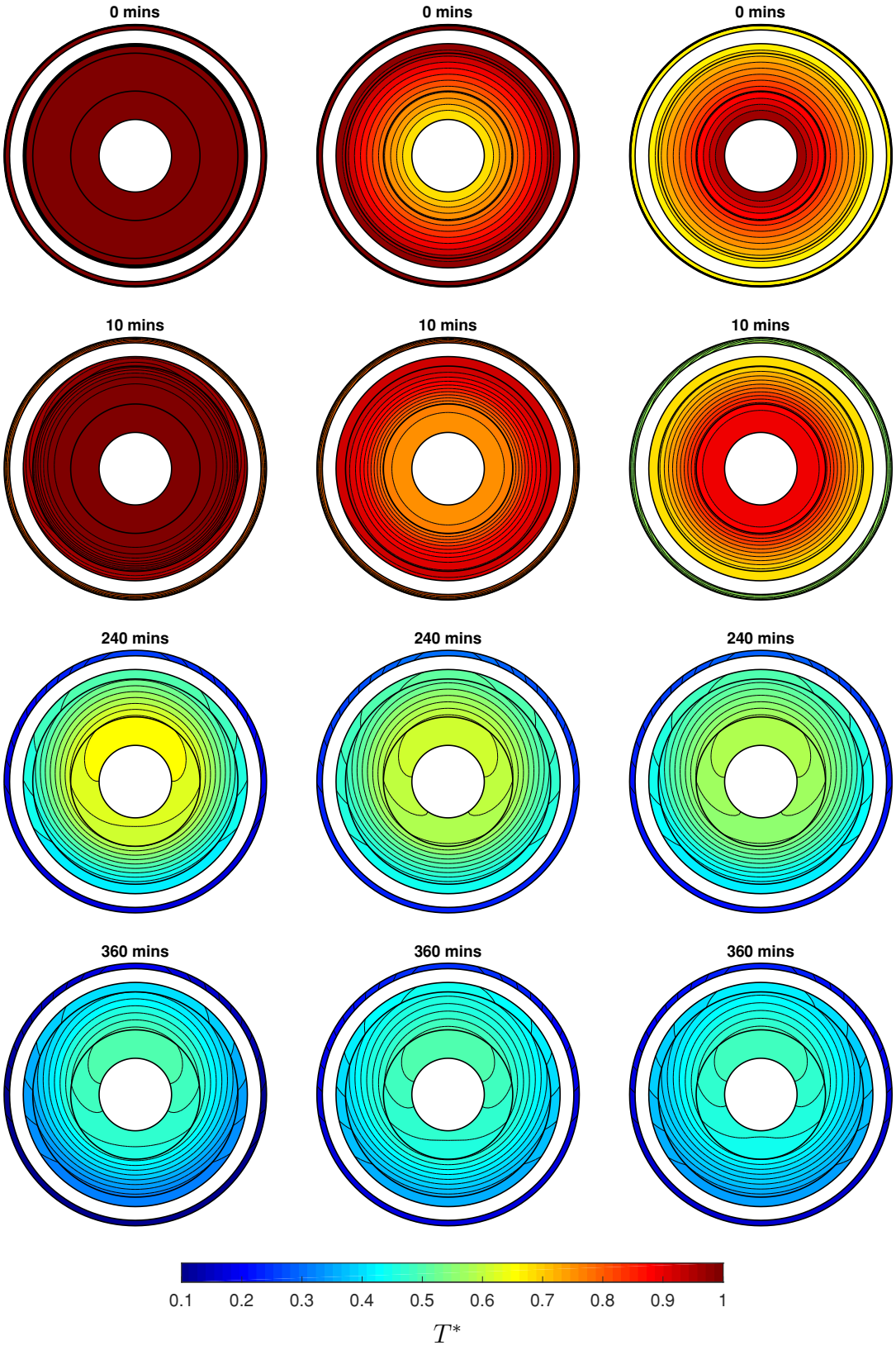

FIGURE 9.16: Temperature contours during shutdown for different starting temperature distributions. *Left:* 900 K uniform. *Middle:* 900 K to 700 K. *Right:* 700 K to 900 K.

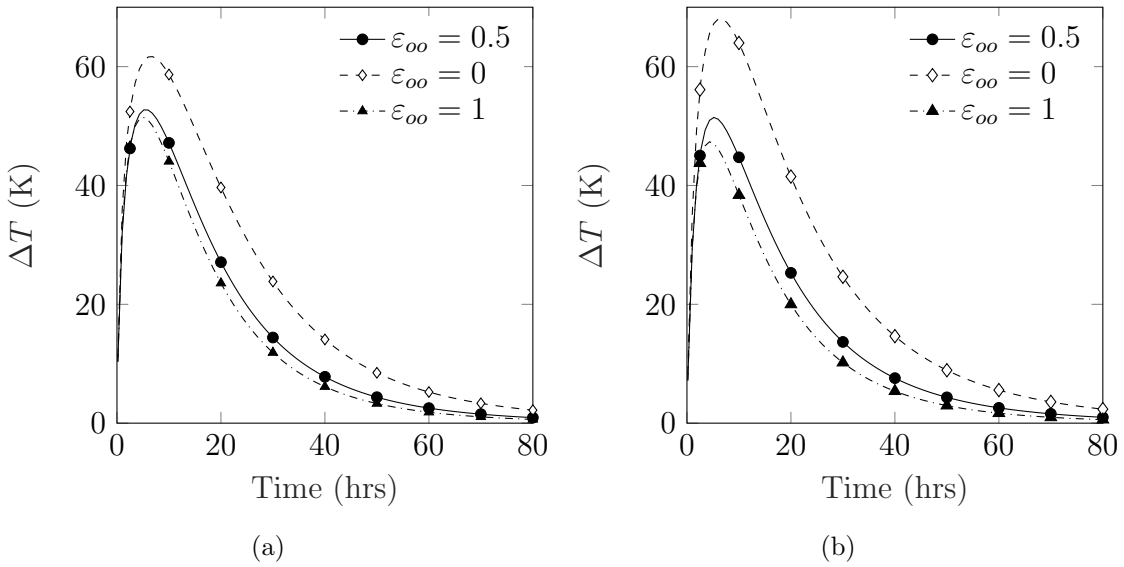

FIGURE 9.17: **a:** Predicted inner surface top-to-bottom temperature difference for different outer casing emissivity's. **b:** Outer surface top-to-bottom temperature difference for these cases.

case is used as a baseline. ε_{oo} values of 0 and 1 are simulated. The value used in the baseline cases was 0.5. The top-to-bottom temperature difference results are shown in figure 9.17.

Reducing the radiative outer casing heat flux to zero has increased both the inner and outer top-to-bottom temperature difference – affecting the outer ΔT more substantially. It also slightly delays the on-set time of peak ΔT. Although a reduced ε_{oo} means that the there is less of a radial temperature gradient in the annulus, and thus a reduced convective heat flux in this region, the outer casing heat transfer is now entirely by natural convection, which is of course strongly asymmetric. The latter effect overpowers the aforementioned reduction in annulus heat transfer. Hence, rotor ΔT can be reduced by increasing the heat transfer uniformly from the outer casing. However, as can be seen from figure 9.18a, the impact is minimal for $\varepsilon_{oo} > 0.5$.

Attempts at enhancing the heat transfer in this auxiliary zone may modify the distribution of the local convective heat flux as well. This effect is now examined by altering the convective heat flux distribution previously shown in figure 9.8. The baseline case has an initial $\dot{q}_{oo}$ ratio between BDC and TDC (Φ_{oo}) of 1.3. Two

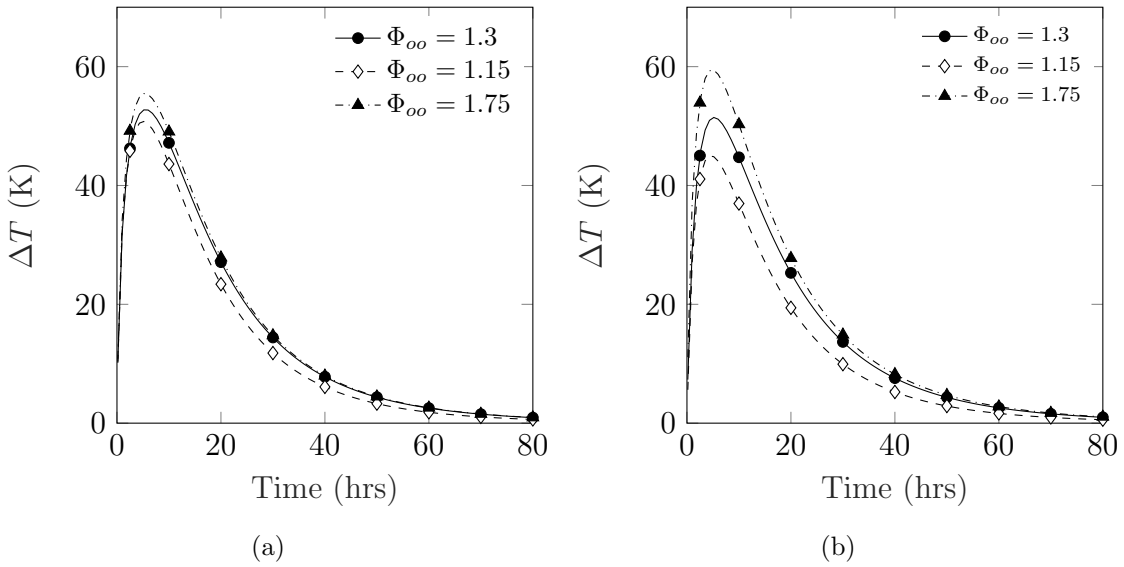

FIGURE 9.18: **a:** Predicted inner surface top-to-bottom temperature difference for different outer casing distributions. **b:** Outer surface top-to-bottom temperature difference for these cases.

further cases with this ratio equal to 1.75 and 1.15 respectively were simulated, again using the ventilated 900 K uniform results as a comparison. Figure 9.18 gives the top-to-bottom temperature difference plots for these cases.

As expected, varying this ratio has had a marked impact on the outer casing ΔT results, where the alteration has been directly applied. However, the difference in rotor ΔT is minimal. Therefore, decreasing the asymmetry of the outer casing natural convective cooling alone is not an effective strategy for reducing rotor top-to-bottom temperature difference.

9.5 Conclusions

Results from both experimental facilities has been exploited to help develop and refine a powerful mathematical model that is capable of simulating the natural convection that occurs in a large civil gas turbine compressor during shutdown cooling. Comparison to experimental results has validated the ability of the model to correctly simulate the severity of rotor top-to-bottom temperature difference observed in the transient cooling cycle. Furthermore, the model allows for the influence of

various design features and temperature distributions to be easily investigated. This is encouraging as an alternative approach to this would involve an extremely computationally expensive and time-consuming conjugate CFD analysis.

It is worth mentioning that this model only simulates a single disk. Therefore, it omits the effects of interaction between various blade rows and the heat conduction that may occur from hotter components in the engine such as the high-pressure turbine. The next logical step in advancing this procedure is thus to extend it to become a multi-component system. Other areas for potential improvements to the prediction method include updating the geometry of the casing and determining whether the insulted boundary condition on the central bore is appropriate.

The importance of the initial temperature distribution has been explored. Running an engine in an idle state prior to shutdown, in order to reduce the total amount of energy contained in the rotor drum, has been shown to be a powerful method of reducing the peak rotor top-to-bottom temperature difference – irrespective of the initial radial temperature gradient. While this technique does suppress the severity of ΔT, it does not alter its on-set time or duration.

Moreover, this study has highlighted the complex interaction of numerous parameters during shutdown cooling. It has been shown that increasing the heat flux from the outer surface of the casing can aid in suppressing rotor ΔT. However, the air distribution in the annulus has proven to be by far the most influential and potentially detrimental contributor in causing the bottom of the rotor to cool faster the top sector. The methodology used to model this phenomenon, namely controlling the bulk fluid temperature profile, has been validated using the experimental results of the RoBo facility. This relatively simple procedure can account for both the induced ventilation caused by having an end of the annulus open to atmosphere, and also the inclusion of compressor blades. The largest uncertainty involved in this modelling procedure remains selecting the appropriate level of this effect that best replicates

the various stages of an engine compressor during shutdown. Whilst the level used for this study was matched to the RoBo experimental cooling cases, and an engine stage may experience a level above or below this, it can be said with certainty that this induced ventilation and its interaction with the blade stages has an adverse effect on rotor thermal bow.

Chapter 10

Rotor Bow Mitigation Strategies

10.1 Introduction

This chapter explores the viability of mitigation strategies designed to suppress rotor bow. The majority of the work focused on two contrasting approaches for alleviating bow: forced air flow cooling, and altering the radiation heat transfer. The methods were examined both numerically and experimentally.

10.2 Forced Air Flow

Previously presented results have shown that the warm air in the upper section of the annulus inhibits the convective heat flux in this region. This issue is then compounded by the introduction of blades as it further suppresses the ability of the warmer air to exit the annulus, more so than it impedes cold air entering in the lower section. Therefore, a potential rotor bow mitigation strategy is to force colder air into this region. This would create a larger temperature difference between the metal and air and thus there is more potential to increase the convective heat flux. Forcing air into the annulus in this manner will also introduce a jet impingement type cooling effect on the rotor. In practical terms, there may be scope to incorporate this into a

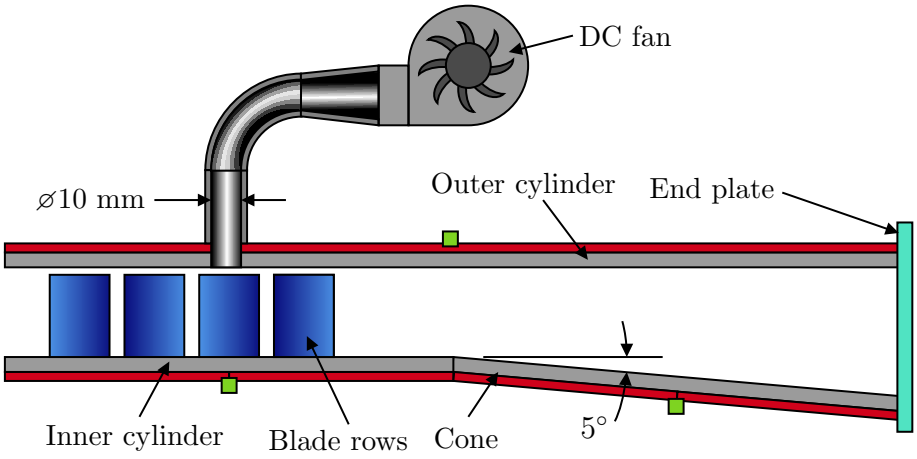

FIGURE 10.1: Schematic of the RoBo facility with a DC fan feeding air into annulus at top-dead-centre.

civil gas turbine through the secondary air system bleed pipes from the high-pressure compressor.

10.2.1 Experimental Results

The RoBo facility has been modified in order to explore the viability of this mitigation strategy. Figure 10.1 gives a schematic highlighting the modification that has been made. The outlet of a DC powered centrifugal fan is ducted through a short section of 10 mm inner diameter tube before entering the annulus at top-dead-centre. The fan used is a 12 V SanAce B97. It is capable of providing maximum air flow rate of 1.85 m^3/min and a maximum static pressure rise of 1950 Pa [92] . A variable DC bench-top power supply is used so the input power can be recorded. The exit velocity was measured using an air velocity meter that has an accuracy of ±3% [108]. The probe was placed at the jet inlet following a transient test; the velocity reading was averaged over a 60 second monitoring period. It was assumed that the jet inlet temperature was ambient.

All test cases were completed with four rows of blades installed (see figure 8.7 on page 122) and the cylinder side end plate removed. The diameter ratio was 1.25. The inner assembly is heated to a steady-state temperature of 100°C while the outer

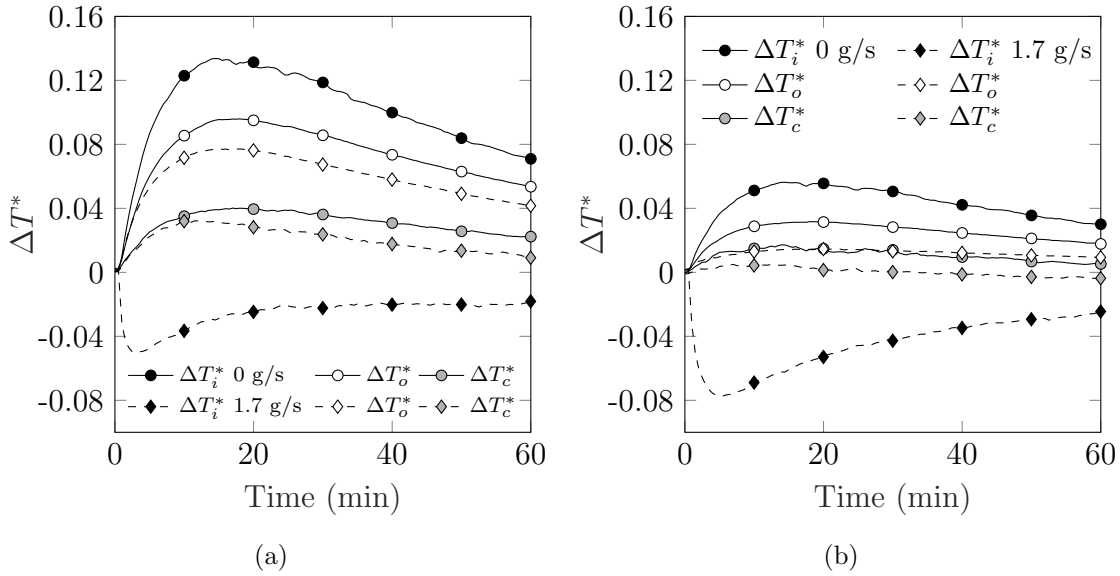

FIGURE 10.2: **a:** Top-to-bottom temperature differences during cooling for forced air flow (dashed lines) at $Re_j = 13,600$, and the baseline case (solid lines). *i:* inner cylinder, *o:* outer cylinder, *c:* inner cone. **b:** Corresponding top-to-side temperature differences.

cylinder is heated to 60°C; this equates to $Ra_{D_i} = 6.3 \times 10^7$. The same experimental procedure as outlined in section 8.2.2 is used, with the additional step of turning on the DC fan at the commencement of the cooling stage.

The first experimental test case examined had an inlet mass flow rate of 1.72 g/s, which equates to $V_J = 17.7$ m/s and $Re_J = 13,600$; the formula $\dot{m} = \rho A_j V_j$ was used to calculate the mass flow rate. This electrical power consumed by the fan was 37.5 W. Figure 10.2a gives the top-to-bottom temperature difference during the cooldown period for this test case (dashed lines) along with the baseline case (solid lines) that has no forced airflow. Recall that the bottom thermocouples on the inner assembly are located at 144°, whereas is it at 180° on the outer cylinder. The conical section (subscript c) results are also included. Figure 10.2b shows the temperature difference between the top and a thermocouple of the side, which is located at 72° on the inner assembly and 60° on the outer cylinder.

The induced air has made a substantial impact in suppressing the inner cylindrical section top-to-bottom temperature difference. This mass flow has even reversed

the effect fully as the top section now cools faster than the bottom section. The observed temperature difference between 0° and 72° is now larger than the 0° to 144° temperature difference. This observation in consistent with jet impingement cooling, as typically the heat transfer distribution for this is strongest close to the origin of the jet and weakens with distance away from this point. The impingement heat transfer rate is highest in the initial cooling stage as this is where the largest wall-to-air temperature difference occurs – leading to a sharp decrease in ΔT^* initially. This effect then begins to diminish as the rotor cools down. Curiously, the general shape of the outer cylinder ΔT^* has not been altered. There are two possible reasons for this: the outer cylinder cooling is driven by the air outside on the annulus; the enhanced cooling of the inner section is predominately due to the impingement effect of the incoming air rather than the presence of cooler air in the upper section, and thus does not have a large influence of the outer cylinder at TDC. The inner cone section lines remain largely similar to the baseline case, which indicates that the induced airflow effect remains localised to the vicinity of the injection point and has not mitigated downstream axially.

The constituent thermocouple signals used in these temperature difference results are given in figure 10.3. As expected, the induced air has caused $T^*_{i,t}$ to cool much faster than the baseline case. The effect is strongest at the commencement of cooldown, which causes the steep negative gradient in ΔT^* seen previously. The strength of this effect then diminishes over time. Both the top and bottom inner cylinder curves now show similar cooling rates. The $T^*_{o,t}$ curve does cool somewhat quicker, owing to the reduced annulus air temperature, but the influence is minimal. It is evident that this new cooling arrangement has not altered the cooling of either the inner or outer cylinder at the bottom of the annulus.

The mass flow rate is now varied in order to gain a better understanding of this mitigation strategy. Figure 10.4a gives the inner cylinder top-to-bottom temperature difference for different mass flows; figure 10.4b gives the corresponding outer cylinder

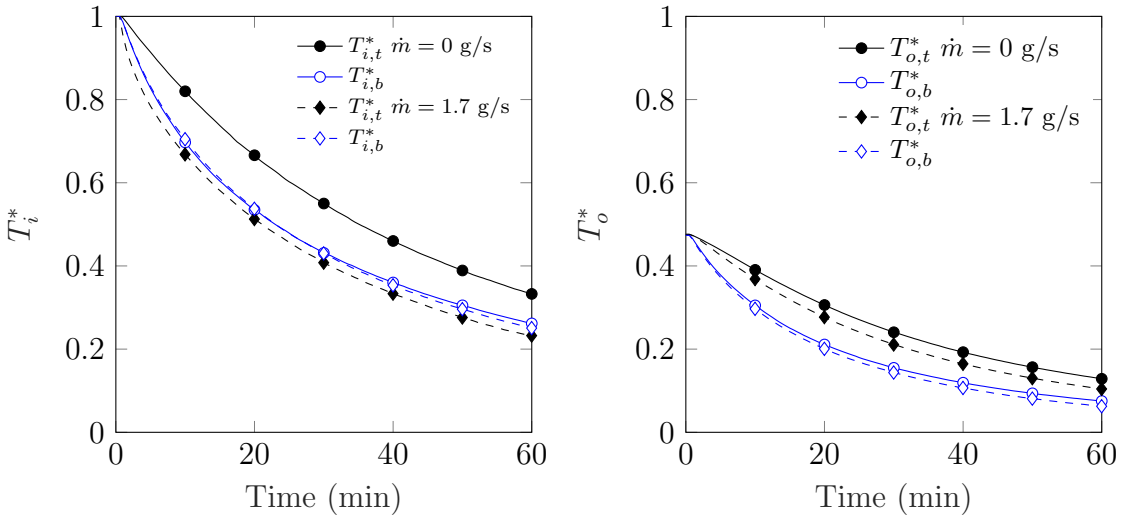

FIGURE 10.3: **a:** Inner cylinder T^* during cooling for forced air flow at $Re_j = 13,600$. **b:** Corresponding outer cylinder temperatures.

ΔT^*. Similar trends in T^* to the 1.72 g/s case are observed. The initial decrease in rotor ΔT^* is proportional to the mass flow rate. Again, this is consistent with jet impingement cooling. There is a near linear reduction in peak inner cylinder ΔT^* with increasing mass flow. There is a slight reduction in outer cylinder ΔT^* with increasing mass flow; however, the magnitude of this is minimal and in no case does it approach a negative value. It is worth noting here that the axial length of the outer cylinder is twice that of the inner cylinder.

The induced air flow has altered the overall rotor cooldown characteristic such that initially there is a negative peak in ΔT^* (when the jet impingement cooling at TDC is strongest). Following this, either a positive peak ΔT^* develops for lower flow rates, or a positive value does not occur at all – for higher flow rates. Figure 10.5 gives the magnitudes for both the negative (white dots) and positive (solid dots) peaks in ΔT^* observed in the different experimental cases. The Reynolds number of the jet is used as the abscissa. A linear best-fit line is added to each data set. The intersection of the solid lines indicates that there is an optimum value of the jet Reynolds number that minimises rotor bow – at a value $\sim 75\%$ lower than the baseline case. For this particular experimental setup, this equated to approximately 10 m/s ($Re_J = 8000$),

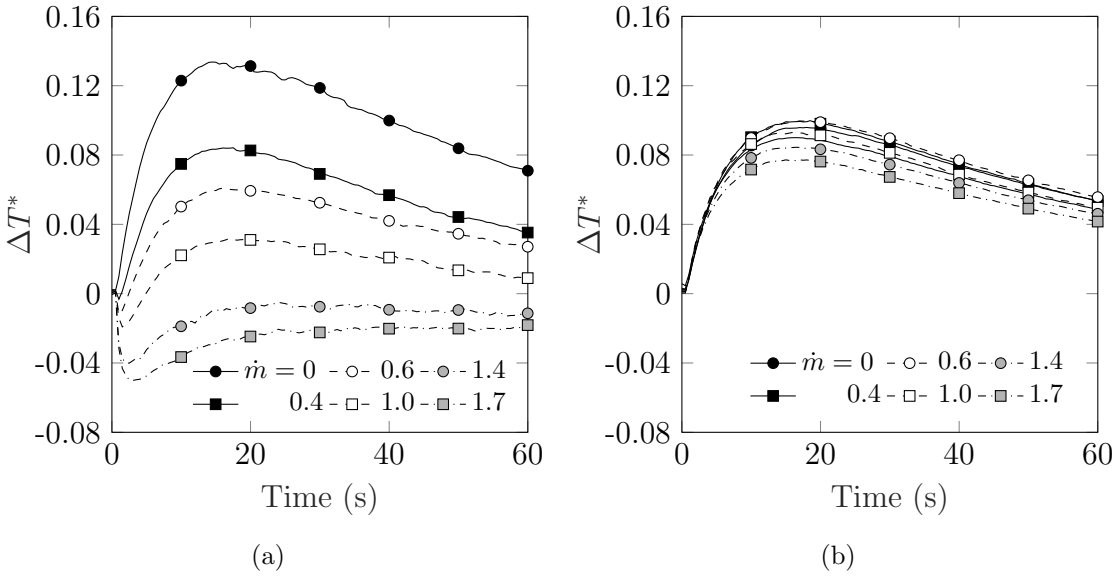

FIGURE 10.4: **a:** Inner cylinder top-to-bottom temperature difference during cooling for forced air flow at various mass flow rates. **b:** Corresponding outer cylinder top-to-bottom temperature difference.

which required an electrical input of just 3 W. This value of Reynolds number will undoubtedly depend on the diameter ratio and axial ventilation. However, this result indicates that this is indeed a viable mitigation strategy that warrants further investigation.

10.2.2 Numerical Model

10.2.2.1 Jet Impingement Shutdown Model Modification

Forcing air into the annulus will undoubtedly lead to 3D flow patterns, which may mean the 2D numerical model previously developed in Chapter 9 could struggle to capture this behaviour. However, the trends observed from the experimental cases have highlighted a potential pathway for including this effect. Recall that one of the key modelling procedures is determining the circumferential annulus air temperature distribution ($T_B(\theta)$). The value at TDC is used to calculate the heat flux for both the rotor and casing. The local heat transfer coefficient at this location is typically comparable on both components. Therefore, reducing this value (in a similar vein to how axial ventilation is included) would not correctly capture the cooling curves as it

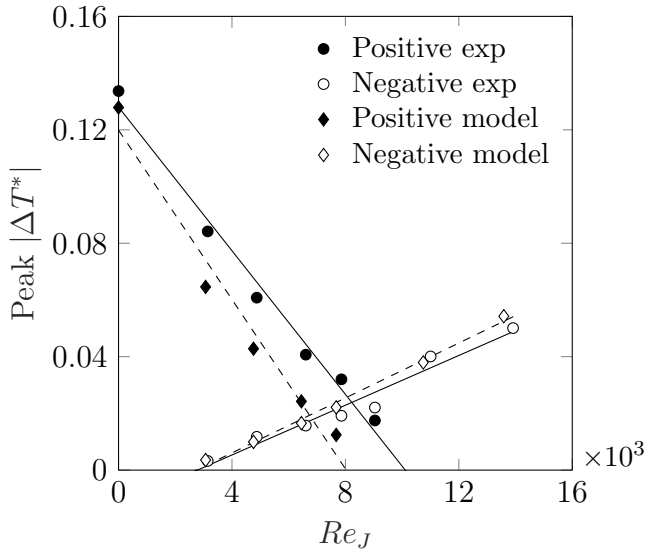

FIGURE 10.5: Absolute value of peak rotor ΔT^* vs. jet Reynolds numbers for the cooling cycle of the RoBo rig at $Dr = 1.25$ and starting $Ra_{D_i} = 6.3 \times 10^7$, with axial ventilation and four blade rows. Solid lines are the linear best-fit of the experimental cases, dashed lines are the linear best-fit of the numerical model cases.

would cause a sharp increase in casing heat flux at this point – which did not happen in the experiments. An alternative approach is to apply an additional heat flux boundary condition on the rotor surface using a correlation for jet impingement heat transfer. Theses correlations are typically provided for an axisymmetric jet directed at an isothermal flat plate. Examining the expected range requirements, Zuckerman and Lior [117] recommend the correlation provided by Wen and Jang [112] for the area-averaged Nusselt number for increasing distance from the stagnation point:

$$\overline{Nu} = 0.116 Re_J^{0.696} Pr^{1/3} (H/D)^{-0.20} (r/D)^{-0.41} \tag{10.1}$$

for $3 \leq H/D \leq 16$, $0 \leq r/D \leq 7.14$, $750 \leq Re \leq 27,000$; where H is the distance between the jet and target, D is the jet diameter and r is the radial distance from the stagnation point. The local Nusselt number can then be determined from the following equation:

$$\overline{Nu} = \frac{2}{r^2} \int_0^r r \cdot Nu \, \mathrm{d}r \tag{10.2}$$

The adiabatic wall temperature is used as the reference temperature in the Nusselt number definition for jet impingement:

$$Nu = \frac{\dot{q} D_J}{k(T_w - T_{aw})} \tag{10.3}$$

This definition means that the correlation is independent of the relative magnitude of the jet and ambient temperatures. The method of Goldstein *et al.* [38] is followed to calculate this temperature. Firstly, effectiveness is defined as:

$$\eta = \frac{T_{aw} - T_r}{T_J^0 - T_f} \tag{10.4}$$

where T_r is the recovery temperature, T_J^0 is the jet total temperature and T_f is the air temperature. T_r is the adiabatic wall temperature when $T_J^0 = T_f$; as the velocities being examined are low, T_r can be calculated as:

$$T_r = T_\infty + \frac{V_J^2}{2c_p} \tag{10.5}$$

Goldstein *et al.* [38] then give the following correlations for effectiveness:

$$\eta = \begin{cases} 0.35 + 0.6e^{-0.01(H/D-2)^{2.2} - 0.1(r/D)^{2.5}} & \text{for} \quad 0 \leq r/D \leq 3.5 \\ 1.193(r/D)^{-0.98} & \text{for} \quad r/D \geq 3.5 \end{cases} \tag{10.6}$$

Thus, eqs. (10.4) to (10.6) can be used to calculate the adiabatic wall temperature. The Nusselt number distribution is averaged in the axial direction since the model is 2D. The mean value of the rotor and casing metal temperatures at 45° was used as T_f

– the value at TDC (based on the metal average) was not used as the impingement flow will likely lead to a localised cool spot on the rotor surface, thus a radial average at this location may not be representative of the bulk air in that region.

This cold spot also necessitates a change to the annulus air circumferential temperature (T_B) distribution that is used to define the natural convective heat flux. In previous simulations, it was modelled as a linear reduction from 0° to 135°. This has been altered such that T_B is assumed constant (as defined in the previous paragraph) from 0° to 45° before reducing linearly to 135°. The value for the upper constant section is taken at the 45° point from the Kuehn & Goldstein correlation calculation.

10.2.2.2 Model Validation

The $Re_J = 13,600$ experimental case from the previous section is used to tune the model input parameters; specifically, the circumferential distance over which the additional impingement heat transfer is imposed was varied so that the magnitude of the peak top-to-bottom negative ΔT^* was matched closely. This approach may be suitable as it is expected that the obstruction caused by the blades may inhibit the impingement effect from propagating circumferentially. The optimum application distance was found to be approximately one blade spacing.

Figure 10.6a shows a comparison of the experimental and calculated ΔT^* for this test case. While the magnitude of $\Delta T^*_{TB,i}$ was tuned, it is very encouraging to see that this has led to an extremely good match at the $\Delta T^*_{TS,i}$ ($T^*_{\theta=0} - T^*_{\theta=72}$) location. The outer cylinder ΔT^* curve is also in good agreement. Encouragingly, this method of modelling the transient impingement heat transfer gives an extremely close match in the overall shape of the rotor cooling curves, which indicates it is correctly capturing the initial strong influence and it's gradual decay as the relative temperature difference between the jet and wall decreases.

Figure 10.6b gives the constituent temperatures of the top and bottom ΔT^* curves.

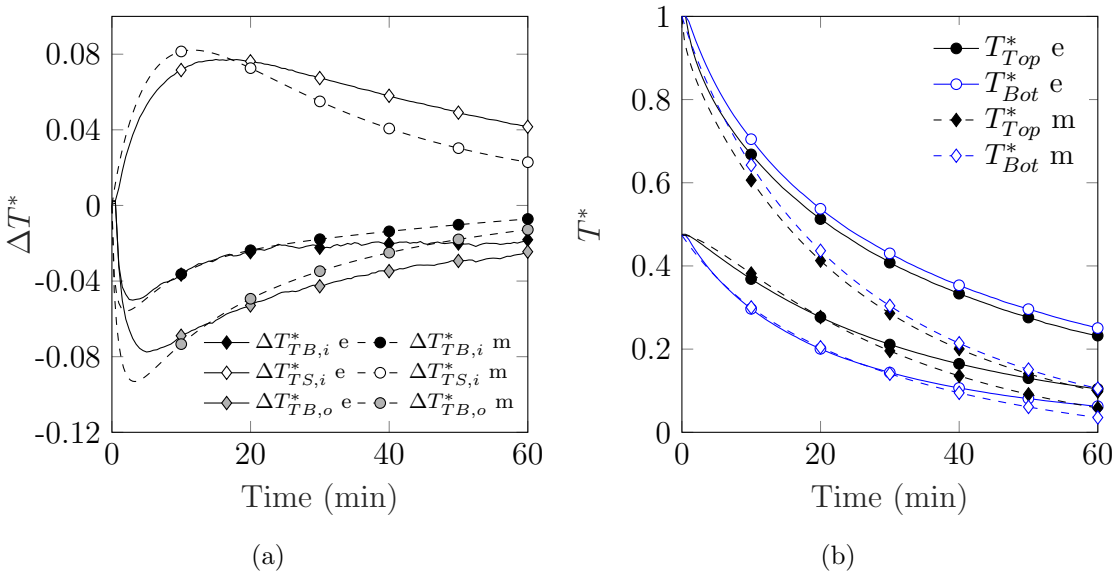

(a) (b)

FIGURE 10.6: **a:** Transient top-to-bottom temperature difference predicted by the model (round markers) compared to the experimental results (diamond markers), with $Re_J = 13,600$. **b:** Constituent temperatures for these curves. The curves that are initially at 1 are the inner cylinder, whereas the lower set of curves are the outer cylinder.

The model does over-predict the cooling rate of the rotor. This issue was also prevalent in the original modelling campaign and may be attributed to the simplification of only modelling the aluminium substrate of the experimental facility. However, this is not a concern as the asymmetric cooling has been captured adequately.

Different jet Reynolds numbers have been simulated and the values of both the positive and negative peak ΔT^* have been included in figure 10.5, which is shown in section 10.2.1. Once again, there is good agreement with the experimental cases, which adds further veracity to the simulation methodology.

10.2.2.3 Engine Conditions

The jet impingement modelling method will now be applied to the compressor stage geometry that has been extensively analysed in Chapter 9. The transient cooling from a 900 K uniform starting temperature distribution was simulated with different jet Reynolds numbers. Axial ventilation is also included. The temperature of the jet

was 300 K throughout the cooling cycle and the jet diameter was 10 mm.

The bow has been previously examined by analysing the temperature difference between nodes at TDC and BDC, as this temperature difference accurately portrayed the deflection of the rotor in the vertical direction. This was appropriate as the circumferential gradient on the outer rotor was gradual. However, in the impingement cases a strong thermal gradient presents itself near the stagnation point, which means that a simple top-to-bottom temperature difference may no longer truly reflect the distortion of the rotor. Therefore, the calculated temperature distribution of the rotor at each time step is applied as a thermal load to a FEA model of the geometry in order to calculate the magnitude of the vertical deflection. MATLAB is used to perform this calculation with the following material properties, which are representative of a nickel-alloy [71]: Young's modulus = 229 GPa, Poisson's ratio = 0.37, and coefficient of linear expansion = 12.7×10^{-6} K^{-1}. The inner bore is fixed in position.

Figure 10.7a gives the top-to-bottom temperature difference of the rotor for various jet Reynolds number cases; figure 10.7b gives the corresponding vertical deflection difference values: $\Delta\delta_y = |\delta_{y,TDC}| - |\delta_{y,BDC}|$, which have been normalised by the annulus height (H). Similar to the experimental cases, there is a steep negative gradient in ΔT^* initially, which leads to a peak in negative deflection at a slightly later time step. The magnitude of the top-to-bottom temperature differnece is no longer directly proportional to the magnitude of the deflection. Although the jet impingement is only directly acting over a small portion of the circumferential area, it is evident that the effect of impingement cooling is dominating the transient cooling cycle – even at very low Reynolds numbers. This can be attributed to the relatively large heat transfer coefficients associated with this cooling approach when compared to natural convection. The effect is so strong in these cases that positive rotor thermal bow is not realised at all throughout the cycle. These results corroborate the experimental findings in that a low Reynolds number impingement jet at TDC can alleviate rotor bow during shutdown cooling.

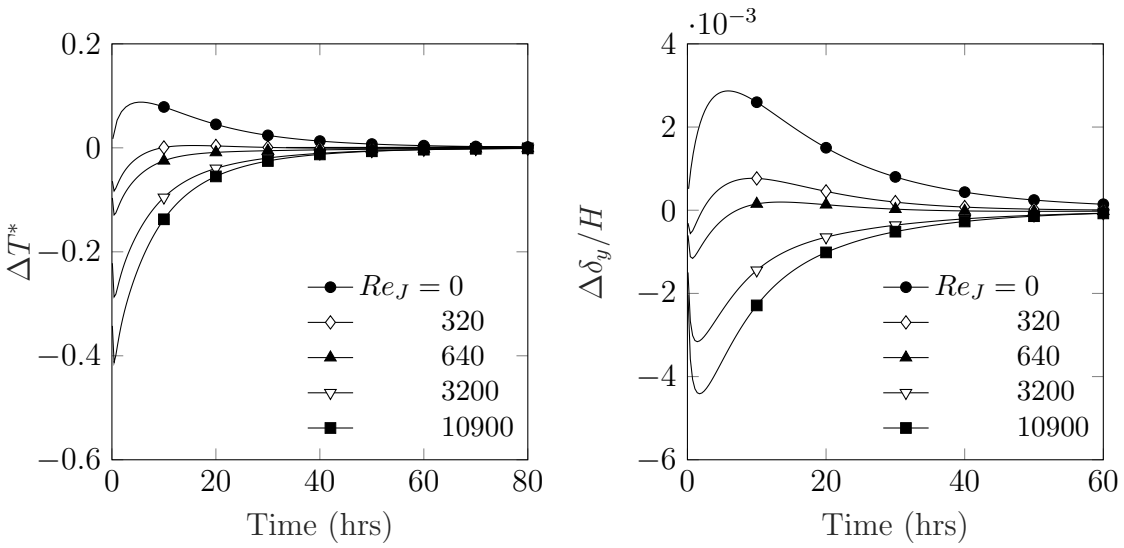

FIGURE 10.7: **a:** Simulated top-to-bottom temperature difference profiles for different Reynolds number jets with a starting temperature of 900 K. **b:** Corresponding vertical deflection magnitudes for these cases. $\Delta\delta_y = |\delta_{y,TDC}| - |\delta_{y,BDC}|$.

Temperature contours at three different cooling times are shown in figure 10.8; the top row has no impingement flow, whereas $Re_J = 10900$ in the bottom row. The first column corresponds to the negative peak in temperature difference for the impingement case. The middle column is the peak ΔT^* in the baseline case. The effect of the impingement flow is clearly seen close to the stagnation point of the jet. This effect is maintained throughout the cooling cycle. It is because of this localisation that the top-to-bottom temperature difference does not correspond to the deflection bow. While the gradient of temperature is large near the stagnation point; no significant thermal stresses were observed in this location in the FEA model. The temperature at BDC remains similar in both cases.

Finally, the jet-to-wall temperature ratio impact was investigated. Further simulations have been conducted with a starting temperature of 500 K uniform; figure 10.9 shows ΔT^* for different Reynolds number cases. Interestingly, the magnitudes of ΔT^* are similar and even slightly larger, even though the starting temperature is 400 K lower. The starting Rayleigh numbers of both thermal conditions are: $Ra_{D_i} = 8.8 \times 10^7$

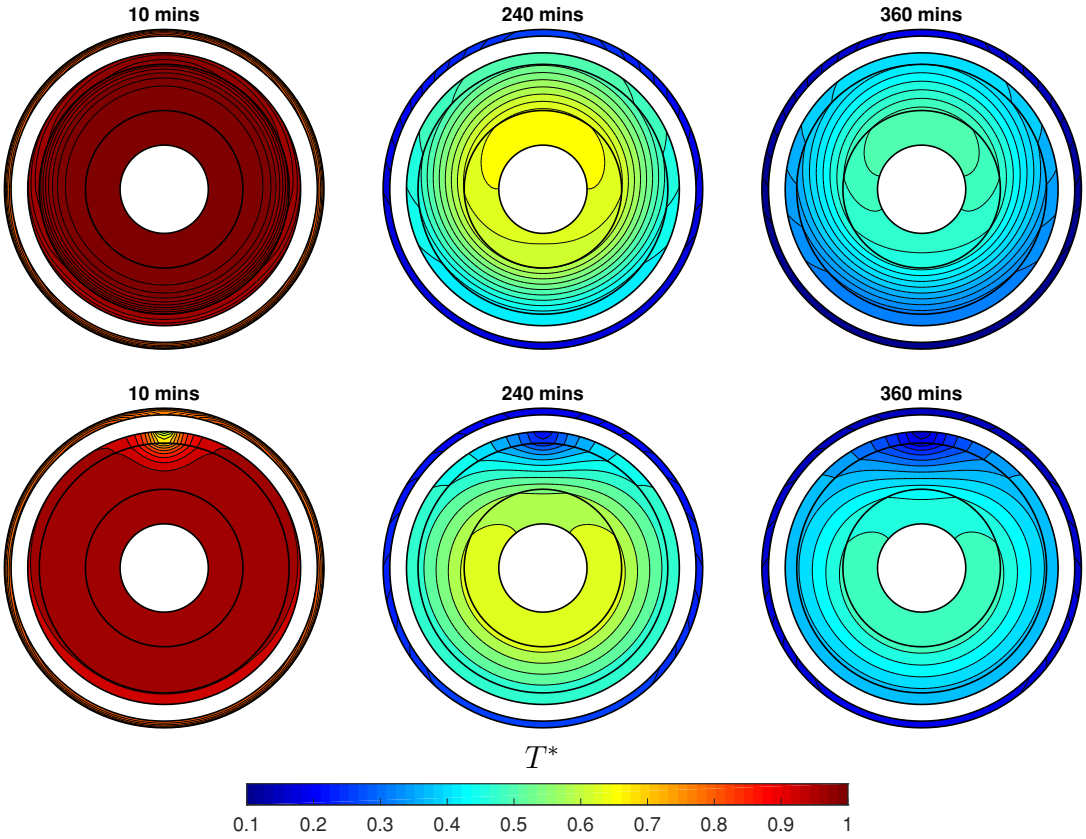

FIGURE 10.8: Simulated temperature contours during cooldown starting from 900 K uniform. $Re_J = 0$ for the top row; $Re_J = 10900$ for the bottom row.

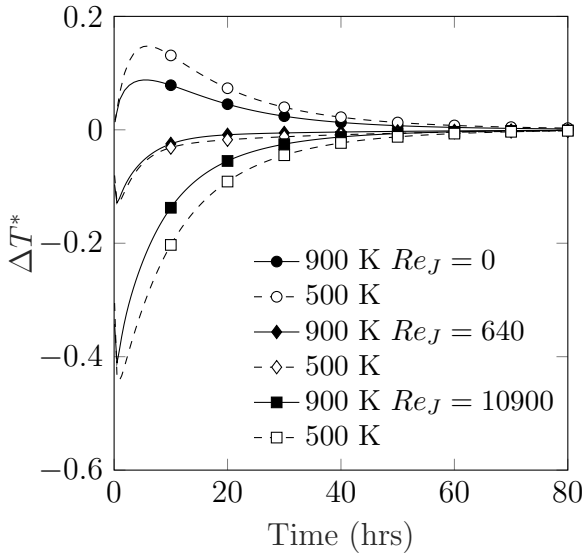

FIGURE 10.9: Simulated top-to-bottom temperature difference profiles for different Re_J with uniform starting temperatures of 900 and 500 K.

for the 500 K case and 4.2×10^7 for the 900 K case. It is encouraging to see this trend as it indicates that the method of defining the applied heat flux in section 10.2.2.1 is valid. Moreover, the results indicate that an optimum jet impingement arrangement can be designed that would be somewhat independent of the initial starting temperature – meaning that idling time of an engine prior to shutdown would not impact the impingement requirements.

10.3 Emissivity Distribution

A completely different method of reducing rotor bow will now be examined. It has been noted in numerous sections of this thesis that radiation heat transfer can have a significant impact on the shutdown cooling of a large civil gas turbine. Therefore, a potential mitigation strategy is altering the circumferential emissivity distribution in order to promote asymmetric radiation heat transfer; this can counteract the asymmetric natural convective heat transfer. Rotor bow occurs because there is more heat transferred away from the bottom sector of the rotor drum than the top; therefore, if the radiation heat transfer in the upper sector is enhanced in combination

with suppressing it in the bottom section, this may help alleviate the severity of bow. Similar to the impingement flow cases, this strategy has been investigated experimentally using the RoBo facility and numerically using the shutdown cooling model.

10.3.1 Experimental Results

The RoBo facility has again been modified in order to test this method of cooling. The emissivity of the inner assembly was 0.95 (painted matt black Rohacell). It is not practical to alter the inner assembly emissivity, as the operator does not have control over the stopping position of the rotor. The outer cylinder inner surface already has quite a low emissivity (unpainted aluminium, $\varepsilon = 0.1$). Therefore, the entire upper half of the outer cylinder inner surface has been painted with a matt black paint in order to increase its emissivity to 0.95. A cross-sectional schematic of the cylindrical section is shown in figure 10.10. Similarly to the forced air flow cases in section 10.2, the inner assembly is heated to a steady-state temperature of 100°C while the outer cylinder is heated to 60°C, equating to $Ra_{D_i} = 6.3 \times 10^7$ and $Dr = 1.25$. The first case considered is the transient cooling test with four rows of blades installed and the cylinder side end-plate removed – the most severe bowed experimental case that was observed.

Figure 10.11 shows the non-dimensional top-to-bottom temperature difference of both the inner and outer cylinders, for the baseline and altered emissivity case. The changes to the internal radiation heat transfer has led to a 25% reduction in peak ΔT^*, but this in-turn has led to a 25% increase in outer ΔT^*. Interestingly, neither the on-set time or duration of bow has been affected.

Figure 10.12 gives constituent thermocouple signals of the aforementioned four cooling curves. Neither the inner or outer cylinder bottom sector cooling rate has been notably impacted by this new emissivity distribution. The overall heat transfer from the inner cylinder upper section has been enhanced, which was the original

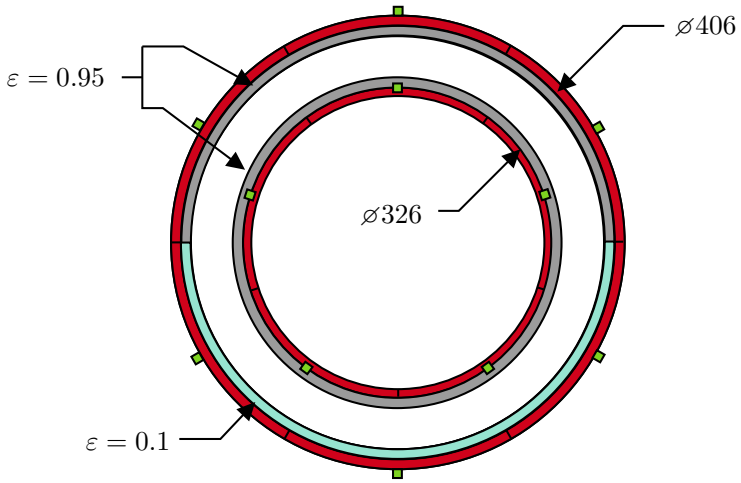

FIGURE 10.10: Axial cross-section schematic of the RoBo facility highlighting the altered emissivity distribution.

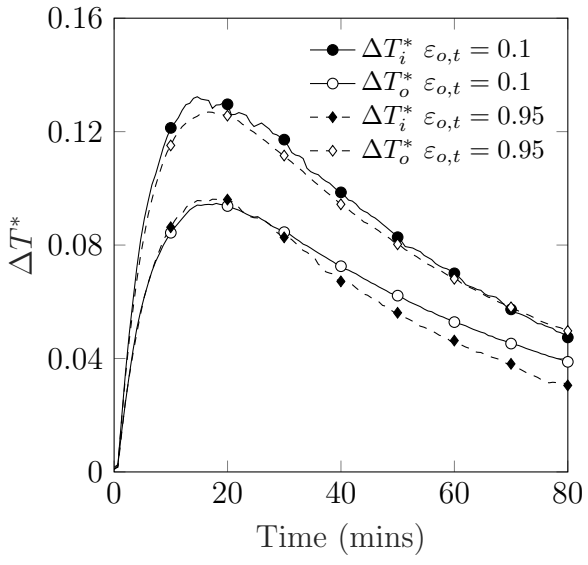

FIGURE 10.11: Experimental inner and outer cylinder top-to-bottom temperature differences for the baseline (round markers) and altered emissivity (diamond markers) cases. Axial ventilation and four blade rows were present. $Ra_D = 6.3 \times 10^7$ and $Dr = 1.25$.

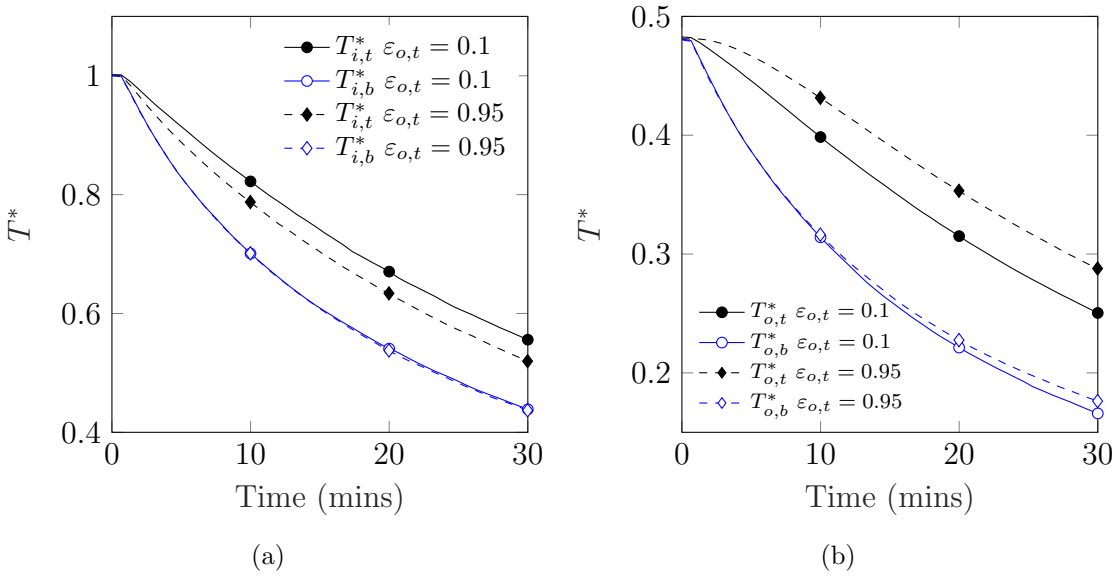

FIGURE 10.12: **a:** Inner cylinder transient cooling temperatures at top and bottom for the baseline and altered emissivity cases. **b:** Outer cylinder transient cooling temperatures for these cases.

goal; this leads to a faster cooling rate at inner TDC and thus less rotor bow. This extra heat is then absorbed by the outer cylinder upper section, since it's reflectivity has been reduced as a consequence of increasing its emissivity. This causes it to cool slower, which in-turn leads to a larger casing bow than the baseline case.

Two further experimental configurations have also been completed. The thermal boundary conditions were identical to the previous cases. Firstly, the ventilation effects were removed by sealing the cylinder end of the facility; the four rows of blades remained. This case is important as the induced ventilation in the RoBo facility is not necessarily representative of all stages of a real engine compressor. The top-to-bottom temperature difference results for both the baseline and altered emissivity cases are given in figure 10.13a. Similar trends are observed; however, the reduction in ΔT^* is more profound: 61% compared to 25% previously. There has been a 36% increase in casing ΔT^*, compared to 25% previously. Therefore, removing the ventilation effect has suppressed the rotor top-to-bottom temperature difference to a greater extent than it has enhanced casing temperature difference.

Figure 10.13b gives ΔT^* results for an unobstructed, sealed annulus. Removal of

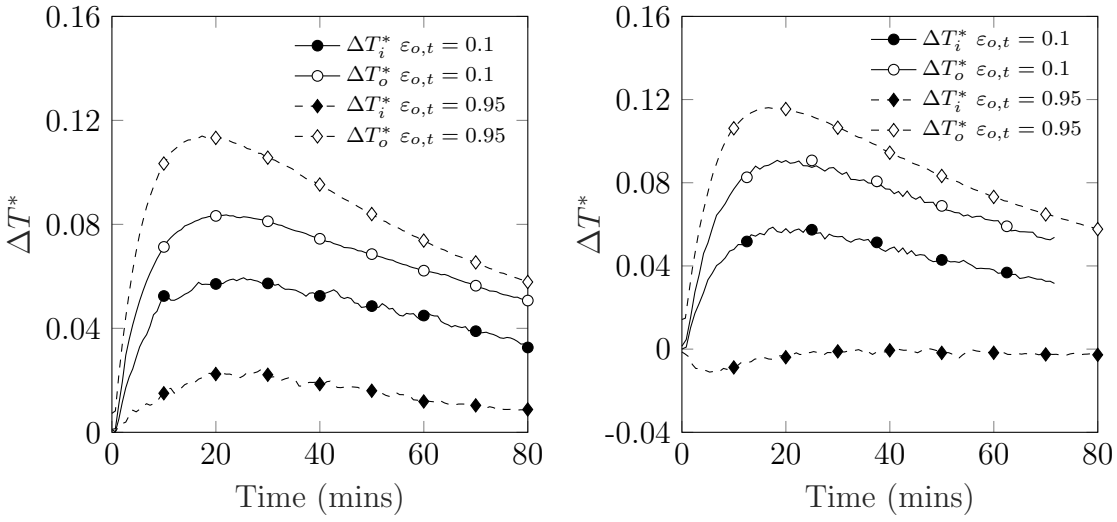

FIGURE 10.13: **a:** Inner and outer cylinder top-to-bottom temperature differences for a sealed cases with four rows of blades. **b:** Inner and outer cylinder top-to-bottom temperature differences for a sealed cases with no blades.

the four rows of blades and the altered emissivity distribution has actually allowed the inner cylinder top section to cool faster than the bottom section, leading to a slight negative ΔT^* for a brief period. Thermal bow has effectively been eradicated entirely for this particular case. Overall, this experimental setup lead to a 115% reduction in ΔT^*, coupled with a 27% increase in casing ΔT^*.

Despite the drawback of increased casing temperature difference, the potential for large reductions in rotor bow warrants further investigation into this mitigation strategy – especially given the higher temperatures and thus increased radiation heat transfer present in an engine.

10.3.2 Numerical Model

The shutdown cooling model can be easily modified to investigate this mitigation strategy. The only alteration required is the emissivity of the casing inner surface: ε_o. The simulated results of the RoBo facility model will be examined before the methodology is applied to the engine-representative geometry.

10.3.2.1 Model Validation

Figure 10.14a shows the simulated and experimental top-to-bottom temperature difference for the altered emissivity cases that have 4 rows of blades and axial ventilation; figure 10.14b gives ΔT^* for the sealed, unobstructed cases. While the outer cylinder magnitude is matched in both configurations, the model does under-predict the amount of inner cylinder ΔT^*. Both peaks were matched for the circumferentially uniform emissivity cases; thus, it is over-predicting the suppression of ΔT^* caused by altering the emissivity. However, the onset time of peak ΔT^* is concurrent in both figures.

The difference in magnitudes is likely a result of the simplified adiabatic boundary condition that is applied to the inner cylinder inner surface. The numerical method does not model and end conduction effects or take into account the trapped volume of hot air inside the RoBo inner assembly. In both the altered and uniform emissivity cases, the initial cooling rate is correctly predicted, but the rotor reaches ambient faster than what was observed in the experiments; this substantiates the aforementioned reason for the disparity between the numerical and experimental results. Therefore, this difference of ~ 4°C here is not a concern, since the purpose of the engine model is to explore the impact of higher starting temperatures and a more representative geometry. Importantly, the model does predict the correct trend in the altered emissivity cases, including a negative peak in ΔT^*.

10.3.2.2 Engine Conditions

An emissivity value of 0.5 was used for both the rotor and casing walls in the original simulations. This has been changed to the extreme case of 0.95 for the upper half of this surface (as if it has been coated with a high-emissivity covering) and lowered to 0.1 on the bottom half (as if it has been highly polished). Figure 10.15a shows the rotor top-to-bottom temperature difference for the axial ventilated cases, for three uniform initial starting temperatures – 500, 700 and 900 K. The corresponding

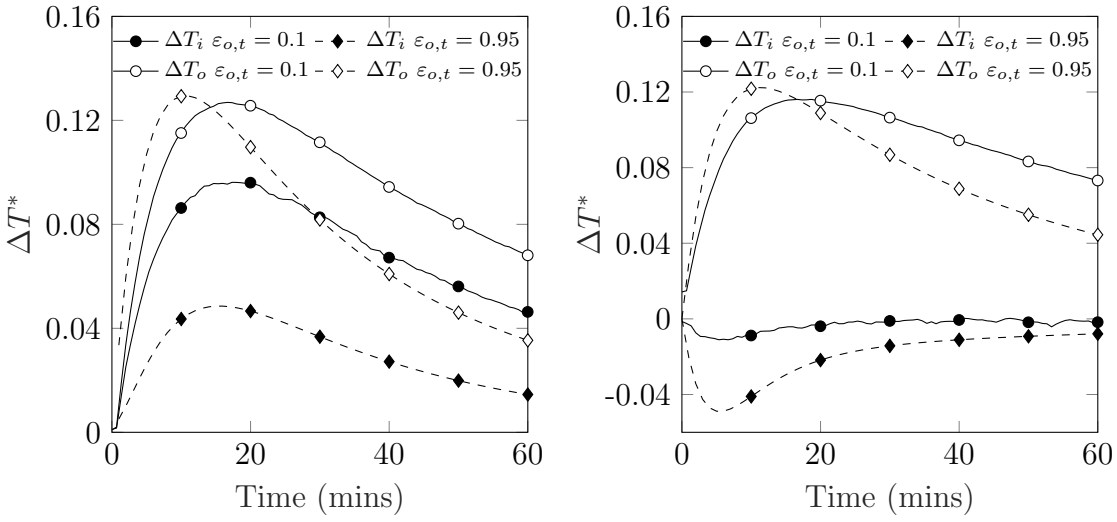

FIGURE 10.14: **a:** top-to-bottom temperature difference for simulated (dashed lines) and experimental results (solid lines) for the altered emissivity cases that have 4 rows of blades and axial ventilation. **b:** Top-to-bottom temperature difference for simulated (dashed lines) and experimental results (solid lines) for the sealed and unobstructed altered emissivity cases.

casing ΔT is shown in figure 10.15b. The general shape of the rotor ΔT curves are akin to those observed in the experimental campaign, which gives confidence to the numerical procedure.

The simulation results presented here show the large influence of altering the casing circumferential emissivity as it has drastically reduced the magnitude of positive rotor ΔT. As the radiation heat transfer is proportional to the fourth power of temperature, the effects of this mitigation strategy become more pronounced as the initial starting temperature is increased. The reduction in positive rotor ΔT coincides with an increase in casing ΔT, as can be seen in figure 10.15b. Upon first inspection, the magnitude of this in the altered emissivity cases seemed detrimental. Although it is an undesirable consequence, the ability of this technique to suppress rotor bow should not be discarded as the structural supports of the casing are unknown, thus the relationship between the thermal gradient and deflection is unknown for a real engine.

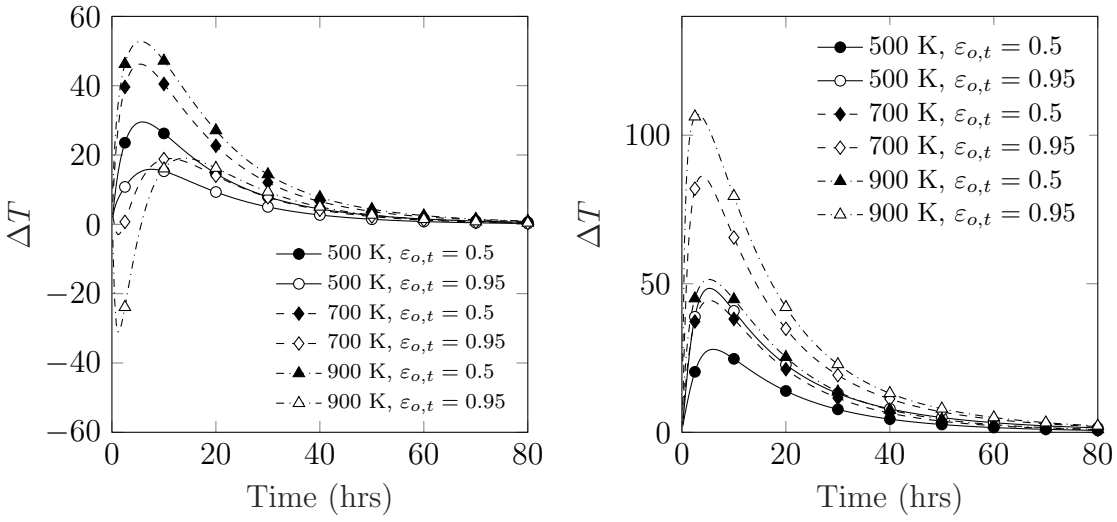

(a) (b)

FIGURE 10.15: **a:** Simulated rotor top-to-bottom temperature difference for 500/700/900 uniform starting temperature cases with and without an altered circumferential casing emissivity. **b:** Corresponding casing top-to-bottom temperature difference curves for these cases.

Figure 10.16 shows the calculated temperature distributions at various stages of the cooling cycle for the baseline and altered casing emissivity case starting at 900 K. While the overall cooling rates are similar; the altered emissivity results display a more axisymmetric temperature profile from 400 minutes onwards – which is favourable from a rotor dynamics point of view. This is evident from the greater concentricity of the black contour band lines.

The 900 K case is now examined in finer detail in order to gain a further insight into the cooling process. Figure 10.17a gives the rotor temperature at top and bottom. Figure 10.17b shows a comparison of the convective and radiative heat flux components at TDC and BDC. Looking at the unaltered case, the radiation heat transfer curves follow similar trajectories, whereas the convection heat transfer at BDC is far greater than TDC, before decaying over time – this is what leads to a positive peak in ΔT. The diamonds marked lines in this figure display the distinct transformation in the radiation heat transfer caused by altering the emissivity. The radiation at BDC for this case is now actually lower than the convective heat flux

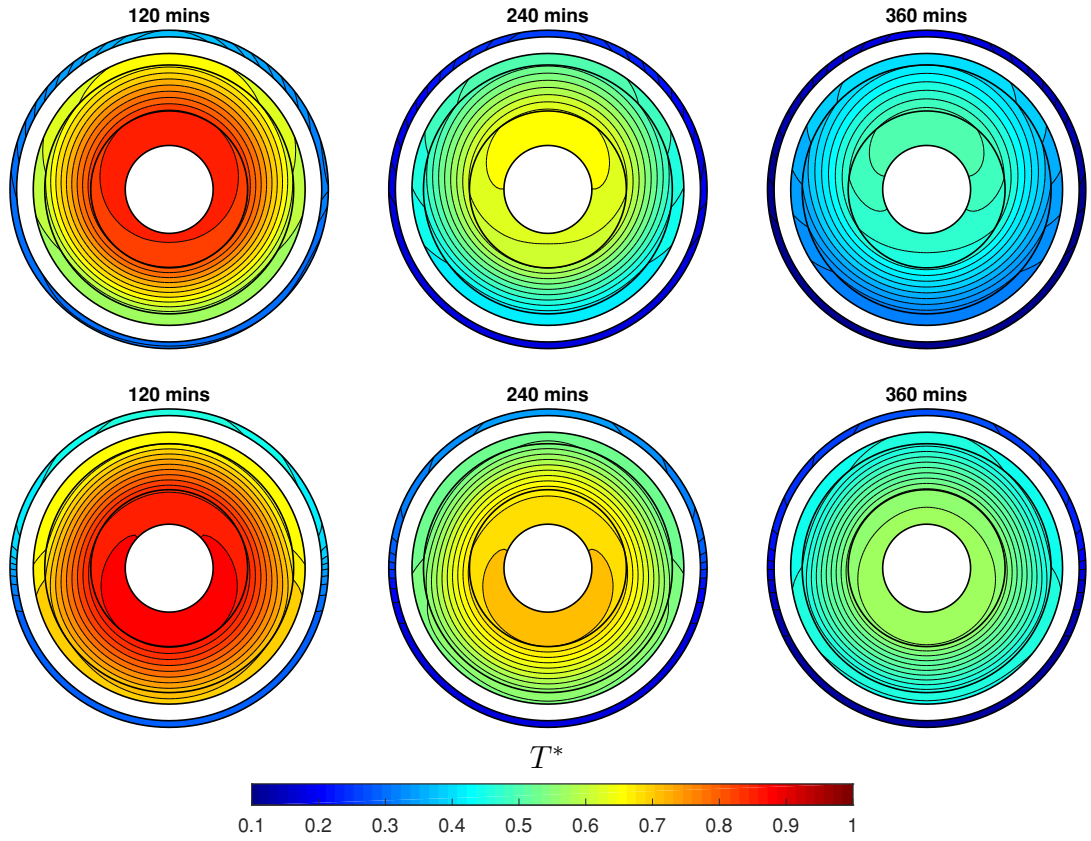

FIGURE 10.16: Simulated temperature distributions at various stages of the cooling cycle starting from 900 K uniform. Top: $\varepsilon_{o,bot}, \varepsilon_{o,top} = 0.5$; bottom: $\varepsilon_{o,bot} = 0.1$ and $\varepsilon_{o,top} = 0.95$;

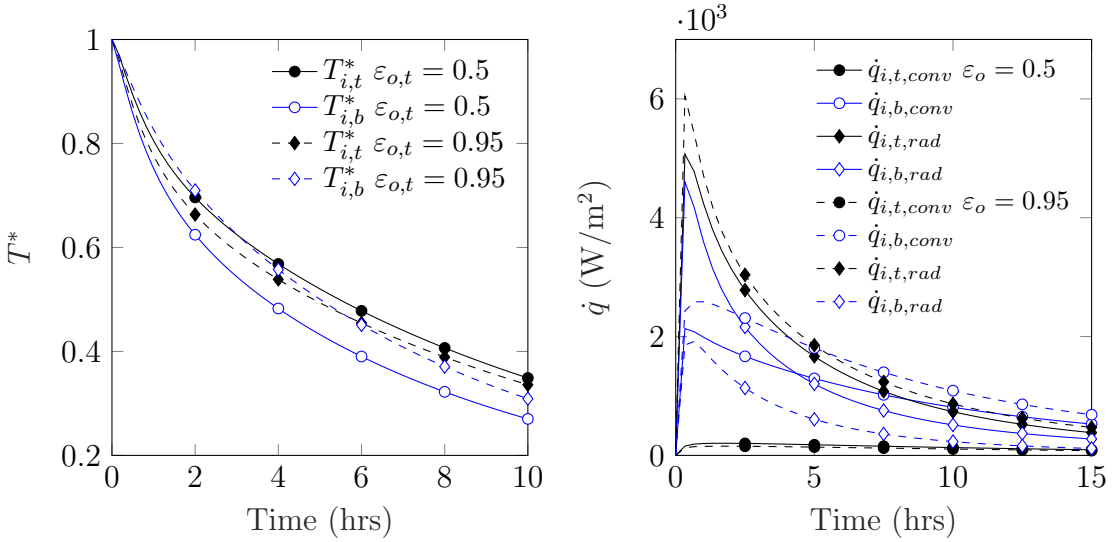

(a) (b)

FIGURE 10.17: **a:** Predicted rotor surface temperatures for the 900 K staring point, with (dashed lines) and without (solid lines) an altered circumferential casing emissivity. **b:** Convective and radiative heat fluxes for these cases.

at this location throughout the entire cooling cycle. The casing is absorbing less heat at BDC, thus it is cooling down faster; this leads to a larger radial temperature gradient and hence a higher convective heat flux when compared to the baseline case. As mentioned previously, the radiative heat flux is strongest at the start of the cooling cycle; as the temperature reduces, so does the difference in this flux between the top and bottom of the rotor. The convective heat flux difference is sustained over a longer period of time – which leads to the subsequent peak in positive ΔT that follows the negative peak.

The heat flux results in figure 10.17b can be used to help determine an optimum circumferential distribution of ε_o that minimises both positive and negative temperature difference. However, this must be carefully balanced against the asymmetry caused by the axial ventilation. The modelling procedure here was designed to mimic the RoBo experimental observations, but the axial effects of a full scale engine remain unknown. Figure 10.18a shows the rotor bow for the 900 K cases for both emissivity distributions with and without axial ventilation effects. When the axial venting effect – that enhances positive ΔT – is no longer present, the negative peak in rotor ΔT is greater. Figure 10.18b shows these results recast in terms of the deflection difference of the rotor. The impingement case with $Re_J = 640$ from the previous section is also included. Both rotor bow suppression techniques show a strong sensitivity to inclusion of axial ventilation.

10.4 Periodic Rotations

As rotor bow develops, it may be tempting to simply rotate the inner assembly by 180°, in an effort to reverse the top-to-bottom thermal gradient. This technique can be explored using the engine compressor disc model. The axial ventilated 900 K uniform initial case reached an inner peak of $\Delta T^* = 0.7$. If for instance, the maximum desired ΔT^* level was nominally set at 50% of this figure, the inner assembly would

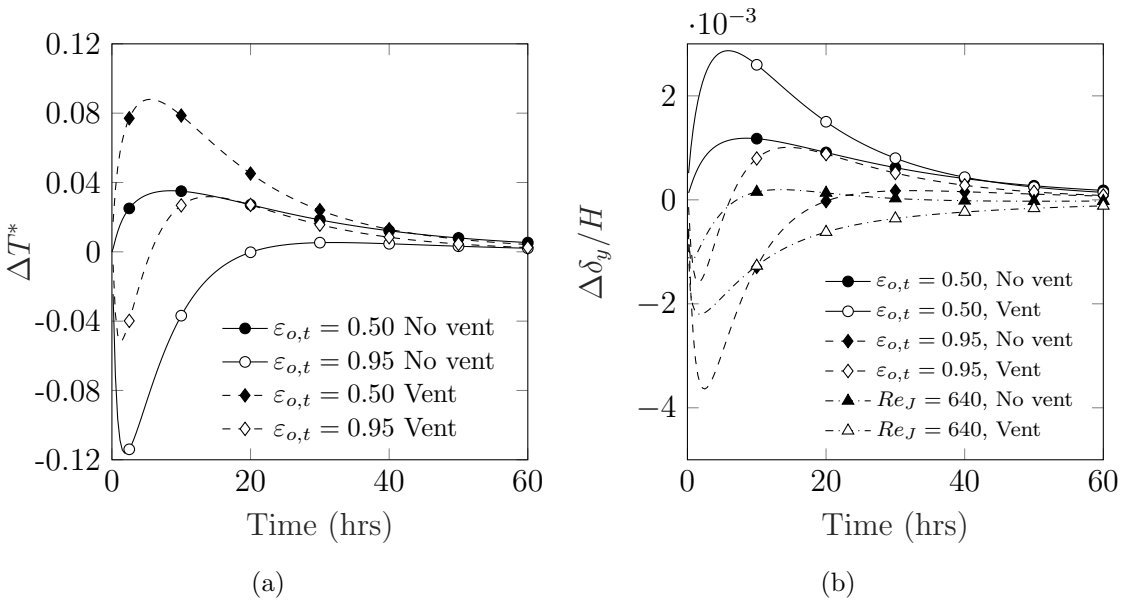

FIGURE 10.18: **a:** Simulated rotor top-to-bottom temperature difference for 900 uniform starting temperature cases with and without an altered circumferential casing emissivity, and ventilation. **b:** Rotor deflection for these cases along with an impingement case with $Re_J = 640$.

need to be rotated every time a peak of 0.35 was reached. This strategy can be simulated by comparing ΔT at each time step to this criterion and rotating the inner mesh temperature distribution 180° prior to the next time step, should this limit be exceeded. Figure 10.19a gives the rotor top-to-bottom temperature difference time history of the simulated periodic rotation case, along with the stationary inner disc case. The disruption to the annular flow field that would inevitably occur in the rotation process is ignored in this simulation, as it is assumed that the time constant associated with re-establishment of the natural convective flow field is small when compared to the cooling time.

In total, seven rotations were required in the cooling cycle in order to limit ΔT to 50% of the peak value from the stationary case. The average time between rotations was 2 hours. Immediately following a rotation, there is an increase in ΔT^*; figure 10.19b elucidates the reason for this. $\Delta \dot{q}_i$ represents the difference in wall heat flux between TDC and BDC. Therefore, a negative value indicates that the heat flux is higher in the bottom section, which drives the typical trends seen in thermal bow.

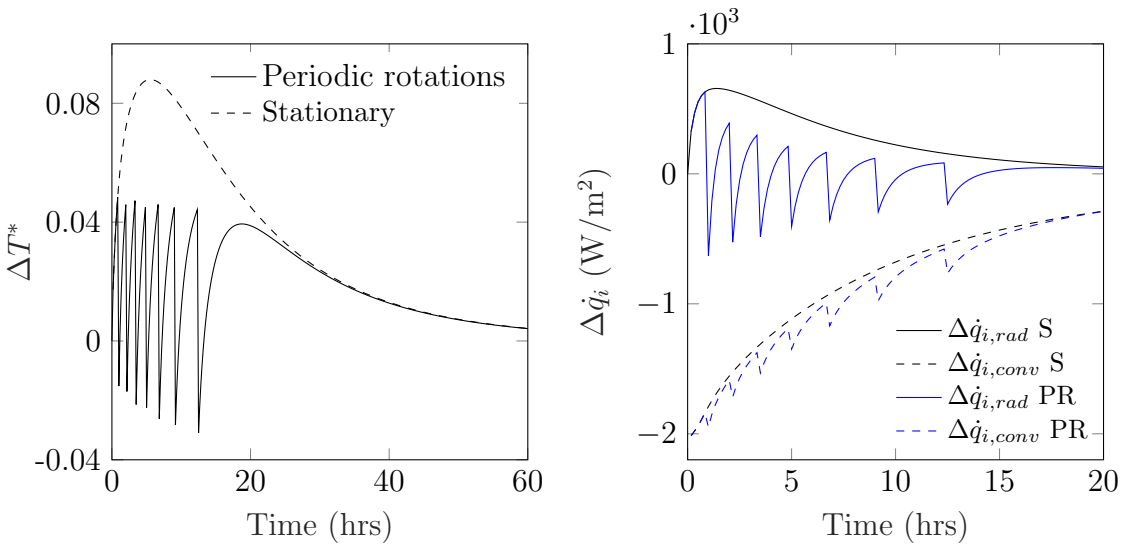

FIGURE 10.19: **a:** Simulated rotor top-to-bottom temperature difference for 900 K uniform starting temperature case with 180° rotations whenever the defined limit of ΔT is reached (50% of the stationary case). **b:** Time history of the difference in inner surface heat flux between the global top and bottom positions, for both the stationary (S) and periodic rotation case (PR).

The heat transfer has been decomposed into its radiative and convective components. Firstly, examining the stationary case, the BDC convection far outweighs the TDC equivalent. This faster temperature decay at the bottom reduces the radiative heat flux in this region and interestingly, $\Delta \dot{q}_{rad}$ actually helps to suppress the asymmetry of $\Delta \dot{q}_{conv}$. When the inner shaft is rotated 180°, the hotter section (now at BDC) leads to a higher local Rayleigh number, which in-turn causes $\Delta \dot{q}_{conv}$ to become more negative. The radiative heat fluxes are now also switched, so the favourable suppression from the stationary case now acts to enhance the convective asymmetry. The outcome of these combined effects explains the observed acceleration in ΔT^*. As the lower section of the inner disc in now hottest, a negative $\Delta \dot{q}$ is necessary to suppress this thermal gradient. However, the enhancement of this variable accelerates ΔT^* to such an extent that numerous rotations are required to satisfy the limit placed on temperature difference.

While it is therefore possible to suppress rotor bow with this technique, it does have

numerous drawbacks. For instance, it would be difficult to ensure exact 180° rotations. Moreover, similarly to continuous slow rotations of the shaft during shutdown, this solution is unfavourable for airframe manufacturers as it could hamper any required maintenance.

10.5 Conclusions

Differing strategies for suppressing rotor bow have been extensively investigated, both numerically and experimentally. Both forced air cooling and altered emissivity mitigation methods have been verified as viable solutions to help alleviate this issue in large civil gas turbines during shutdown cooling.

Forcing air into the annulus at top-dead-centre leads to impingement heat transfer on this section of the rotor. The relatively large heat transfer coefficients, coupled with a sizeable jet-to-wall temperature difference, means that low Reynolds number jets are powerful enough to completely suppress positive rotor bow. The shutdown cooling model has been successfully enhanced to simulate this effect, which has added veracity to the usefulness of this strategy. However, it is worth noting here that as the numerical prediction method is 2D, it does not capture any complicated 3D interaction effects that would be associated with an impinging jet, such as those observed by Pilkington [83], who simulated an incoming jet in the can combustor region of an industrial gas turbine during shutdown.

Although the emissivity altering method does cause a larger thermal gradient on the casing, the benefit of rotor bow suppression is not to be ignored. Furthermore, it may be easier to implement this method in an engine. An uncertainty surrounding this approach though is the question of how the emissivity of the rotor and casing evolve throughout the service life of an engine, and whether the desired distribution can be maintained.

It has been shown that an optimum configuration exists for both mitigation strategies. However, these configurations are equally sensitive to the level of induced axial ventilation occurring at a given cross-section. An incorrect match may lead to a peak in negative rotor bow that could be even larger than the original positive peak. Therefore, correctly predicting this ventilation effect will be critical when specifying a system suited to an engine design. Overall, the results of both strategies are very encouraging and warrant further investigation as potential solutions to eliminate rotor bow entirely as an operational risk of large civil gas turbines.

Chapter 11

Auxiliary Zone Cooling

11.1 Introduction

Potential cooling strategies for the auxiliary zone will now be examined: end wall ventilation and port venting. The desired outcome is to reduce the air temperature in this region uniformly such that any components in the zone are not at risk of any damage that may be caused by exceeding their respective temperature limits for an extended period of time, during shutdown cooling. The ExCITE facility has been modified to investigate these effects.

Recall that the inner wall of the auxiliary zone is close to the casing of the main gas path. The impact of the casing heat flux distribution was previously examined numerically in section 9.4.3. It was found that while enhancing the asymmetry of the casing heat flux does increase casing bow, there was a weak coupling to the rotor bow for the cases examined. Increasing the heat flux from the casing uniformly decreased both casing bow and rotor bow marginally.

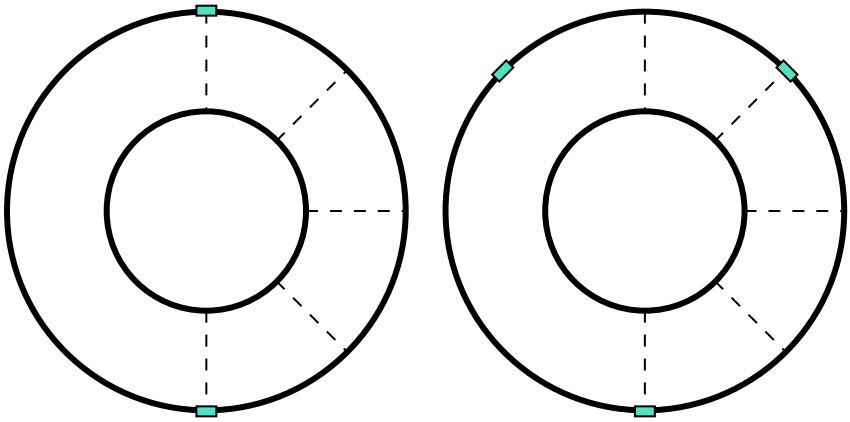

FIGURE 11.1: Schematic of port venting arrangements of the ExCITE facility. Left: TB. Right: TS B.

11.2 Port Venting

The first method of cooling that was investigated was port venting. This involves various arrangements of openings to help induce a ventilation flow. Figure 11.1 shows a schematic of the different arrangements that were tested. Each blue square represents a hole at the central axial location of the rig that is ⌀64 mm, which is approximately 5% of the axial length. The left image (coined TB – top and bottom) has an opening at 0° and 180°. The right image has openings at ±45° as well as 180° (coined TS B – top-sides and bottom). The dashed lines represent the thermocouple traverse locations. The ports can also be seen later in figure 11.4. A steady-state experimental test was conducted. The inner cylinder temperature was held constant at 100°C, which equates to $Ra_{D_i} = 2.8 \times 10^9$ when $T_s - T_\infty$ is used in the definition. Measurements were taken once the outer cylinder thermocouples reached a steady-state – changed by < 0.1°C over a twenty-minute period.

Figure 11.2a gives the air temperature at $0.25H$ for both vented cases, along with the sealed case for reference. Both port vented cases show a similar trend: the air temperature at BDC has been reduced but little variation is observed at TDC. The TS B values in the upper section are slightly lower than the TB case; this is likely due to their being a larger total aperture area. The inner surface equivalent conductivity for these cases is shown in figure 11.2. A natural draft has been created

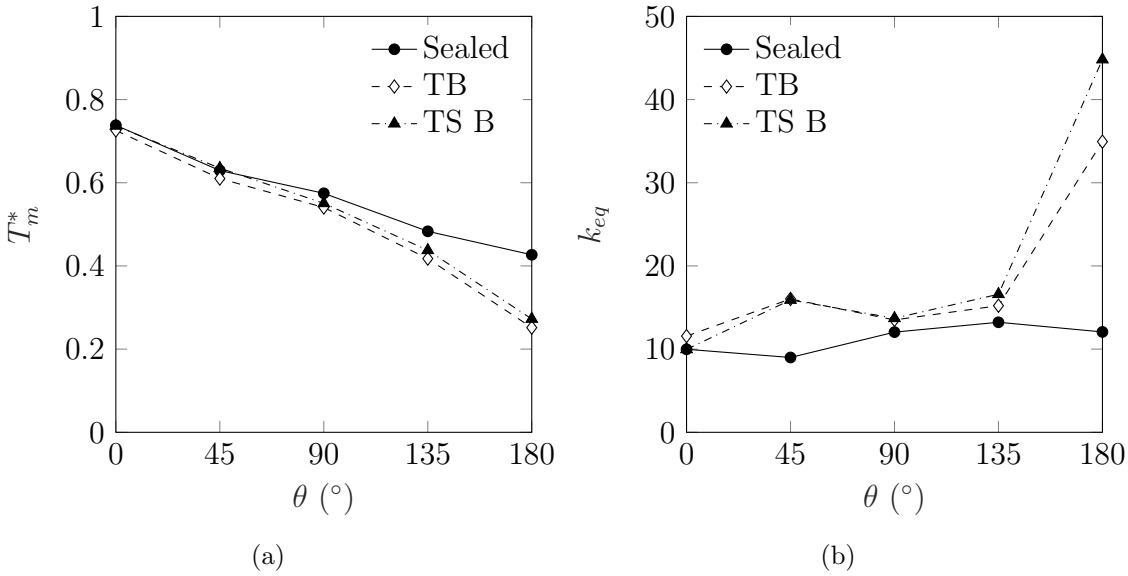

FIGURE 11.2: **a:** Air temperature measurements for port vents cases. **b:** Inner wall equivalent conductivity measurements for port vent cases.

and the incoming cold air has caused a localised area of high heat transfer at BDC. Although this draft must mean that warm air is existing in the upper section, it only reduces the mid-annulus temperatures by an inconsequential amount. The inner wall heat flux at BDC is approximately 3.5 times larger than the sealed case for the TB arrangement and 4.5 times greater for the TS B case. The TS B case has twice the outlet area in the upper half when compared to the TB case; this allows more warm air to exit. The exiting air must be replaced by incoming cooler ambient air. Thus, the larger draft induced in the TS B is the reason for the higher heat flux observed in this case.

Infrared camera measurements were also obtained for these experiments. Figure 11.3 shows the inner cylinder surface temperature field obtained by a camera looking at BDC, when mounted 20 mm outside of the outer cylinder, for the TB case. The sharp blue horizontal line on the left hand side is the thermocouple probe body and should be ignored. The sharp red horizontal line is a joint in the rohacell material. The shorter series of horizontal lines on the left are reflective markers on the cylinder surface at 5° intervals. The dashed red circle indicates the size of ⌀64 mm opening.

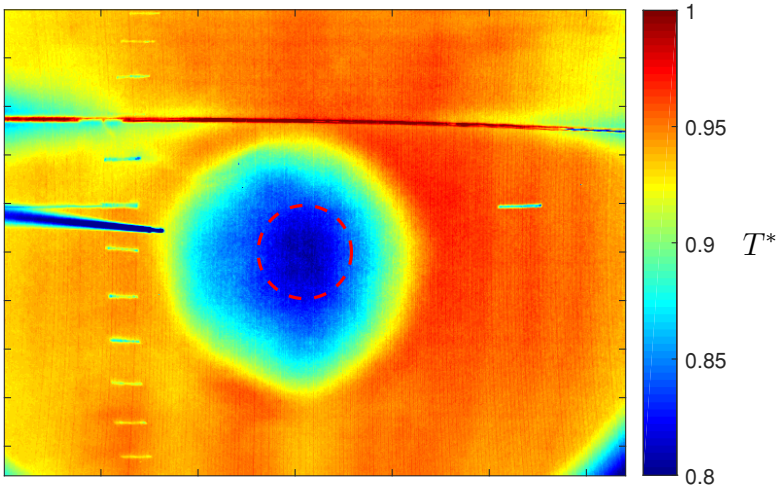

FIGURE 11.3: Infrared camera measurement of the inner cylinder surface at BDC for the TB port vented case. The dashed line indicates the ⌀64 mm opening.

The cold spot created by the induced draft impinging on the inner cylinder surface is clearly evident. The characteristics are typical of a jet impingement type flow where the peak heat transfer is near the stagnation point and it decays in an axisymmetric fashion away from this point. The effects of the jet have diminished entirely by 15° away from the stagnation point.

This impingement will increase the casing bow. However, there are many components in this zone in an actual engine meaning it is highly unlikely that the jet will reach the inner cylinder unimpeded, so this should not be a concern. Overall, the port venting configurations examined here are effective at reducing the air temperature at BDC but not in the upper sections in the annulus.

11.3 End Wall Venting

An alternative method of cooling for the auxiliary zone is leaving a small annular gap where the end wall meets the outer cylinder in order to promote a draft. Referring back to the large civil gas turbine schematic given in figure 1.1, this corresponds to the right-hand side of the auxiliary zone where the turbine casing meets the bypass

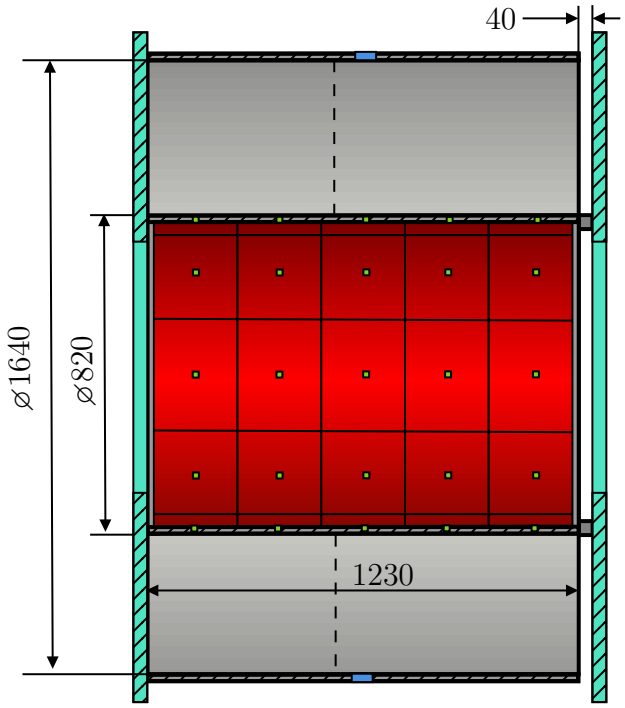

FIGURE 11.4: Schematic of the end wall venting arrangement of the ExCITE facility.

wall. This can be replicated in the ExCITE facility by simply stepping back one of the acrylic end plates; figure 11.4 shows a schematic of this. A full annular gap of 40 mm width is specified, which is 3% of the axial length. The gap created between the inner cylinder and the end plate is sealed. The air temperature probe measurement plane is 715 mm from the gap. The experimental procedure was identical to the aforementioned port vent cases: $T_i = 100°\text{C}$, $Ra_{D_i} = 2.1 \times 10^9$, $Dr = 2$.

The $0.25H$ air temperatures are shown in figure 11.5a, along with the sealed and TS B port vent case. The end wall venting has caused a substantial decrease in the overall bulk air temperature when compared to the sealed case. The fall is slightly more pronounced at BDC (34% fall) than at TDC (25% fall). It is encouraging that such a significant fall in temperature is observed at a distance more than half of the rig axial width away from the opening. The equivalent conductivity of the inner wall is shown in figure 11.5b. The end wall vent has led to an overall increase in the wall heat flux, surprisingly the peak now occurs at 90°. Moreover, there is no localised cold spot as was observed in the port vent case. Overall, this result highlights the

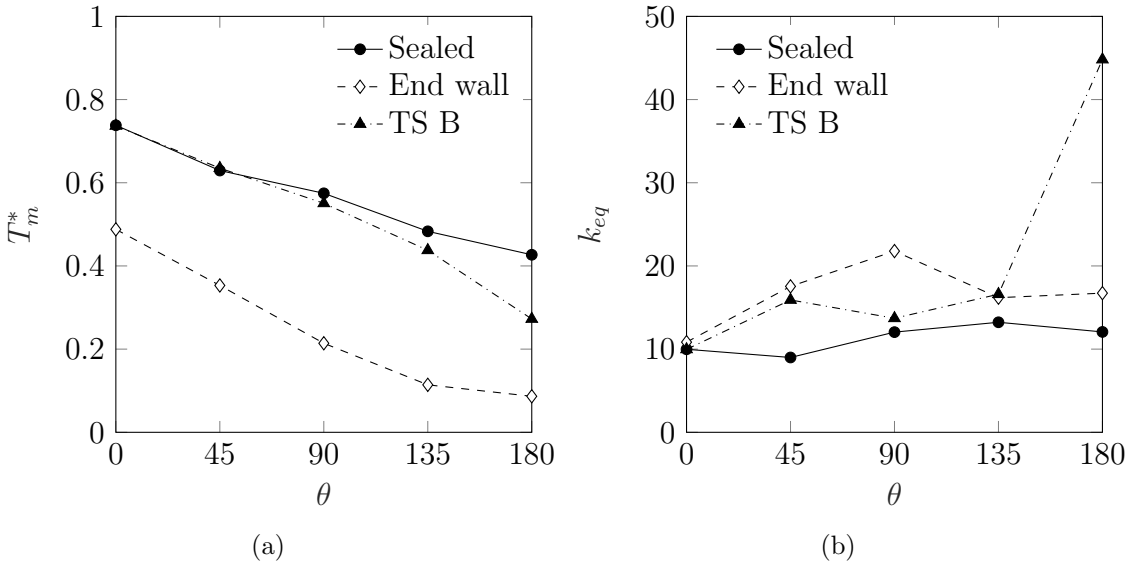

FIGURE 11.5: **a:** Air temperature measurements for end wall vent case. **b:** Inner wall equivalent conductivity measurements for end wall vent case.

effectiveness of this at strategy at cooling components throughout the entire auxiliary zone.

The impact of obstructions has been investigated by including the large cuboid which was previously tested for the sealed cases in section 7.4 in Chapter 7. Separate end wall vented cases were completed with the obstruction at TDC (coined OB T) and BDC (OB B). The mid-annulus air temperatures are shown in figure 11.6. Apart from slight reductions at 90°, both cases show near identical profiles to the unobstructed case. The equivalent conductivity profiles were also very similar.

In a real engine design, it may be unfeasible for the entirety of this end wall junction to be open, for structural purposes. One further experimental configuration (Mod) was completed where the end wall opening between 45° and 135° was completely sealed on both sides, leaving only the top 90° and bottom 90° sectors open – as it is expected that these regions are contributing most to the enhanced cooling. The box obstruction was also placed at BDC. Mid-annulus air temperatures for this case are also shown in figure 11.6. Whilst this configuration has only half of the venting area when compared to the previous end wall cases, it has retained the majority of

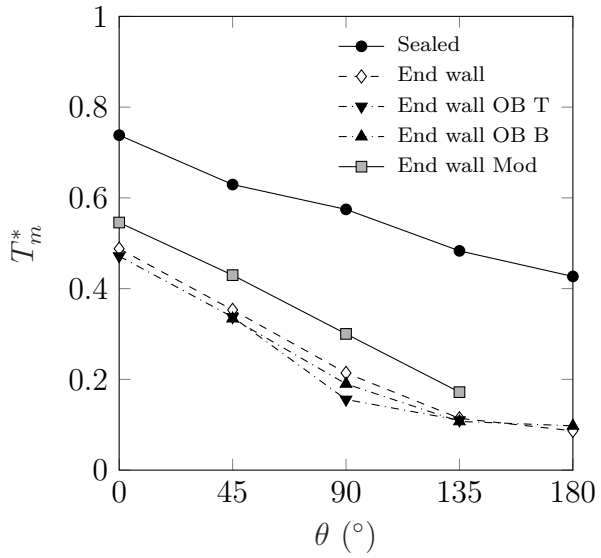

FIGURE 11.6: Air temperature measurements for end wall vent cases with obstructions. The modified end wall case is also included.

the air cooling enhancement effect. This is very promising result. Furthermore, it highlights that it is indeed the top 90° and bottom 90° sectors that are essential to this strategy as they allow for the largest natural draft to be created.

11.4 Heat Flux Fluctuations

The unsteady heat flux measurements are of interest here as they can help provide further insight into both auxiliary zone cooling strategies. The method outlined in section 7.3 was used to capture these results. Data was recorded at 32 Hz and averaged over a 60 second period. The unsteady heat flux has been non-dimensionalised here using the wall-to-ambient temperature difference. A video sequence of the Nusselt number fluctuations gives a good insight into the flow field evolution. A single frame each of the sealed, TB port vent and end wall vented cases are shown in figure 11.7 that highlights the main flow features.

The features of the sealed cases have been previously discussed in detail in section 7.3. The lower half of the sealed case appears bare, which indicates a very steady flow field. Between 90° and 45° we see alternating hot and cold streaks. The top

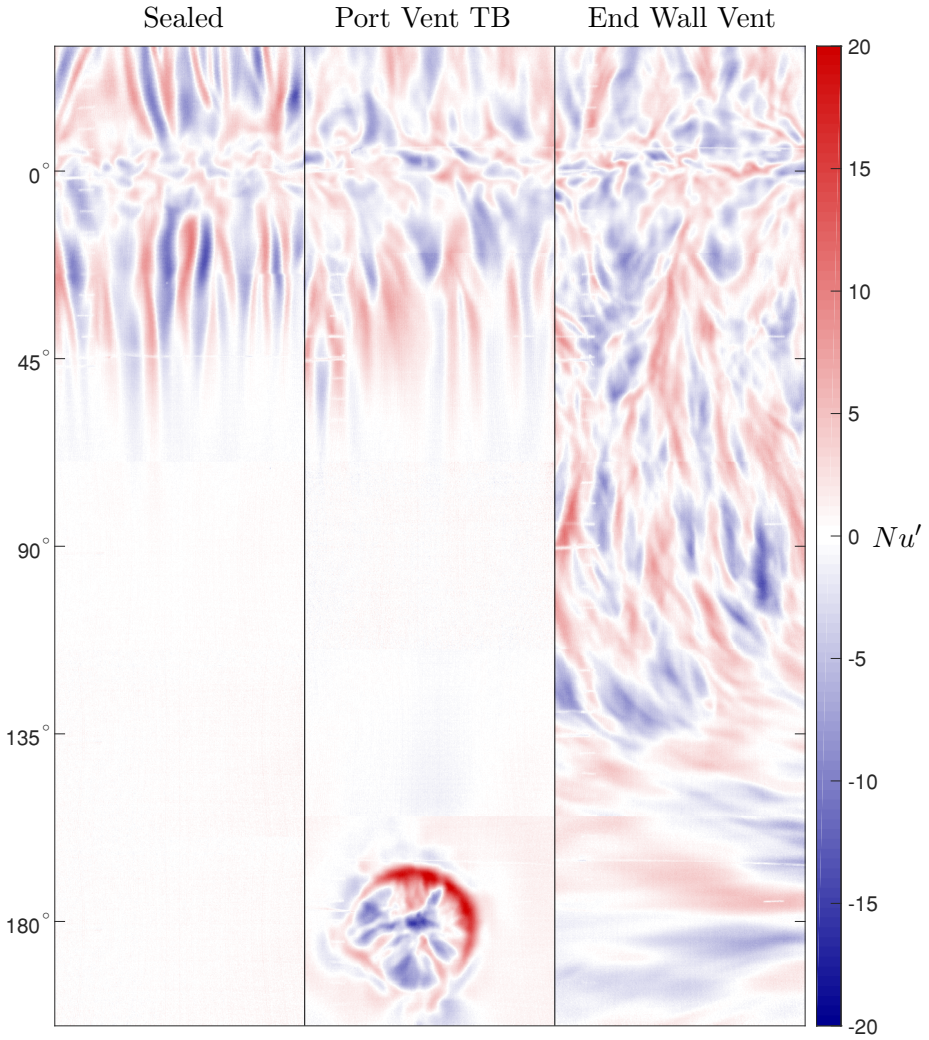

FIGURE 11.7: Example inner surface Nusselt number fluctuations for the sealed, TB port vent and end wall vented cases.

section is turbulent where these streaks from either side are colliding.

The influence of the impingement jet can be clearly seen at BDC of the port vent case. The fluctuations largely remain localised to the same area as highlighted in the steady state contour in figure 11.3, as the region between 70° and 150° shows no unsteady features. Although air is exiting through the outer cylinder port vent at TDC, the contours for this cases largely resemble the sealed case, which correlates to the steady state heat flux measurements being similar at this location.

The end wall case contour exhibits some vastly different features to the previous cases. The end wall opening is to the right of the contour, 615 mm away from its centreline. Firstly, at BDC, the large oblong shapes shown in figure 11.7 moves horizontally from right to left. This highlights the deep penetration of the ambient air that is inhaled in this experimental configuration. Moving upwards from this point, the features follow an arcing path as they ascend, becoming vertical in their direction of motion by 90°. Some remnants for the alternating hot/cold streak profile observed in the sealed case does remain, but the outlines are more jagged, which gives a more turbulent look to the contour. Similarities can be made at TDC across all three cases. However, the end wall vent case does show the mitigation of the air out of the annulus as the features are directed slightly towards the right.

11.5 Transient Cooling Effects

The impact of both the port and end wall venting on the transient cooling behaviour will now be examined. These experiments involve measuring the metal and air temperatures as the facility cools from a steady state of $Ra_{D_i} = 2.1 \times 10^9$. Figure 11.8a shows the top-to-bottom inner cylinder temperature difference during the cooling cycle for the sealed, port vented, and end wall vented case. The central mat row of thermocouples are used, i.e. directly in-line with the port vents and 615 mm

away from the end wall vent. The constituent thermocouple signals for these curves are shown in figure 11.8b.

Examining the port vent case, the bottom section cools slightly quicker than the corresponding sealed case, owing to the impingement caused by the natural draft. However, this enhancement quickly diminishes as the overall temperature reduces, which leads to the peak ΔT^* magnitude matching the sealed case. The port venting has marginally reduced the on-set time of peak ΔT, and the jaggedness of the ΔT^* curve indicates an increase in unsteadiness during the cooling cycle. It is difficult to see this unsteadiness in figure 11.8b due to the small magnitude of the fluctuations. As there is a through-flow of air in the TB case, it would have been expected that the upper section would also cool quicker. There are possible two reasons why this was not observed: the opening size was too small to make a significant impact; the plume region is already well-mixed because of the high Ra (see figure 7.10a on page 107) and thus, any additional mixing caused by the draft did not have much effect.

The reduction in mid-annulus air temperatures causes the inner cylinder to cool down faster in the end wall venting cases. The rate of cooling increase is larger for the bottom section – which correlates well to the steady-state air temperature measurements in figure 11.5a. The consequence of this is a 25% increase in inner surface top-to-bottom temperature difference.

The influence on rotor ΔT^* of increasing the asymmetry and changing the overall magnitude of the auxiliary zone inner wall heat flux during shutdown was investigated previously in section 9.4.3, using the numerical model. The results showed that for a 900 K starting temperature, a 25% increase in casing ΔT^* caused a 9% increase in rotor ΔT^*. However, increasing the overall cooling rate tends to suppress rotor ΔT^*. Therefore, the increase in the overall cooling rate caused by end wall venting will help to offset any rise in rotor ΔT^* that may occur due to altering the asymmetry of the casing heat flux.

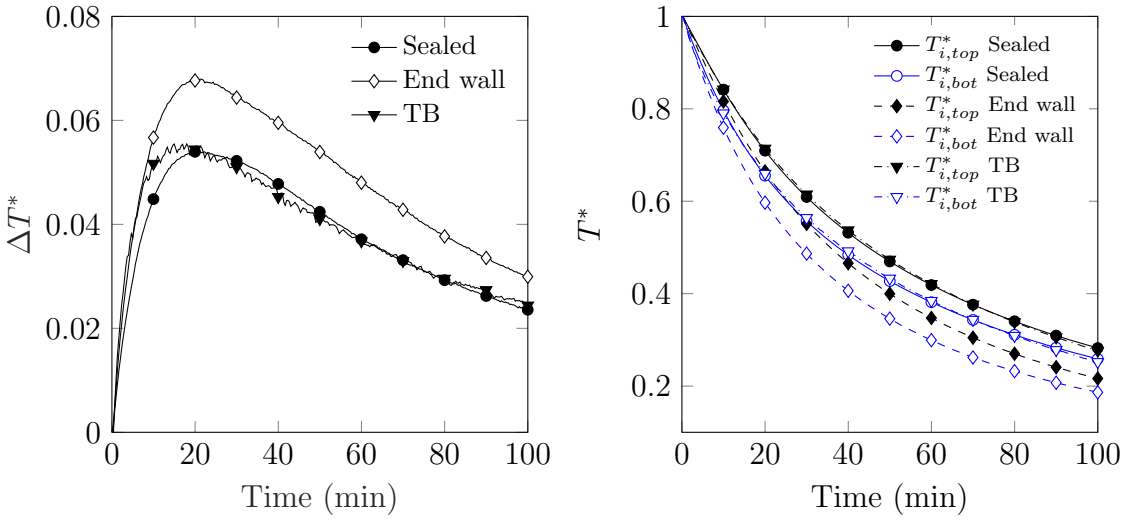

FIGURE 11.8: **a:** Inner cylinder top-to-bottom temperature difference for the transient cooling of the ExCITE facility with different ventilation arrangements. **b:** The constituent temperature signals for the ΔT^* curves.

11.6 Conclusions

Two potential methods for cooling the auxiliary zone of a large gas turbine during shutdown have been investigated experimentally. The port venting arrangements that were studied did help to decrease the bulk fluid temperature at BDC, but were ineffective at this task at TDC, as the effects remains localised to the lower sector.

The dramatic effects of end wall venting has been displayed in numerous ways. It has caused a large drop in air temperature at all circumferential locations, thoroughly outperforming the port vent configurations in this regard. The penetration of the cooling effect is also significant. Although the end wall opening was only 3% of the axial span, the temperature probe readings that are 0.58 times the axial span away from the opening had T^* values of 0.1 at BDC. The heat fluctuation contours also indicate that the effects extend further inwards from this point.

Furthermore, the inclusion of an obstruction at either the top or bottom of the annulus did not lessen the cooling response. A real engine will have many more obstructions than the experimental setup but nonetheless, the results are very

encouraging. Another important factor to consider is the circumferential placement of the supports that are needed to connect the inner and outer components: these should be placed close to the lateral positions ($\theta = \pm 90°$) as this gives the maximum allowable vertical distance between the top and bottom openings.

The end wall venting method does have a potential drawback in that it did increase the inner surface ΔT^*, which could have a knock-on effect on rotor bow. However, the massive reductions in air temperature that as possible with this simple method of cooling may outweigh this negative. Further work is needed to characterise the relationship between the penetration depth and the opening size, along with obstruction interaction, but overall, end wall venting has been validated as a viable mitigation strategy for auxiliary zone cooling during shutdown cooling of a civil gas turbine.

Chapter 12

Conclusions and Future Work

12.1 Conclusions

As a large civil gas turbine is cooling following operation, natural convective flows develop. These flows can lead to numerous issues. The ability to predict and understand this transient behaviour of a gas turbine is becoming increasingly more important. However, this has proven to be extremely difficult owing to the complex nature of the flow physics and its dependency on a large number of parameters.

Two sophisticated experimental facilities, that simulate the natural convective flow field during shutdown cooling of a large civil gas turbine, have been designed and commissioned. Careful control of the thermal boundary conditions has been achieved through the use of discrete heater mats and a PID control loop system. The design of the rigs allowed for the influence of numerous features to be investigated, which has helped to increase understanding of these flow fields. The RoBo facility models the high-pressure compressor region of a gas turbine, where rotor bow has been found to be an issue. The versatile design allowed for an investigation into the influence on natural convective heat transfer of the following parameters: non-isothermal wall thermal boundary conditions, diameter ratio, inner surface cone angle, axial

ventilation, and inclusion of obstructions. The larger ExCITE facility simulates the shutdown condition of the auxiliary zone of a gas turbine.

A low-cost, robust thermocouple probe has been developed that allows for accurate temperature measurements in a natural convective boundary layer.; from this the local heat flux can be determined with reasonable uncertainty. An vast numerical and experiment analysis conclusively showed that conduction error has been reduced significantly by mounting a portion of the wire parallel to the heated surface. An optimum value of this wire length was obtained.

An extensive experimental study conducted on the RoBo facility has shown that the overall heat transfer in a non-isothermal concentric annulus is adequately captured by isothermal correlations when the area-averaged temperature difference is used, as the local heat flux is dominated by the local radial temperature difference. This finding was validated up to a diameter ratio of 1.50, which is applicable to the majority of the main gas path of a large civil gas turbine. Furthermore, a shallow inner wall cone angle did not alter the heat transfer behaviour.

Results from non-isothermal outer tests on the ExCITE facility, which has a larger diameter ratio ($Dr = 2$), did not give as strong a correlation to previously published results for isothermal cases when compared to the RoBo rig findings. However, on the whole, the use of an equivalent conductivity has been shown to be a very useful way of correlating the heat data from many different boundary conditions and geometries with Rayleigh number. Inclusion of an obstruction, which represented a component that may be in the auxiliary zone of an engine, did not cause any disruption to the bulk fluid temperature profile.

An IR camera method has been developed that allows for a full surface measurement of heat flux fluctuations. This non-intrusive method provides a lot of information about the unsteady temperature field, allowing for detailed qualitative descriptions. The results were also in good agreement with CFD predictions.

An experimental investigation into the impact of installation effects on the natural convective flow field in a gas turbine has led to some key discoveries. Steady-state open-ended traverses have highlighted that the induced natural draft amplifies the top-to-bottom difference in inner wall heat flux, which in-turn increases the severity of thermal bow. Furthermore, the interaction between axial ventilation and blade rows has been found to be critical in defining the severity of thermal rotor bow. Therefore, it is imperative that these effects are included and captured correctly in order for a prediction method to be effective.

Results from both experimental facilities have been incorporated into a novel shut-down cooling model, that can adequately simulate the transient cooling cycle. The formulation allows for the effects of the axial ventilation and blade row interaction to be included. The model has ben tuned to match the cooldown results of the RoBo facility. Thus, the largest uncertainty involved in this modelling procedure remains selecting the appropriate level of this ventilation that best replicates the various stages of an engine compressor during shutdown. Application of the model to engine-representative geometry of one disk showed that reducing the total amount of energy contained in the rotor drum, by idling prior to shutdown, reduces the severity of rotor bow – irrespective of the initial metal radial temperature gradient.

Two viable solutions to help alleviate thermal rotor bow in large civil gas turbines during shutdown cooling have been presented: jet impingement cooling at the top of the annulus, and circumferentially non-uniform emissivity distributions. Forcing air into the annulus at top-dead-centre leads to impingement heat transfer on this section of the rotor. The relatively large heat transfer coefficients, coupled with a sizeable jet-to-wall temperature difference, means that low Reynolds number jets are powerful enough to completely suppress positive rotor bow. Radiative heat flux can exceed the magnitude of natural convective heat fluxes in engine conditions, so manipulating the circumferential distribution of emissivity can offset the inherent asymmetry of the natural convection. Both of these strategies must be carefully

matched to anticipated levels of bow so that large peaks in negative bow are not introduced.

Two potential methods for reducing the air temperatures in the auxiliary zone on an engine were investigated experimentally on the ExCITE facility: port venting and end-wall venting. The port venting arrangements that were studied did help to decrease the bulk fluid temperature at BDC, but were ineffective at this task at TDC, as the effects remains localised to the lower sector. End-wall venting proved to be very effective as it caused a large drop in air temperature at all circumferential locations, when compared to the sealed case. It has been shown that any supports needed in the end-wall venting section should be placed close to the lateral positions ($\theta = \pm 90°$) as this gives the maximum allowable vertical distance between the top and bottom openings.

12.2 Future Work

There is scope for some further tests conditions on the ExCITE facility, which were not completed due to time constraints. These include: outer cylinder boundary layer measurements, non-isothermal inner cylinder temperature distributions and axially-varying inner cylinder distributions. This data could then be used to further validate the CFD method presented in Chapter 7. Although this method is computationally intense, it is not unfeasible to include obstructions and openings in order to compare to the experimental conditions. This would be the first step in determining what level of detail is required in an auxiliary zone in order to predict air temperatures during shutdown cooling.

One of the key findings from this work was the strong interaction between the axial ventilation and obstructions. A large uncertainty surrounds how this phenomenon scales to a full engine design. The next logical experimental campaign should further investigate this condition in an attempt to elucidate how the size of the opening,

penetration depth, obstruction geometry and Rayleigh number interact to set the circumferential distribution of convective heat flux. The experimental campaign in chapter 8 had the opening at the concentric cylinder side of the facility, with the other end sealed (see figure 6.2 on page 80). It would be interesting to reverse this arrangement and repeat the transient cooling experiments. This arrangement may be more representative of the flow conditions in a large civil gas turbine, due to the rising annulus line in the direction of the flow.

The shutdown cooling model can either be advanced to include more compressor stages, or the method of defining the local heat flux can be implemented into a purpose-built FEA solver. The second option allows for a more complicated engine geometry to be simulated and account for conduction heat transfer between engine components – including the important high-pressure turbine. This aspect will be very important in improving the prediction of on-set time of peak rotor bow, as there will undoubtedly be axial temperature gradients in the engine at the commencement of shutdown. However, either approach would require the knowledge obtained from the previous paragraph. Overall, this would lead to a robust, efficient shutdown temperature prediction method. Comparison to engine temperature data during shutdown, if it is available, would provide an invaluable validation data set. This in-turn can be used to optimise any of the mitigation strategies that have been developed.

12.3 Final Remarks

Experimental investigations into simplified representations of an engine has provided a greater fundamental understanding of the natural convective heat flow that is occurring during transient shutdown cooling. Two sophisticated and adaptable facilities have been developed, along with feasible mitigation strategies for the unwanted consequences of shutdown.

References

[1] Sagheer Ahmad. Rotor Casing Contact Phenomenon in Rotor Dynamics – Literature Survey. *Journal of Vibration and Control*, 16(9):1369–1377, 2010.

[2] A. A. Y. AlWaaly, M. C. Paul, and P. S. Dobson. Effects of Thermocouple Electrical Insulation on the Measurement of Surface Temperature. *Applied Thermal Engineering*, 89:421–431, 2015.

[3] D. Angeli, G. S. Barozzi, M. W. Collins, and O. M. Kamiyo. A Critical Review of Buoyancy-Induced Flow Transitions in Horizontal Annuli. *International Journal of Thermal Sciences*, 49(12):2231–2241, 2010.

[4] Tommaso Astarita and Giovanni Maria Carlomagno. *Infrared Thermography for Thermo-Fluid-Dynamics*. Springer Berlin Heidelberg, 2013.

[5] Leonardo Baldassarre and Michele Fontana. Modeling of Rotor Bow During Hot Restrat in Centrifugal Compressors. In *39th Turbomachinery Symposium*, pages 1–8, 2010.

[6] Olivier Bardon and Ludovic Garnier. Natural Heat Convective Coefficient Measurements Around a Large-Diameter Cylindrical Surface Equipped with Axial Fins. *Nuclear Technology*, 201(2):103–112, 2018.

[7] W Beckmann. Die Wärmeübertraegung in zylindrischen Gasschichten bei natürlicher Konvektion. *Forschung auf dem Gebiete des Ingenieurwesens*, 2(5):165–178, 1931.

[8] Adrian Bejan. *Convection Heat Transfer*. John Wiley & Sons, 4th edition, 2013.

[9] Robin E Bentley, editor. *Handbook of Temperature Measurement*, volume 1. Springer, 1998.

[10] E. H. Bishop. Heat Transfer by Natural Convection of Helium Between Horizontal Isothermal Concentric Cylinders at Cryogenic Temperature. en. *Journal of Heat Transfer*, 110(1):109–115, February 1988.

[11] E.H. Bishop, C.T. Carley, and R.E. Powe. Natural Convective Oscillatory Flow in Cylindrical Annuli. *International Journal of Heat and Mass Transfer*, 11(12):1741–1752, 1968.

[12] B. Blackwell and R. Moffat. Design and Construction of a Low-Velocity Boundary-Layer Temperature Probe. *Journal of Heat Transfer*, 97(2), 1974.

[13] D. Born, P. Stein, G. Marinescu, S. Koch, and D.l Schumacher. Thermal Modeling of an Intermediate Pressure Steam Turbine by Means of Conjugate Heat Transfer–Simulation and Validation. *Journal of Engineering for Gas Turbines and Power*, 139(3):031903, 2017.

[14] Edimilson Braga and Marcelo de Lemos. Natural Convection in Turbulent Regime in Concentric and Eccentric Horizontal Annular Regions. In *8th AIAA/ASME Joint Thermophysics and Heat Transfer Conference*, 2002.

[15] V. I. Bubnovich and P. M. Kolesnikov. Conjugate Transient Heat Transfer in Laminar Natural Convection in a Horizontal Cylindrical Annulus. 51(4):1175–1181, 1986.

[16] Yunus Cengel. *Heat and Mass Transfer, A Practical Approach*. McGraw-Hill, 3rd edition, 2006.

[17] R. Cheesewright. Turbulent Natural Convection from a Vertical Plane Surface. *Journal of Heat Transfer*, 90(1):1–6, 1968.

[18] S. W. Churchill and M. Bernstein. A Correlating Equation for Forced Convection From Gases and Liquids to a Circular Cylinder in Crossflow. *Journal of Heat Transfer*, 99(2):300–306, 1977.

[19] S. W. Churchill and H. Chu. Correlating Equations for Laminar and Turbulent Free Convection from a Horizontal Cylinder. *International Journal of Heat and Mass Transfer*, 18(9):1049–1053, 1975.

[20] S. W. Churchill and H. Chu. Correlating Equations for Laminar and Turbulent Free Convection from a Vertical Plate. *International Journal of Heat and Mass Transfer*, 18(11):1323–1329, 1975.

[21] Crydom. PMP Series Control Relays Datasheet, 2017. `http://www.crydom.com/en/products/catalog/pmp-nova22-proportional-control.pdfhttp://www.crydom.com/en/products/catalog/pmp-nova22-proportional-control.pdf`, Last accessed on 07-07-2020.

[22] C. P. Desai and K. Vafai. Experimental and Numerical Study of Buoyancy-Induced Flow and Heat Transfer in an Open Annular Cavity. *International Journal of Heat and Mass Transfer*, 39(10):2053–2066, 1996.

[23] C.P. Desai and K. Vafai. An Investigation and Comparative Analysis of Two- and Three-Dimensional Turbulent Natural Convection in a Horizontal Annulus. *International Journal of Heat and Mass Transfer*, 37(16):2475–2504, 1994.

[24] P. Dhopade and B. Tang. CFD Methodology Report for Fire Zone Thermal Modelling after Engine Shutdown, 2020. Internal Report.

[25] M. P. Dyko and K. Vafai. Three-Dimensional Natural Convective States in a Narrow-Gap Horizontal Annulus. *Journal of Fluid Mechanics*, 445:1–36, 2001.

[26] A. Ebadi, F. Mehdi, and C. M. White. An Exact Integral Method to Evaluate Wall Heat Flux in Spatially Developing Two-Dimensional Wall-Bounded Flows. *International Journal of Heat and Mass Transfer*, 84:856–861, 2015.

[27] Edmund Optics. The Correct Material for Infrared Applications. `https://www.edmundoptics.eu/knowledge-center/application-notes/optics/the-correct-material-for-infrared-applications#introduction`, Last accessed on 07-07-2020.

[28] M. Elfner, A. Schulz, H. Bauer, and K. Lehmann. A Novel Test Rig for Assessing Advanced Rotor Blade Cooling Concepts, Measurement Technique and First Results. In *Proceedings of the ASME Turbo Expo 2017: Turbomachinery Technical Conference and Exposition*, V05AT16A015. ASME, 2017.

[29] Evonik. Rohacell IG-F Product Information, 2020. `http://www.rohacell.com/product/rohacell/en/products-services/rohacell-ig-ig-f/`, Last accessed on 12-01-2020.

[30] F. R. Caldwell. Thermocouple Materials. *National Bureau of Standards Monograph 40*, 1960.

[31] B. Farouk and S. Guceri. Laminar and Turbulent Natural Convection in the Annulus Between Horizontal Concentric Cylinders. *Journal of Heat Transfer*, 104(4):631–636, 1982.

[32] C. E. Fisher and K. S. Ball. Plume Dynamics in Natural Convection in a Horizontal Cylindrical Annulus. *Journal of Heat Transfer*, 121(3):598–602, 1999.

[33] K. Fukuda, Y. Miki, and S. Hasegawa. Analytical and Experimental Study on Turbulent Natural Convection in a Horizontal Annulus. *International Journal of Heat and Mass Transfer*, 33(4):629–639, 1990.

[34] K. Fukuda, Y. Miki, N. Taniguchi, K Morita, and S Hasegawa. Direct Simulation and Large Eddy Simulation of Turbulent Natural Convection in Horizontal Annulus. *Memoirs of the Faculty of Engineering, Kyushu University*, 51(4), 1991.

[35] G. Gaussorgues. *Infrared Thermography*. Springer Netherlands, 1994.

[36] William George and Steven Capp. A Theory for Natural Convection Turbulent Boundary Layers next to Heated Vertical Surfaces. *International Journal of Heat and Mass Transfer*, 22(6):813–826, 1979.

[37] E. K. Glakpe, C. B. Watkins, and J. N. Cannon. Constant Heat FLux Solutions for Natural Convection Between Concentric and Eccentric Horizontal Cylinders. *Numerical Heat Transfer*, 10(3):279–295, 1986.

[38] R. J. Goldstein, K. A. Sobolik, and W. S. Seol. Effect of Entrainment on the Heat Transfer to a Heated Circular Air Jet Impinging on a Flat Surface. *Journal of Heat Transfer*, 112(3):608–611, 1990.

[39] UIUC Applied Aerodynamics Group. UIUC Airfoil Coordinates Database. `https://m-selig.ae.illinois.edu/ads/coord_database.html#N`, Last accessed on 07-07-2020.

[40] Jon Hemmerdinger. Flight Global: P&W fix will cut PW1100G start-up delay in half, 2016. `http://www.flightglobal.com/pandw-fix-will-cut-pw1100g-start-up-delay-in-half/120323.article`, Last accessed on 17-04-2020.

[41] R. A. W. M. Henkes and C. J. Hoogendoorn. Numerical Determination of Wall Functions for the Turbulent Natural Convection Boundary Layer. *International Journal of Heat and Mass Transfer*, 33(6):1087–1097, 1990.

[42] V. Hindasageri, R. P. Vedula, and S. V. Prabhu. Thermocouple Error Correction for Measuring the Flame Temperature with Determination of Emissivity and Heat Transfer Coefficient. *Review of Scientific Instruments*, 84(2):024902, 2013.

[43] N. E. Holgate, P. T. Ireland, and E. Romero. The Effects of Combustor Cooling Features on Nozzle Guide Vane Film Cooling Experiments. *Journal of Turbomachinery*, 141(1):011005, 2019.

[44] J. Howell, R. Siegel, and P. Mengüç. *Thermal Radiation Heat Transfer*. CRC Press, 5th edition, 2011.

[45] M. Itoh, N. Nishiwaki, and M. Hirata. A New Method of Correlating Heat-Transfer Coefficients for Natural Convection in Horizontal Cylindrical Annuli. *International Journal of Heat and Mass Transfer*, 13(8):1364–1368, 1970.

[46] W. M. Kays, B. Weigand, and M. E. Crawford. *Convective Heat and Mass Transfer*. McGraw-Hill, 4th edition, 2005.

[47] S. Kenjereš and K. Hanjalić. Prediction of turbulent thermal convection in concentric and eccentric horizontal annuli. *International Journal of Heat and Fluid Flow*, 16(5):429–439, 1995.

[48] Benjamin Kirollos. *Aerothermal Optimisation of Novel Cooling Schemes for High Pressure Components using Combined Theoretical, Numerical and Experimental Techniques*. PhD thesis, University of Oxford, 2015.

[49] Benjamin Kirollos and Thomas Povey. High-Accuracy Infra-Red Thermography Method Using Reflective Marker Arrays. *Measurement Science and Technology*, 28(9), 2017.

[50] K. Kitamura, F. Kami-iwa, and T. Misumi. Heat Transfer and fluid flow of Natural Convection around Large Horizontal Cylinders. *International Journal of Heat and Mass Transfer*, 42(22):4093–4106, 1999.

[51] Chris J. Kobus. True Fluid Temperature Reconstruction Compensating for Conduction Error in the Temperature Measurement of Steady Fluid Flows. *Review of Scientific Instruments*, 77(3), 2006.

[52] J. C. Y. Koh and J. F. Price. Laminar Free Convection From a Nonisothermal Cylinder. *Journal of Heat Transfer*, 87(2):237–241, 1965.

[53] P. M. Kolesnikov and V. E. Bubnovich. Non-Stationary Conjugate Free-Convective Heat Transfer in Horizontal Cylindrical Coaxial Channels. *International Journal of Heat and Mass Transfer*, 31(6):1149–1156, 1988.

[54] T. H. Kuehn and R. J. Goldstein. A Parametric Study of Prandtl Number and Diameter Ratio Effects on Natural Convection Heat Transfer in Horizontal Cylindrical Annuli. *Journal of Heat Transfer*, 102(4):768–770, 1980.

[55] T. H. Kuehn and R. J. Goldstein. An Experimental and Theoretical Study of Natural Convection in the Annulus between Horizontal Concentric Cylinders. *Journal of Fluid Mechanics*, 74(4):695–719, 1976.

[56] T. H. Kuehn and R. J. Goldstein. An Experimental Study of Natural Convection Heat Transfer in Concentric and Eccentric Horizontal Cylindrical Annuli. *Journal of Heat Transfer*, 100(4):635–640, 1978.

[57] T. H. Kuehn and R. J. Goldstein. Correlating Equations for Natural Convection Heat Transfer between Horizontal Circular Cylinders. *International Journal of Heat and Mass Transfer*, 19(10):1127–1134, 1976.

[58] T. H. Kuehn and R. J. Goldstein. Numerical Solution to the Navier-Stokes Equations for Laminar Natural Convection about a Horizontal Isothermal Circular Cylinder. *International Journal of Heat and Mass Transfer*, 23(7):971–979, 1980.

[59] K. S. Kulkarni, S. Han, and R. J. Goldstein. Numerical Simulation of Thermal Boundary Layer Profile Measurement. *Heat and Mass Transfer*, 47(8):869–877, 2011.

[60] K. S. Kulkarni, U. Madanan, T. W. Simon, and R. J. Goldstein. Experimental Validation of a Boundary Layer Convective Heat Flux Measurement Technique. *Journal of Heat Transfer*, 140(7):074501, 2018.

[61] R. Kumar and M. Keyhani. Flow Visualization Studies of Natural Convective Flow in a Horizontal Cylindrical Annulus. *Journal of Heat Transfer*, 112(3):784–787, 1990.

[62] Ranganathan Kumar. Study of Natural Convection in Horizontal Annuli. *International Journal of Heat and Mass Transfer*, 31(6):1137–1148, 1988.

[63] G. Labonia and G. Guj. Natural Convection in a Horizontal Concentric Cylindrical Annulus: Oscillatory Flow and Transition to Chaos. *Journal of Fluid Mechanics*, 375:179–202, 1998.

[64] C. F. Lange, F. Durst, and M. Breuer. Wall Effects on Heat Losses from Hot-Wires. *International Journal of Heat and Fluid Flow*, 20(1):34–47, 1999.

[65] B. Laveau, R. S. Abhari, M. E. Crawford, and E. Lutum. High Resolution Heat Transfer Measurements on the Stator Endwall of an Axial Turbine. *Journal of Turbomachinery*, 137(4):041005, 2015.

[66] W.M. Lewandowski and S. Leble. Study of Free Convective Heat Transfer from Horizontal Conic. *International Journal of Heat and Mass Transfer*, 46(25):4925–4934, 2003.

[67] R. Maffulli, L. He, P. Stein, and G. Marinescu. Fast Conjugate Heat Transfer Simulation of Long Transient Flexible Operations Using Adaptive Time Stepping. *Journal of Turbomachinery*, 140(9):091005, 2018.

[68] F. M. Mahfouz. Heat Convection Within an Eccentric Annulus Heated at Either Constant Wall Temperature or Constant Heat Flux. *Journal of Heat Transfer*, 134(8):082502, 2012.

[69] G. Marinescu, W. F. Mohr, A. Ehrsam, P. Ruffino, and M. Sell. Experimental Investigation Into Thermal Behavior of Steam Turbine Components–Temperature Measurements With Optical Probes and Natural Cooling Analysis. *Journal of Engineering for Gas Turbines and Power*, 136(2):021602, 2014.

[70] A. E. McLeod and E. H. Bishop. Turbulent Natural Convection of Gases in Horizontal Cylindrical Annuli at Cryogenic Temperatures. *International Journal of Heat and Mass Transfer*, 32(10):1967–1978, 1989.

[71] *Metallic Materials Properties Development and Standardization (MMPDS) Handbook - 11.* Battelle Memorial Institute, 2016.

[72] Waldemar Minkina and Sebastian Dudzik. *Infrared Thermography: Errors and Uncertainties.* John Wiley & Sons, 2009.

[73] T. Misumi, K. Suzuki, and K. Kitamura. Fluid Flow and Heat Transfer of Natural Convection around Large Horizontal Cylinders: Experiments with Air. *Heat Transfer Asian Research*, 32(4):293–305, 2003.

[74] Morgan Advanced Materials. Superwool Technical Manual. `https://www.morganthermalceramics.com/media/6915/superwool-manual.pdf`, Last accessed on 11-09-2020.

[75] A. V. Murray, P. T. Ireland, and E. Romero. Development of a Steady-State Experimental Facility for the Analysis of Double-Wall Effusion Cooling Geometries. *Journal of Turbomachinery*, 141(4):041008, 2019.

[76] National Instruments. NI 9214 and TB-9214 Datasheet, 2016. `https://www.ni.com/pdf/manuals/375138a_02.pdf`, Last accessed on 07-07-2020.

[77] J. C. Nicholas, E. J. Gunter, and P. E. Allaire. Effect of Residual Shaft Bow on Unbalance Response and Balancing of a Single Mass Flexible Rotor–Part I: Unbalance Response. *Journal of Engineering for Power*, 98(2):171–181, 1976.

[78] Herbert Oertel, editor. *Prandtl's Essentials of Fluid Mechanics*. Springer, 2nd edition, 2004.

[79] P. H. Oosthuizen. Free Convective Heat Transfer From Horizontal Cones. *Journal of Heat Transfer*, 95(3):409–410, 1973.

[80] Optris GmbH. Optris PI-640 Datasheet. `http://www.optris.co.uk/thermal-imager-optris-pi-640`, Last accessed on 07-07-2020.

[81] E. L. M. Padilla and A. Silveira-Neto. Large-Eddy Simulation of Transition to Turbulence in Natural Convection in a Horizontal Annular Cavity. *International Journal of Heat and Mass Transfer*, 51(13-14):3656–3668, 2008.

[82] G. Petrone, E. Chénier, and G. Lauriat. Three-Dimensional Study of Multiple Transitions for Natural Convection in Horizontal Annuli. *International Journal of Heat and Mass Transfer*, 49(7-8):1231–1241, 2006.

[83] A. Pilkington, B. Rosic, and S. Horie. Methods for Controlling Gas Turbine Casing Flows During Engine Shutdown. *International Journal of Turbomachinery Propulsion and Power*, 3(2):17, 2018.

[84] A. Pilkington, B. Rosic, K. Tanimoto, and S. Horie. Prediction of Natural Convection Heat Transfer in Gas Turbines. *International Journal of Heat and Mass Transfer*, 141:233–244, 2019.

[85] Andrew Pilkington. *Numerical Prediction of Natural Convection in Gas Turbines*. PhD thesis, University of Oxford, 2018.

[86] R. E. Powe, C. T. Carley, and E. H. Bishop. Free Convective Flow Patterns in Cylindrical Annuli. *Journal of Heat Transfer*, 91(3):310–314, 1969.

[87] R. E. Powe, C. T. Carley, and S. L. Carruth. A Numerical Solution for Natural Convection in Cylindrical Annuli. *Journal of Heat Transfer*, 93(2):210–220, 1971.

[88] G. D. Raithby and K. G. T. Hollands. A General Method of Obtaining Approximate Solutions to Laminar and Turbulent Free Convection Problems. In *Advances in Heat Transfer*. Volume 11, pages 265–315. 1975.

[89] Rao, Y.i and Miki, Y. and Fukuda, K. and Takata, Y.and Hasegawa, S. Flow Patterns of Natural Convection in Horizontal Cylindrical Annuli. *International Journal of Heat and Mass Transfer*, 28(3):705–714, 1985.

[90] V. V. Reddy, K. Selvam, and R. De Prosperis. Gas Turbine Shutdown Thermal Analysis and Results Compared With Experimental Data. In *Proceedings of the ASME Turbo Expo 2016: Turbomachinery Technical Conference and Exposition. Volume 5C: Heat Transfer*. V05CT18A005. ASME, 2016.

[91] W. M. Rohsenow, J. P. Hartnett, and Y. I. Cho, editors. *Handbook of Heat Transfer*. McGraw-Hill, 3rd edition, 1998.

[92] Sanyo Denki. SanACE B97 technical specifications. `http://products.sanyodenki.com/en/sanace/dc/blower/9BMC12P2G001/`, Last accessed on 07-07-2020.

[93] D.L. Schultz and T. Jones. *Heat Transfer Measurements in Short-Duration Hypersonic Facilities*. DTIC Document AGARD AG-165, 1973.

[94] D. L. Siebers, R. F. Moffatt, and R. G. Schwind. Experimental, Variable Properties Natural Convection From a Large, Vertical, Flat Surface. *Journal of Heat Transfer*, 107(1):124–132, 1985.

[95] Smith, E. O. and de Baar, J. H. S. and Neely, A. J. A Sobol' Sequence Parametric Analysis of Rotor Thermal Bow in Gas Turbines. In *Proceedings of the ASME Turbo Expo 2018: Turbomachinery Technical Conference and Exposition. Volume 7A: Structures and Dynamics*, V07AT33A010. ASME, 2018.

[96] E. O. Smith, A. J. Neely, and A. P. Butcher. Experimental Observations of Thermal Bow due to Natural Convection on a Gas Turbine Compressor Rotor Shaft Analogue. In *Proceedings of the ASME Turbo Expo 2016: Turbomachinery Technical Conference and Exposition. Volume 5C: Heat Transfer*, V05CT18A006. ASME, 2016.

[97] Evan Oscar Smith. *A Parametric Study of Compressor Rotor Thermal Bow in Aerospace Gas Turbines*. PhD thesis, University of New South Wales, 2017.

[98] Evan Oscar Smith and Andrew J. Neely. The Effect of Aircraft Integration Design on Gas Turbine Shaft Thermal Bow and the Newkirk Effect. In *Volume 5A: Heat Transfer*, V05AT11A009. ASME, 2014.

[99] E. M. Sparrow, R. Eichhorn, and J. L. Gregg. Combined Forced and Free Convection in a Boundary Layer Flow. *Physics of Fluids*, 2:319, 1959.

[100] Stratasys. Vero Material Data Sheet. `https://www.stratasys.com/materials/search/vero`, Last accessed on 07-07-2020.

[101] John R. Taylor. *An Introduction to Error Analysis: The Study of Uncertainties in Physical Measurements*. University Science Books, 2nd edition, 1997.

[102] P. Teertstray and M. M. Yovanovichz. Comprehensive Review of Natural Convection in Horizontal Circular Annuli. In *7th AIAA/ASME Joint Thermophysics and Heat Transfer Conference*, 1998.

[103] Temperature-Electromotive Force Reference Functions and Tables for the Letter-Designated Thermocouple Types Based on the ITS-90, 2014. https://srdata.nist.gov/its90/menu/menu.html, Last accessed on 07-07-2020.

[104] Thomson. Minture Components and Systems. http://www.thomsonlinear.com/downloads/bearings_guides/Miniature_Components_Systems_bren.pdf, Last accessed on 07-07-2020.

[105] A. Tisarev, S. Falaleev, C. Koch, M. Nagorski, and S. Staudacher. Natural Cooling Affecting the Restart of Micro Gas Turbine. In *Proceedings of the ASME Turbo Expo 2016: Turbomachinery Technical Conference and Exposition. Volume 8: Microturbines, Turbochargers and Small Turbomachines; Steam Turbines*, V008T23A019. ASME, 2016.

[106] M. Topel, M. Genrup, M. Jöcker, J. Spelling, and B. Laumert. Operational Improvements for Startup Time Reduction in Solar Steam Turbines. *Journal of Engineering for Gas Turbines and Power*, 137(4):042604, 2015.

[107] M. Topel, M. Jöcker, S. Paul, and B. Laumert. Differential Expansion Sensitivity Studies During Steam Turbine Startup. *Journal of Engineering for Gas Turbines and Power*, 138(6):062102, 2016.

[108] TSI. Model 8345/8346/8347/8347A VELOCICALC Air Velocity Meters Operation and Service Manual, 2002. http://www.tsi.com/getmedia/6f4ba610-a352-4fce-b178-c3683e97334d/1980277E-Model-8345-8346-8347-8347A-Mnl?ext=.pdf, Last accessed on 07-07-2020.

[109] T. Tsuji and Y. Nagano. Characteristics of a Turbulent Natural Convection Boundary Layer along a Vertical Flat Plate. *International Journal of Heat and Mass Transfer*, 31(8):1723–1734, 1988.

[110] K. Vafai, C. P. Desai, S. V. Iyer, and M. P. Dyko. Buoyancy Induced Convection in a Narrow Open-Ended Annulus. *Journal of Heat Transfer*, 119(3):483–494, 1997.

[111] E. Van De Sande and B. J. G. Hamer. Steady and Transient Natural Convection in Enclosures between Horizontal Circular Cylinders (Constant Heat Flux). *International Journal of Heat and Mass Transfer*, 22(3):361–370, 1979.

[112] Mao-Yu Wen and Kuen-Jang Jang. An Impingement Cooling on a Flat Surface by Using Circular Jet with Longitudinal Swirling Strips. *International Journal of Heat and Mass Transfer*, 46(24):4657–4667, 2003.

[113] Stephen Whitaker. Forced Convection Heat Transfer Correlations for Flow in Pipes, Past Flat Plates, Single Cylinders, Single Spheres, and for Flow in Packed Beds and Tube Bundles. *AIChE Journal*, 18(2):361–371, 1972.

[114] K. T Yang, J. L Novotny, and Y. S. Cheng. Laminar Free Convection from a Nonisothermal Plate Immersed in a Temperature Stratified Medium. *International Journal of Heat and Mass Transfer*, 15(5):1097–1109, 1972.

[115] Chun-Lang Yeh. Numerical Investigation of the Three-Dimensional Natural Convection inside Horizontal Concentric Annulus with Specified Wall Temperature or Heat Flux. *JSME International Journal Series B Fluids and Thermal Engineering*, 45(2):301–306, 2002.

[116] M. Zhuo, L. Yang, K. Xia, and L. Yu. A New Computational Method for Predicting the Thermal Bow of a Rotor. *Proceedings of the Institution of Mechanical Engineers, Part C: Journal of Mechanical Engineering Science*, 233(12):4372–4380, 2019.

[117] Neil Zuckerman and Noam Lior. Impingement Heat Transfer: Correlations and Numerical Modeling. *Journal of Heat Transfer*, 127(5):544–552, 2005.

Appendix A

Correlation for Natural Convection in a Horizontal Annulus

This section gives the steps in calculating k_{eq} from the method derived by Kuehn & Goldstein [57]. It is based on a conduction film at the surface of each cylinder, and an intermediate layer at a bulk fluid temperature – T_B. The method is valid for both laminar and turbulent flow. Equations A.1 and A.2 shows the expression for mean Nusselt number for convection on the inner cylinder and outer cylinder respectively.

$$\overline{Nu}_{D_{i,conv}} = \frac{2}{\ln\left[1 + \frac{2}{\left[\left(0.518Ra_{Di}^{1/4}\left[1+\left(\frac{0.559}{Pr}\right)^{3/5}\right]^{-5/12}\right)^{15} + (0.1Ra_{Di}^{1/3})^{15}\right]^{1/15}}\right]} \quad \text{(A.1)}$$

$$\overline{Nu}_{D_{o,conv}} = \frac{2}{-\ln\left[1 - \frac{2}{\left\{\left(\left[\left(\frac{2}{1-e^{-0.25}}\right)^{5/3} + (0.587Ra_{Do}^{1/4})^{5/3}\right]^{3/5}\right)^{15} + (0.1Ra_{Do}^{1/3})^{15}\right\}^{1/15}}\right]} \tag{A.2}$$

The temperature difference in Ra is $T_w - T_B$, hence these equations cannot be evaluated until T_B is known. As heat coming from the inner cylinder must equal heat going into the outer cylinder, T_B is found from equation A.3 below:

$$\frac{T_B - T_o}{T_i - T_b} = \frac{\overline{Nu}_{D_{i,conv}}}{\overline{Nu}_{D_{o,conv}}} \tag{A.3}$$

In practise, four or five iterations are required to find $\bar{T}_b$ from an initial guess so that equations A.2 and A.1 can be evaluated. The overall Nusselt number for natural convection can then be calculated by:

$$\overline{Nu'}_{D_{i,conv}} = \frac{2}{\ln\left[\frac{1 + 2/\overline{Nu}_{D_{i,conv}}}{1 - 2/\overline{Nu}_{D_{o,conv}}}\right]} \tag{A.4}$$

The overall Nusselt number by conduction is:

$$\overline{Nu'}_{D_{i,cond}} = \frac{2}{\ln(D_o/D_i)} \tag{A.5}$$

Equations A.4 and A.5 are then combined to find the overall Nusselt number:

$$\overline{Nu'}_{D_i} = [(\overline{Nu'}_{D_{i,conv}})^{15} + (\overline{Nu'}_{D_{i,cond}})^{15}]^{1/15} \tag{A.6}$$

Finally k_{eq} is given by dividing equation A.6 by equation A.5:

$$\overline{k}_{eq} = \frac{\overline{Nu'}_{D_i}}{\overline{Nu'}_{D_{i,cond}}} \tag{A.7}$$

Appendix B

Uncertainty Analysis

B.1 Convective heat flux

A least squares method is used to fit the points to the equation:

$$T = A + Bx \tag{B.1}$$

The least squares method gives the following equations for the constants:

$$A = \frac{\sum x^2 \sum T - \sum x \sum xT}{\Delta} \tag{B.2}$$

$$B = \frac{N \sum xT - \sum x \sum T}{\Delta} \tag{B.3}$$

$$\Delta = \sum x^2 - \left(\sum x\right)^2 \tag{B.4}$$

It is assumed that the uncertainty in measurements of T are equal, which is justifiable since it is the same thermocouple. Least squares fitting usually assumes that the uncertainties in the x measurements are negligible. The uncertainty of T is then:

$$\sigma_T = \sqrt{\frac{1}{N-2}\sum_{i-1}^{N}\left(T_i - A - Bx_i\right)^2} \tag{B.5}$$

The uncertainty in x can then be accounted for by converting it to an equivalent uncertainty in T [101]. This equation also assumes that all uncertainties in x are equivalent, again a reasonable assumption.

$$\sigma_{T,eq} = \sqrt{\sigma_T^2 + \left(B\sigma_x\right)^2} \tag{B.6}$$

The bias error of the thermocouple also needs to be accounted for. A type K thermocouple calculates temperature by fitting a linear temperature curve to a measured millivolt signal:

$$T = V_o + Gx \tag{B.7}$$

The quoted accuracy of this type of thermocouple ($2\sigma_{TC}$) is ± 2°C or $\pm 0.75\%$, over a temperature range of -270 to 1260°C. Any uncertainty in V_o will have no effect on the calculation of $\dot{q}$ as it depends on a temperature gradient. If it assumed that all of the inaccuracy is in the gain (G), then the maximum error of the true temperature slope is $\pm 0.6\%$. This highlights the advantage of this measurement technique. Using the method of propagation of errors applied to the equation above for B, and the bias error shown above, the uncertainty in the (slope) convective heat flux is:

$$\sigma_B = \sqrt{\sigma_{T,eq}^2 \frac{N}{\Delta} + \sigma_{B,b}^2} \tag{B.8}$$

This gave an uncertainty range of 3.5 to 14% to a 95% confidence interval ($\pm 2\sigma_B$)

B.2 Radiative Heat Flux

In order to estimate the uncertainty in the radiative heat flux, it is assumed that it can be modelled as infinitely long isothermal concentric cylinders. The net heat transfer from the inner surface is then given by equation B.9 [44].

$$\dot{q}_{io,rad} = \frac{\sigma \left(T_i^4 - T_o^4\right)}{\frac{1}{\varepsilon_i} + \frac{1-\varepsilon_o}{\varepsilon_o}\left(\frac{r_i}{r_o}\right)} \tag{B.9}$$

Applying the propagation of error method [101] to this equation yields:

$$\sigma^2_{\dot{q}_{io,rad}} = \left(\frac{\partial \dot{q}_{io,rad}}{\partial T_i}\right)^2 \sigma^2_{T_i} + \left(\frac{\partial \dot{q}_{io,rad}}{\partial T_o}\right)^2 \sigma^2_{T_o} + \left(\frac{\partial \dot{q}_{io,rad}}{\partial \varepsilon_i}\right)^2 \sigma^2_{\varepsilon_i} + \left(\frac{\partial \dot{q}_{io,rad}}{\partial \varepsilon_o}\right)^2 \sigma^2_{\varepsilon_o} \tag{B.10}$$

Assuming an uncertainty in the temperatures of $\pm 2°C$ and 10% uncertainty in both surface emissivity's gives a typical overall uncertainty of 11 to 13%.